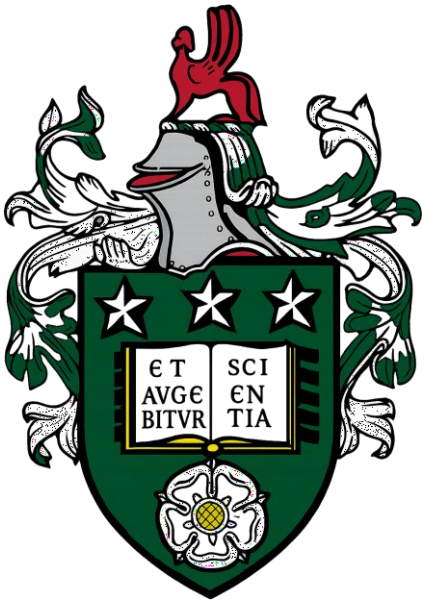
Comparing extensional fault evolution across the continental to oceanic rifting transition in the northern East African Rift and Afar Depression.



University of Leeds

School of Earth and Environment

Submitted in accordance with the requirements for the degree of Doctor of Philosophy

December 2025

By

Thamer Ahmed Alghamdi

Declaration Statement

The candidate confirms that the work submitted is their own and that appropriate credit has been given where references have been made to the work of others.

The candidate understands that the thesis may be screened using text-matching software to verify its originality.

Generative AI tools were used only to assist with proofreading and grammar checking; no original scientific content, interpretations, or results were generated by AI.

This copy has been supplied on the understanding that it is copyright material and that no quotation from the thesis may be published without proper acknowledgement.

The right of Thamer Ahmed Alghamdi to be identified as the author of this work has been asserted in accordance with the Copyright, Designs, and Patents Act 1988.

© 2025, The University of Leeds, Thamer Ahmed Alghamdi

Acknowledgments

I would like to express my deepest gratitude to my wife, ***Jumana***, whose patience, support, and encouragement have carried me through every stage of this PhD. Her strength and understanding made it possible for me to continue, even during the most difficult of moments. I am equally grateful to my children, ***Ziyad*** and ***Elyas***, whose smiles and company remind me of what truly matters and keep me motivated throughout this long journey.

My heartfelt thanks go to my parents, who have always believed in me and supported my education from the beginning. Their values, guidance, and prayers were a constant source of strength. I also extend my appreciation to my brothers, sisters, and extended family, who stood beside me with encouragement and reassurance.

I am also thankful to my friends, both in the UK and Saudi Arabia, who provided advice, understanding, and companionship whenever needed.

I owe special thanks to my supervisors, ***Dr Richard Collier, Dr Emma Bramham,*** and ***Dr Taija Torve*****la** for their guidance, expertise, and consistent support throughout this research. Their feedback shaped the direction of this thesis, and their trust in my work helped me to reach this point. I am truly grateful for their time and commitment.

I sincerely appreciate everyone who has contributed to my academic and personal journey. This achievement would not have been possible without your support.

Abstract

The Afar Depression is located at one of the world's most complex plate boundaries, where the Red Sea, Gulf of Aden, and the Main Ethiopian Rift meet in a triple-junction system linking continental and oceanic rifting. Although the Afar region is widely recognised as a key location for understanding the transition from continental extension to seafloor spreading, the relationships between fault growth, magmatism, block rotation, and the redistribution of strain remain poorly constrained at the surface scale. This thesis addresses this problem by providing an integrated zone-by-zone quantitative analysis of fault geometry, displacement, segmentation, linkage, cross-cutting relationships, and minimum apparent strain across three contrasting rift domains: the North Afar Depression (Zone 1), North Main Ethiopian Rift (Zone 2), and East Afar Depression (Zone 3).

This study combines manual fault mapping of 2,500 normal faults using 30 m resolution DEM map in QGIS environment with a suite of Python-based quantitative analyses of apparent fault length (L), apparent maximum displacement (Dmax), Dmax/L scaling behaviour, displacement-profile classification, segmentation and linkage metrics, and cross-section-based minimum strain calculations. These datasets are integrated with information from published geological maps and stratigraphic constraints to reconstruct the spatial and temporal evolution of deformation across the three zones. Analysis of Dmax and L data and log-log plots of Dmax/L show that across three zones, fault morphology population are consistent with a hybrid growth model.

The results show that Zone 1 is characterised by numerous short, low-displacement faults with mainly single- and multi-peak profiles, dominated by soft linkages and a southward increase in minimum strain along the southern Danakil margin, consistent with a structurally transitional rift sector in which strain has begun to localise but is still distributed across many mechanically immature, partly linked segments before migrating eastward into more axial Afar structures. Zone 2 is dominated by short, mechanically young faults within the central Wonji belt, where strain is tightly focused into a narrow NNE-trending magmatic rift and older border faults are now largely inactive. Zone 3 records the interaction between the Afar and Gulf of Aden rifts, combining Early Pleistocene grabens with very young Afar- and Gulf of Aden-aligned axial segments, producing a heterogeneous strain field linked to ongoing block rotation and extension relocation.

These findings provide new evidence confirming that the northern East African Rift and Afar Depression evolved as a diachronous, segmented triple junction rather than a simple

linear progression from continental to oceanic rifting. The combined patterns of fault maturity, strain localisation, and cross-cutting relationships are consistent with kinematic models that involve anticlockwise rotation of the Danakil Block and clockwise rotation of the internal Afar crustal blocks. More broadly, this thesis demonstrates that under the continental to oceanic rifting transition, strain can shift rapidly between neighbouring structural domains and that fault growth in magma-assisted systems is strongly influenced by resurfacing, magmatic intrusion, and block kinematics. These conclusions have implications for global models of rift evolution, the role of magmatism in strain accommodation, and the development of plate boundaries approaching continental break-up.

Table of Contents

Comparing extensional fault evolution across the continental to oceanic rifting transition in the northern East African Rift and Afar Depression. 1

Declaration Statement 2

Acknowledgments 3

Abstract 4

Table of Contents 3

List of Figures 8

List of Tables 1

Chapter 1: Introduction 1

1.1 Rationale of the research 1

1.2 Gaps in knowledge 2

1.3 Hypotheses 4

1.4 Research aim 5

1.5 Specific objectives 5

1.6 Thesis outlines 6

Chapter 2: Literature review 8

2.1 Introduction 8

2.2 Rift tectonic and continental breakup 10

2.3 Fault growth and scaling relationship 12

2.4 Fault linkage and relay structures 16

2.5 Fault segmentation and interaction 18

2.6 Strain accommodation in rift systems 20

2.7 Geological background 22

2.7.1 Regional geology of the East African Rift System 22

2.7.2 Geological setting of the Afar Depression 24

2.7.3 Geological framework of the Study Zones 28

2.7.3.1 Zone 1: North Afar Depression (NAD) 28

2.7.3.2 Zone 2: North Main Ethiopian Rift (NMER) 30

2.7.3.3 Zone 3: Eastern Afar Depression (EAD) 31

Chapter 3: Methodology 35

3.1 Introduction 35

3.2 Data acquisition 35

3.3 Data processing **36**
3.4 Data analysis **39**
3.4.1 Fault picking method 39
3.4.2 Fault digitising methods 42
3.4.3 Fault sampling scenarios 44
3.5 Statistical Analysis **45**
3.5.1 Fault geometry analysis 46
3.5.1.1 Fault length (L) 46
3.5.1.2 Fault maximum displacement (D_{max}) 47
3.5.1.3 Fault spatial distribution 49
3.5.1.4 Fault orientation 50
3.5.2 Fault displacement profiles 51
3.5.3 Fault linkage analysis 51
3.5.4 Minimum strain elongation (*e*) 53
3.5.5 Cross-cutting relationship 56
3.5.6 Fault maturity and surface geological units 58
3.6 Data limitation and error **59**
3.7 Data quality control (QC) **60**
Chapter 4: Quantitative analysis of faulting geometries in the North Afar Depression (NAD) **62**
4.1 Introduction **62**
4.2 North Afar Depression (NAD; Zone 1) **63**
4.3 Results **64**
4.3.1 Fault geometry analysis 65
4.3.1.1 Fault Spatial Distribution 65
4.3.1.2 Fault Length (L) 68
4.3.1.3 Fault Maximum Displacement (Dmax) 70
4.3.2 Fault displacement profiles 71
4.3.2.1 Single-peak profiles 71
4.3.2.2 Multi-peak profiles 73
4.3.2.3 Irregular-peak profiles 75
4.3.3 Fault linkage analysis 77
4.3.3.1 Soft Linked (SL) 78
4.3.3.2 Hard Linked (HL) 79
4.3.4 Minimum strain analysis of NAD (Zone 1) 82

4.3.4.1 Cross-section Profiles 82
4.3.4.2 Analysis of Elongation (e) 85
4.3.5 Fault maturity and geological surface units 85
4.4 Discussion **88**
4.4.1 Fault size and scaling (NAD) 88
4.4.2 Segmented faults and linkage (NAD) 90
4.4.3 Minimum strain distribution (NAD) 92
4.4.4 Influence of geological surface units on fault scaling (NAD) 94
4.5 Conclusion **95**
Chapter 5: Analysis of Scaling Properties of Normal Fault Growth in the North Main Ethiopian Rift (NMER) **97**
5.1 Introduction **97**
5.2 The North Main Ethiopian Rift (NMER; Zone 2) **98**
5.3 Results **99**
5.3.1 Fault geometry analysis 100
5.3.1.1 Fault spatial distribution 100
5.3.1.2 Fault Length (L) 101
5.3.1.3 Fault maximum displacement (Dmax) 103
5.3.2 Fault displacement profiles 104
5.3.2.1 Smooth single-peak profiles 105
5.3.2.2 Multi-peak profiles 107
5.3.2.3 Irregular-peak profiles 109
5.3.3 Fault-zone segmentation and linkage 111
5.3.3.1 Soft linked (SL) 111
5.3.3.2 Hard linked (HL) 113
5.3.4 Fault distribution across surface units 114
5.3.5 Minimum strain analysis of NMER (Zone 2) 119
5.3.5.1 Cross-section profiles 120
5.4 Discussion **123**
5.4.1 Fault size characteristics 123
5.4.2 Segmentation and linkage of fault zones 125
5.4.3 Apparent strain localisation 127
5.5 Conclusion **130**
Chapter 6: Quantitative Analysis of the Spatial and Temporal Evolution of Normal Faults during an Advanced Stage of Rifting: The Eastern Afar Depression (EAD) and Ethiopia–Djibouti Transition Zone. **132**

6.1 Introduction **132**
6.2 East afar depression study zone 3 ..... **133**
6.3 Results **136**
6.3.1 Fault geometric analysis 136
6.3.1.1 Fault spatial distribution 136
6.3.1.2 Fault Length (L) 138
6.3.1.3 Fault Maximum Displacement (D*max*) 140
6.3.2 Fault displacement profile 140
6.3.2.1 Single-peak profiles 140
6.3.2.2 Multi-peak profiles 143
6.3.2.3 Irregular-peak profiles 144
6.3.3 Fault segmentation and linkage 146
6.3.3.1 Soft linkage (SL) 146
6.3.3.2 Hard linkage (HL) 146
6.3.4 Fault distribution across surface units 148
6.3.5 Cross-cutting analysis 152
6.3.6 Minimum strain analysis of EAD (Zone 3) 135
6.4 Discussion **138**
6.4.1 Fault size distributions 138
6.4.2 Fault-zone segmentation and linkage 139
6.4.3 Minimum strain localisation 141
6.4.4 Cross-cutting relationships 143
6.5 Conclusion **145**
Chapter 7: Discussion and conclusion **147**
7.1 Fault size distribution **149**
7.2 Fault segmentation and linkage **154**
7.3 Minimum strain localization **157**
7.4 Tectonic evolution across the continental–oceanic rifting transition **163**
7.5 Implications for the thesis hypotheses **173**
7.6 Implications of the research **176**
7.7 Limitations and uncertainties **178**
7.8 Conclusion **178**
7.9 Future work **180**
References **183**

Appendix A **194**
Appendix B **279**

List of Figures

Figure 2.1: Overview geological map showing the locations of the three study zones: Zone 1, North Afar Depression (NAD); Zone 2, North Main Ethiopian Rift (NMER); and Zone 3, Eastern Afar Depression (EAD). Geological units are grouped into volcanic, intrusive, sedimentary and basement categories according to stratigraphic age to provide regional geological context for the study areas. Base geology adapted from Rime et al. (2022) **9**

Figure 2.2: Conceptual model illustrates the progressive stages of continental rift evolution, from initial boundary faulting exploiting inherited crustal weaknesses, through the development of incipient and internal faults, to magma-dominated segments and eventual continental rupture leading to oceanic spreading. This synthesis, based on analogue modelling and observations from the Main Ethiopian Rift and Afar Depression, highlights the increasing interaction between magmatism and tectonics during rift maturation. Modified after Ebinger (2005), Corti (2009), and Agostini et al. (2011), in Corti (2012) **10**

Figure 2.3: Conceptual model of fault network evolution, illustrating the progressive stages from initiation to through-going fault zones. (a) Early stage with isolated, short (2–10 km), low-displacement fault segments; (b) intermediate stage characterised by interaction and linkage between fault tips, forming soft-linked relay ramps; and (c) mature stage where strain localises onto a few long (>10 km), high-displacement through-going faults, with abandoned segments preserved in the hanging wall. Modified from Gawthorpe and Leeder (2000) **12**

Figure 2.4: Conceptual models of fault growth adapted from Kim and Sanderson (2005). (a) Constant D_{max}/L ratio model, in which fault length (L) and maximum displacement (D_{max}) increase proportionally from initiation, maintaining a constant ratio throughout growth. (b) Increasing D_{max}/L ratio model, in which the D_{max}/L ratio increases during fault growth, reflecting proportionally greater displacement relative to fault length over time. (c) Constant-length model, after Walsh et al. (2002), in which fault length increases rapidly during the early stages of fault growth before remaining approximately constant as displacement continues to accumulate. (d) Fault linkage model (Peacock and Sanderson, 1991; Cartwright et al., 1995; Kim et al., 2000), in which newly linked fault segments may initially exhibit anomalously low displacement for their length, or overlapping segments may show locally high displacement; however, with continued deformation, the fault system tends to return to a self-similar scaling relationship **14**

Figure 2.5: Evolutionary stages of a relay ramp showing the progressive linkage of two overlapping fault segments. (a) Isolated segments with no interaction; (b) development of an intact relay ramp between overlapping fault tips; (c) progressive rotation and strain concentration within the relay ramp; (d) breaching of the relay ramp, leading to hard linkage; and (e) abandonment of the upper ramp and formation of a breached low ramp. Modified after Peacock and Sanderson (1991) and Çiftçi and Bozkurt (2007) **17**

Figure 2.6: (a) Schematic of the displacement distribution on an elliptical fault surface, with variations in fault length (L) and height (H). The tip loop defines the outer boundary of the fault surface, along which displacement decreases to zero. The shading density/saturation increases towards the fault centre and represents the relative displacement values on the fault surface. The surface of the upper block intersects the fault surface at line A–B, and the lower panel (b) depicts the displacement (d) versus distance (x) profile along that intersection, with maximum displacement (D_{max}) occurring near the centre of the fault (Kim and Sanderson, 2005) **18**

Figure 2.7: Conceptual diagrams illustrating the two end-member models for the development of segmented-fault arrays. Panels (a), (c), and (d) show the three stages of fault growth, whereas panels (b) and (e) show the displacement–distance profiles for fault traces along the block surfaces. Both isolated and coherent fault models can include hard-linked segments (formed by the breach of relay zones or fault surface bifurcation) and soft-linked segments (connected via relay ramps) at different stages of evolution. The shaded regions in (b) highlight the displacement deficits between adjacent segments that are not caused by continuous deformation within the relay zones. In the isolated fault model, points of maximum displacement are retained at segment centres, whereas the coherent model tends to produce smoother aggregate profiles at all stages of development (Walsh et al., 2003) **19**

Figure 2.8: Conceptual 3D diagram illustrating fault geometry and the main components of relative movement. The diagram depicts the throw (vertical displacement), heave (horizontal extension), and strike-slip components along the fault plane, as well as the net slip vector and fault orientation defined by the strike and dip. These geometric parameters form the basis for quantifying brittle strain in extensional rift settings. Adapted from Burg (2020) **21**

Figure 2.9: Structural framework of the Main Ethiopian Rift showing border faults (black) and axial Wonji Fault Belt segments (blue), with the MER divided into the SMER, CMER, and NMER. Modified from Keir et al. (2015) **24**

Figure 2.10: Geological map of the Afar Depression showing the distribution of volcanic, sedimentary, and intrusive units and significant fault systems. The volcanic unit's range in age from the Oligocene to the Quaternary, and the central axial rift segments demonstrate the prevalence of Quaternary volcanics. The sedimentary units are primarily located on the rift margins, notably near the Danakil and Somali plate boundaries. Intrusive units are exposed within the central structural highs, indicating magmatic processes during repeated rifting. Adapted from Rime et al. (2022) **26**

Figure 2.11: Rift dynamics of the Afar Depression illustrating major active and ancient rift segments, transfer zones and plate boundaries. The map highlights key structural features, including the Erta Ale–Tat'Ali Transfer Zone (ETTZ) and Goba'Ad Discontinuity, which partition strain between magmatic and tectonic rift sectors. Plate motions and active deformation zones are shown relative to the Nubian Plate. After Corti (2009), Pagli et al. (2014), Doubre et al. (2017), Viltres et al. (2020), Moore et al. (2021), and Sangha et al. (2022) **28**

Figure 2.12: Geological map of the North Afar Depression (location shown in Figure 2.1), highlighting volcanic units (ISv, Gv, Rv), syn-rift sediments (Pes, Hs), major normal faults, and the positions of the Harak and Dadar grabens and Mat Ala volcano. Compiled and simplified from Rime et al. (2022) **29**

Figure 2.13: Simplified geology and structure of the NMER (location shown in Figure 2.1), showing border faults, axial Wonji Fault Belt segments, and principal surface units (Qv, Pov/Q2v, and Hs/Pes). Compiled from Rime et al. (2023) for the northern part and reclassified USGS province mapping southward **31**

Figure 2.14: Generalised geology and structures of the Eastern Afar Depression (EAD) (location shown in Figure 2.1), showing major grabens (Immino, Dobi, Hanle, Gaggade), the Makarassou Fault, principal transfer zones (e.g. Gamarri–Alol), and volcanic units (ISv, IMv, eSv, mRv, Gv, Rv) with syn-rift sediments (Pes, Hs). Compiled and simplified after Rime et al. (2023), with volcanic ages from Lahitte et al. (2003) **33**

Figure 3.1: Workflow used to process the ASTER DEM data, including DEM import and mosaicking, study-area shapefile creation, hillshade generation, raster clipping, and visualisation optimisation for fault mapping and analysis **39**

Figure 3.2: Conceptual block diagrams illustrating fault-length and cut-off mapping. The red dots represent the top cut-off points, and the yellow dots represent the corresponding bottom cut-off points. (a) Schematic displacement profile showing the mapped cut-off points along the fault and the projected fault length. (b) Three-dimensional conceptual representation showing the corresponding top and bottom cut-offs along the fault scarp, with their x, y and z coordinates used to define fault geometry **40**

Figure 3.3: Conceptual and representative DEM-derived examples illustrating the application of the fault cut-off-picking method. The conceptual diagram illustrates the effect of surface modification on mapped and projected cut-offs. The DEM examples show the locations of A–A′ topographic profiles across representative fault scarps. (a) A well-preserved fault scarp, where distinct changes in slope define the mapped top and bottom cut-offs. (b) A modified fault scarp, where the surface expression is less clearly preserved. The corresponding elevation profiles illustrate how the mapped cut-offs were identified and used to determine apparent displacement **42**

Figure 3.4: Preservation-controlled mapping of fault cut-offs from DEM data. (a) Conceptual block diagram showing how erosion and surface burial affect fault-scarp visibility; red points mark top cut-offs (footwall) and yellow points mark bottom cut-offs (hanging wall). (b) Hillshade/pseudo-colour DEM example (2 km scale) showing mapped eroded top cut-offs (red), buried bottom cut-offs (yellow), and dashed interpolated traces where the scarp is obscured. Apparent displacement (D) and D_{max} were measured between observed cut-offs, while projected fault length was estimated by extending the visible trace where continuity indicated further propagation **45**

Figure 3.5: Diagram showing the top cut-off fault trace marked with multiple sampling points (red dots) from one tip to the other; each point (T) represents its recorded (x, y) coordinates **47**

Figure 3.6: Diagram showing fault picking along the fault trace while accounting for changes in orientation. Red dots represent the top cut-off, and yellow dots represent the bottom cut-off **48**

Figure 3.7: Conceptual illustration defining the displacement components used in this study. Apparent displacement (d) is assumed to represent dip-slip movement within the fault plane. Throw represents the vertical component of displacement, whereas heave represents the horizontal component. The top and bottom cut-offs represent the reference points used to measure apparent fault-scarp displacement from the DEM 49

Figure 3.8: Fault linkage styles and evolution illustrated using DEM interpretations (left) and corresponding conceptual 3-D block diagrams (right). Red dots indicate top cut-offs (footwall), and yellow dots indicate bottom cut-offs (hanging wall). (A–a) Soft linkage: overlapping fault segments are connected by a relay ramp, allowing displacement transfer between mechanically distinct segments. (B–b) Hard linkage via the footwall: a connecting fault breaches the relay zone and forms a continuous fault trace. (C–c) Hard linkage via the hanging wall: a connecting fault breaches the relay zone and establishes a through-going fault trace. These examples illustrate the progression from soft to hard linkage as fault segments become geometrically connected and displacement becomes increasingly localised **53**

Figure 3.9: Schematic diagram illustrating the elongation method used to calculate minimum horizontal strain. The reconstructed pre-faulting length (L_0) represents the sum of the lengths of the originally continuous layer segments, whereas L_1 represents the present-day horizontal distance between the profile endpoints after fault-related extension. Elongation (e) was calculated as $(L_1 - L_0)/L_0$ and expressed as a percentage. This method provides a geometrical estimate of the minimum strain accommodated by faulting and does not account for distributed or ductile deformation **55**

Figure 3.10: Worked example illustrating the measurement of the reconstructed pre-faulting length (L_0) and present-day extended length (L_1) used to calculate minimum horizontal elongation. (a) DEM showing the location of the representative A–A′ profile across mapped normal faults. (b) Corresponding topographic profile showing successive fault cut-offs and the individual preserved surface lengths (l_1–l_6) measured between them. (c) The individual surface lengths were summed to reconstruct L_0, while (d) L_1 was measured as the present-day horizontal distance between the same profile endpoints (A–A′). The resulting L_0 and L_1 values were used to calculate the minimum horizontal elongation (e) **56**

Figure 3.11: Block diagram illustrating a cross-cutting fault relationship, where Fault Plane 2 offsets and truncates Fault Plane 1, indicating that Fault 2 is younger. This geometric configuration helps constrain the relative timing of faulting events in extensional systems. Modified after Barnett et al. (1987, 1991) **57**

Figure 3.12: Cross-cutting fault scenario. Two normal fault scarps (Fault Scarps 1 and 2) intersect, forming a cross-cutting zone where the younger scarp truncates the older one. The red and yellow dots mark the mapped top and bottom cut-off vertices, respectively..... **58**

Figure 4.1: (a) Regional map of the Afar Depression showing its position relative to the Red Sea, Gulf of Aden, and East African Rift systems. The inset shows the broader location of the Afar Depression in the Horn of Africa. (b) Local map of Study Zone 1 in the North Afar Depression (NAD), highlighting key structural features including the Mat'Ala volcano, Harak Graben, and Dadar Graben. Basemap derived from ASTER GDEM data obtained from USGS Earth Explorer (basemap from ASTER GDEM Version 3; NASA/METI/AIST/Japan Spacesystems and U.S./Japan ASTER Science Team, 2019..... **64**

Figure 4.2: Spatial distribution of faults in Zone 1 (North Afar Depression [NAD]). (a) Digitised fault traces mapped from the DEM. (b) Line map highlighting structural trends. (c) Rose diagram showing the dominant NNW–SSE strike (~167°). (d) Kernel density map of fault traces, with the highest densities in the southern sector and lower values to the north. Basemap from ASTER GDEM v3 (NASA/METI/AIST/Japan Spacesystems and U.S./Japan ASTER Science Team, 2019, 2019) **67**

Figure 4.3: Frequency distribution of fault length in Zone 1 (NAD). The histogram shows that most faults are short to intermediate in length, with most values falling below 4 km..... **70**

Figure 4.4: Log–log plot of maximum displacement (D_{max}) versus fault length (L) for 350 faults in Zone 1 (NAD). Dashed lines represent constant displacement–length ratios (D/L = 1, 0.1, 0.01 and 0.001). The fitted power-law regression is D_{max} = 0.4909L^0.6395 (R^2 = 0.3011, $p < 0.001$) **70**

Figure 4.5: Frequency distribution of maximum displacement (D_{max}) for 350 mapped faults in Zone 1 (NAD). The histogram shows that the dataset is strongly skewed towards small displacements,

with most values below 200 m and relatively few faults exceeding this range..... **71**

Figure 4.6: Location and displacement characteristics of representative single-peak faults F050 and F049 in Zone 1 of the North Afar Depression (NAD). (a) DEM showing the locations of faults F050 and F049 within Zone 1. (b) 3D DEM view of fault F050 showing the mapped top and bottom cut-offs across the fault scarp. (c) Along-strike displacement–length (D–L) profile of F050, showing displacement increasing towards a single maximum displacement (D_{max}) before decreasing towards the opposite fault tip. (d) 3D DEM view of fault F049 showing the mapped top and bottom cut-offs across the fault scarp. (e) Along-strike displacement–length (D–L) profile of F049, similarly showing a single displacement maximum. Red and yellow points in the 3D DEM views represent the mapped top and bottom cut-offs, respectively…..... **72**

Figure 4.7: Log–log plot of maximum displacement (D_{max}) versus fault length (L) for faults in Zone 1 (NAD). Smooth single-peak faults are shown by orange triangles (n = 35), with the power-law regression D_{max} = 0.1344L^0.8219 (R^2 = 0.3869; $p < 0.001$). Multi-peak and irregularly peaked faults are shown by grey triangles (n = 315) for comparison..... **73**

Figure 4.8: Location and displacement characteristics of representative multi-peak faults F011 and F094 in Zone 1 of the North Afar Depression (NAD). (a) DEM showing the locations of faults F011 and F094 within Zone 1. (b) Three-dimensional DEM view of fault F011 showing the mapped top and bottom cut-offs across the fault scarp. (c) Along-strike displacement–length (D–L) profile of F011, showing multiple displacement maxima separated by intervening minima. (d) Three-dimensional DEM view of fault F094 showing the mapped top and bottom cut-offs across the fault scarp. (e) Along-strike displacement–length (D–L) profile of F094, similarly showing multiple displacement maxima separated by intervening minima. Red and yellow points represent the mapped top and bottom cut-offs, respectively **74**

Figure 4.9: Log–log plot of maximum displacement (D_{max}) versus fault length (L) for faults in Zone 1 (NAD). Multi-peak faults are shown by blue triangles (n = 71), with the power-law regression D_{max} = 0.0284L^1.0088 (R^2 = 0.3823; $p < 0.001$). Smooth single-peak and irregularly peaked faults are shown by grey triangles (n = 279) for comparison **75**

Figure 4.10: Location and displacement characteristics of representative irregularly peaked faults F108 and F076 in Zone 1 of the North Afar Depression (NAD). (a) DEM showing the locations of faults F108 and F076 within Zone 1. (b) Three-dimensional DEM view of fault F108 showing the mapped top and bottom cut-offs along the fault scarp. (c) Along-strike displacement–length (D–L) profile of F108, showing more than three displacement maxima separated by intervening minima. (d) Three-dimensional DEM view of fault F076 showing the mapped top and bottom cut-offs along the fault scarp. (e) Along-strike displacement–length (D–L) profile of F076, similarly showing multiple displacement maxima and intervening minima characteristic of an irregularly peaked profile. Red and yellow points represent the mapped top and bottom cut-offs, respectively **76**

Figure 4.11: Log–log plot of maximum displacement (D_{max}) versus fault length (L) for faults in Zone 1 (NAD). Irregularly peaked faults (orange triangles, n = 244) are compared with smooth single-peak and multi-peak faults (grey triangles, n = 106). The power-law regression for the irregularly peaked population is D_{max} = 1.0712L^0.5443 (R^2 = 0.1959; $p < 0.001$) **78**

Figure 4.12: Example of soft linkage between overlapping normal-fault segments in Zone 1 (NAD). (a) Three-dimensional DEM view showing Faults 1 and 2 separated by an intervening relay zone. Red and yellow points indicate the mapped top and bottom cut-offs, respectively. (b–c) Along-

strike displacement–length (D–L) profiles of Faults 1 and 2, showing displacement variations along the interacting fault segments. (d) Schematic representation of the soft-linkage geometry **80**

Figure 4.13: Representative example of hard linkage in Zone 1. (a) Three-dimensional DEM showing two fault segments that are physically connected across a breached relay ramp, producing a continuous surface fault trace. The mapped top and bottom cut-offs delineate the fault scarp and show the geometry of the linkage zone. (b) Schematic illustrating the geometric configuration of the linked segments; this is not a displacement–length (D–L) profile..... **81**

Figure 4.14: Log–log plot of maximum displacement (D_{max}) versus fault length (L) for hard-linked and non-hard-linked faults in Zone 1 (NAD). Hard-linked faults are plotted using the total length of the linked fault structure rather than the lengths of the individual constituent segments. Non-hard-linked faults comprise the non-linked (NL) and soft-linked (SL) populations. The power-law regression for the hard-linked population is D_{max} = 2.2351L^0.4478 (R^2 = 0.138) **82**

Figure 4.15: Geological map and cross-sectional profiles used to calculate minimum apparent extensional strain across Zone 1 of the North Afar Depression. The map shows the locations of profiles A–A′ to H–H′, arranged from south to north. The cross-sections show the present-day surface topography and principal fault-controlled features intercepted by each profile. Reconstructed pre-extension surface segments (L_0) are separated at the major fault offsets identified along each profile, and their summed length ($\sum L_0$) represents the reconstructed pre-extension surface length. The present-day cross-profile length (L_1) is also shown for each profile. The accompanying plot summarises the resulting minimum apparent elongation values from south to north. Cross-sections were derived from ASTER GDEM v3; geological units are after Rime et al. (2023) **85**

Figure 4.16: Number of faults classified within each mapped geological surface unit in Zone 1 (n = 350), arranged from older to younger surface units. Unit identifiers correspond to those shown on the geological map in Figure 4.15. Question marks indicate uncertain geological attribution on the source geological map **87**

Figure 4.17: Log–log plot of maximum displacement (D_{max}) versus fault length (L) for faults classified according to mapped geological surface unit in Zone 1 (n = 350). Each point represents an individual fault and is coloured according to its mapped geological surface unit. Pes and Hs represent sedimentary units, whereas Rv, Gv, Gv?, ISv and ISv? represent volcanic units. The geological-unit populations show substantial overlap in D_{max}–L space……..... **87**

Figure 4.18: Boxplots of maximum displacement (D_{max}) for faults classified according to mapped geological surface unit in Zone 1 (n = 350), arranged from older to younger surface units. Boxes represent the interquartile range (IQR), horizontal lines indicate median values, whiskers extend to 1.5 × IQR, and points beyond the whiskers represent outliers. Geological-unit identifiers correspond to those shown on the geological map in Figure 4.15. Question marks indicate uncertain geological attribution on the source geological map **88**

Figure 4.19: Boxplots of D_{max}/L for faults classified according to mapped geological surface unit in Zone 1 (n = 350), arranged from older to younger surface units. Boxes represent the interquartile range (IQR), horizontal lines indicate median values, whiskers extend to 1.5 × IQR, and points beyond the whiskers represent outliers. Geological-unit identifiers correspond to those shown on the geological map in Figure 4.15. Question marks indicate uncertain geological attribution on the source geological map **89**

Figure 5.1: Regional and local settings of the North Main Ethiopian Rift (NMER). (a) Regional context of the Afar Depression and adjoining rifts within the northern East African Rift System. Major plates and margins are indicated (Nubian, Somali), with the Red Sea and Gulf of Aden shown; the dashed box outlines the enlarged area in panel (b). (b) Close-up of the NMER axial zone between the Ethiopian and Somali plateaus, highlighting the key physiographic and volcanic features, including Kone, Fantale, Awash, and Lake Basaka. The base map is satellite imagery draped over a digital elevation model. Basemap from USGS Earth Explorer (USGS, 2024) **101**

Figure 5.2: Spatial distribution and orientation of faults in Zone 2 of the North Main Ethiopian Rift (NMER). (a) Fault traces mapped from DEM data draped on shaded topography. (b) Extracted linework showing the mapped fault traces. (c) Rose diagram showing the dominant NW–SE fault orientation (~030°) with a subordinate NE–SW set. Basemap from ASTER GDEM v3 (NASA/METI/AIST/Japan Spacesystems and U.S./Japan ASTER Science Team, 2019) **102**

Figure 5.3: Kernel density map of mapped normal fault traces in Zone 2 (NMER). Colours show fault density (faults/km²) estimated from kernel density analysis, plotted against local easting and northing (km). High-density clusters along the central part of the map correspond to the axial rift zone, whereas lower densities occur towards the margins **103**

Figure 5.4: Frequency distribution of fault length in Zone 2 (NMER; n = 900). The distribution is strongly skewed towards shorter fault lengths, with more than half of the mapped faults measuring <2.5 km. Fault frequency decreases progressively with increasing length, and faults >10 km are rare **104**

Figure 5.5: Log–log plot of maximum displacement (D_{max}) versus fault length (L) for 900 faults in Zone 2 (NMER). Dashed lines represent constant displacement–length ratios (D/L = 1, 0.1, 0.01 and 0.001). The fitted power-law regression is D_{max} = 0.7698L^0.6007 (R^2 = 0.2614) **105**

Figure 5.6: Frequency distribution of maximum displacement (D_{max}) for the 900 mapped faults in Zone 2 of the North Main Ethiopian Rift (NMER). D_{max} ranges from 10 to 1,045 m, with the distribution strongly skewed towards lower displacement values. Nearly half of the mapped faults have D_{max} values below 100 m, whereas displacements above 200 m are relatively rare and only a few faults exceed 1,000 m **106**

Figure 5.7: Log–log plot of maximum displacement (D_{max}) versus fault length (L) for faults in Zone 2 (NMER; n = 900). Smooth single-peak faults are highlighted (n = 280), whereas multi-peak and irregularly peaked faults (n = 620) are shown in grey for comparison **107**

Figure 5.8: Examples of smooth single-peak fault displacement profiles in Zone 2 (NMER). (a) DEM showing the locations of the two example faults, F049 and F026. (b, d) Three-dimensional views of the fault scarps F049 and F026, respectively (vertical exaggeration ×3), showing the mapped top and bottom cut-offs used to calculate displacement along the fault traces. (c, e) Corresponding along-strike displacement profiles for F049 and F026, respectively, showing the location of maximum displacement (D_{max}). Both examples display broadly single-peaked displacement profiles, with displacement increasing towards a maximum within the fault trace and decreasing towards the fault tips **108**

Figure 5.9: Log–log plot of minimum fault length versus maximum displacement (D_{max}) for faults in Zone 2. The highlighted dataset (blue triangles) shows fault segments (n = 518), plotted relative to the total fault population (grey triangles, n = 900) **109**

Figure 5.10: Examples of multi-peak displacement–length (D–L) profiles from Zone 2 (NMER). (a) DEM showing the locations of the two example faults, F249 and F453. (b, d) Three-dimensional views of the fault scarps F249 and F453, respectively (vertical exaggeration ×3), showing the mapped top and bottom cut-offs used to calculate displacement along the fault traces. (c, e) Corresponding along-strike D–L profiles for F249 and F453, respectively. F249 displays two distinct displacement maxima separated by an intervening minimum, whereas F453 shows two displacement maxima with a less pronounced intervening minimum. These geometries are characteristic of the multi-peak displacement-profile class..... **109**

Figure 5.11: Log–log plot of minimum fault length (L) versus apparent maximum displacement (D_{max}) for faults in Zone 2. Faults are separated by displacement–length profile type: irregular profiles (yellow triangles, n = 238) and smooth and multi-peak profiles (grey triangles, n = 662). Both groups plot within the same general scaling envelope, but irregular profiles extend to greater lengths and higher displacements, reflecting their predominance among the largest structures in the dataset **110**

Figure 5.12: Examples of irregular displacement–length (D–L) profiles from Zone 2 (NMER). (a) DEM showing the locations of the two example faults, F006 and F028. (b, d) Three-dimensional views of the fault scarps F006 and F028, respectively (vertical exaggeration ×3), showing the mapped top and bottom cut-offs used to calculate displacement along the fault traces. (c, e) Corresponding along-strike D–L profiles for F006 and F028, respectively. Both faults display irregular displacement profiles characterised by multiple local displacement maxima and intervening minima along strike **111**

Figure 5.13: Example of soft linkage between two normal-fault segments in Zone 2 (NMER). (a) DEM view showing Faults A and B arranged in an overlapping en-echelon geometry and separated by an intervening relay zone. (b) Corresponding along-strike displacement profiles for Faults A and B, showing displacement variations towards the interacting fault tips. The faults remain physically separated at the surface and are therefore classified as soft linked..... **112**

Figure 5.14: Hard linkage across a breached relay ramp in Zone 2 (NMER). Faults A and B merged across a breached relay ramp to form a continuous, through-going scarp, illustrating the transition from independent segments to a hard-linked fault. Linkage-zone location..... **113**

Figure 5.15: Log–log plot of maximum displacement (Dmax) versus total fault length (L) for hard-linked and non-hard-linked faults in Zone 2 of the North Main Ethiopian Rift (NMER). Hard-linked faults are plotted using the total length of each connected hard-linked structure rather than the lengths of the individual constituent segments. Non-hard-linked faults comprise the non-linked (NL) and soft-linked (SL) populations. The fitted power-law regression for the hard-linked composite population Dmax = 0.6552L^0.6021 ($R^2 = 0.2834$, $p < 0.001$; n = 63) ……**114**

Figure 5.16: Log–log plot of fault length (L) against maximum displacement (D_{max}) for faults classified according to mapped geological surface unit in Zone 2 of the North Main Ethiopian Rift (NMER). Each point represents an individual mapped fault, with colours indicating geological surface units. Units are listed in approximate chronological order from oldest to youngest, with approximate age ranges and the number of mapped faults (n) shown in the legend. Faults within the volcanic units span a broad range of lengths and maximum displacements and include many of the longest and highest-displacement structures, whereas faults mapped within the sedimentary units Pes and Hs are concentrated mainly within shorter to intermediate fault lengths and lower to moderate D_{max} values. Considerable overlap occurs between geological units, indicating that geological surface age and lithology alone do not explain the observed variation in fault size

..... **116**

Figure 5.17: Boxplots of maximum displacement (D_{max}) for faults classified according to mapped geological surface unit in Zone 2 of the North Main Ethiopian Rift (NMER). Geological surface units are arranged in approximate chronological order from oldest to youngest, with approximate age ranges and the number of mapped faults (n) shown beneath each unit. D_{max} is plotted on a logarithmic scale. Volcanic units span a broad range of maximum displacements and include many of the highest-displacement faults, whereas faults mapped within the sedimentary units Pes and Hs are concentrated predominantly at lower to moderate D_{max} values. Considerable overlap occurs between geological units, indicating that maximum fault displacement does not show a simple monotonic relationship with geological surface age..... **117**

Figure 5.18: Boxplots of D_{max}/L ratios for faults classified according to mapped geological surface unit in Zone 2 of the North Main Ethiopian Rift (NMER). Geological surface units are arranged in approximate chronological order from oldest to youngest, with approximate age ranges and the number of mapped faults (n) shown beneath each unit. D_{max}/L is dimensionless and plotted on a logarithmic scale. The distributions show substantial variability and overlap between geological units and do not define a simple monotonic relationship between D_{max}/L and geological surface age. Geological unit codes and approximate age ranges are summarised in Table 5.5 ..... **118**

Figure 5.19: Cross-section analysis and minimum apparent extensional strain across Zone 2 of the North Main Ethiopian Rift (NMER). (a) Geological map and shaded-relief DEM of Zone 2 showing the locations of cross-sections A–A′, B–B′ and C–C′ and the principal geological and structural features of the study area. (b) NW–SE topographic cross-sections A–A′, B–B′ and C–C′, extending across the rift and showing the Ankober Border Fault, axial rift valley, Arboye Border Fault and the Fentale and Dofen volcanic centres. The orange markers indicate fault-related horizontal heave along each cross-section, and the blue lines show the reconstructed cross-section length (L_1). (c) Summary of the original cross-section length (L_0), reconstructed length (L_1), and calculated minimum apparent extensional strain (elongation) for each profile. (d) Variation in minimum apparent extensional strain across Zone 2, increasing from 62% along A–A′ to 83% along B–B′ and 91% along C–C′. The topographic profiles in (b) are vertically exaggerated for visualisation only; horizontal measurements used to calculate minimum apparent extensional strain were derived from the DEM/map geometry rather than from the vertically exaggerated profiles. DEM basemap from ASTER GDEM v3 (NASA/METI/AIST/Japan Spacesystems and U.S./Japan ASTER Science Team, 2019); geological mapping modified after Persits et al (1997) and Rime et al. (2022), with major border faults modified after WoldeGabriel et al. (2008) **121**

Figure 5.20: Summary tectonic map of the northern Main Ethiopian Rift (NMER), showing the Quaternary Koka, Boset and Fentale–Dofan magmatic segments, the major Miocene border faults (Ankober, Asela–Sire and Arboye) and the adjacent Baso–Werena, Adama, Ziway–Shalla and Kerayou basins. The map also shows the distribution and orientation of faults and volcanic centres within the axial magmatic segments relative to the older border-fault systems. S1–S5 indicate field sample locations in the original study, and E–E′ marks the location of the geological cross-section presented in Figure 3 of Wolfenden et al. (2004). Map simplified and modified after Wolfenden et al. (2004) **127**

Figure 6.1: Regional and local settings of Zone 3 in the Eastern Afar Depression (EAD). (a) Regional map of the Afar Depression and Gulf of Aden showing the position of Zone 3 (dashed box) on the eastern flank of the EAD between the Tendaho–Goba'ad Rift and the Danakil Block. (b)

Enlarged view of Zone 3 showing the main grabens (Immino, Dobi, Hanlé, and Gaggadé) and the Asal–Ghoubbet basin, bounded to the east by the Makarrassou Fault. Country boundaries and coastlines are shown for reference purposes. Basemap from USGS EarthExplorer (USGS, 2024) **132**

Figure 6.2: (a) Map of manually digitised normal fault traces from the 30 m-resolution DEM, showing the distribution of faults across Zone 3 in the Eastern Afar Depression (EAD). (b) Simplified line drawing of the mapped fault network. (c) Rose diagram showing the principal fault-orientation populations, dominated by NW–SE and NE–SW trends (n = 1,250). Basemap from ASTER GDEM v3 (NASA/METI/AIST/Japan Spacesystems and U.S./Japan ASTER Science Team, 2019) **134**

Figure 6.3: Fault-density map of Zone 3 showing spatial variation in mapped fault density (faults km^{-2}). Darker red areas represent zones of higher mapped fault concentration. Fault traces were manually mapped from the 30 m-resolution DEM, and the density surface was generated in QGIS **135**

Figure 6.4: Geological and structural map of Zone 3 in the Eastern Afar Depression (EAD), showing the principal grabens (Immino, Dobi, Hanlé, Gaggadé and Asal–Ghoubbet), the Makarrassou and Gamari border faults, and intervening uplifted blocks. Volcanic and sedimentary surface units are colour-coded according to mapped age (Hs, Pes, Rv, Gv, mRv, eSv, IMv and ISv), with mapped normal fault traces shown in black. Basemap from ASTER GDEM v3 (NASA/METI/AIST/Japan Spacesystems and U.S./Japan ASTER Science Team, 2019); geology modified after Rime et al. (2022) **136**

Figure 6.5: Log–log plot of apparent maximum displacement (D_{max}) versus apparent fault length (L) for mapped normal faults in Zone 3. The data show an overall positive relationship described by the power-law regression D_{max} = 0.6705L^0.6398 (R^2 = 0.4222). Most faults plot between the reference envelopes D_{max}/L = 0.01–0.1, with fewer approaching D_{max}/L = 0.001; the D_{max}/L = 1 line is shown as an upper reference envelope. The reference lines follow Dmax = cL, where c = 1, 0.1, 0.01 and 0.001. (Walsh and Watterson, 1988; Cowie and Scholz, 1992; Kim and Sanderson, 2005; Lathrop et al., 2022) **137**

Figure 6.6: Frequency distribution of fault lengths in Zone 3 of the EAD. The histogram shows a positively skewed distribution, with most faults between 2,000–7,500 m and relatively few long faults exceeding 20,000 m **137**

Figure 6.7: Histogram showing the frequency distribution of apparent maximum displacement (D_{max}) for 1,250 normal faults in Zone 3 (EAD) **138**

Figure 6.8: Log–log plot of apparent maximum displacement (D_{max}) versus apparent fault length (L) for Zone 3, showing the remaining fault-segment population (grey; n = 1,138) and the single-peak fault population (orange; n = 112). The dotted line shows the power-law regression fitted to the single-peak faults (D_{max} = 0.6314L^0.6486; R^2 = 0.2677) **139**

Figure 6.9: Examples of single-peak (bell-shaped) displacement profiles in Zone 3. (a) DEM showing the locations of representative faults F085 and F191. (b) Oblique DEM view of F085 showing the digitised top and bottom cut-offs and fault scarp (vertical exaggeration ×3). (c) Corresponding along-strike displacement–distance profile for F085, showing a single displacement maximum (D_{max}). (d) Oblique DEM view of F191 showing the digitised top and bottom cut-offs and fault scarp (vertical exaggeration ×3). (e) Corresponding along-strike displacement–distance profile

for F191, showing a single displacement maximum (D_{max}) **140**

Figure 6.10: Log–log plot of apparent maximum displacement (D_{max}) versus apparent fault length (L) for Zone 3, highlighting multi-peak faults (blue; n = 542) relative to faults with single-peak and irregular-peak displacement profiles (grey; n = 708). The dotted line shows the power-law regression fitted to the multi-peak population (D_{max} = 0.7162L^0.638; R^2 = 0.1931) **141**

Figure 6.11: Examples of multi-peak displacement–distance profiles in Zone 3. (a) DEM showing the locations of representative faults F073 and F075. (b) Oblique DEM view of F073 showing the digitised top and bottom cut-offs and fault scarp (vertical exaggeration ×3). (c) Corresponding along-strike displacement–distance profile for F073, showing multiple displacement peaks separated by an intervening trough and the position of D_{max}. (d) Oblique DEM view of F075 showing the digitised top and bottom cut-offs and fault scarp (vertical exaggeration ×3). (e) Corresponding along-strike displacement–distance profile for F075, showing multiple displacement peaks separated by intervening troughs and the position of D_{max} **142**

Figure 6.12: Log–log plot of apparent maximum displacement (D_{max}) versus apparent fault length (L) for Zone 3 faults, highlighting irregular-peak profiles (yellow; n = 596) relative to the combined single-peak and multi-peak population (grey; n = 654). The dotted line shows the power-law regression fitted to the irregular-peak population (D_{max} = 0.2195L^0.7612; R^2 = 0.383) **143**

Figure 6.13: Examples of irregular-peak displacement–distance profiles in Zone 3. (a) DEM showing the locations of representative faults F521 and F426. (b) Oblique DEM view of F521 showing the digitised top and bottom cut-offs and fault scarp (vertical exaggeration ×3). (c) Corresponding along-strike displacement–distance profile for F521, showing multiple local displacement maxima and the position of D_{max}. (d) Oblique DEM view of F426 showing the digitised top and bottom cut-offs and fault scarp (vertical exaggeration ×3). (e) Corresponding along-strike displacement–distance profile for F426, showing multiple local displacement maxima and the position of D_{max} **143**

Figure 6.14: Number of mapped faults classified according to geological surface unit in Zone 3 of the Eastern Afar Depression (EAD). Geological units are arranged in approximate chronological order from old to young based on their mapped age ranges. The Early Pleistocene volcanic unit (Q1v) contains the largest proportion of the mapped fault population. Fault abundance does not show a simple monotonic relationship with geological surface age **146**

Figure 6.15: Log–log plot of apparent fault length (L) against apparent maximum displacement (D_{max}) for faults classified according to mapped geological surface unit in Zone 3 of the Eastern Afar Depression (EAD). Each point represents an individual mapped fault (n = 1,250), with colours indicating the geological surface units. The Q1v unit contains the largest mapped fault population and spans a broad range of fault lengths and maximum displacements. Considerable overlap occurs between the geological units, indicating that fault size does not show a simple systematic relationship with geological surface age **146**

Figure 6.16: Boxplots of apparent maximum displacement (D_{max}) for faults classified according to mapped geological surface unit in Zone 3 of the Eastern Afar Depression (EAD). Volcanic units are arranged in approximate chronological order from oldest to youngest, followed by the sedimentary units. The distributions show substantial variability and overlap between geological

units and do not define a simple monotonic relationship between maximum fault displacement and geological surface age. The Pleistocene sedimentary unit (Pes) contains only one mapped fault (n = 1) and is therefore represented by a single observation **147**

Figure 6.17: Boxplot showing the distribution of D_{max}/L ratios for faults within different geological units in Zone 3 of the Eastern Afar Depression (EAD). Faults in the Manda Rift Volcanics (M2v) display the widest range of values, whereas younger volcanic and sedimentary units (Q3v, Q2v, Pov, and Hs) exhibit narrower distributions. The Early Pleistocene volcanic unit (Q1v) contains the largest fault population, with a moderate central tendency and numerous outliers **148**

Figure 6.18: Fault-orientation sets in Zone 3. Faults were digitised from the DEM hillshade and colour-coded by orientation: Set A (green; broadly E–W), Set B (orange; NW–SE), Set C (red; NNW–SSE), and Set D (blue; N–S to NNE–SSW). The map shows the spatial distribution of each set and the zones where differently oriented faults overlap, particularly in the central and eastern parts of the study area. The rose diagrams below the map summarise the dominant strike of each orientation set using the same colour scheme. Basemap from ASTER GDEM v3 (NASA/METI/AIST/Japan Spacesystems and U.S./Japan ASTER Science Team, 2019) **131**

Figure 6.19: (a) Map showing Set A (green) and Set D (blue) faults in the western part of Zone 3, with rose diagrams indicating their dominant orientations. (b) Enlarged DEM view of the Immino Graben margin, where a continuous E–W scarp (Set A) is intersected by several shorter N–S scarps (Set D) that terminate against it. (c) Google Earth oblique perspective of the same area. The long E–W escarpment (Fault Scarp 3) forms the main graben margin, whereas two shorter N–S scarps (Fault Scarps 1 and 2) die out against it, confirming the mapped cross-cutting geometry. DEM basemap from ASTER GDEM v3 (NASA/METI/AIST/Japan Spacesystems and U.S./Japan ASTER Science Team, 2019imagery from Google Earth™, accessed 2025 ..... **132**

Figure 6.20: (a) Map showing Set A (green) and Set B (orange) faults, with rose diagrams illustrating their strike ranges. (b) Zoomed DEM panel highlighting a zone where sub-parallel E–W scarps are truncated or slightly offset at intersections with NW–SE faults that remain straight and continuous. (c) Google Earth oblique view of the same sector showing a long E–W escarpment (Fault Scarp 1) overprinted by multiple NW–SE scarps (Fault Scarp 2 and associated faults), confirming the cross-cutting relationship. DEM basemap from ASTER GDEM v3 (NASA/METI/AIST/Japan Spacesystems and U.S./Japan ASTER Science Team, 2019imagery from Google Earth™, accessed 2025..... **133**

Figure 6.21: (a) Map showing Set C (red) and Set D (blue) faults, with rose diagrams summarising their strike distributions. (b) Enlarged DEM view of a fault zone where N–S scarps are intersected by NNW–SSE faults; the N–S scarps become discontinuous or fragment into shorter segments at the intersections. (c) Google Earth oblique perspective of the same area. NNW–SSE scarps (dashed red lines) form long, continuous ridges that cut across a series of N–S faults (blue), confirming the mapped cross-cutting geometry. DEM basemap from ASTER GDEM v3 (NASA/METI/AIST/Japan Spacesystems and U.S./Japan ASTER Science Team, 2019); imagery from Google Earth™, accessed 2025 ..... **134**

Figure 6.22: Schematic summary of the relative cross-cutting relationships between the principal fault-orientation sets identified in Zone 3. In the western part of the study area, E–W-oriented faults locally predate N–S-oriented faults; in the central part, E–W-oriented faults locally predate NW–SE-oriented faults; and in the eastern part, N–S-oriented faults locally predate NNW–SSE-oriented faults. These relationships represent local relative-age constraints derived from mapped fault intersections and should not be interpreted as demonstrating a uniform temporal rotation of

fault orientations across the whole of Zone 3. Arrow orientations and positions are schematic and not scale **135**

Figure 6.23: Cross-section analysis and minimum apparent extensional strain across Zone 3 of the Eastern Afar Depression (EAD). (a) Geological map of Zone 3 showing the main geological units and structural framework of the study area. (b) Topographic cross-sections A–A′, B–B′ and C–C′ across Zone 3, showing the principal grabens, volcanic centres and Makarrassou Fault system. Orange markers indicate mapped fault-related offsets along each profile, while the blue arrows show the reconstructed profile length (L_1). (c) Summary of the reconstructed pre-faulting length (L_0), present-day extended profile length (L_1), calculated elongation $e = (L_1 - L_0)/L_0$, and corresponding minimum apparent extensional strain.. (d) Variation in minimum apparent extensional strain across Zone 3, decreasing from 72% along A–A′ to 50% along B–B′ and 27% along C–C′ from the south-east towards the north-west. These values represent minimum apparent fault-related extension because unresolved, buried, or volcanically obscured faults are not included in the surface-based reconstruction **136**

Figure 6.24: (a) Regional rift dynamics of the Afar Depression, showing the interaction between the Afar, Red Sea, Gulf of Aden and Main Ethiopian Rift systems, together with the location of the Eastern Afar Depression (EAD) and the Gamarri–Abli Transfer Zone. Modified after Rime et al. (2023). (b) Hill-shaded DEM of the Gamarri–Abli Transfer Zone showing the principal grabens, including Manda, Dobi, Gaggadé and Asal–Ghoubbet. (c) Colour-coded fault traces in Zone 3 illustrating spatial variations in fault orientation across the transfer zone, with older blue–green fault sets preserved predominantly in the northern part of the transfer zone and younger red–orange NW–SE to NNW–SSE-oriented fault sets occurring farther south and east **143**

Figure 7.1: Log–log plot of fault displacement versus fault length for faults from the Afar–NMER study areas, together with previously published global fault displacement–length data from Gillespie et al. (1992) and Bailey et al. (2005). Grey crosses represent the global dataset, while coloured crosses represent EAD (Zone 3), NMER (Zone 2), and NAD (Zone 1). Solid diagonal lines indicate constant D/L ratios of 1, 0.1, 0.01, and 0.001, defining the upper, middle, and lower fault-displacement envelopes. The inset illustrates idealised displacement–distance profiles for different D/L ratios **149**

Figure 7.2: Log–log displacement–length (D–L) plots for mapped faults across the three study zones. (a) Combined D–L distribution for all faults from NAD (Zone 1), NMER (Zone 2), and EAD (Zone 3), together with a conceptual fault-growth model used for comparison with the observed distributions. (b) D–L distribution for NAD (Zone 1), shown alongside the propagation fault-growth model. (c) D–L distribution for NMER (Zone 2), shown alongside the mixed fault-growth model (constant-length and hybrid growth). (d) D–L distribution for EAD (Zone 3), shown alongside the hybrid fault-growth model. Dashed reference lines indicate constant D/L ratios of 0.1, 0.01, and 0.001. The conceptual fault-growth models are modified after Nicol et al. (2016), Jackson et al. (2017), and Rotevatn et al. (2019) **150**

Figure 7.3: Log–log plot of apparent fault length (L) versus apparent maximum displacement (D_{max}) for all mapped faults in Zones 1–3, coloured by displacement-profile type (smooth single-peak, multi-peak, and irregular-peak). Dashed lines show constant D/L ratios (1, 0.1, 0.01, and 0.001), and the three dashed fields mark the Stage 1, Stage 2, and Stage 3 domains in the segmentation–linkage model. The cartoons on the right illustrate the corresponding geometries: isolated single-peak segments (Stage 1), soft-linked multi-segment arrays (Stage 2), and hard-linked composite

fault zones (Stage 3), modified from Kim and Sanderson (2005) **155**

Figure 7.4: Summary of the spatial variation in minimum apparent fault-related elongation across the three study zones. The upper panels show the geological setting and locations of the cross-rift transects used for the minimum-strain analysis, and the lower panels show the corresponding elongation values along the transect directions. (a) Zone 1 (NAD), where minimum apparent elongation decreases overall northwards from approximately 50% in the southern profiles to approximately 3% in the northernmost profile. (b) Zone 2 (NMER), where minimum apparent elongation increases north-eastwards from approximately 62% to approximately 90%. (c) Zone 3 (EAD), where minimum apparent elongation decreases north-westwards from approximately 72% to approximately 27%. These values were derived from DEM-based line-length balancing and represent minimum apparent fault-related strain rather than total tectonic extension **157**

Figure 7.5: GPS-constrained back-rotation model of the Danakil Block relative to Nubia, showing the progressive closure of the Danakil Depression and the relationship between its width, present-day GPS-derived velocities and inferred age. Back-rotation of 10° closes the northern part of the depression, whereas a total rotation of approximately 25° is required to close the southern part. Assuming a constant GPS-derived Danakil–Nubia rotation rate of 1.9 ± 0.1° Myr^{-1}, the inferred age of Danakil Block rotation is approximately 9.3 ± 4 Ma. Red dashed boxes indicate the approximate locations of Zone 1 (NAD) and Zone 3 (EAD) investigated in this study. Modified from McClusky et al. (2010) **159**

Figure 7.6: Regional tectonic and topographic setting of the Ethiopian Rift, showing earthquake focal mechanisms, relocated earthquake depths, and the location of the geodetic array used to constrain present-day deformation across the Main Ethiopian Rift. The solid line marks the position of the geodetic array. The red dashed box and arrow indicate the approximate location of Zone 2 (NMER) investigated in this study. Modified from Bendick et al. (2006) **160**

Figure 7.7: Tectonic settings of the three study zones along the northern East African Rift and Afar Depression. (a) Rift dynamics map of the Afar Depression and surrounding rift systems, showing the locations of the three study zones (NAD, NMER, and EAD). Modified from Rime et al. (2023), based on Corti (2009), Doubre et al. (2017), Moore et al. (2021), Pagli et al. (2014), Ruch et al. (2021), Sangha et al. (2022), and Viltres et al. (2020). ETTZ = Erta Ale–Tat'Ali Transfer Zone. (b–d) DEM-derived hillshade maps: (b) Zone 1, highlighting the main Afar rift-bounding faults; (c) Zone 3, showing en-échelon grabens linked to the Afar and Gulf of Aden rifts; and (d) Zone 2, illustrating the narrow axial belt of the Main Ethiopian Rift **163**

Figure 7.8: Tectonostratigraphic evolution of the Afar Depression and surrounding regions, modified from Rime et al. (2023). Time-slice maps show the pre-rift configuration and subsequent stages at approximately 30, 19, 13, 8, 5, 2.5, and 1 Ma and at present, illustrating the progressive opening of the Red Sea and Gulf of Aden rifts, anticlockwise rotation of the Arrata (Danakil) Block, and localisation of deformation in Central Afar, the Danakil Depression, and the Tendaho–Goba'Ad–Asal system. The reconstruction is based on a GPlates kinematic model combined with regional geological and stratigraphic constraints and is intended as a conceptual, schematic representation of Afar rift evolution (Rime et al., 2023) **169–171**

List of Tables

Table 4.1: Summary of the key quantitative parameters for the three study areas. Zone 1 (NAD), Zone 2 (NMER), and Zone 3 (EAD) differ in mapped area, fault number, mean length, mean maximum displacement (Dmax), dominant strike, and average fault density. These values provide a descriptive overview of the structural characteristics of each zone; detailed interpretations are presented in Chapter …….……**78**

Table 4.2: Statistical summary of fault geometry in Zone 1 (NAD, n = 350). The values show the minimum, maximum, and mean fault lengths (L) and maximum displacement (Dmax) derived from manually mapped fault traces ……..... **68**

Table 4.3: Statistical summary of smooth single-peak faults in Zone 1 (NAD, n = 35). The values show the minimum, maximum and mean fault lengths (L) and maximum displacements (Dmax) **72**

Table 4.4: Statistical summary of multi-peak profiles in Zone 1 (NAD, n = 71). Values show the minimum, maximum, and mean fault length (L) and maximum displacement (Dmax) **74**

Table 4.5: Statistical summary of irregularly peaked faults in Zone 1 (NAD, n = 244). Values show the minimum, maximum and mean fault length (L) and maximum displacement (Dmax) **76**

Table 4.6: Statistical summary of displacement-profile classes in Zone 1 of the North Afar Depression (NAD; n = 350). Faults were classified as single-peak, multi-peak and irregularly peaked according to the shapes of their displacement–length (D–L) profiles. The table reports the minimum, maximum and mean fault length (L) and maximum displacement (Dmax) for each profile class **93**

Table 5.1: Statistical summary of fault geometry in Zone 2 (NMER, n = 900). The table reports the minimum, maximum, and mean values for fault length (L) and maximum displacement (Dmax), derived from manually mapped fault traces digitised from the DEM **103**

Table 5.2: Statistical summary of single-peak faults in Zone 2 (NMER, n = 280). Values show the minimum, maximum, and mean for fault length (L) and maximum displacement (Dmax) **106**

Table 5.3: Statistical summary of multi-peak faults in Zone 2 (NMER, n = 382). The table reports the minimum, maximum, and mean values for the fault length (L) and maximum displacement (Dmax) derived from manually mapped fault traces **108**

Table 5.4: Statistical summary of irregular faults in Zone 2 (NMER, n = 238). The table reports the minimum, maximum, and mean values for fault length (L) and maximum displacement (Dmax) derived from manually mapped fault traces **110**

Table 5.5: Summary of the principal volcanic and sedimentary surface units used to classify mapped faults in Zone 2, showing geological-unit codes, concise unit descriptions and approximate age ranges. Age assignments follow the geological and tectonostratigraphic framework used in this study, based on Rime et al. (2022, 2023) and Persits et al..... **116**

Table 6.1: Summary statistics (min–max–mean) for apparent fault length (L) and apparent maximum displacement (Dmax) of 1,250 normal faults in Zone 3 (EAD) **139**

Table 6.2: Summary statistics (min–max–mean) for fault length (L) and Dmax of single-peak displacement profiles in Zone 3 (n = 112) **141**

Table 6.3: Summary statistics (min–max–mean) for apparent fault length (L) and apparent maximum displacement (Dmax) of multi-peak displacement profiles in Zone 3 (n = 542) **143**

Table 6.4: Summary statistics (min–max–mean) for apparent fault length (L) and apparent maximum displacement (Dmax) of irregular-peak displacement profiles in Zone 3 (n = 596) **144**

Table 6.5: Summary of the volcanic and sedimentary geological surface units used to classify faults in Zone 3 of the Eastern Afar Depression (EAD). Units within each rock-type group are arranged in approximate chronological order from oldest to youngest. Geological-unit codes, concise descriptions and approximate age ranges are shown to clarify the classifications used in the fault-frequency, L–Dmax and Dmax/L analyses **148**

Table 7.1: Summary statistics of fault geometries for the three study zones. The table lists the number of mapped faults, minimum, maximum, and mean fault lengths (L), and minimum and maximum displacements (Dmax) for Zones 1 (NAD), 2 (NMER), and 3 (EAD). For the NMER, these statistics refer only to intra-rift faults resolved in the DEM and do not include the older, highly eroded rift-margin border faults, which are likely to form hard-linked fault sets with some longer than 50 km (after Ebinger and Casey, 2001) **149**

Table 7.2: Summary of minimum, maximum and mean fault length (L) and maximum displacement (Dmax) for each displacement-profile type in the three study zones (NAD, NMER and EAD) **155**

Chapter 1: Introduction

1.1 Rationale of the research

Fault development is a fundamental process that controls the structural evolution of continental rifts and the transition from continental rifting to oceanic spreading at continental margins. Understanding how normal faults initiate, grow, interact, and link through time is therefore essential for improving our understanding of crustal deformation, basin evolution, and the development of continental margins. In addition, active rift systems are commonly associated with significant seismic hazards, making the study of fault evolution important for both scientific understanding and hazard assessment (e.g. Ebinger and Hayward, 1996; Ebinger, 2005; Corti, 2009). Normal faults typically initiate as isolated fault segments (e.g. Anders and Schlische, 1994; Gawthorpe et al., 1994; Childs et al., 2017), which may accumulate increasing amounts of displacement over time. As these isolated segments evolve, they interact and link to form larger fault systems that control basin architecture, create accommodation space, and influence the location of sedimentary depocentres (Anders and Schlische, 1994; Gawthorpe et al., 1994; Childs et al., 2017).

The stratigraphic record of the basin and the geomorphic record of its margins reflect the structure of the bounding fault zone, as well as the subsequent subsidence of the hanging wall, uplift of the footwall, and reorganisation of drainage (e.g. Prosser, 1993; Morley, 1999; Gawthorpe and Leeder, 2000; Meyer et al., 2002). Thus, the manner in which basin-bounding faults develop, link, and accumulate displacement plays a major role in determining where, when, and how much sediment will accumulate, and where and how much strain will be focused (Dawers and Underhill, 2000; Gupta and Scholz, 2000; Childs et al., 2017).

One of the most difficult aspects of studying fault development is that the available constraints tend to fall into two broad categories: those that are limited in scope (either spatially or temporally) and those that are general in nature (Cowie and Scholz, 1992; Kim and Sanderson, 2005; Corti, 2009; Lathrop et al., 2022). Few studies have used a consistent approach to investigate the complete continuum of fault development from early distributed continental rifting to later magma-assisted axial rift segments near the break-up. Accordingly, the Main Ethiopian Rift (MER) and Afar Depression offer a unique opportunity to address this problem in an area spanning the continuum of fault development and the transition from continental to oceanic-type rifting (Ebinger, 2005; Corti, 2009). Additionally, present-day kinematic data indicate that the Danakil Block, a

microplate located within the Afar triple junction between the Red Sea, Gulf of Aden and Main Ethiopian Rift, is rotating anticlockwise relative to Africa, resulting in changes in fault orientations, cross-cutting relationships between fault sets of differing orientations, and a progressive concentration of deformation into narrower axial belts in the Afar Depression (McClusky et al., 2010). These kinematic observations provide the regional tectonic framework for interpreting variations in fault orientation, linkage and strain localisation across the Afar Rift system and therefore form an important context for this study.

This study addresses these knowledge gaps by applying a consistent DEM-based structural mapping and analysis methodology across three tectonic domains representing successive stages of continental rifting: Zone 1, the North Afar Depression (NAD), representing distributed continental rifting; Zone 2, the North Main Ethiopian Rift (NMER), representing a more localised continental rift; and Zone 3, the East Afar Depression (EAD), representing the magma-assisted continental–oceanic transition.

For each zone, faults were mapped from high-resolution DEMs, and quantitative fault properties such as fault length (L), apparent maximum displacement (Dmax), displacement–length (D–L) scaling, displacement-profile shape, segmentation state, linkage style (soft versus hard), and minimum cross-section strain were extracted. These fault parameters were then compared among zones to determine (1) how fault populations differ across various stages of rifting, (2) where strain becomes localised during the continental–oceanic transition, and (3) how variations in orientation, linkage, and maturity in the Afar region relate to the anticlockwise rotation of the Danakil Block and reorganisation of the extension direction (McClusky et al., 2010; Childs et al., 2017; Lathrop et al., 2022). By treating these three areas within a single framework, this study aims to provide setting-specific constraints on fault development, linkage, and strain localisation in an active rift system that is undergoing a transition from continental rifting to oceanic-type spreading.

1.2 Gaps in knowledge

Although much research has been conducted on actively developing rift zones, considerable uncertainty remains regarding fault-segment lengthening, fault-zone linking, and accommodation of faults when rifting transitions from the continental interior to the incipient margins of the ocean. Studies that follow the same rift system through several stages of evolution using a single, consistent approach are relatively rare (Ebinger, 2005; Corti, 2009; Bastow and Keir, 2011). This limits our ability to recognise the factors that control the localisation of faults at each stage of the rifting process.

Most displacement length (D–L) databases primarily include non-volcanic single-phase rifts or sedimentary rifts. Consequently, fault-growth models have been less well tested in tectono-magmatic environments similar to those of the Afar Depression and North Main Ethiopian Rift, and empirical datasets from these areas are generally underdeveloped and difficult to apply to mixed sedimentary–volcanic environments (Muirhead et al., 2016; Pan et al., 2022). In addition, little is known about the evolution through time of segment lengths and linkages during rifting, and few studies have documented how linkage patterns evolve as rifting progresses (Corti, 2009; Rime et al., 2023).

The added complexity of variable lithologies creates further uncertainty because many studies have analysed volcanics and sediments separately, whereas in nature, both can interact mechanically and influence fault nucleation, propagation, and linkage (Peacock and Sanderson, 1991; Rime et al., 2022). Furthermore, the diversity of empirical methods used to study fault systems, differences in directional measures, and inconsistencies in the use of DEM-derived throws, heaves, and strains reduce the strength of inter-rift comparisons (Morewood and Roberts, 2002; Wright et al., 2012). Finally, the early stages of fault-growth processes are poorly resolved, and there are limited examples of natural D–L through-time constraints for fault systems (Lathrop et al., 2022), contributing to ongoing debates concerning fault-growth processes and their application to rift systems affected by magmatism. Addressing these uncertainties is essential for improving our understanding of fault evolution, strain localisation and continental breakup, as well as for evaluating whether existing fault-growth models are applicable to tectono-magmatic rift systems.

This thesis addresses these uncertainties through a consistent DEM-based analytical approach that compares the spatial fault architecture, lithological setting and temporal evolution of fault systems across contrasting rift segments of the Afar–Main Ethiopian Rift system (NAD, NMER and EAD). Specifically, this study investigates how fault growth, linkage and strain localisation vary across different stages of continental rifting. To evaluate these questions, three hypotheses were formulated and tested throughout this thesis.

1.3 Hypotheses

This thesis tests three related hypotheses regarding how normal faults grow, link, and localise strain across the continental–oceanic rifting transition in the northern East African Rift and Afar Depression.

Hypothesis 1: Strain localisation changes systematically between rift domains

If continental rifting evolves through progressive focusing of deformation, then the studied sectors should show systematic differences in the amount and distribution of the minimum apparent strain. Specifically, strain should be more strongly localised in narrower, more mature rift segments (e.g. the Wonji belt in the NMER or the active magmatic segments in the EAD) than in wider rift domains that may represent an earlier stage in local rift architecture (e.g. the northern NAD). This hypothesis follows published models in which strain migrates from early border-fault systems towards younger axial volcanic segments as rifting advances (Hayward and Ebinger, 1996; Ebinger, 2005; Corti, 2009; Nixon et al., 2014).

Hypothesis 2: Fault growth follows established displacement–length (D–L) scaling and fault linkage models

Normal faults in the Afar region are expected to follow established global models of displacement–length scaling and progressive fault linkage. If these models apply, the mapped faults across all three zones will show (a) positive D–L scaling trends and (b) a transition from isolated segments to interacting relays and finally to hard-linked fault zones. Therefore, differences in Dmax/L, displacement profile shape, and linkage type are expected to reflect relative maturity and vary systematically between zones at different stages of rifting (Walsh and Watterson, 1988; Childs et al., 2017; Kim and Sanderson, 2005).

Hypothesis 3: Fault orientation and cross-cutting relationships record the kinematic evolution of the Danakil Block and Afar triple junction

If the Afar rift system evolved through the anticlockwise rotation of the Danakil microplate and the clockwise rotation of the internal Afar blocks (Rime et al., 2023; McClusky et al., 2010), then the fault populations should preserve a record of this reorganisation. Older faults in transfer zones (particularly in the EAD) are expected to retain earlier orientations, whereas younger faults should align with the present extension direction associated with the Afar–Red Sea–Gulf of Aden kinematics. Consequently, cross-cutting relationships, orientation clusters, and changes in strain localisation should

be consistent with a diachronous reorientation of the stress field driven by block rotation and the progressive linkage of the triple junction. To test these hypotheses, the following research aim was developed.

1.4 Research aim

The overall aim of this research is to understand how normal faults grow and interact through different stages of continental rifting by quantitatively characterising and comparing DEM-derived fault-system architecture in subaerial settings across the continental–oceanic transition in the North Afar Depression (NAD), North Main Ethiopian Rift (NMER), and East Afar Depression (EAD).

To achieve this aim, the study was guided by specific objectives that quantified and compared the geometric and spatial characteristics of normal fault systems across the three study zones, including fault scaling (L–Dmax), displacement profile types, segmentation and linkage style, surface-unit context, minimum (apparent) strain, and cross-cutting/orientation patterns. Together, these objectives constrain how fault growth, linkage, and strain localisation vary between rift domains and how these variations relate to the wider tectono-kinematic evolution of the Afar–MER system.

1.5 Specific objectives

- **Cross-zone fault geometry and scaling (Chapters 4–6)**

  Build uniform DEM-based fault inventories for Zones 1–3; extract fault length (L) and apparent maximum displacement (D_{max}); derive D–L relationships and D_{max}/L as maturity proxies; and map spatial fault distributions with zone-by-zone statistics.
- **Displacement-profile behaviour (Chapters 4–6)**

  Construct along-strike displacement profiles and classify them as single-peak, multi-peak, or irregular; relate profile type to segmentation state, linkage style, and D_{max}/L; and evaluate how profile types vary along the continental–oceanic transition.
- **Segmentation and linkage (Chapters 4–6)**

  Identify segment boundaries, relays, and overlaps; classify linkages as soft (immature) or hard (mature); and quantify linkage frequency and geometry between zones relative to maturity proxies.
- **Fault maturity across surface units (Chapters 4–6)**

Assign faults to mapped surface units (lithostratigraphic/age groups from the Afar geological map and updates), test for differences in D_{max}/L, profile type, and linkage between units, and account for preservation and resurfacing biases.

- **Minimum strain (elongation) from cross-sections (Chapters 4 and 6)**

  Estimate minimum extensional strain using line-length balancing: for each cross-section, measure the present-day deformed length of the marker line (L_1), compare it with the pre-extension reference length (L_0), and compute elongation as $e=(L_1-L_0)/L_0$; apply obliquity corrections where profiles deviate from the section normal to the mean fault strike; and summarise the results by zone (and by surface unit, where applicable).

- **Orientation, cross-cutting relationships, and kinematic context (Chapter 6)**

  Analyse fault orientations and build a cross-cutting matrix that combines fault–fault and fault-surface-unit relationships to infer the relative timing of fault sets and rift stages. These orientation, timing, and localisation patterns are compared with geodetic evidence for anticlockwise Danakil Block rotation to test its control on fault re-orientation and deformation focusing.

1.6 Thesis outlines

- **Chapter1: Introduction.**
  Frames the problem of how normal faults grow and interact during continental rifting, outlines the regional context of the Afar–Main Ethiopian Rift system, states the research rationale, aim, and specific objectives, and summarises the thesis structure.

- **Chapter 2: Literature review.**
  Synthesises the current understanding of rift tectonics and continental breakup, fault growth and scaling (D–L), segmentation and linkage, and strain localisation in active rifts. Review methods commonly used to quantify upper-crustal deformation in subaerial settings, with an emphasis on DEM-based fault mapping and displacement profile analysis.

- **Chapter 3 Describes the data and methodology.**
  The DEM acquisition and processing (30 m ASTER), fault trace digitisation, identification of top/bottom cut-offs, extraction of fault length (L) and apparent maximum displacement (D_{max}), construction and classification of a long-strike displacement profiles, linkage mapping (soft vs. hard), assignment to surface units, cross-section design, and minimum-strain (line-length) calculations

including obliquity corrections are described. Details of quality control and reproducibility (QGIS/Python).

- **Chapter 4 – Results from Zone 1- North Afar Depression (NAD).**

  Presents uniform fault inventory and statistics, *D–L* scaling and D_{max}/L, displacement profile types, segmentation and linkage patterns, unit-based maturity contrasts, and minimum-strain estimates across cross-sections. Reports orientations and key cross-cutting relationships relevant to the early rift stages.

- **Chapter 5 – Results from Zone 2 -North Main Ethiopian Rift (NMER).**
  Reports geometry and scaling, evolution of displacement profile types, segmentation/linkage metrics within axial fault belts, unit-based maturity differences, and minimum-strain results. Summarises the orientations and cross-cutting relations indicative of rift focusing.

- **Chapter 6: Results from Zone 3 - East Afar Depression (EAD).**
  Documents long, displacement-efficient faults and strongly localised deformation: geometry and scaling, displacement profile distributions, segmentation/linkage, and unit-based maturity. Presents orientation patterns and cross-cutting relationships and evaluates the kinematic context in light of anticlockwise Danakil-Block rotation.

- **Chapter 7: Discussion and conclusions.**
  Synthesises results across Zones 1–3 to evaluate how fault growth, segmentation, linkage, and strain localisation evolve from distributed continental rifting to mature axial deformation. We compared the findings with published rift models, considered controls such as structural inheritance and regional kinematics, and outlined the implications for fault-system evolution in the Afar–MER region. Finally, it discusses the main contributions and limitations of the study and provides recommendations for future work.

The aims and hypotheses set out in this chapter need to be framed within a wider understanding of how rifts and normal faults develop. The next chapter therefore reviews the key literature on rift tectonics, normal fault growth, displacement–length scaling, fault segmentation and linkage, and strain localisation in active rift settings. This review provides a conceptual foundation for the data, methods, and results presented in the remainder of this thesis.

Chapter 2: Literature review

2.1 Introduction

Understanding how faults grow, interact, and accommodate strain is fundamental to interpreting the evolution of continental rifts (Cowie and Scholz, 1992; Kim and Sanderson, 2005; Walsh and Watterson, 1988). Over the past four decades, research has provided detailed insights into fault kinematics, scaling relationships, and segmentation–linkage processes in both volcanic and non-volcanic rift settings (Mansfield and Cartwright, 2001; Peacock and Sanderson, 1991; Walsh et al., 2003). However, despite this progress, many uncertainties remain regarding how these processes vary across different stages of rift development, particularly in magma-rich environments such as the Afar Depression and the adjacent East African Rift System (EARS) (Ebinger, 2005; Rime et al., 2023). This chapter reviews the existing literature on these topics and identifies the specific gaps that this study aims to address in the literature.

This study focuses on three areas distributed across the Afar Depression and northern Main Ethiopian Rift: The North Afar Depression (NAD; Zone 1), the North Main Ethiopian Rift (NMER; Zone 2), and the Eastern Afar Depression (EAD; Zone 3) (Figure 2.1). These study zones provide contrasting tectono-magmatic settings in which fault growth, segmentation, linkage and strain accommodation can be compared.

To begin, this chapter introduces the general principles of continental rifting, including the key stages of extension and global models that explain the transition from continental to oceanic lithosphere (Buck, 1991; Ebinger, 2005; McKenzie, 1978). It then examines fault growth and scaling relationships, highlighting how displacement–length (D–L) scaling has been used to infer fault maturity and rift evolution (Cowie and Scholz, 1992; Kim and Sanderson, 2005; Walsh and Watterson, 1988). The following sections explore fault segmentation and relay structures, emphasising how segments evolve and link to form complex fault systems (Peacock and Sanderson, 1991; Peacock, 2002; Walsh et al., 2003), and fault linkage and interaction, where soft and hard linkages, overlapping faults, and relay zones are investigated to understand their role in rift architecture (Mansfield and Cartwright, 2001; Peacock and Sanderson, 1994).

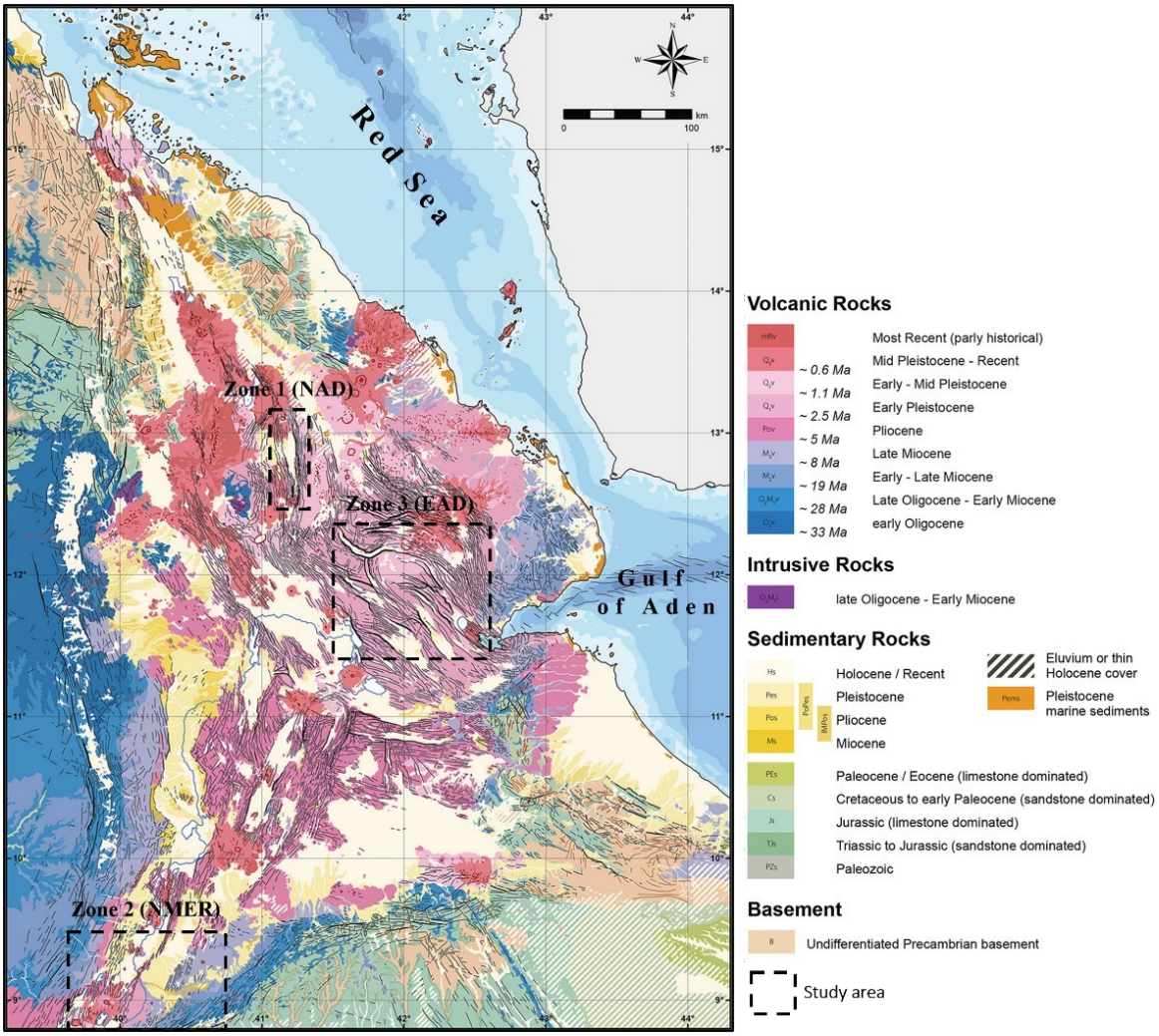


Figure 2.1: Overview geological map showing the locations of the three study zones: Zone 1, North Afar Depression (NAD); Zone 2, North Main Ethiopian Rift (NMER); and Zone 3, Eastern Afar Depression (EAD). Geological units are grouped into volcanic, intrusive, sedimentary and basement categories according to stratigraphic age to provide regional geological context for the study areas. Base geology adapted from Rime et al. (2022).

In addition, this review considers how strain is accommodated across rift zones by comparing distributed and localised deformation and examining quantitative approaches used to assess strain from fault throw and heave (Morewood and Roberts, 2002). The geological setting of the Afar Depression and NMER is then presented, providing the regional tectonostratigraphic context required to interpret the structural observations made in this study (Rime et al., 2023; Bastow et al., 2005). Finally, this chapter identifies key gaps in knowledge, particularly regarding the influence of magmatism on fault growth, the degree of segmentation and linkage across different rift sectors, and the lack of comparative quantitative studies using a DEM (Bastow and Keir, 2011; Rime et al., 2023).

2.2 Rift tectonic and continental breakup

Continental rifting represents the initial stage of continental lithosphere breakup and may ultimately lead to the formation of new ocean basins. It begins with lithospheric extension, which progressively thins and weakens the continental lithosphere, resulting in normal faulting, basin subsidence, and commonly associated volcanism (McKenzie, 1978; Buck, 1991). As extension continues, deformation evolves through progressive localisation of strain, increasing magmatic activity, and eventual rupture of the continental lithosphere, culminating in the initiation of seafloor spreading (Ebinger, 2005; Rime et al., 2023).

The duration and style of each stage vary according to crustal composition, inherited structural heterogeneity, mantle dynamics, and the relative contribution of tectonic and magmatic extension (Corti, 2009; Bastow and Keir, 2011). In magma-rich rifts, dyke intrusion may accommodate part of the extensional strain, thereby reducing the amount of displacement accommodated by normal faulting, whereas magma-poor rifts primarily accommodate extension through brittle fault slip (Keir et al., 2015; Muirhead et al., 2016). These differences influence fault growth, strain localisation, and the architecture of evolving rift s

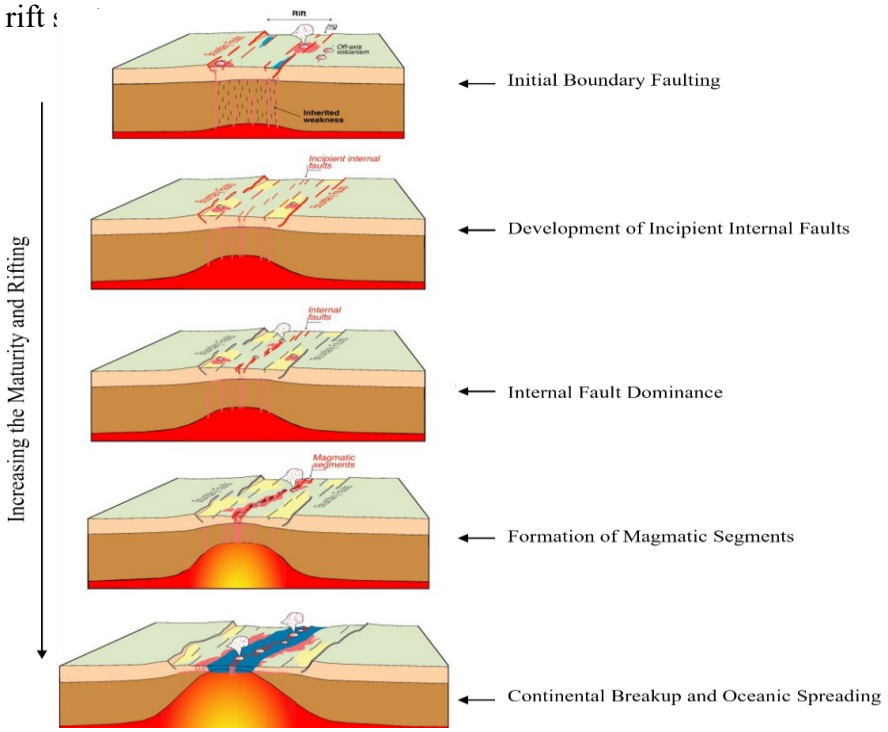


Figure 2.2: Conceptual model illustrating the progressive stages of continental rift evolution, from initial boundary faulting exploiting inherited crustal weaknesses, through the development of incipient and internal faults, to magma-dominated segments and eventual continental rupture leading to oceanic spreading. This synthesis, based on analogue modelling and observations from the Main Ethiopian Rift and Afar Depression, highlights the increasing interaction between magmatism and tectonics during rift maturation. Modified after Ebinger (2005), Corti (2009), and Agostini et al. (2011) in Corti (2012).

Figure 2.2 shows a widely referenced model of rift evolution (Corti, 2012), summarised here as an example of the progressive change from boundary faulting, where strain first exploits inherited crustal weaknesses, to the generation of internal faults that dominate the rift interior as faulting propagates inboard. As extension continues along the rift, magmatic intrusion increasingly dominates over fault slip, giving way to magmatic segments of the rift that accommodate most of the strain. As a culmination of rift development, the continuity of faulting and increasing magmatism ultimately leads to continental rupture and initiation of oceanic spreading (Ebinger, 2005; Corti, 2009; Agostini et al., 2011). This staged model is also useful for interpreting rift architecture in East Africa, where magmatism and tectonics affect rift architecture at varying levels within rift zones.

More broadly, rift systems vary in terms of the ratio of tectonic stretch to magmatism, given the variables associated with each rifting process. In magma-poor situations, such as the North Sea or Basin and Range Province, extension is mainly accommodated by brittle faulting and half-graben development (Walsh and Watterson, 1988; Cowie and Scholz, 1992). Magma-rich rifts, such as Iceland or the East African Rift System (EARS), display dyke intrusions and sills, which alter fault propagation and lower fault throws, so that part of the extensional strain is accommodated by magmatic processes alongside significant fault slip (Keir et al., 2015; Muirhead et al., 2016). Similarly, recent geodetic and seismic observations suggest that magmatic and tectonic rifting processes often act concurrently and that episodic magma intrusions interact with fault slip during rift formation and evolution.

The differences between magma-rich and magma-poor rift sectors have important implications for fault growth and rift architecture because they accommodate extensional strain through different mechanisms. In magma-rich rifts, a proportion of the extensional strain is accommodated by dyke intrusion rather than fault slip, thereby reducing the amount of strain accommodated by normal faulting and influencing fault geometry, displacement accumulation, and fault growth (Keir et al., 2015; Muirhead et al., 2016). By contrast, magma-poor rifts accommodate most of the extensional strain through brittle faulting, resulting in fault slip becoming the dominant mechanism of strain accommodation. Consequently, differences in the relative contributions of tectonic faulting and magmatic intrusion may influence fault growth and are likely to affect displacement–length (D–L) scaling characteristics. Although the magnitude of these differences varies between tectonic settings, stages of rift evolution, and local geological conditions, these contrasting styles of strain accommodation provide an important

framework for interpreting fault growth and displacement–length (D–L) scaling in the contrasting rift settings investigated in this study.

2.3 Fault growth and scaling relationship

Understanding how faults grow and accumulate slip is important for reconstructing the mechanical evolution of rift systems. Fault growth studies provide interpretations of the processes that affect the localisation of strain and the evolution of rift architectures over time (Walsh and Watterson, 1988; Cowie and Scholz, 1992; Gawthorpe and Leeder, 2000). Classical growth models suggest that faults initiate as isolated segments, each developing displacement from the outset in a predictable relationship with their lengths (Walsh and Watterson, 1988). These faults may continue to grow laterally and accumulate displacement until they interact with neighbouring faults. Subsequent linkage between faults can further modify the displacement profiles and scaling relationships, producing more complex fault geometries (Kim and Sanderson, 2005).

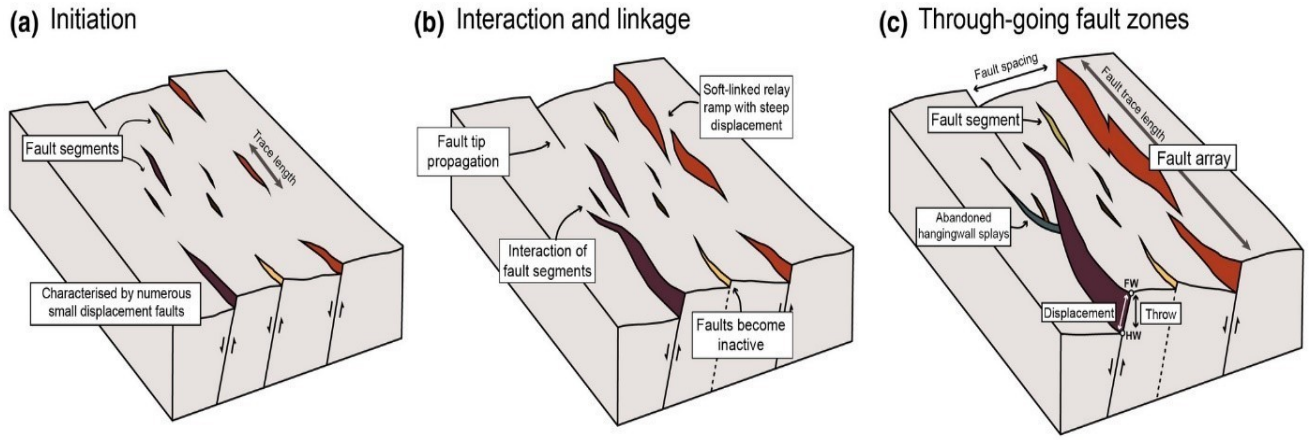


Figure 2.3: Conceptual model of fault network evolution, illustrating the progressive stages from initiation to through-going fault zones. **(a)** Early stage with isolated, short (2–10 km), and low-displacement fault segments; **(b)** intermediate stage characterised by interaction and linkage between fault tips, forming soft-linked relay ramps; and **(c)** mature stage where strain localises onto a few long (>10 km), high-displacement through-going faults, with abandoned segments preserved in the hanging wall. Modified from Gawthorpe and Leeder (2000).

Several studies have indicated a near-linear relationship between fault length (L) and maximum displacement (Dmax) on log–log plots, which has generally been interpreted as evidence of self-similar growth, where both length and displacement increase proportionally from fault initiation to maturity (Cowie and Scholz, 1992; Kim and Sanderson, 2005). The displacement–length scaling relationship is commonly expressed as:

$$D = cL^n$$

where D is fault displacement, L is fault length, c is a scaling coefficient, and n is the scaling exponent. For geometrically self-similar fault growth, n is expected to be close to 1, although natural fault populations commonly show scatter around this relationship (Cowie and Scholz, 1992).

In general, longer faults have larger displacements, indicating that growth is controlled by both propagation and slip accumulation. However, field data indicate some scatter around the scaling relationship, which is attributed to lithological contrasts, mechanical layering, fault interaction, and intrusion by magmatic dykes or sills (Peacock, 2002; Walsh et al., 2003; Pan et al., 2022). This demonstrates some variability in fault scaling and suggests that, while the underlying process remains broadly self-similar, the slope or ratio of the L–D relationship can vary depending on the local structural and rheological conditions of the rift.

Natural D–L datasets are influenced by both geological controls and measurement uncertainty. Geological factors such as lithology, mechanical layering, fault interaction, linkage state and magmatic intrusion can modify the amount of displacement accumulated relative to fault length. In addition, fault lengths may be underestimated where fault tips are poorly exposed, buried, eroded or below the spatial resolution of the dataset, while displacement estimates depend on the preservation and identification of suitable offset markers. Differences in whether individual fault segments or entire linked fault systems are measured can also affect the calculated scaling relationship. Consequently, scatter in D–L datasets may reflect both genuine variations in fault-growth behaviour and differences in preservation, sampling and measurement methods (Cowie and Scholz, 1992; Kim and Sanderson, 2005).

Displacement profiles provide further insight into fault growth mechanisms. Faults exhibit displacement profiles that are approximately elliptical or bell-shaped in many rift settings, with maximum displacement in the centre, tapering towards the fault tips (Walsh and Watterson, 1988; Cowie and Scholz, 1992).

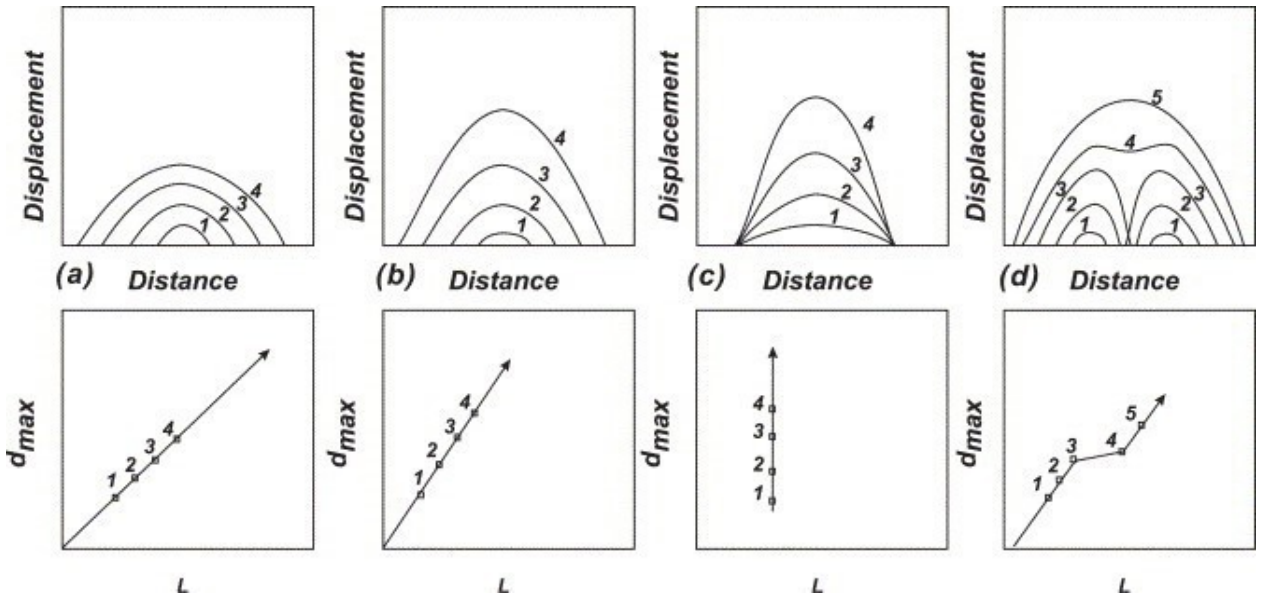


Figure 2.4: Conceptual models of fault growth adapted from Kim and Sanderson (2005). **(a)** Constant D_{max}/L ratio model, in which fault length (L) and maximum displacement (D_{max}) increase proportionally from initiation, maintaining a constant ratio throughout growth. **(b)** Increasing D_{max}/L ratio model, in which the D_{max}/L ratio increases during fault growth, reflecting proportionally greater displacement relative to fault length over time. **(c)** Constant-length model, after Walsh et al. (2002), in which fault length increases rapidly during the early stages of fault growth before remaining approximately constant as displacement continues to accumulate. **(d)** Fault linkage model (Peacock and Sanderson, 1991; Cartwright et al., 1995; Kim et al., 2000), in which newly linked fault segments may initially exhibit anomalously low displacement for their length, or overlapping segments may show locally high displacement; however, with continued deformation, the fault system tends to return to a self-similar scaling relationship.

The scaling between fault length and displacement provides an additional proxy for assessing fault maturity. According to the models of Kim and Sanderson (2005) (Figure 2.4), faults generally follow a self-similar growth trend, in which displacement and length increase proportionally from initiation. Based on a global compilation of normal faults, they defined reference displacement–length envelopes and showed that fault arrays typically evolve through three characteristic stages: an initial stage in which isolated faults propagate towards one another; a soft-linkage stage in which overlapping segments interact across a relay zone and aggregate fault length increases more rapidly than maximum displacement; and a hard-linkage stage in which breaching of the relay produces a throughgoing fault, such that subsequent growth is accommodated mainly by increasing displacement rather than further lengthening (Peacock and Sanderson, 1991; Kim and Sanderson, 2005).

Simple reference lines, such as idealised Dmax–L relationships, are often used as convenient benchmarks within these global envelopes when comparing different datasets. Studies have improved our understanding of fault growth styles by distinguishing between propagating and constant-length growth modes. Nicol et al. (2005) demonstrated

that many normal faults exhibit two phases of growth. The first phase is characterised by a period of rapid lateral propagation, during which both the length and displacement increase simultaneously. The second phase occurs when the fault tips reach a point of equilibrium and no longer propagate, and additional slip is accommodated by increasing the displacement at a near-constant length. Conversely, some faults exhibit propagating growth behaviour, in which fault length and displacement increase synchronously (Rotevatn et al., 2019). As a result, faults with comparable total lengths can have significantly different displacement histories and locations on D–L plots, and the interplay and interactions between neighbouring fault segments can transform the overall character of the fault system from a more propagating to a more constant-length, displacement-dominant style of growth. In terms of displacement-profile geometry, isolated faults typically exhibit relatively simple profiles with a single displacement maximum, whereas interacting or linked fault segments may exhibit more complex, multi-peaked profiles reflecting displacement maxima associated with individual segments (Kim and Sanderson, 2005).

At the scale of individual rift sectors, extension in magma-rich rifts can be accommodated by a combination of brittle faulting and magmatic intrusion, with the relative contribution of these processes varying spatially and through different stages of rift development (Keir et al., 2006; Bastow and Keir, 2011; Keir et al., 2015).

Therefore, deviations from an ideal self-similar scaling trend can arise owing to linkage, interaction, and changes in growth modes. New fault systems formed through linkage may exhibit temporarily lower displacement–length ratios than expected, and fault arrays containing overlapping soft-linked faults may display localised higher displacement–length ratios. Additionally, the presence of hybrid magmatic–tectonic behaviour can alter the distribution of strain between faults and intrusions, thereby modifying the distribution of displacement–length ratios. However, these anomalies typically disappear as deformation continues, and the fault system returns to a self-similar scaling relationship (Kim and Sanderson, 2005; Nicol et al., 2005). Furthermore, in magma-rich rift environments, such as parts of the Afar Depression, magmatic activity can modify displacement–length ratios by allowing extension without corresponding slip on the surface fault (Pan et al., 2022; Peacock, 2002).

When interpreting the evolutionary history of a rift based on scaling relationships, it is important to recognise that the interaction between tectonics and magmatism, as well as the segmentation and linkage of faults, influence fault geometry and scaling behaviour. The study of fault growth and scaling therefore provides a useful framework for

understanding the evolution of continental rifts. By comparing length–displacement relationships, displacement-profile shapes and linkage characteristics, it is possible to evaluate the development of fault networks and their role in accommodating tectonic extension. Despite extensive previous studies and global compilations of fault displacement–length scaling, fewer studies have quantitatively compared fault populations across contrasting tectono-magmatic sectors within the same evolving rift system. This represents an important gap in magma-rich rift settings such as Afar, where variations in magmatic intrusion, fault interaction and linkage may modify displacement accumulation relative to fault length. Therefore, this thesis uses D_{max}–L scaling as a comparative metric, together with displacement-profile geometry and fault-linkage characteristics, to assess fault maturity and spatial variations in strain across the Afar Depression and North Main Ethiopian Rift and to compare these fault populations with global scaling envelopes and fault-growth models.

2.4 Fault linkage and relay structures

Fault linkage represents the process by which previously isolated fault segments evolve into longer and more continuous fault systems, which is a key control on strain propagation and rift basin architecture (Peacock and Sanderson, 1991; Walsh et al., 2003). Classical models describe a transition from soft linkages, characterised by intact relay zones accommodating displacement gradients between overlapping fault tips (Peacock and Sanderson, 1994), to hard linkages formed when these relay zones rotate, narrow and breach to create throughgoing faults (Mansfield and Cartwright, 2001) (Figure 2.5). In three dimensions, faults that appear soft-linked at the surface may be hard-linked at depth owing to the elliptical geometry of displacement on fault planes (Figure 2.5). This geometry means that subsurface fault overlaps can occur before linkage is visible at the surface, so surface observations alone may underestimate the true degree of connectivity within a fault network.

Although this soft-to-hard progression is widely documented in analogue models and field studies of non-magmatic settings (Peacock, 2002), its applicability to magma-rich environments, such as the Afar Depression, remains uncertain (Rime et al., 2023). A comparison of studies suggests that fault-linkage behaviour varies between tectonic settings. In particular, differences in magmatic activity and extension direction may influence the development and preservation of relay structures and the progression from soft linkage to relay breaching (Fossen and Rotevatn, 2016). Moreover, differences in methodological approaches, ranging from detailed structural mapping of individual relay ramps to network-scale displacement analyses, also contribute to varying interpretations

of linkage timing and evolution (Walsh et al., 2003; Kim and Sanderson, 2005).

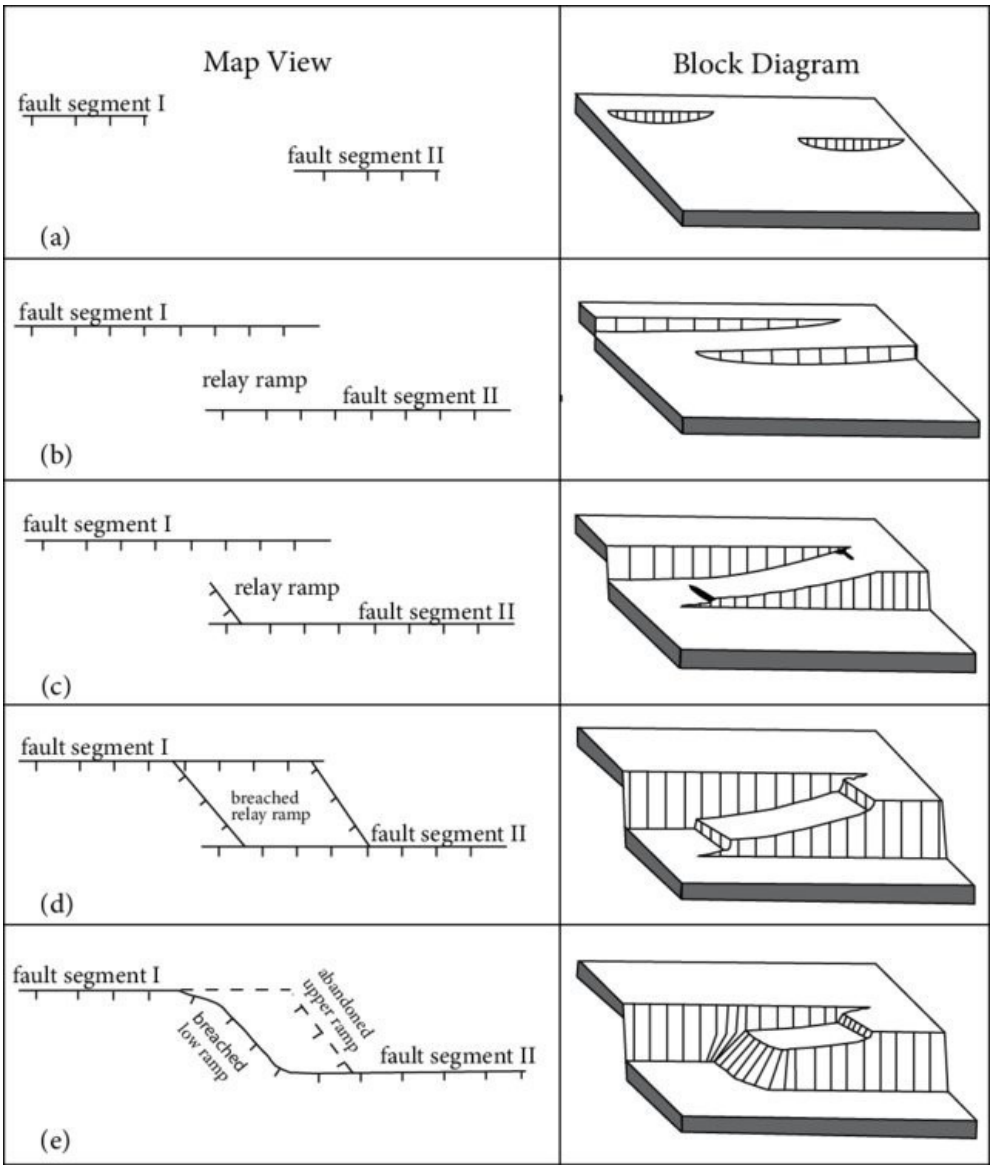


Figure 2.5: Evolutionary stages of a relay ramp showing the progressive linkage of two overlapping fault segments. **(a)** Isolated segments with no interaction; **(b)** development of an intact relay ramp between overlapping fault tips; **(c)** progressive rotation and strain concentration within the relay ramp; **(d)** breaching of the relay ramp, leading to hard linkage; and **(e)** abandonment of the upper ramp and formation of a breached low ramp. Modified after Peacock and Sanderson (1991) and Çiftçi and Bozkurt (2007).

Though both magma-rich and magma-poor rifts display evidence of relay breaching that influences fluid and sediment pathways (Fossen and Rotevatn, 2016), few studies have systematically compared these environments, leaving open questions about whether classical relay models adequately capture their three-dimensional behaviour (Roche et al., 2021; Pan et al., 2022). Together, these studies indicate that fault linkage and relay structures are dynamic, multiscale processes influenced by local mechanical properties and broader tectono-magmatic regimes. This understanding provides a framework for evaluating linkage behaviour in the Afar Depression and North Main Ethiopian Rift,

where this thesis aims to address the current lack of comparative, quantitative analysis across contrasting rift settings.

2.5 Fault segmentation and interaction

Fault segmentation describes how normal faults are divided into discrete segments that propagate, overlap, and evolve during rift development, influencing strain localisation and the architecture of rift basins (Peacock and Sanderson, 1991; Walsh et al., 2003). Walsh et al. (2003) distinguished two end-member models for the development of segmented normal faults: the isolated fault model, in which segments initiate and evolve independently before interaction, and the coherent fault model, in which segments grow together as components of a larger fault system (Figure 2.6). These models make a conceptual separation between isolated, discrete faults, which typically have simple bell-shaped displacement profiles, and segmented faults, where multiple overlapping segments interact and create multi-peaked displacement profiles as they couple and mature (Mansfield and Cartwright, 2001; Walsh et al., 2003) (Figure 2.6).

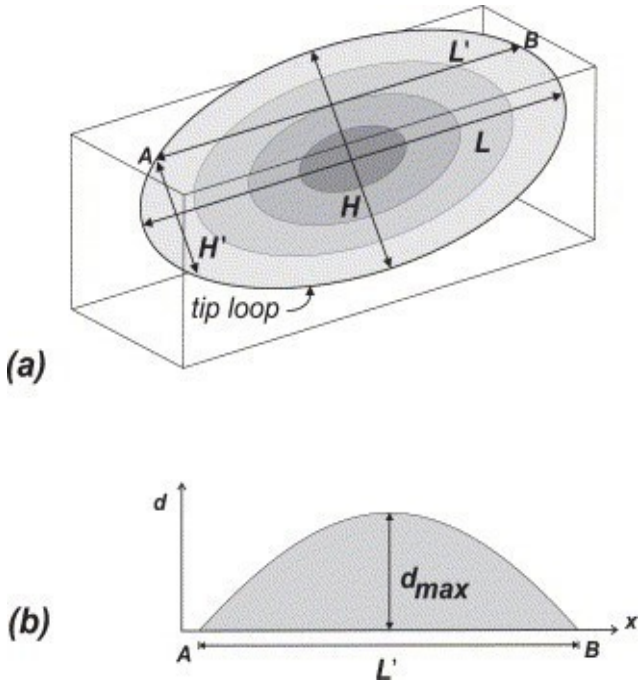


Figure 2.6: **(a)** Schematic of the displacement distribution on an elliptical fault surface, with variations in fault length (L) and height (H). The tip loop defines the outer boundary of the fault surface, along which displacement decreases to zero.The shading density/saturation increases towards the fault centre and represents the relative displacement values on the fault surface. The surface of the upper block intersects the fault surface at line A–B, and the lower panel **(b)** depicts the displacement (d) versus distance (x) profile along that intersection, with maximum displacement (Dmax) occurring near the centre of the fault (Kim and Sanderson, 2005).

While previous work has examined segmentation behaviour in analogue experiments and magma-free rift systems (Peacock, 2002), this type of work regarding magma-rich

environments, such as the Afar Depression, is poorly constrained (Rime et al., 2023). Comparisons between magma-rich rifts (e.g. the Afar Depression) and magma-poor rifts (e.g. the North Main Ethiopian Rift) suggest that magmatism and oblique extension may change segmentation geometry and rates of segment interaction, often produce more irregular and asymmetric fault arrangements than expect (Fossen and Rotevatn, 2016; Roche et al., 2021). Furthermore, methods ranging from high-resolution scarp mapping to network-scale analysis may shape different views and timings for segmentation and interaction (Kim and Sanderson, 2005; Pan et al., 2022). Both spatial and temporal analyses of fault segmentation therefore need to account for differences in tectono-magmatic setting and data scale when comparing different rift systems.

These contrasting growth models are also reflected in their displacement profiles: the isolated fault model retains distinct displacement maxima associated with individual segment centres, whereas the coherent fault model develops smoother aggregate displacement profiles as the fault array evolves (Walsh et al., 2003).

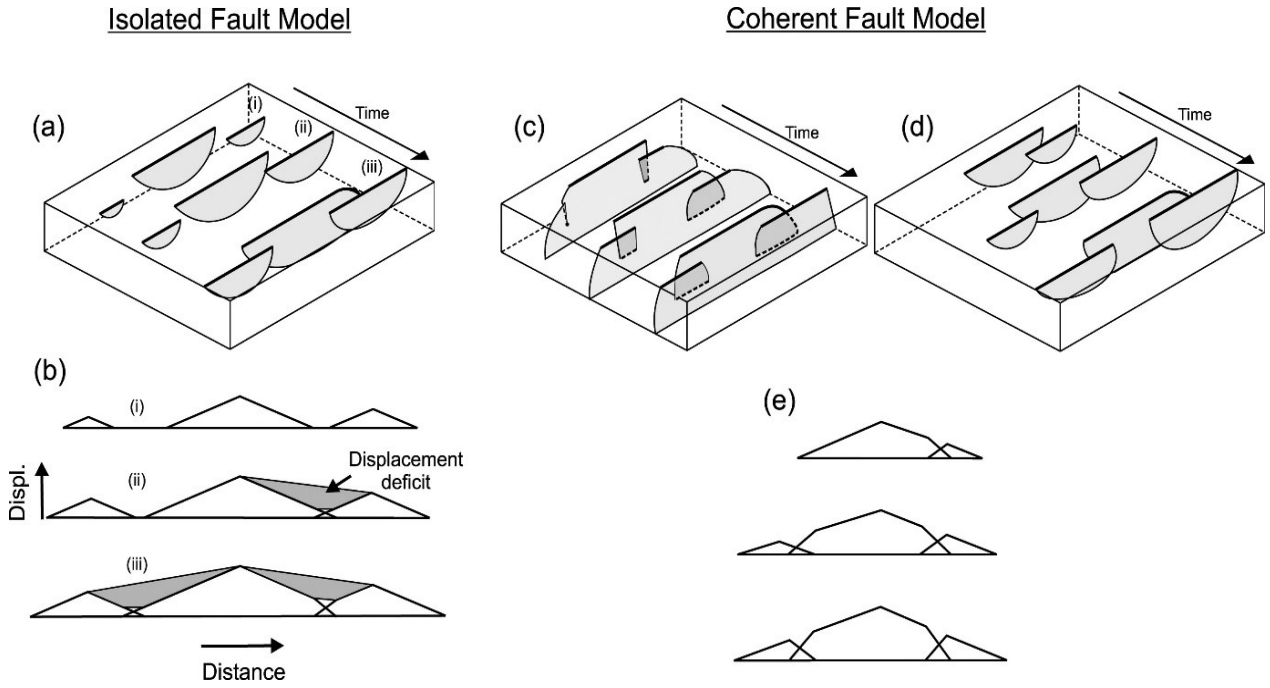


Figure 2.7: Conceptual diagrams illustrating the two end-member models for the development of segmented-fault arrays. Panels **(a)**, **(c)**, and **(d)** show the three stages of fault growth, whereas panels **(b)** and **(e)** show the displacement–distance profiles for fault traces along the block surfaces. Both isolated and coherent fault models can include hard-linked segments (formed by the breach of relay zones or fault surface bifurcation) and soft-linked segments (connected via relay ramps) at different stages of evolution. The shaded regions in (b) highlight the displacement deficits between adjacent segments that are not caused by continuous deformation within the relay zones. In the isolated fault model, points of maximum displacement are retained at segment centres, whereas the coherent model tends to produce smoother aggregate profiles at all stages of development (Walsh et al., 2003).

In summary, these studies indicate that fault segmentation and interaction are dynamic, multiscale processes governed by local mechanics and broader tectono-magmatic regimes. This framework will be used to investigate and discuss fault-segmentation patterns in the Afar Depression and North Main Ethiopian Rift in the context of isolated and segmented fault geometries, with respect to rift evolution and strain accommodation across contrasting rift environments.

2.6 Strain accommodation in rift systems

Strain accommodation in rift systems refers to the partitioning of the total extensional deformation (strain) among brittle faulting, ductile deformation, and, in some cases, magmatic processes. Understanding how strain is accommodated provides important insights into the mechanical evolution of rift basins and their transition from continental extension to eventual break-up (Ebinger and Hayward, 1996; Corti, 2009). In fault-dominated (magma-poor) systems, strain is typically concentrated on a small number of high-displacement border faults that bound asymmetric half-graben basins, with subsidiary intrarift fault arrays accommodating more localised extension (for example, the Basin and Range Province). In these settings, the scaling relationships between fault length (L) and displacement (d) often reflect mature fault geometries that have accumulated significant slips over time. In contrast, magma-rich systems, such as portions of the East African Rift System (EARS) and the Afar Depression, show a more distributed strain pattern, where magmatic intrusion (dykes and sills) accommodates a significant proportion of extension, reducing fault throw and influencing the overall geometry and maturity of the fault network (Keir et al., 2015; Rime et al., 2023).

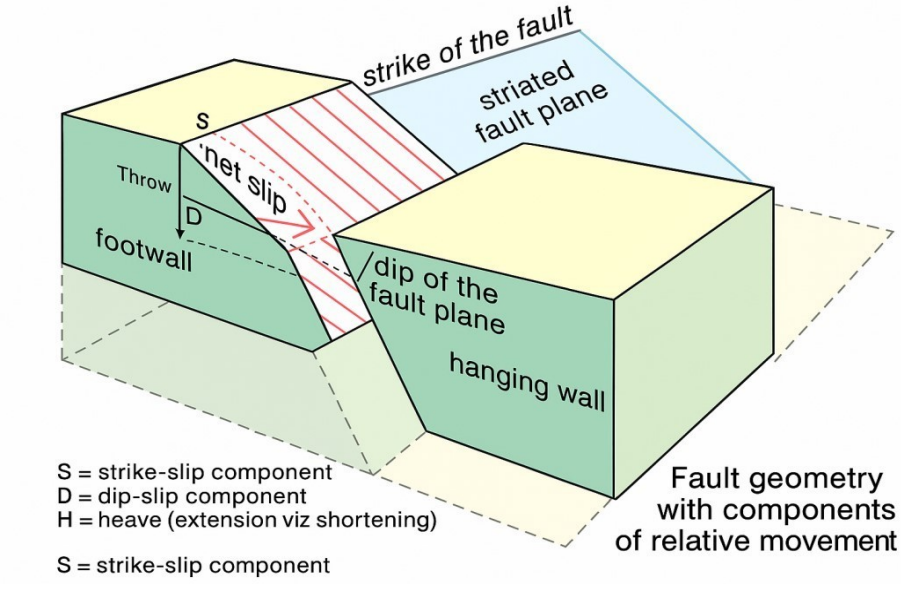


Figure 2.8: Conceptual 3D diagram illustrating fault geometry and main components of relative movement. The diagram depicts the throw (vertical displacement), heave (horizontal extension),

and strike-slip components along the fault plane, as well as the net slip vector and fault orientation defined by the strike and the dip. These geometric parameters form the basis for quantifying brittle strain in extensional rift settings. Adapted from Burg (2020).

The style of strain accommodation is also dependent on rift maturity and type. In the early stages of rifting, strain is often accommodated over many small, unlinked faults, resulting in a low total displacement and complex segmentation pattern. In more mature rifts, faults propagate laterally and link together, producing fewer and longer faults, an overall higher amount of displacement, and a greater proportion of the total strain accommodated on major structures. In magma-poor systems, the accommodation of more strain on fewer fault structures leads to the formation of continuous border faults, whereas in magma-rich settings, intrusive processes actively redistribute strain patterns even in the later stages of rifting. As continental breakup nears, strain can become even more focused along discrete zones, which may morph into spreading centres where magmatic accretion is the dominant process (Ebinger, 2005; Corti, 2009).

Quantifying strain accommodation requires a clear and robust framework. Geological approaches, such as measuring fault heave (the horizontal component of dip-slip displacement perpendicular to fault strike) and throw (the vertical component of dip-slip displacement) from digital elevation models, provide an integrated record of brittle strain over geological timescales. In contrast, geodetic and seismic datasets capture short-term deformation, often over-representing transient magmatic strain events relative to long-term fault slip (Shmela et al., 2021). Methodological differences, particularly in spatial resolution, temporal coverage, and scale of analysis, can result in contrasting interpretations. For example, microfaults and small-scale structures may be evident in high-resolution field or DEM mapping but remain undetected in regional-scale satellite geodesy studies.

These differences result in an incomplete understanding of the localisation or distribution of strain associated with the different types of rift systems in this region. This issue is usually greatest in transitional systems, where the fault maturity changes from relatively evolved fault systems in the north to magmatically influenced, distributed strain patterns towards the oceanic portion of the rift. Although brittle faulting is an important mechanism of crustal extension, magmatic intrusion can accommodate a substantial proportion of extension in magma-rich rift settings and redistribute strain between fault systems. To resolve these issues, this study used an unequivocal DEM-based approach to quantify fault-related strain accommodation across contrasting rift settings in the Afar Depression and North Main Ethiopian Rift. This approach will allow for a direct appreciation and comparison of strain patterns with respect to their fault maturity, styles

of linkage, and degree of magmatic influence, and ultimately supports an interpretive framework of rift evolution from the point of rift initiation to the further stages of rifting.

2.7 Geological background

2.7.1 Regional geology of the East African Rift System

Variations in lithospheric strength and magma input along the East African Rift System (EARS) control the initiation of normal faults as discrete segments, which later link to form through-going zones of extension (TZEs). The rift stretches for > 3,000 km from the Afar triple junction to the Malawi Rift (Figure 2.9), providing a natural laboratory to follow the transition from diffuse continental extension to organised plate separation and, locally, incipient seafloor spreading (Corti, 2009; Ebinger and Casey, 2001). Tectonically, the EARS is one limb of Red Sea–Gulf of Aden–Afar triple-junction system (McKenzie and Morgan, 1969), and its geometry is strongly guided by inherited Precambrian fabrics, that is, mobile belts and sutures that focus strain into segmented basins around the Tanzania Craton (McConnell, 1972).

Geophysical constraints show pronounced along-strike gradients: the crustal thickness decreases from ~35 km in the central Main Ethiopian Rift (MER) to ~24–26 km in northern Afar, accompanied by a drop in effective elastic thickness from ~20 km to < 6 km (Maguire et al., 2006; Keranen and Klemperer, 2008; Ebinger and Hayward, 1996; Ebinger et al., 1999). Taken together, these data imply that progressive thermal weakening and higher melt availability towards the Afar node-shorten segment spacing, encourage relay-ramp development, and favour hard linkage by diking rather than soft overlap maintained by border-fault systems. The Afar sector thus offers a prime natural example of a continent–ocean transition (Corti, 2009; Ebinger and Casey, 2001).

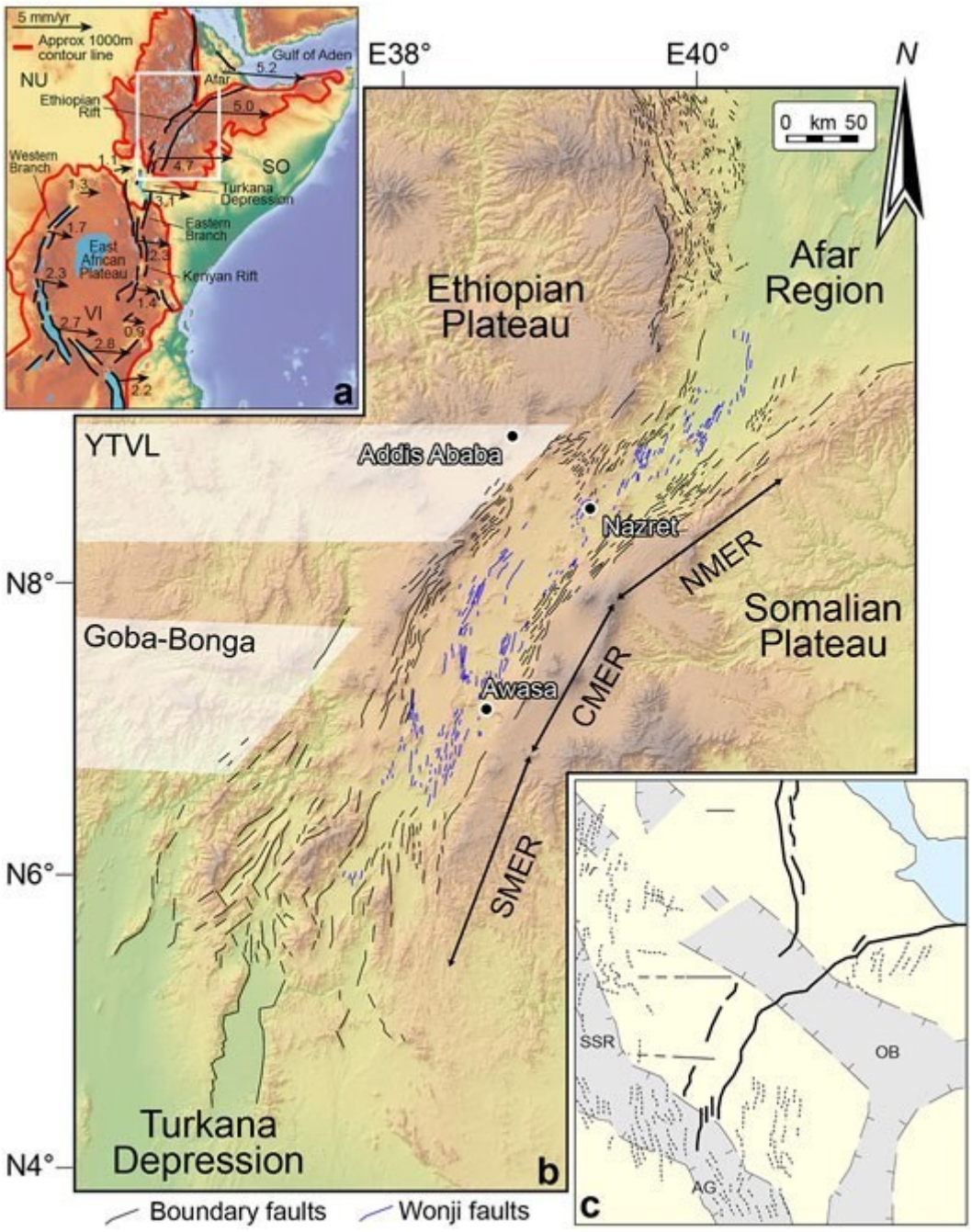


Figure 2.9: Structural framework of the Main Ethiopian Rift showing border faults (black) and axial Wonji Fault Belt segments (blue), with MER sectoring into the SMER, CMER, and NMER. *Modified from* Keir et al. (2015).

The EARS is subdivided into the northern, central, and southern sectors, complementing the classical eastern–western branch. The northern sector (Afar and Ethiopian rifts) is magma-rich and thin-crusted, and rift-axis intrusion within the MER and Afar yields short segment spacing and early progression from overlapping segments to through-going, dykes -linked structures (Maguire et al., 2006; Keranen and Klemperer, 2008; Ebinger and Casey, 2001). The central sector (Kenya–Tanzania rifts) overlies reactivated Proterozoic belts around the Tanzania Craton; Miocene–Quaternary volcanism with moderate

thinning produces mixed architectures, where soft linkages across relay zones remain common and segment maturity varies along the strike (Chorowicz, 2005; McConnell, 1972). The southern sector (Malawi/Nyasa Rift and neighbours) is relatively magma-poor and mechanically dominated; a thicker crust and larger elastic thickness favour long border-fault segments with wider overlaps and later linkage, consistent with a more brittle rift end-member (Morley and Ngenoh, 1999; Ebinger and Casey, 2001). This tripartite classification therefore predicts a northward shift from fault-dominated to magmatically assisted linkage, illustrated on the MER map (Figure 2.9) by the transition from Miocene border faults to the axial Wonji Fault Belt of en-échelon magmatic segments (Keir et al., 2015; Maguire et al., 2006; Keranen and Klemperer, 2008; Chorowicz, 2005; Morley and Ngenoh, 1999; Ebinger and Casey, 2001).

2.7.2 Geological setting of the Afar Depression

The Afar Depression lies at the intersection of three major tectonic plates: the Arabian, Nubian/Somali, and African plates. It represents the northern end of the EARS and the only subaerial part of the system where the entire process from continental rifting to oceanic spreading can be observed (Figure 2.10). Wolfenden et al. (2004), Corti (2009) and Rime et al. (2023) emphasised that this triple-junction geometry, formed by the interaction of the Red Sea, Gulf of Aden and MER axes, is responsible for the partitioning of strain and segmentation of the region since the Miocene. The Afar Depression is characterised by extreme crustal thinning, mantle uplift, and widespread fissural volcanic activity associated with the Afar mantle plume (Bastow and Keir, 2011). Variations in lithospheric strength and melt supply are the two main factors controlling fault segmentation; towards the Afar node, a high melt flux results in closer segment spacing and the formation of relay ramps that develop into through-going structures by intrusion-driven linkage (Pagli et al., 2014). Therefore, the Afar Depression provides a unique natural setting to study the mechanical–magmatic transition from brittle, fault-controlled deformation to magmatically assisted, localised strain accommodation.

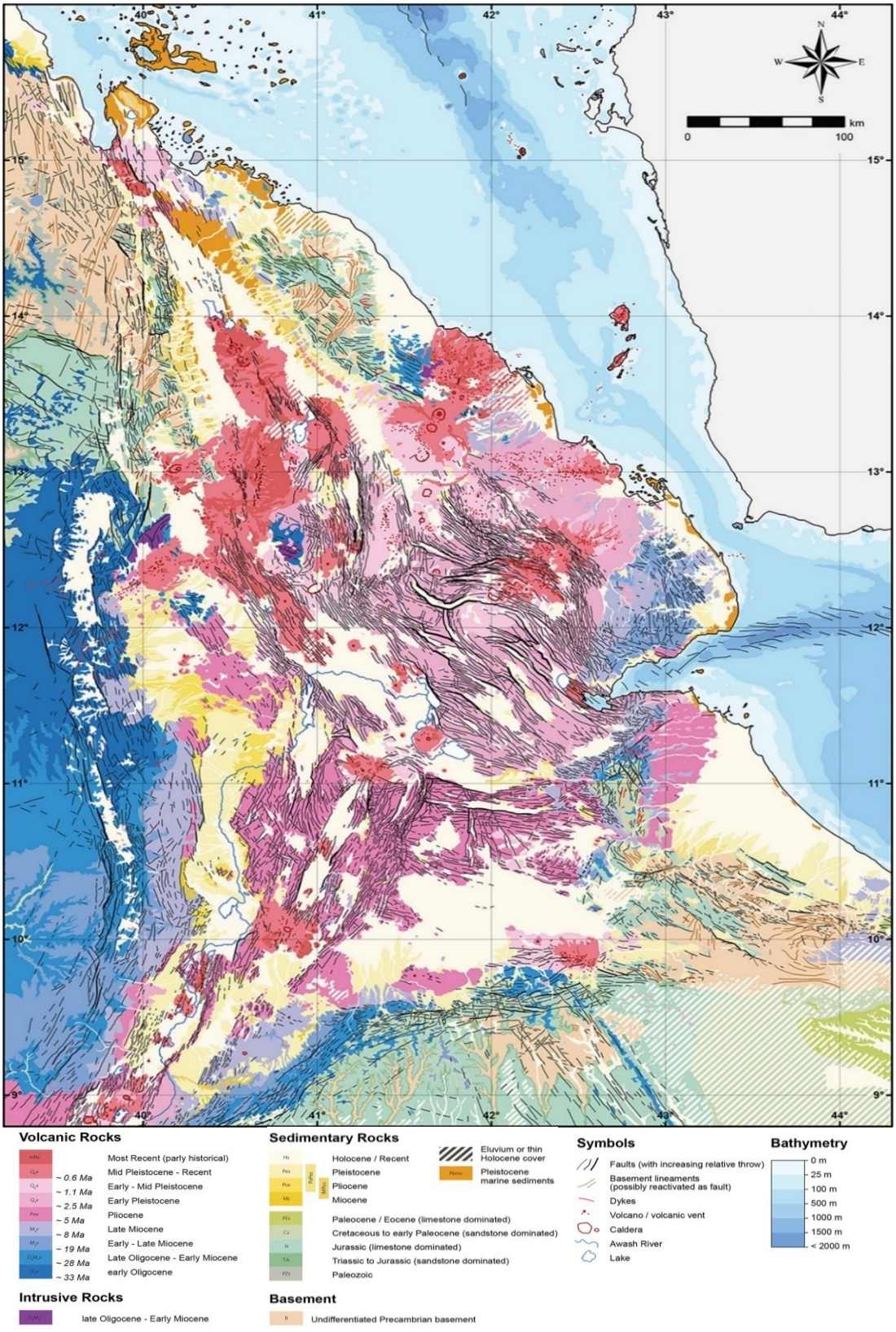


Figure 2.10: Geological map of the Afar Depression showing the distribution of volcanic, sedimentary, and intrusive units and significant fault systems. The volcanic units age from the Oligocene to the Quaternary, and the central axial rift segments demonstrate that Quaternary volcanics are prevalent. The sedimentary units are primarily located on the rift margins, notably near the Danakil and Somali plate boundaries. Intrusive units are exposed within the central structural highs, indicating magmatic processes during repeated rifting. Adapted from Rime et al. (2022).

Litho-stratigraphically, the Afar region comprises a volcanic–sedimentary succession ranging from the Oligocene to Holocene (Figure 2.10). Rime et al. (2023) established a new chronological framework for the lithostratigraphy of the Afar region by reconciling previous geochronology, geochemistry and field mapping. The volcanic succession consists of Oligocene–Miocene flood basalts (O_1v–O_2M_1v), Miocene M_3v–M_2v flows, Pliocene Pov series, and Pleistocene mRv and Q_3v–Q_1v basalts, each representing successive episodes of mantle-derived magmatism during rifting (Rime et al., 2023). Alternating phases of basaltic fissure eruptions and lacustrine deposition produced mechanically layered sequences that influenced fault propagation and rift-zone preservation (Rime et al., 2023; Rooney, 2020). Younger basaltic units along the rift axis decrease crustal friction and promote dyking-assisted linkage relative to older, more rigid flank rocks.

Structurally, the Afar Depression is composed of a patchwork of fault-bounded grabens and magmatic segments accommodating both brittle extension and ductile intrusion (Figure 2.11). Two large-scale transfer systems, the Erta Ale–Tat' Ali Transfer Zone (ETTZ) and the Goba'Ad Discontinuity, separate the depression into distinct kinematic domains in which strain is partitioned between fault slip and dykes intrusion (Corti, 2009). These zones act as long-lived accommodation structures that evolve from soft relay overlaps into hard, intrusion-linked connections as magmatism intensifies and crust thins. Magmatic segments currently active in the depression, including Manda Inakir, Manda Hararo, and Asal–Ghoubbet, show well-developed fissure systems, calderas, and linear arrays of volcanic centres, indicating the increasingly localised nature of deformation in the axial zone (Bastow and Keir, 2011; Rime et al., 2023). Overall, the structural characteristics of the Afar Depression indicate that it is an advanced rift sector in which magmatic processes have largely superseded tectonic faulting as the dominant mechanism of extension of the crust. This framework underpins the later analysis of segmentation and linkage evolution in Zones 1 (NAD), 2 (NMER), and 3 (EAD), which represent increasing levels of rift maturity within the Afar system.

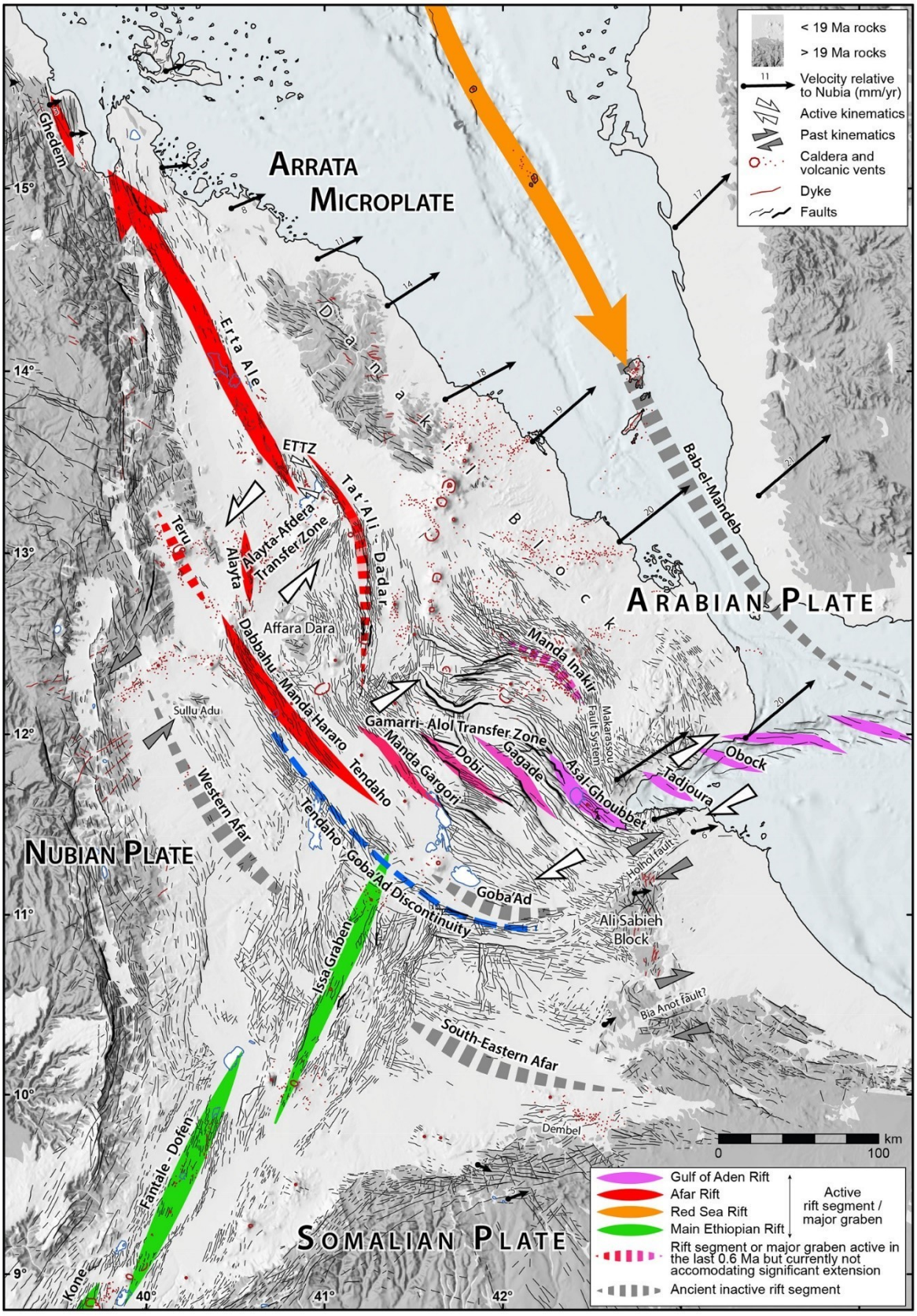


Figure 2.11: Rift dynamics of the Afar Depression illustrating major active and ancient rift segments, transfer zones and plate boundaries. The map highlights key structural features, including the Erta Ale–Tat'Ali Transfer Zone (ETTZ) and Goba'Ad Discontinuity, which partition strain between magmatic and tectonic rift sectors. Plate motions and active deformation zones are shown relative to the Nubian Plate. After Corti (2009), Doubre et al. (2017) and Moore et al. (2021) Pagli et al. (2014) Sangha et al. (2022) and Viltres et al. (2020).

2.7.3 Geological framework of the Study Zones

2.7.3.1 Zone 1: North Afar Depression (NAD)

The North Afar Depression (NAD), located in the northernmost part of the Afar Rift System, has undergone crustal thinning and segmented basin development since the Miocene (Figure 2.12). The NAD is bounded to the east by the Danakil Block, a continental crustal block that separates the Afar Depression from the southern Red Sea and has undergone counter-clockwise rotation during the development of the Afar–Red Sea rift system (Rime et al., 2023). Within this region, the transition from Miocene, widely distributed rifting and extensive basaltic volcanism to Pliocene–Pleistocene localised rifting and volcanism represents a change from mechanically controlled faulting to increased magmatic control (Bastow et al., 2005; Ebinger and Casey, 2001; Bastow and Keir, 2011). As such, the NAD provides a transitional architectural setting ideal for evaluating how individual fault segments develop, connect and link in a magma-influenced rift environment.

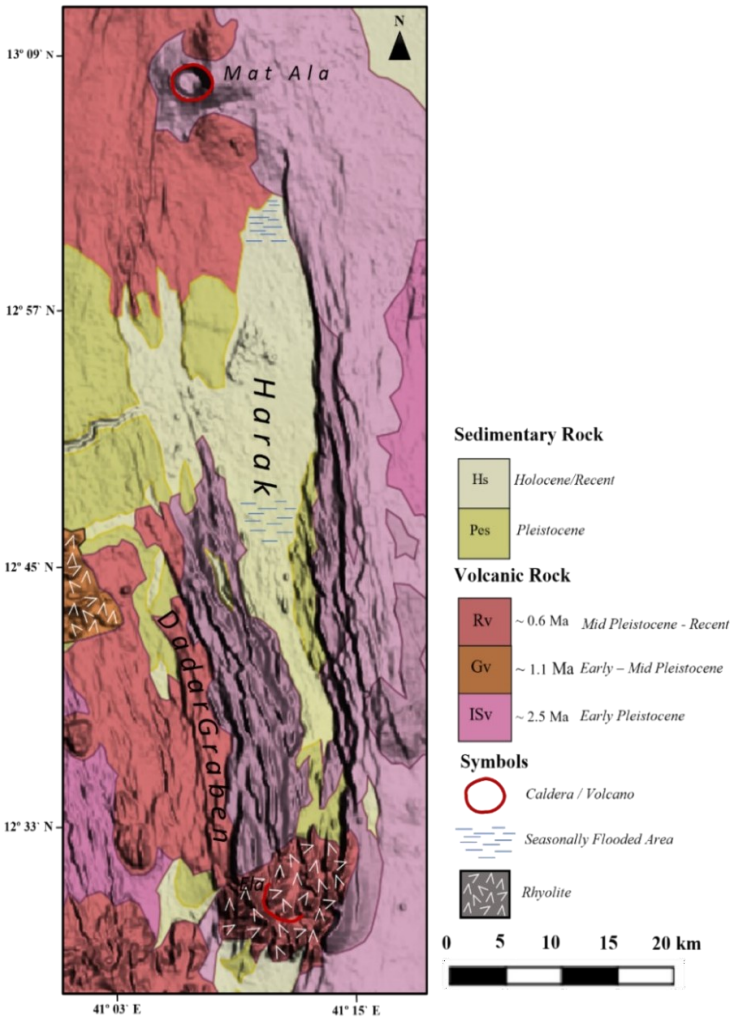


Figure 2.12: Geological map of the North Afar Depression (location shown in Figure 2.1), highlighting volcanic units (ISv, Gv, Rv), syn-rift sediments (Pes, Hs), major normal faults, and the positions of Harak and Dadar grabens and Mat Ala volcano. Compiled and simplified from Rime et al. (2022).

Stratigraphic layers consist of Early Pleistocene to Holocene volcanic and sedimentary units that create mechanically layered sequences directly affecting fault propagation. The youngest unit (Recent Volcanics) comprises basaltic lavas, scoria cones and minor pyroclastic material (< 0.6 Ma); these overlie the Gulf Volcanics (Gv; ~1.1–0.6 Ma), composed primarily of tholeiitic fissure basalts, which in turn overlie the Ignimbrite Series (ISv; ~7.1 Ma) of silicic ignimbrites and pumiceous tuffs (Varet, 2018). The ISv? and Gv? areas highlight zones of uncertainty owing to limited exposure and the need for further refinement in mapping. Additionally, a silicic dome in the southern NAD, interpreted as rhyolitic in composition and early– to mid-Pleistocene in age, represents the locus of concentrated magma ascent along segment tips (Rime et al., 2022). From a mechanical standpoint, alternating competent ignimbrite layers and less competent basalt layers promote the formation of relays and influence whether overlying relays evolve into hard linkages via intrusion or remain as soft relay zones.

Fault-bounded basins in the Harak system contain syn-rift sediments, including Holocene–Recent (Hs) lacustrine clays, fluvial sands and alluvial fan deposits that cover the basin floor, and Pleistocene (Pes) unit's indicative of earlier subsidence stages (Gasse and Street, 1978). Seasonal flooding of the northern–central Harak plain preserves finer-grained facies but obscures scarps in imagery, creating a potential observational bias for displacement–length analysis (Rime et al., 2023). These stratigraphic and hydrologic conditions nevertheless provide natural markers for tracking progressive segment growth and identifying abandoned linkages.

The structural fabric of the NAD consists of large-scale N–S normal-fault arrays oriented parallel to the rift axis, intersected by smaller-scale NE–SW transfer faults that accommodate lateral strains and stepovers. The Harak Graben is a major structural feature in the area, extending for more than 50 km and varying in width from approximately 3 to 10 km. Its floor contains recent sedimentary deposits and is seasonally flooded, particularly within the low-lying parts of the graben (Varet and Gardo, 2020). The south-eastern margin of the Harak Graben is characterised by a relay zone between overlapping segments (Rime et al., 2023; Wolfenden et al., 2004; Ebinger and Hayward, 1996). Collectively, the spatial distribution of volcanic centres, fissure-fed flows and mapped scarps indicates short fault-segment spacing and active transfer zones within a magma-influenced rift setting (Rime et al., 2023; Bastow and Keir, 2011). These characteristics make the NAD an appropriate setting for investigating length–displacement scaling and relay-zone evolution.

Present-day geodetic and seismic observations show that deformation remains active

across northern Afar. Regional GPS measurements record ongoing relative motion between the Arabian, Nubian and Somalian plates, providing the present-day kinematic framework for deformation in the NAD (Reilinger and McClusky, 2011; Rime et al., 2023). Seismic observations also show active, predominantly shallow earthquakes across the Afar Depression, indicating continuing upper-crustal deformation associated with rifting (Asefa and Ayele, 2021). Together, these observations show that the NAD remains within an actively deforming part of the Afar rift system.

2.7.3.2 Zone 2: North Main Ethiopian Rift (NMER)

The North Main Ethiopian Rift (NMER) forms the northern sector of the MER between the Ethiopian and Somalian plateaus, trending N50–55°E from Afar to Lake Koka (Figure 2.13). It records the classic transition from Miocene border-fault rifting to Quaternary axial magmatic segmentation, providing a natural laboratory for fault growth, relay development and linkage (Bonini et al., 2005; Corti, 2009).

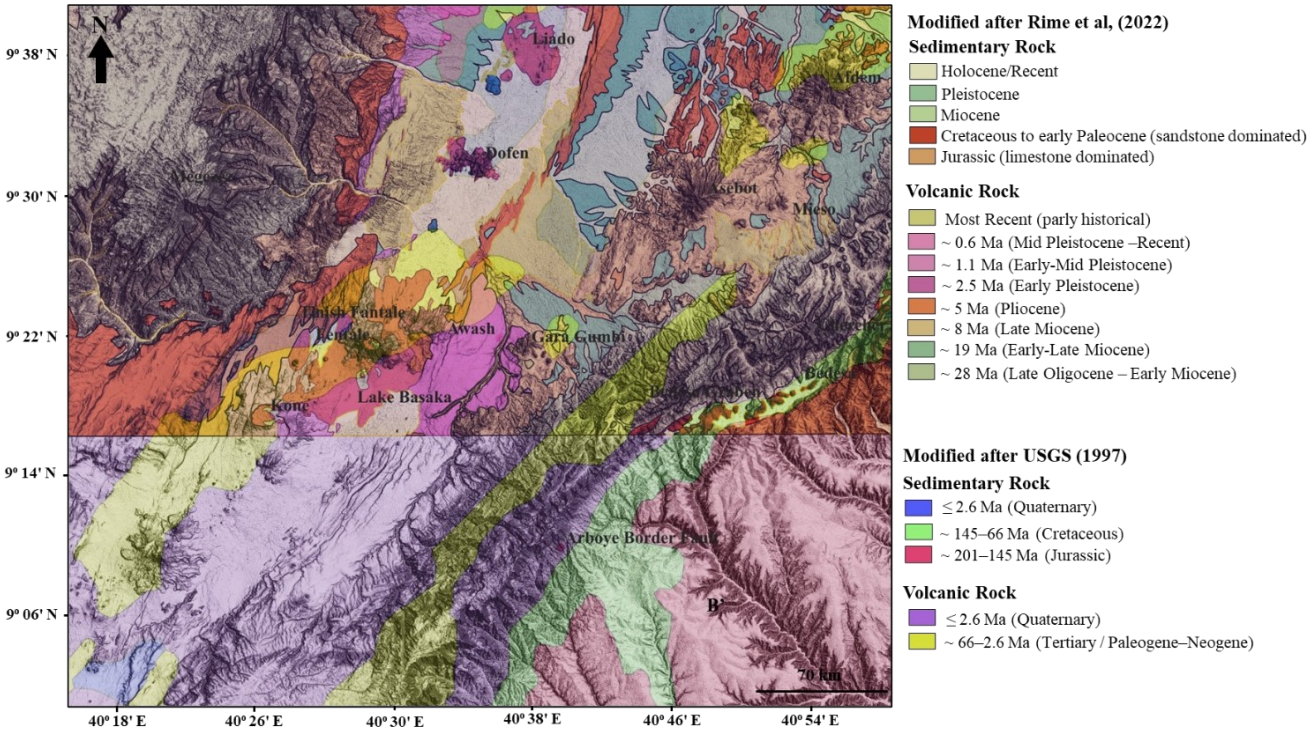


Figure 2.13: Simplified geology and structure of the NMER (location shown in Figure 2.1), showing border faults, axial Wonji Fault Belt segments, and principal surface units (Qv, Pov/Q2v, and Hs/Pes). Compiled from Rime et al. (2023) for the northern part and reclassified USGS province mapping southward.

Major NE–SW border faults initiated at ~10–11 Ma and defined a ~80 km-wide valley. Since ~2.5 Ma, strain has migrated into a ~20 km-wide axial belt, the Wonji Fault Belt (WFB), composed of right-stepping, en-échelon magmatic segments (typically 20–60 km long) that act as embryonic spreading centres (Ebinger and Hayward, 1996; Maguire et al., 2006; Keir et al., 2015). This shift from border faults to axial magmatic segments

shortens segment spacing, increases relay frequency, and favours hard linkage by diking compared with earlier soft overlaps along the flanks (Agostini et al., 2011; Keir et al., 2015).

The crustal and volcanic framework of the NMER records this transition from border-fault-controlled extension towards increasingly localised deformation within the axial Wonji Fault Belt. Seismic observations from the Ethiopia–Afar Geoscientific Lithospheric Experiment (EAGLE) show that crustal thickness and effective elastic thickness decrease northwards towards Afar (Maguire et al., 2006). Stratigraphically, pre-rift Eocene–Oligocene basalts and volcaniclastic rocks are overlain by Miocene syn-rift basalts and silicic units, followed by extensive Quaternary activity with calderas, fissure basalts and scoria cones concentrated within the axial WFB (Mohr and Zanettin, 1988; Acocella et al., 2003; Hutchison et al., 2016).

For the mapping used in Figure 2.13, the Afar geological synthesis for the northernmost part of Zone 2 was merged with a reclassified USGS province map to the south, generalising three principal surface units relevant for segmentation analysis: Qv (Quaternary basaltic lava fields forming axial magmatic segments), Pov/Q2v (felsic centres and older silicic edifices marking segment tips and accommodation zones), and minor Hs/Pes (lacustrine and alluvial fills that archive displacement history) (Rime et al., 2023; Persits et al., 1997). The combined presence of a thick volcanic succession, inward migration of faulting, and sustained melt supply support the interpretation that the NMER is an intermediate-to-mature rift sector in which magmatic intrusion plays a primary role in segment linkage (Corti, 2009; Keir et al., 2015).

Present-day geodetic and seismic observations show that extension remains active across the NMER. Regional GPS measurements record continuing divergence between the Nubian and Somalian plates, while deformation in the northern MER is concentrated towards the axial rift system and the Wonji Fault Belt (Reilinger and McClusky, 2011; Rime et al., 2023). Seismicity within the MER is predominantly shallow and occurs along both the rift axis and margins, indicating continuing upper-crustal brittle deformation (Asefa and Ayele, 2021). These observations are consistent with the progressive localisation of present-day strain towards the axial part of the NMER.

2.7.3.3 Zone 3: Eastern Afar Depression (EAD)

The Eastern Afar Depression (EAD), located in eastern Afar within the Afar triple-junction region (Figure 2.1), lies where the Red Sea, Gulf of Aden and Main Ethiopian Rift systems converge. This setting creates a zone of high melt supply and crustal

thinning, where deformation is focused on narrow axial belts and Precambrian anisotropies limit the length of individual segments (Rime et al., 2023; Lahitte et al., 2003). In this tectono-magmatic setting, fault segmentation and linkage may be influenced by interactions between faulting and magmatic intrusion. Thus, EAD is a key location for studying complex rift behaviour.

From the Late Miocene to the Holocene, the volcanic history records a transition from extensive fissural volcanism to concentrated magmatic activity along the rift centre. The Stratoid Series and related stratigraphic units (Immino and Early Stratoids; ~7.1–4 Ma) comprise widespread basaltic and tuffaceous units (Bastow et al., 2005). Subsequent volcanic activity became increasingly localised towards the active rift segments, with Gulf Basalts along the margins of the Manda Hararo rift segment range broadly from about 1.1 to 0.6 Ma, whereas younger fissure-fed basaltic volcanism within the Manda Hararo and Manda Inakir rift segments is predominantly younger than ~0.6 Ma (Lahitte et al., 2003). Holocene rift volcanics (<0.5 Ma) are largely fissure-fed basalts and pyroclastics along active magmatic segments, such as Manda Inakir and Manda Hararo, demonstrating the important role of magmatic intrusion in present-day rifting (Grandin et al., 2009; Rime et al., 2023).

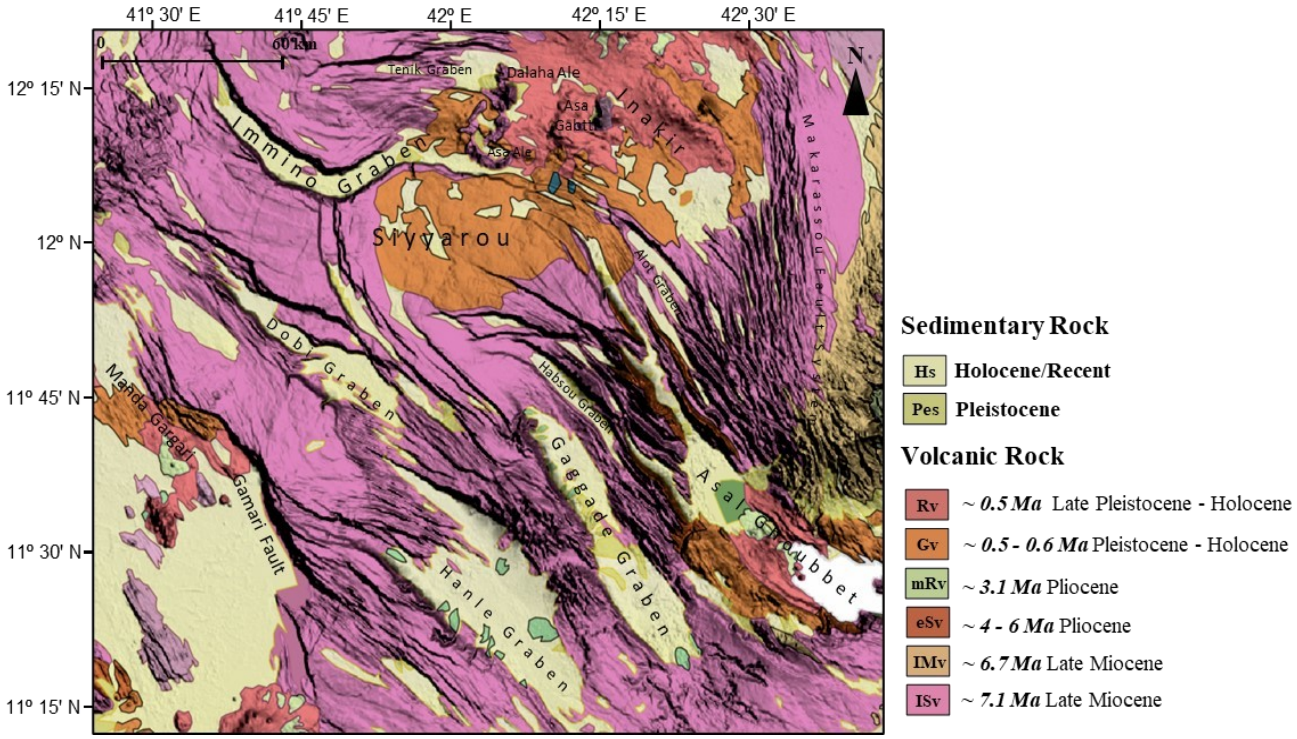


Figure 2.14: Generalised geology and structures of the Eastern Afar Depression (EAD) (location shown in Figure 2.1), showing major grabens (Immino, Dobi, Hanle, Gaggade), the Makarassou Fault, principal transfer zones (e.g. Gamarri–Alol), and volcanic units (ISv, IMv, eSv, mRv, Gv, Rv) with syn-rift sediments (Pes, Hs). Compiled and simplified after Rime et al. (2023), with volcanic ages from Lahitte et al. (2003).

Sedimentation within the rift mirrors the pulsating tectono-magmatic activity. Alluvial–lacustrine deposits drape lows created by faulting and record episodes of subsidence, whereas halite–evaporites accumulated in the most subsided arid basins, preserving records of basin development (Rime et al., 2023). These stratigraphic units provide markers for examining the relationship between sedimentation and fault development.

Normal-fault arrays trending NE–SW define the Gaggade, Hanle, Dobi and Immino Grabens and smaller basins such as Alol, Habsou and Tenik in the EAD. Long transfer systems accommodate variations in deformation along the rift (Rime et al., 2023). The Makarassou Fault is the primary rift-bounding structure on the eastern margin of the EAD (Figure 2.14) and controls rift geometry and strain localisation, whereas the Gamarri–Alol transfer accommodates along-axis variations in deformation (Rime et al., 2023; Wolfenden et al., 2004).

Active volcanic centres, including Dalaha Ale, Asa Gabtti, Asa Ale, Bovawil, Manda Gargari, Manda Inakir and Siyyarou, are spatially associated with the propagating rift system, illustrating the close relationship between volcanism and rift propagation in Afar (Lahitte et al., 2003).

Spatiotemporal patterns in the EAD document the progression of rift propagation from the Danakil Sector (~11 Ma) to the Goba'Ad–Tendaho segments (~1.1–0.6 Ma), and onwards to the Manda Hararo axis (~0.2 Ma), marking a shift from border-fault-controlled extension to axial intrusion-controlled deformation. Present-day geodetic and seismic observations show that deformation across central-eastern Afar remains spatially variable and strongly influenced by magmatic activity. GPS and InSAR measurements indicate that strain is distributed across a broad zone, with much of the present-day deformation concentrated along active magmato-tectonic segments (Pagli et al., 2014; Doubre et al., 2017; Rime et al., 2023). Seismic activity and earthquake swarms within Afar provide further evidence of continuing brittle deformation and magmatic processes at depth (Rime et al., 2023; Asefa and Ayele, 2021). These observations indicate that present-day strain in the EAD is accommodated through the interaction of faulting and magmatic intrusion.

Together with the high frequency of Holocene diking and the localisation of strain along the Makarassou margin, these trends confirm that the EAD is a late-stage rift sector approaching the continent–ocean transition (Corti, 2009; Ebinger, 2005; Grandin et al., 2009). Owing to its maturity, Zone 3 provides the best comparison for examining end-member behaviours of segment spacing, relay persistence, and hard-linkage threshold

across the three study zones.

This chapter outlines the geological and tectonic framework of the East African Rift System (EARS), highlighting how variations in lithospheric strength, magma supply, and inherited structures influence fault segmentation and linkage. This regional and local context provides a geological basis for interpreting the fault systems examined in this study. The following chapter builds on this background by describing the datasets, mapping procedures, and analytical methods used to quantify fault geometry, segmentation, linkage, and strain across the study zone.

Chapter 3: Methodology

3.1 Introduction

This chapter outlines the methodologies used to map and analyse the surface expression of normal faults within the Afar Depression and the Main Ethiopian Rift to characterise and compare rifting processes across zones spanning the transition from continental to initial oceanic rifting environments. This section introduces the datasets and software used to support the analysis and explains the rationale for preparing the ASTER DEMs in QGIS. The methods for manually digitising fault traces and cut-off points are then described, including the extraction of geometric attributes (fault length and maximum displacement) and the analysis of displacement–length statistics. Displacement profiles are categorised into types, segmented and linked faults are identified using overlap and relay criteria, and cross-cutting relationships are mapped to establish relative timing. Finally, minimum elongation (apparent strain) is used as a summative metric in the subsequent chapters. The chapter concludes with an explanation of the limitations of the mapping methodology and potential mapping and processing errors, together with the quality-control measures implemented to ensure consistent and repeatable results.

3.2 Data acquisition

Remote-sensing techniques are fundamental for studying the morphological features of the Earth's surface, particularly in tectonically active regions. Digital Elevation Models (DEMs) are widely used in fault studies to investigate deformation patterns and surface expressions of fault systems (Begg and Mouslopoulou, 2010). In this study, the DEM data provided the primary foundation for analysing fault geometry at various stages of continental rifting. The DEMs were acquired from the NASA Earthdata portal and were derived from the Advanced Spaceborne Thermal Emission and Reflection Radiometer (ASTER). ASTER GDEM provides elevation data at a spatial posting of approximately 30 m (1 arc-second), providing consistent topographic coverage across the three study zones (NASA/METI/AIST/Japan Spacesystems and U.S./Japan ASTER Science Team, 2019).

Independent validation of ASTER GDEM Version 3 against more than 23,000 geodetic ground-control points over the conterminous United States reported an overall vertical RMSE of 8.52 m and a linear error at 95% confidence (LE95) of 16.70 m, although accuracy varies with land-cover and terrain conditions (Gesch et al., 2016). These values provide a general indication of ASTER GDEM performance rather than a site-specific

accuracy estimate for the Afar region. The approximately 30 m spatial posting was considered appropriate for this regional-scale study because the analysis focuses primarily on kilometre-scale fault traces and associated topographic scarps. However, small scarps and fault-tip positions approaching or below the DEM resolution may not be reliably resolved, and this limitation is considered when interpreting the mapped fault geometry. ASTER GDEM was selected because it provides consistent regional topographic coverage across all three study zones at a common spatial resolution, allowing the fault-mapping methodology to be applied consistently throughout the study area.

A total of 43 DEM granules were used to cover the entire study region. Each granule corresponds to a specific tile of the Earth's surface on a fixed grid. When merged, these tiles provided seamless coverage across the three zones of interest: Zone 1 (North Afar Depression), Zone 2 (North Main Ethiopian Rift), and Zone 3 (Eastern Afar Depression**).** The combined dataset enabled comprehensive tracing and mapping of fault scarps, which is essential for capturing variations in fault length, displacement, segmentation, and linkage.

In addition to elevation data, geological age constraints were integrated using regional stratigraphic datasets from recent Afar compilations and maps (Rime et al., 2022). These age maps contextualised the spatial distribution of faults and supported interpretations of fault growth and cross-cutting relationships. Age information was particularly useful for identifying fault populations affecting different lithostratigraphic units and for understanding the progressive development of fault systems in the region. Together, these data sources form the basis for a detailed quantitative analysis of fault geometry and rift evolution in one of the most active continental rift systems on Earth.

3.3 Data processing

Data processing was carried out using QGIS version 3.32.0 (QGIS Development Team, 2023), which was employed to visualise, manage and analyse spatial data across the study area. In the first step, all 43 ASTER DEM granules were imported into QGIS. Each granule is a raster tile of a larger satellite scene and is stored as a grid-structured data object holding a single elevation value in each cell (Burrough and McDonnell, 1998)**.** In aggregate, the granules provided full spatial coverage of the study areas. After uploading, the granules were mosaicked into a continuous raster, which removed boundary artefacts and elevation jumps between adjacent tiles, resulting in a seamless elevation model. Spatial resolution continuity is important for a uniform study of fault scarps, basins, and

other relief features of tectonic landforms.

A hillshade model was then generated from the merged DEM to enhance the visibility of subtle variations in the terrain. Hillshade simulates solar illumination across the surface using light and shadow to emphasise elevation changes. It is particularly useful for identifying faint geomorphic features, such as fault scarps, lineaments, and low-relief break zones. However, hillshade was used as a visualisation aid rather than as the sole basis for identifying and mapping faults. Fault scarps identified from the hillshade were assessed together with the underlying DEM, elevation profiles and geological context to reduce potential misinterpretation of illumination-related features**.** In this study, the azimuth of the light source was set at 315° (northwest-facing), which is commonly used in geological mapping to enhance east- and south-facing features. The altitude angle was generally set at 45°, although minor adjustments were made in low-relief areas to enhance topographic contrast. Because the visibility of topographic features in a single direction hillshade can depend on their orientation relative to the illumination direction, directional hillshades were also used selectively to examine the terrain under different illumination angles**.** A vertical exaggeration factor (z-factor) of 0.0009 was applied and adjusted slightly between the zones to enhance the elevation differences while maintaining a natural terrain representation.

In the final step, the merged raster was clipped into an independent file for each study region, according to a predefined boundary shapefile. For each zone, a pseudo-colour DEM and its respective Hillshade were created to assist with visual interpretation. This strategy enabled a detailed examination of the topography of each zone and supported the compilation of the fault map and structural analyses. Clipping reduced the amount of data handled and focused the analysis on the most relevant regions by filtering out areas that did not play significant roles in the study.

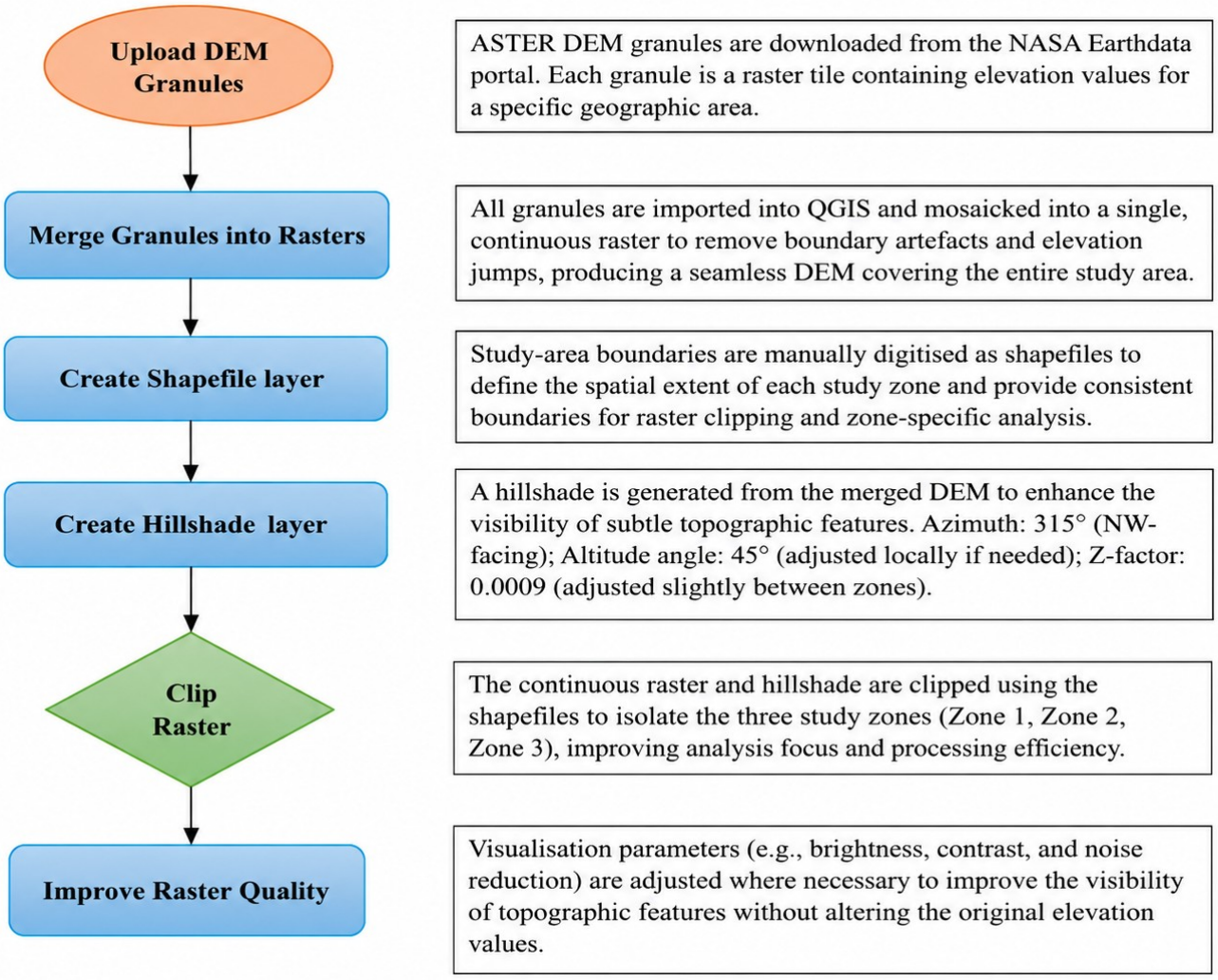


Figure 3.1: Workflow used to process the ASTER DEM data, including DEM import and mosaicking, study-area shapefile creation, hillshade generation, raster clipping, and visualisation optimisation for fault mapping and analysis.

3.4 Data analysis

3.4.1 Fault picking method

Fault cut-offs were manually mapped to identify the upper and lower boundaries of fault scarps and to extract key geometric parameters. Each fault was characterised by two cut-offs: the top cut-off, representing the highest visible point at the edge of the scarp on the footwall side, and the bottom cut-off, representing the lowest visible point where the scarp intersects the hanging-wall surface. In practice, these cut-offs were identified from changes in slope across the fault scarp and checked against elevation profiles extracted from the DEM. For each cut-off point, the horizontal coordinates (***x*** and ***y***) and elevation (*z*) were recorded to define the three-dimensional geometry of the fault scarp.

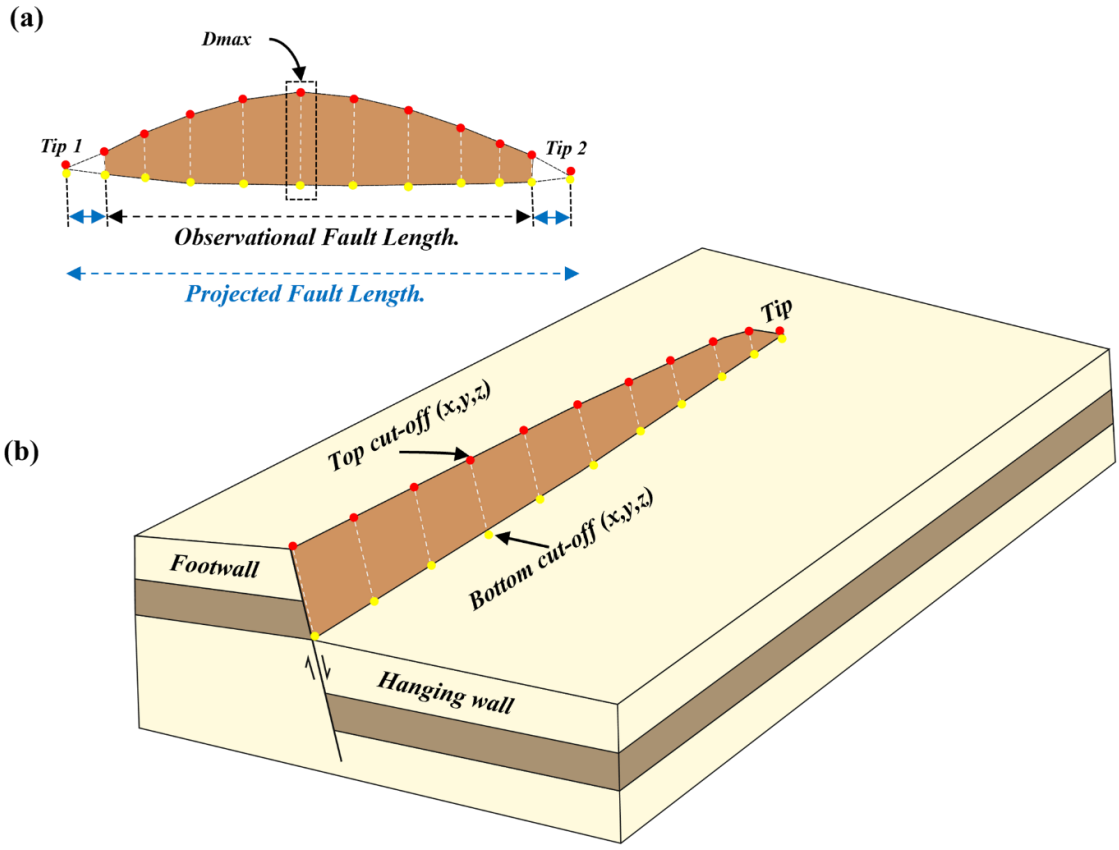


Figure 3.2: Conceptual block diagrams illustrating fault-length and cut-off mapping. The red dots represent the top cut-off points, and the yellow dots represent the corresponding bottom cut-off points. **(a)** Schematic displacement profile showing the mapped cut-off points along with the fault and the projected fault length. **(b)** Three-dimensional conceptual representation showing the corresponding top and bottom cut-offs along the fault scarp, with their *x*, *y* and *z* coordinates used to define fault geometry.

From the mapped cut-offs, three principal geometric parameters were derived: fault length (*L*), apparent displacement (*D*), and maximum apparent displacement (*D*max). Fault length was initially determined from the mapped surface trace, with projected fault length used where appropriate as described below. Displacement was determined between

corresponding top and bottom cut-off points across the fault scarp, while maximum apparent displacement (*D*max) represents the largest displacement measured along an individual fault. This mapping and measurement approach provides a consistent basis for comparing fault geometry across the study areas.

The surface expression of a fault scarp may, however, be modified by erosion and deposition. The mapped cut-offs therefore do not necessarily represent the original structural position of the pre-deformational surfaces. To account for this, the method distinguishes between observed (mapped) cut-offs and original (projected) structural cut-offs. The observed top cut-off represents the preserved upper limit of the fault scarp, whereas the projected top cut-off represents the interpreted continuation of the footwall surface before modification. Similarly, the observed bottom cut-off represents the visible lower limit of the fault scarp, whereas the projected bottom cut-off represents its interpreted position before burial or modification.

In this study, displacement parameters were calculated using the mapped top and bottom cut-offs because these features could be identified consistently from the available DEM. Although erosion or deposition may result in some underestimation of the original fault displacement, using the mapped cut-offs provides a consistent and reproducible approach across the dataset.

To demonstrate how the conceptual cut-off-picking method was applied to the actual DEM data, Figure 3.3 presents representative topographic profiles across mapped fault scarps. The examples show how changes in slope across the scarp were used to identify the mapped top and bottom cut-offs and illustrate the difference between a well-preserved and a modified surface expression.

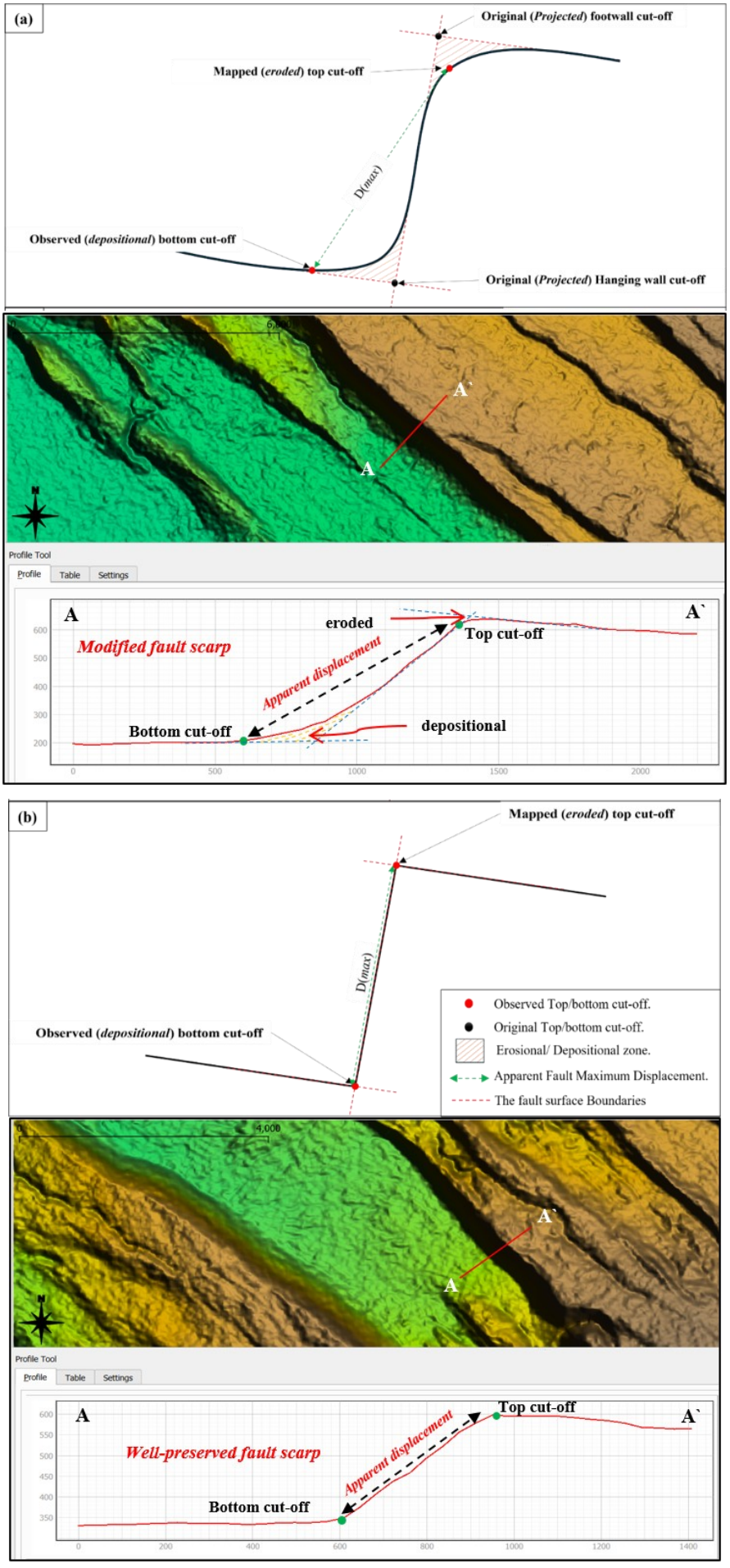


Figure 3.3: Conceptual and representative DEM-derived examples illustrating the application of the fault cut-off-picking method. The conceptual diagram illustrates the effect of surface modification on mapped and projected cut-offs. The DEM examples show the locations of A–A′

topographic profiles across representative fault scarps. **(a)** A well-preserved fault scarp, where distinct changes in slope define the mapped top and bottom cut-offs. **(b)** A modified fault scarp, where the surface expression is less clearly preserved. The corresponding elevation profiles illustrate how the mapped cut-offs were identified and used to determine apparent displacement.

As illustrated by the real examples in Figure 3.3, the position of the cut-offs was determined from the preserved topographic expression of each fault rather than from a theoretical reconstruction of the original fault surface. In well-preserved scarps, the top and bottom cut-offs are represented by relatively distinct changes in slope. In modified scarps, these changes may be less distinct owing to modification of the surface, increasing uncertainty in the position of the mapped cut-offs. The same mapping criteria were therefore applied consistently across the study areas to minimise differences introduced by preservation conditions. The cut-off points were not positioned at a fixed spacing along each fault. Instead, points were manually digitised at locations required to capture variations in fault-scarp geometry. Consequently, point spacing varied according to the geometry and preservation of the fault scarp and the spatial resolution of the DEM.

The total fault length (L) was initially mapped by tracing each fault from tip to tip along the preserved top cut-off. This provided the observed surface length of the fault based on its visible expression at the resolution of the DEM. However, the observed surface length may underestimate the true structural length where fault tips have been modified by erosion or buried beneath younger deposits. To account for this limitation, the projected fault length was estimated by extending the visible fault trace along the inferred direction of fault propagation, based on the continuity and alignment of adjacent fault segments (Figure 3.2).

The observed fault length therefore provides a conservative measure of the preserved surface expression, whereas the projected fault length provides an estimate of the total fault geometry where parts of the fault trace are degraded or obscured. In this study, the projected fault length was used as the standard metric to maintain consistency between faults with different preservation conditions. Although this introduces some uncertainty associated with interpreting poorly preserved fault tips, the same criteria were applied consistently across the dataset.

3.4.2 Fault digitising methods

The fault database was digitised in QGIS using the attribute table for the systematic recording and organisation of key fault attributes. This preliminary process is essential before any geometrical statistical analysis can be performed, as it allows each digitised fault point to be clearly identified. Each digitised point on a fault was systematically

labelled based on a predefined identification scheme. The prefix “F” indicated a fault and was followed by a number identifying the fault (e.g. “001”), then the position of each point with respect to the cut-off (“t” for top or “b” for bottom). Each point was then disambiguated in terms of its spatial location in the study area: east (“E”), west (“W”), north (“N”), or south (“S”). Finally, the points were numbered (e.g. 1, 2, and 3) along the fault trace. For example, “F001_t_E_1” is the first top digitised point on Fault 001 in the eastern part of the zone, and “F001_b_E_1” is the corresponding bottom cut-off point. This digitisation scheme enabled accurate characterisation of fault points and substantially simplified the fault dataset for geometrical analysis in Python.

3.4.3 Fault sampling scenarios

Fault sampling in the study area was influenced by the preservation of fault scarps, which varied owing to processes such as erosion, burial by sedimentary or volcanic deposits, and subsequent surface modification. These processes may partially obscure the surface expression of older fault scarps and therefore affect the accuracy of fault-trace identification, particularly when mapping the top and bottom cut-off points using a DEM (McPhillips and Scharer, 2018). Consequently, the mapping approach was adjusted according to the visibility and condition of surface features in different parts of the study area. In regions where fault scarps were well preserved, they appeared clearly in the DEM as distinct breaks in topographic slope across the fault scarp, making it straightforward to identify the top cut-off on the footwall and the bottom cut-off at the base of the hanging wall. In these settings, faults were digitised along their full length, and fault geometry could be mapped with relatively low uncertainty.

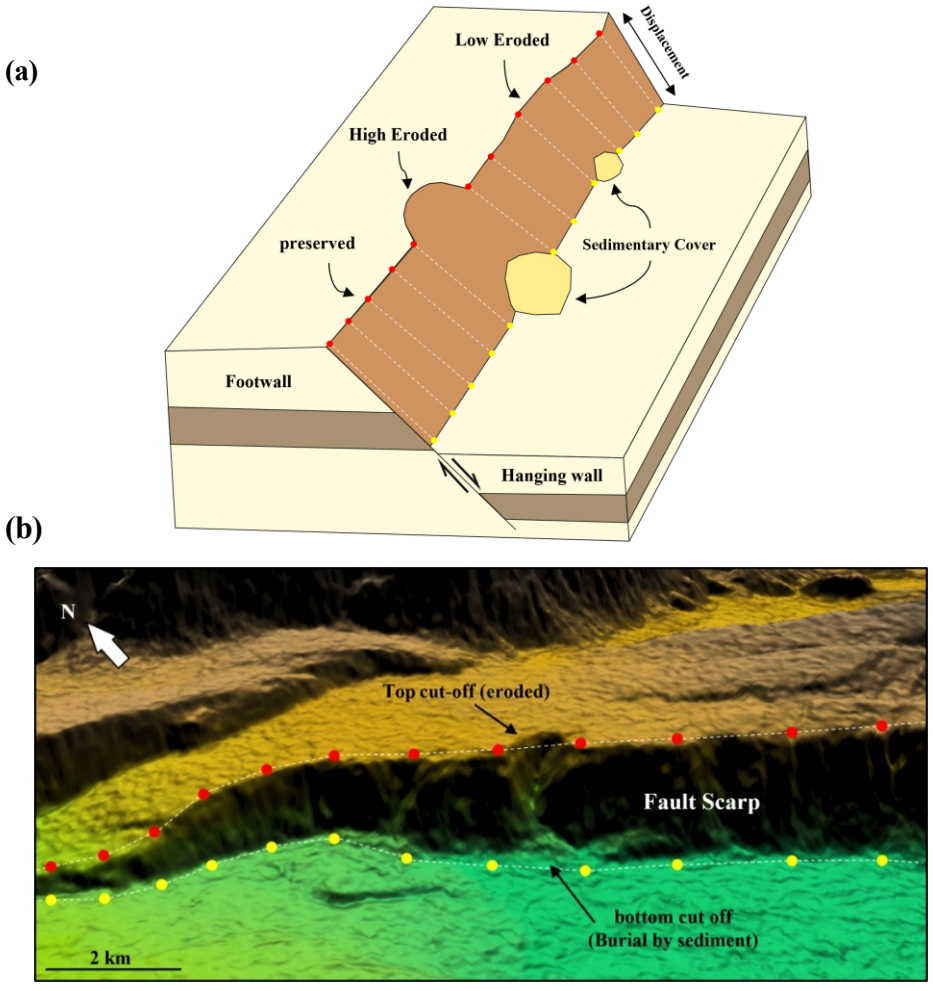


Figure 3.4: Preservation-controlled mapping of fault cut-offs from DEM data. **(a)** Conceptual block diagram showing how erosion and surface burial affect fault-scarp visibility; red points mark top cut-offs (footwall) and yellow points mark bottom cut-offs (hanging wall). **(b)** Hillshade/pseudo-colour DEM example (2 km scale) showing mapped eroded top cut-offs (red), buried bottom cut-offs (yellow), and dashed interpolated traces where the scarp is obscured.

Apparent displacement (*D*) and *D*max were measured between observed cut-offs, while projected fault length was estimated by extending the visible trace where continuity indicated further propagation.

In contrast, some faults were more difficult to trace because of poor preservation. This typically resulted from erosion of the upper scarp or burial by alluvial deposits or volcanic flows (Pollard and Fletcher, 2005). Such conditions make it challenging to identify the exact cut-off points and introduce uncertainty in defining the fault surface. In these cases, faults were mapped using the visible segments, and where continuity of the fault trace indicated further propagation, the trace was projected along its inferred direction. These interpretive criteria were consistently applied across the dataset to maintain a uniform mapping approach and to minimise differences in fault measurements arising from variable preservation conditions.

3.5 Statistical Analysis

This section describes the statistical methods employed to analyse approximately 2,500 mapped subaerial normal faults across the three study areas. The apparent fault length (L) and apparent maximum displacement (Dmax) were used to quantify the geometry of faults, both of which are essential for understanding the scaling behaviour and growth patterns in extensional settings (Childs et al., 2017; Lathrop et al., 2022). The spatial distribution and orientation of faults were also analysed to characterise the array-scale organisation within each zone and provide a framework for examining segmentation and linkage through the analysis of fault overlap, step-over, and relay-ramp geometries (Peacock and Sanderson, 1991).

Displacement profiles were categorised as single-, multi-, or irregularly peaked to capture along-strike displacement variability, which indicates the level of segmentation (Childs et al., 2017). An apparent minimum strain (elongation) was reported as a summary metric for extension, and the relative chronology was established by compiling the cross-cutting relationships. Finally, fault maturity was assessed in relation to surface geological units using regional Afar maps (Rime et al., 2022), relating geometric and kinematic indicators to mapped lithostratigraphy. All calculations and figures were generated in Python using a custom script run in the Spyder IDE with NumPy for array-based numerical work, pandas for table management, Matplotlib for figure production, and SciPy for specific tasks (such as spline fitting). Full documentation of the script is provided in Appendix A to ensure transparency and reproducibility.

3.5.1 Fault geometry analysis

3.5.1.1 Fault length (L)

The fault length (L) is defined as the cumulative total horizontal length along the mapped trace of each fault, measured from tip to tip at the top cut-off (i.e. the footwall scarp edge). Because the DEM provides a 30 m resolution, this "apparent" length represents the full fault extent as resolved by the elevation data. The measurement began by digitising a series of closely spaced vertices along each fault's top-cut-off trace in QGIS, ensuring uninterrupted coverage from one tip to the other. The Easting (x) and Northing (y) coordinates of each vertex were exported via the attribute table into Excel for initial quality control, verifying the correct point order and removing duplicates or gaps before statistical processing in Python.

The cumulative fault length was calculated by summing the horizontal distances between successive vertices along the mapped top-cut-off trace. This approach preserves changes in fault-trace geometry rather than representing fault length as a straight-line distance between the two fault tips. The calculation was implemented using a Python script developed for this study (Alghamdi, 2025). The horizontal distance between each pair of successive vertices was calculated using the following equation:

$$\Delta L = \sqrt{(x_{top1} - x_{top2})^2 + (y_{top1} - y_{top2})^2} \qquad eq.3.1$$

where and are the horizontal coordinates of two consecutive top-cut-off vertices. The total fault length (L) was then obtained by summing the successive segment lengths (ΔL) from one fault tip to the other.

Where the preserved surface expression did not extend to the interpreted fault tip, the projected fault trace was used as described in Section 3.4.1 (Fault picking method). By summing the segment lengths between each pair of adjacent top-cut-off vertices, the full fault length was recovered while following bends and changes in orientation along the mapped trace. This piecewise-linear approach preserves the planimetric geometry of the fault scarp and avoids the underestimation associated with simple endpoint or straight-line approximations (Watterson, 1986; Cowie and Scholz, 1992).

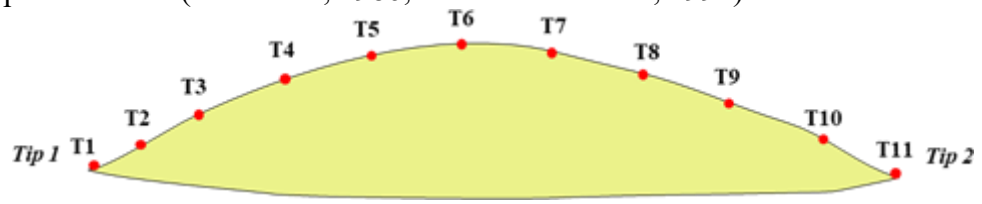


Figure 3.5: This diagram shows the top cut-off fault trace marked with multiple sampling points (red dots) from one tip to the other; each point (T) represents its recorded (x, y) coordinates.

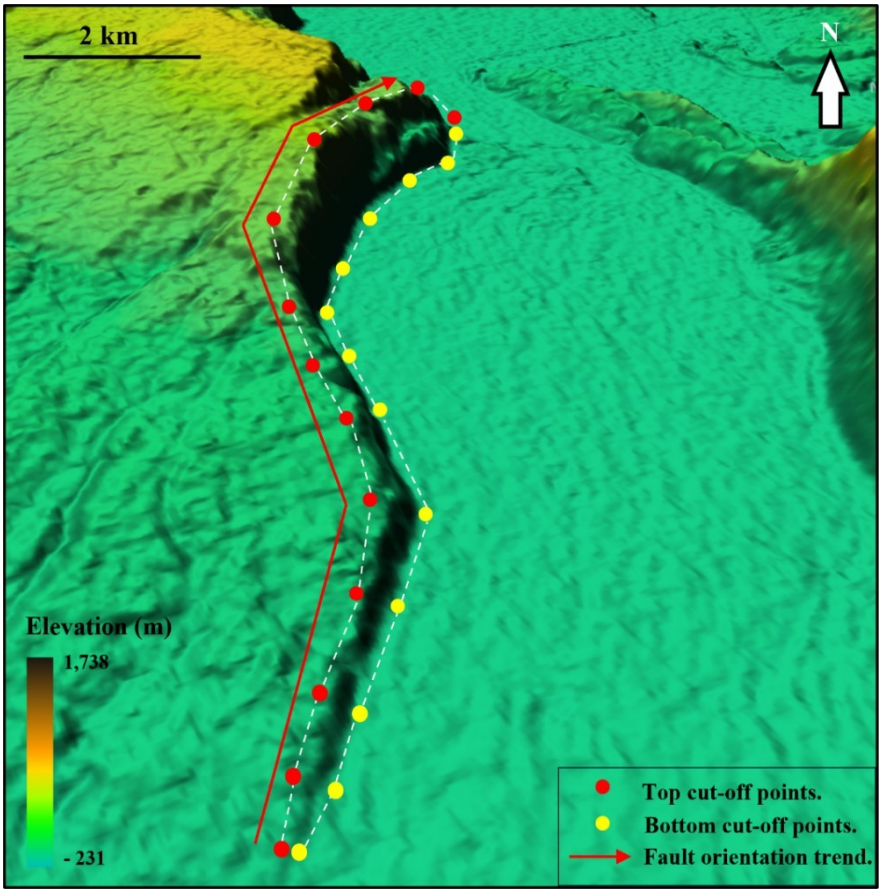


Figure 3.6: This diagram shows fault picking along the fault, considering any change in orientation. The fault curves (red dots) represent the top cut-off, and (yellow dots) represent the bottom cut-off.

3.5.1.2 Fault maximum displacement (D_{max})

To determine the maximum displacement of each fault, the apparent displacement (*d*) along the entire fault trace must first be calculated. Fault displacement represents the relative movement between the footwall and hanging wall blocks within the fault plane. In this study, fault displacement is assumed to be dip-slip, as the DEM data do not independently constrain the direction of movement along the fault plane. This is distinguished from fault throw, which represents the vertical component of displacement.

In this study, apparent displacement was derived from paired measurements between the top cut-off (footwall crest) and bottom cut-off (hanging-wall base) identified on the DEM surface (Figure 3.6). These cut-offs were manually digitised in QGIS to ensure that each top point was paired with a corresponding bottom point along the same section of the scarp, including portions affected by erosion or burial.

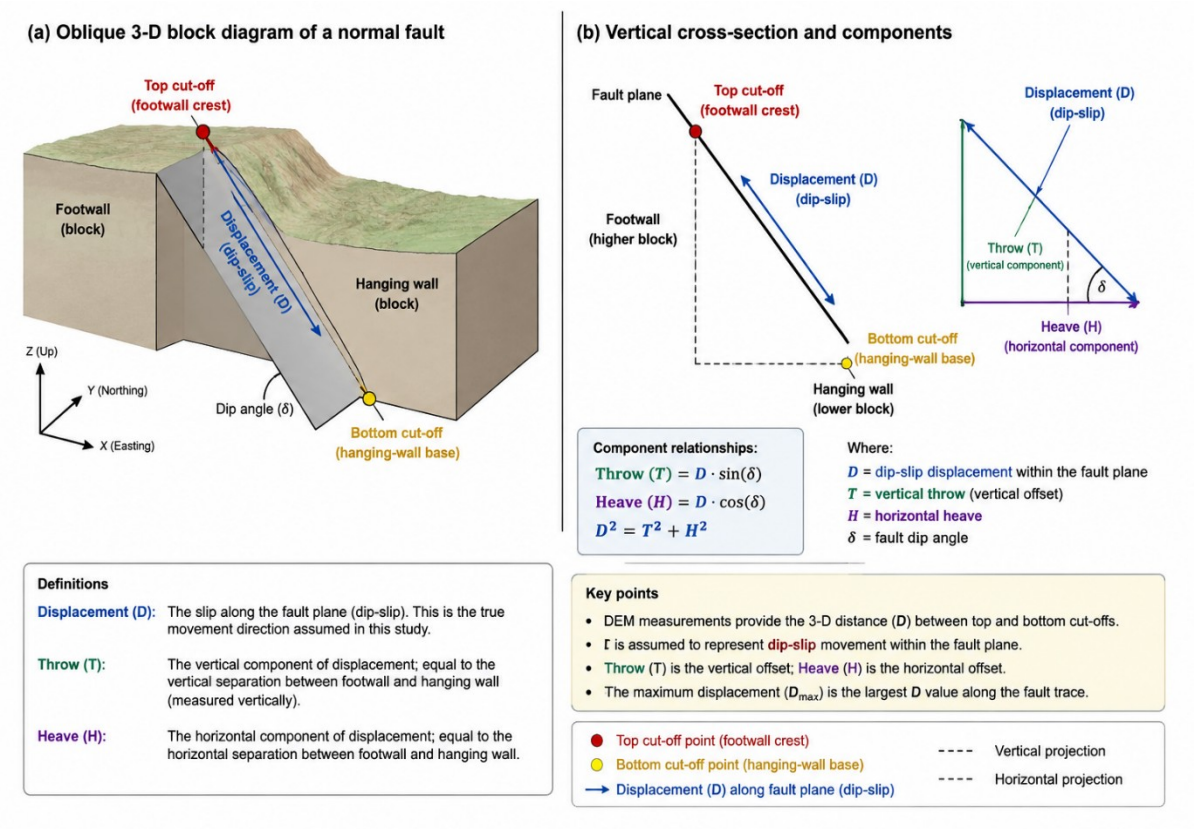


Figure 3.7: Conceptual illustration defining the displacement components used in this study. Apparent displacement (*d*) is assumed to represent dip-slip movement within the fault plane. Throw represents the vertical component of displacement, whereas heave represents the horizontal component. The top and bottom cut-offs represent the reference points used to measure apparent fault-scarp displacement from the DEM.

For every paired location, planimetric coordinates and elevation values (*x, y, z*) were recorded in a projected coordinate system (UTM, metres) to ensure spatial accuracy in distance calculations. The apparent displacement for each pair (*d*) was then calculated as the three-dimensional Euclidean distance between the top and bottom cut-offs:

$$d_i = \sqrt{(x_{topi} - x_{boti})^2 + (y_{topi} - y_{boti})^2 + (z_{topi} - z_{topi})^2} \qquad eq.3.2$$

The locations of the paired top and bottom cut-off points were not selected arbitrarily. Points were manually positioned where the fault-scarp geometry could be reliably identified from the DEM, with each top cut-off paired with the corresponding bottom cut-off across the same section of the scarp. Point spacing was therefore variable rather than fixed and depended on the geometry and preservation of the fault scarp and the spatial resolution of the DEM.

This calculation incorporates differences in horizontal position and elevation between each paired top and bottom cut-off to determine their three-dimensional separation. The process was automated using a Python routine that read the exported vertex coordinates

from QGIS and computed the displacement values for all top–bottom pairs along each fault. This method captures the distribution of apparent displacements and reflects natural variations along strike caused by segmentation, erosion, or burial. Once all individual displacements (d_i) were determined, the maximum fault displacement (D_{max}) was identified as the highest measured value along the fault trace:

$$D_{max} = \max\ (d_i). \qquad \textit{eq.3.3}$$

This pick-the-maximum approach is widely adopted in structural geology and fault growth studies to represent the largest preserved offset on fault (Watterson, 1986; Scholz, 2002). Using D_{max} provides a consistent and reproducible metric for comparing faults of different lengths and preservation states and is fundamental for establishing empirical relationships between displacement and length (D–L scaling) (Cowie and Scholz, 1992; Childs et al., 2017). Because D_{max} is less sensitive to local measurement noise than the average displacement, it provides a robust indicator of the fault's kinematic maturity and cumulative slip potential.

3.5.1.3 Fault spatial distribution

The spatial distribution of faults was examined to identify differences in fault density and areas of high deformation in each study area. These results provide a quantifiable framework for evaluating strain localisation and structural clustering. All mapped fault traces were first reviewed for topology errors and then converted to a common coordinate reference system (UTM Zone 37N, WGS 1984) to ensure that all mapped faults were spatially consistent. A fault density surface was then created from the vector layer of the mapped faults by applying the Kernel Density Estimation (KDE) function in the heatmap algorithm of the Raster Analysis Toolbox in QGIS (version 3.32), which estimates the density of line features (faults) per unit area. A search radius of 1 km was selected after testing different bandwidths to balance the smoothing and spatial detail. The input layer consisted of a vector shapefile containing all mapped fault traces, and the output was a continuous raster layer representing fault density as faults/km². The raster cell size was set to 100 m to match the effective resolution of the derivative maps.

The resulting raster was symbolised using a red-to-yellow colour ramp, where darker red areas represent higher concentrations of faults and lighter colours indicate more isolated faults. To further analyse the relationship between the spatial distribution of faults and regional topography, a fault-density raster was overlain on both the DEM and Hillshade layers to visualise how fault clustering relates to topographic elements such as grabens,

ridges, and volcanic centres. In general, areas of high fault density correspond to locations of high strain localisation and structural linkage, whereas areas of low density indicate more distributed faulting. This method provides a repeatable, data-driven approach for identifying fault clusters, linkage zones, and structural trends indicative of the degree of rift segmentation and the extent to which deformation is focused over time (Childs et al., 2017; Cowie et al., 2005).

3.5.1.4 Fault orientation

Fault orientation is described by strike and dip: strike is the azimuth of the horizontal line on the fault plane measured clockwise from geographic north, and dip is the angle of maximum inclination measured perpendicular to strike. Together, they define the plane's attitude and underpin kinematic interpretation. In this study, only the strike is reported from map-view traces; the dip was not estimated from the 30 m DEM because DEM-derived dips are unreliable at this resolution.

Strike was computed from the upper (footwall) cut-off polylines to maintain a consistent reference with length and displacement measurements. In QGIS, the Line Direction Histogram tool was used to calculate the line segment azimuths and plot length-weighted rose diagrams. Eight angular bins (45° sectors) were employed after testing coarser and finer binning; length weighting emphasised the contribution of longer fault segments to the orientation signal. The resulting rose diagrams summarise the dominant strike families and facilitate comparisons across zones.

For reproducibility, azimuths were measured 0–180° (axial data folded for bidirectional symmetry), the bin count was set to 8, length weighting was enabled, and the same projected CRS (UTM, metres) was used as in the rest of the analysis. Outputs were checked against the hillshade to confirm that the mapped traces represented tectonic scarps rather than volcanogenic or erosional features. Length-weighted roses are preferred because they better represent the structural grain than simple count-weighted plots in fault-trace datasets.

3.5.2 Fault displacement profiles

Displacement profiles were generated from the digitised fault cut-off points using a custom Python script. The script calculated apparent displacement along each fault trace and produced a displacement–distance curve that describes how slip varies from tip to tip. Three main profile patterns were identified by examining the shape and number of peaks within these curves. Faults exhibiting a single, approximately symmetrical, bell-shaped peak were classified as single-peak profiles, representing faults with simple geometries and continuous displacement distribution. Profiles displaying two or three distinct peaks were grouped as multi-peak profiles, reflecting faults composed of two or more interacting segments that have not yet been fully linked. Faults showing four or more irregularly spaced peaks were classified as irregularly peaked profiles, indicating complex internal structures formed by the linkage of multiple segments and/or repeated growth and reactivation events.

This classification is based on the observable geometric features of displacement–distance curves and reflects the structural characteristics of fault growth recognised in previous studies (e.g. Walsh and Watterson, 1988; Cowie and Scholz, 1992; Peacock and Sanderson, 1991). Analysing these profile types identifies how slip is distributed along faults and provides insights into segmentation and linkage behaviour. Increasing profile complexity from single peak to irregularly peaked can be used as an indicator of fault maturity, with multi-peak and irregularly peaked profiles generally representing more advanced stages of fault growth and linkage. The resulting dataset forms the basis for subsequent analyses of fault segmentation and evolutionary patterns across the study zones.

3.5.3 Fault linkage analysis

Fault linkage analysis investigates how neighbouring fault segments interact and connect during progressive rift evolution (Figure 3.8). In structural-geological terms, fault linkage describes the mechanical and geometric relationships between adjacent segments that control the fault propagation, displacement transfer, and fault system architecture. The transition from isolated to connected segments marks the evolution from immature (soft-linked) to mature (hard-linked) systems as strain becomes progressively localised along major rift-bounding zones.

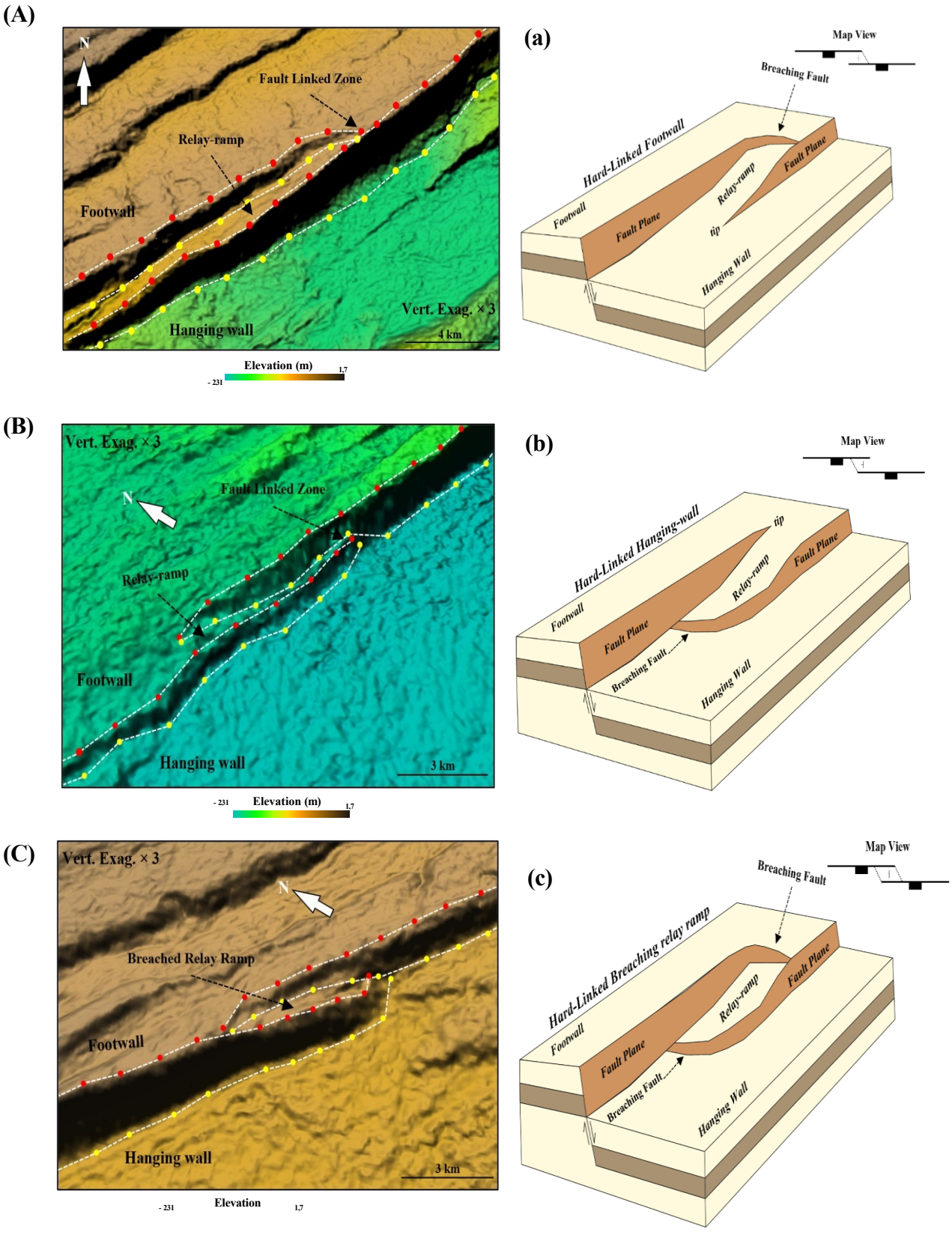


Figure 3.8: Fault linkage styles and evolution illustrated using DEM interpretations (left) and corresponding conceptual 3-D block diagrams (right). Red dots indicate top cut-offs (footwall), and yellow dots indicate bottom cut-offs (hanging wall). **(A–a)** Soft linkage: overlapping fault segments are connected by a relay ramp, allowing displacement transfer between mechanically distinct segments. **(B–b)** Hard linkage via the footwall: a connecting fault breaches the relay zone and forms a continuous fault trace. **(C–c)** Hard linkage via the hanging wall: a connecting fault breaches the relay zone and establishes a through-going fault trace. These examples illustrate the progression from soft to hard linkage as fault segments become geometrically connected and displacement becomes increasingly localised.

All fault traces were mapped and digitised in QGIS using the upper (footwall) cut-off to maintain consistency with length and displacement measurements. Linkage relationships were evaluated using the 30 m ASTER DEM, along with hillshade and slope visualisations. Fault pairs showing overlapping tips, converging traces, or shared deformation zones were flagged as potential linkage sites. Potential linkage sites were identified from the spatial relationships between neighbouring fault traces, including overlap or close approach of fault tips, changes in scarp geometry, and continuity between adjacent fault segments. These relationships were then checked using the DEM, hillshade and slope visualisations**.** Each pair was inspected in 2-D and 3-D, and local displacement–distance profiles were analysed to assess slip transfer between segments. Two linkage types were identified: soft and hard linkages.

Soft linkages are geometric and kinematic connections between overlapping or en-échelon segments that have not yet intersected (Figure 3.8 A–a). The segments are connected via a relay ramp or a distributed deformation zone, across which the displacement is transferred gradually. On the DEM, such structures appear as gently dipping, saddle-shaped surfaces between adjacent scarps, and displacement–distance profiles show smoothly overlapping curves with low-amplitude transfer. These configurations represent an immature linkage stage in which faults remain mechanically distinct but interact through distributed strain within the relay.

Hard linkages develop when neighbouring segments become physically connected by relay breaching or direct intersection, forming a single through-going fault plane (Figure 3.8 B–b, C–c). The connecting segment initiates in either the footwall or hanging-wall block, cuts across the former relay zone, and establishes full geometric and kinematic continuity. Displacement profiles typically show localised highs at the breach point, indicating efficient slip transfer along a unified structure. Hard linkage therefore characterises a mature stage of fault growth with strong strain localisation.

3.5.4 Minimum strain elongation (*e*)

The minimum horizontal strain in each profile was calculated using the method of elongation, which provides a measure of extension associated with fault-related deformation. Elongation (e) is defined as the relative change in length between the reconstructed pre-faulting length (L_0) and the present-day extended length (L_1):

$$\boldsymbol{e = \frac{L_1 - L_0}{L_0}} \qquad \textit{eq.3.4}$$

Here, L_0 represents the reconstructed pre-faulting length of the originally continuous layer, whereas L_1 represents its present-day length after fault-related extension. This provides a geometrically defined estimate of the minimum horizontal elongation associated with faulting, assuming that deformation is accommodated by the mapped fault-related extension and that no appreciable ductile strain or loss of layer area has occurred.

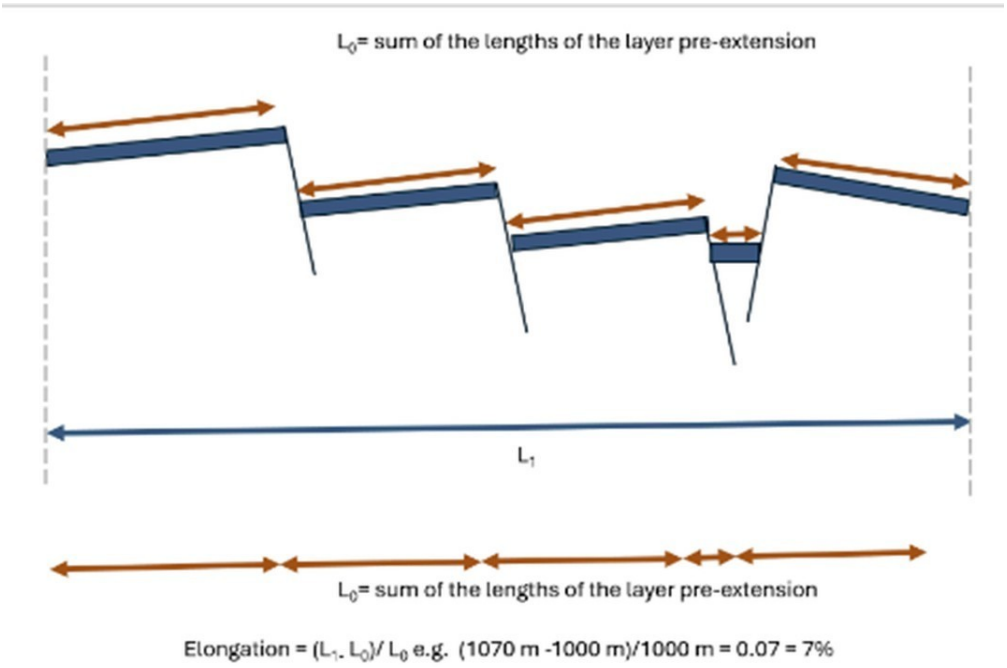


Figure 3.9: Schematic diagram illustrating the elongation method used to calculate minimum horizontal strain. The reconstructed pre-faulting length (L_0) represents the sum of the lengths of the originally continuous layer segments, whereas L_1 represents the present-day horizontal distance between the profile endpoints after fault-related extension. Elongation (e) was calculated as $(L_1 - L_0)/L_0$ and expressed as a percentage. This method provides a geometrical estimate of the minimum strain accommodated by faulting and does not account for distributed or ductile deformation.

As illustrated schematically in Figure 3.9, elongation was calculated along a series of profiles approximately normal to the mean fault strike in each area of investigation. For each profile, the pre-elongation length (L_0) was reconstructed from the DEM-derived topographic profile by measuring the preserved surface lengths between successive fault cut-offs along the profile. These individual surface lengths were then summed to obtain the reconstructed pre-faulting length (L_0). The post-elongation length (L_1) was measured as the horizontal distance between the same profile endpoints after fault-related extension. The ratio $(L_1 - L_0)/L_0$ gives the minimum apparent strain, expressed as a percentage elongation.

A worked example of this measurement procedure is shown in Figure 3.10. The example illustrates how the individual surface lengths between successive fault cut-offs were measured from a representative topographic profile and summed to determine L_0, and how L_1 was measured between the same profile endpoints.

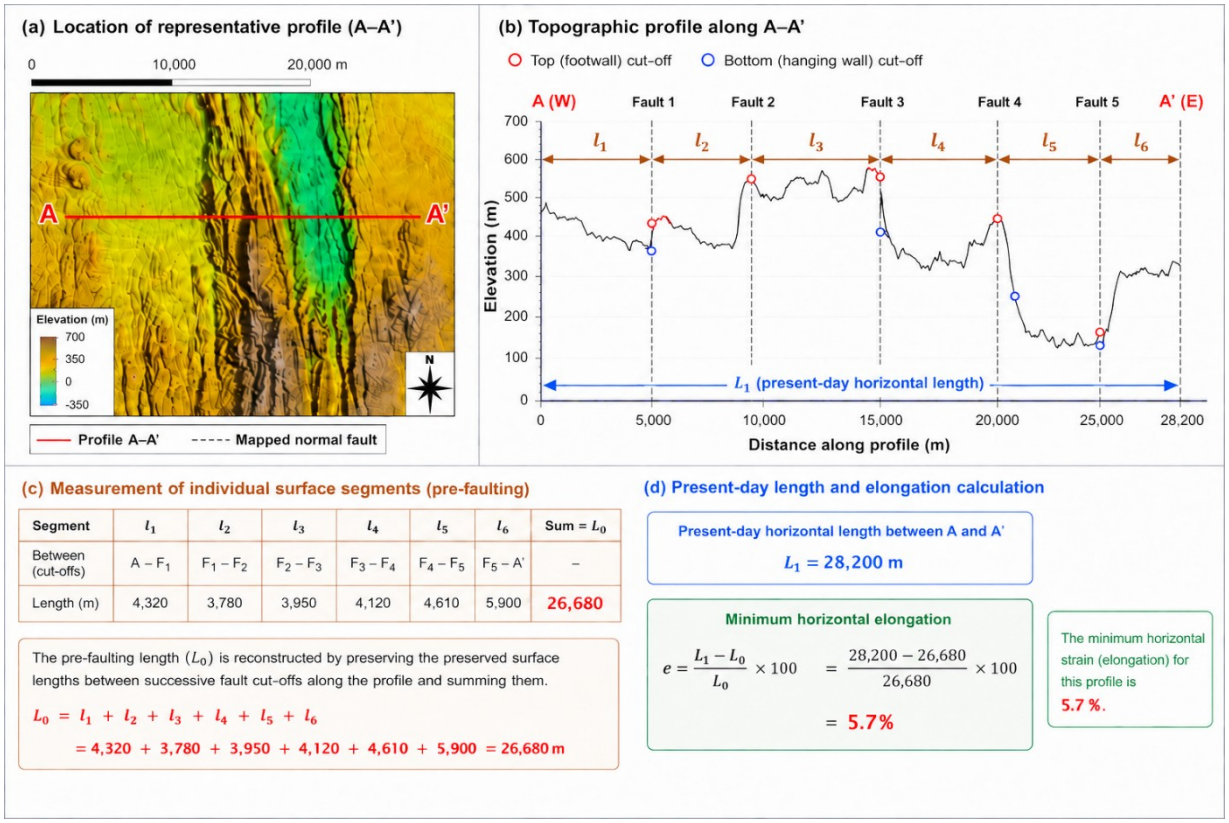


Figure 3.10: Worked example illustrating the measurement of the reconstructed pre-faulting length (L_0) and present-day extended length (L_1) used to calculate minimum horizontal elongation. **(a)** DEM showing the location of the representative A–A′ profile across mapped normal faults. **(b)** Corresponding topographic profile showing successive fault cut-offs and the individual preserved surface lengths (l_1–l_6) measured between them. **(c)** The individual surface lengths were summed to reconstruct L_0, while **(d)** L_1 was measured as the present-day horizontal distance between the same profile endpoints (A–A′). The resulting L_0 and L_1 values were used to calculate the minimum horizontal elongation (e).

Faults are regarded as geometric discontinuities whereby the original layer length is increased through the action of discrete displacements, and the method therefore provides an estimate of the fault-controlled strain associated with horizontal stretching of the crust. No account is taken of distributed or ductile strain that may occur. Owing to the nature of the geometrical data derived from the 30 m ASTER GDEM, the calculated values represent minimum apparent strain; the actual strain may be greater where fault scarps have been degraded, buried, or are below the spatial resolution of the DEM.

Profiles were constructed in QGIS from digitised fault traces. The measurements used to determine L_0 and L_1 were processed in Python, and the resulting elongation values were expressed as percentages to facilitate comparison between different profiles. Profiles were placed approximately normal to the dominant fault strike (within ±10°) to minimise angular bias. Spatial variations in e were plotted along a north–south transect to show the

degree to which strain was localised or distributed across each zone.

3.5.5 Cross-cutting relationship

Cross-cutting relationships provide a fundamental structural tool for establishing the relative timing of fault activation. If one fault displaces or truncates another, the displaced structure is interpreted as older than the cutting fault (Fossen, 2010). Understanding the faulting sequence is essential for reconstructing the evolution of deformation and the development of fault networks during rifting. This analysis is especially valuable in regions where multiple fault generations overlap or interact, providing insights into the progressive stages of fault growth, linkage, and reactivation.

In this study, cross-cutting relationships were manually mapped in QGIS by identifying

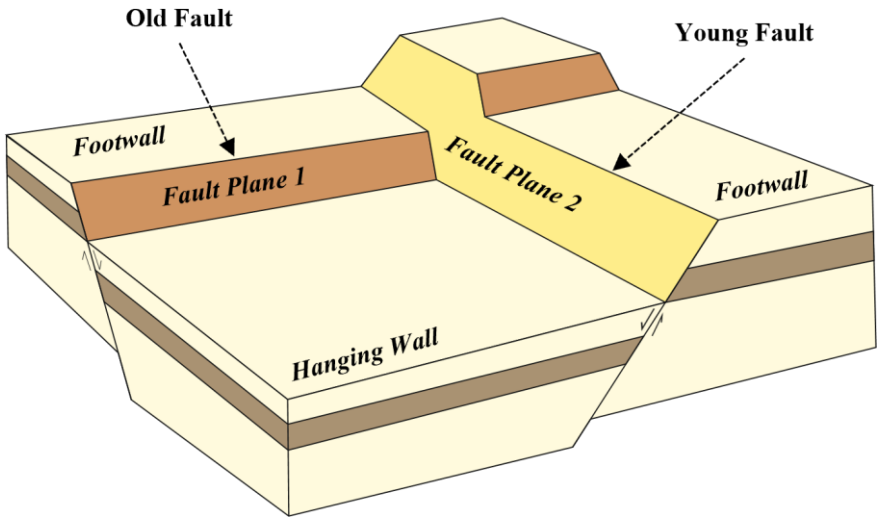


Figure 3.11: Block diagram illustrating a cross-cutting fault relationship, where Fault Plane 2 offsets and truncates Fault Plane 1, indicating that Fault 2 is younger. This geometric configuration helps constrain the relative timing of faulting events in extensional systems (modified after Barnett et al., 1991; Barnett et al., 1987).

slope breaks and elevation changes in the DEM. The top and bottom cut-offs of each fault scarp were digitised, allowing the continuity, termination and offset of intersecting fault traces to be examined. The following recognition criteria were applied to interpret the relative timing of intersecting fault segments. Younger faults were interpreted to cross-cut older faults where the younger fault trace clearly offset or disrupted the continuity of the older fault trace (Fossen, 2010). Where a fault trace continued across an intersection without an observable offset or termination, no cross-cutting age relationship was assigned from that intersection alone. Where the displacement on one fault diminished or terminated adjacent to the trace of another fault, the intersection was interpreted as a tip-line relationship rather than unequivocal cross-cutting, providing information on the relative fault-growth sequence (Giba et al., 2012; Kim and Sanderson, 2005). Younger fault segments that cut across pre-existing relay zones and contribute to the transition

from soft- to hard-linked geometries were interpreted as evidence of sequential fault-segment interaction and progressive linkage (Cartwright et al., 1995; Peacock and Sanderson, 1991).

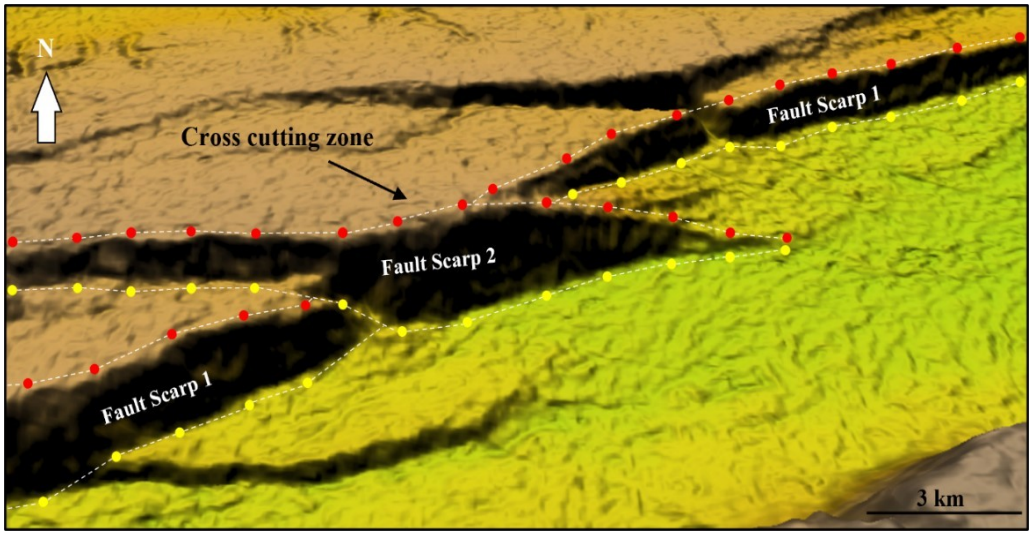


Figure 3.12: Cross-cutting fault scenario. Two normal Fault Scarps (Fault Scarps 1 and 2) intersect, forming a cross-cutting zone where the younger scarp truncates the older one. The red and yellow dots mark the mapped top and bottom cut-off vertices, respectively.

These criteria yield a systematic and reproducible framework for assigning relative ages to fault segments and deciphering the hierarchical arrangement of faults within rifts. In practice, each fault intersection was visually inspected in the plan view (DEM and Hillshade) to identify geometric offsets, terminations, or local warping of the strata. Only intersections exhibiting unequivocal cross-cutting evidence were classified; ambiguous cases (e.g. where erosion or burial obscured the relationship) were left unassigned to avoid misinterpretation.

Although DEM-based mapping is effective for regional coverage, the interpretation of cross-cutting relationships can be difficult because faults may reuse older fracture surfaces, terminate in diffuse deformation zones, or be covered by alluvial or volcanic rocks. In such cases, the base or top of the scarp may be absent in the DEM, and the cut-off positions may be poorly constrained. In addition, the DEM resolution may be inadequate to represent subtle vertical displacements or narrow deformation bands, especially in low-relief areas. Therefore, interpretations were made conservatively, and cross-cutting relationships were assigned only where clear evidence was visible in both planimetric and elevation data (e.g. truncation of a basal scarp or measurable offset).

3.5.6 Fault maturity and surface geological units

To examine how fault maturity relates to surface geology, the fault database was integrated with regional geological units using the 1:3,100,000 geological map of the Afar Depression and southern Red Sea–Gulf of Aden compiled by Rime et al. (2022). The map and associated shapefiles were downloaded from Zenodo (DOI: 10.5281/zenodo.7351643) and provided a consistent tectonostratigraphic framework compiled from published maps, radiometric ages, and remote-sensing interpretations (Rime et al., 2023).

The geological shapefiles were imported into QGIS v3.32, re-projected to match the fault data, and clipped to the extent of each study zone. Polygons were attributed to the dominant lithostratigraphic unit (volcanic, sedimentary, or mixed volcanic–sedimentary) and mapped age following the original legend, allowing each fault to be spatially correlated with the surface unit that it cuts or offsets.

Within each zone, faults were grouped according to the geological unit containing their mapped surface trace. This provided a means of evaluating fault maturity in relation to the age of the exposed surface unit. However, the age of the geological unit was not assumed to represent the absolute age of fault initiation, because younger faults may cut older geological units and older fault scarps may be partly obscured by younger volcanic or sedimentary deposits. Instead, surface-unit age was used as a relative contextual indicator of fault development and preservation. Faults preserved across older units may record a longer history of displacement accumulation and linkage, whereas faults restricted to younger units may record deformation that post-dates the formation of those units. However, these relationships were not interpreted from surface-unit age alone. Maximum displacement–length (Dmax/L) ratios and displacement-profile characteristics (single-peak, multi-peak and irregularly peaked) were therefore considered together with surface-unit age to assess relative differences in fault maturity and linkage. Thus, geological-unit age provides a temporal and geological context for interpreting fault development rather than a direct measure of fault age.

The overlay was implemented in QGIS using Spatial Join and Intersect to associate each mapped fault segment with the geological polygon that it intersects. The resulting attribute tables were exported to Python for statistical analysis and plotting (e.g. Dmax/L vs. unit age for each zone). This integrated structural–geological workflow provides a reproducible basis for testing the influence of lithology and stratigraphy on fault propagation, linkage style, and maturity across the Afar Depression.

3.6 Data limitation and error

The results of this study are based on ASTER GDEM elevation data with a spatial posting of approximately 30 m. Published validation of ASTER GDEM Version 3 over the conterminous United States reported an overall vertical RMSE of 8.52 m (Gesch et al., 2016); however, this value provides a general indication of dataset performance rather than a site-specific accuracy estimate for the Afar region. At this spatial resolution, smaller faults, narrow deformation zones, and subtle vertical displacements may be unresolved or smoothed, while elevation artefacts, particularly on steep volcanic slopes, may introduce additional uncertainty. Therefore, the apparent fault lengths and apparent displacements derived from the mapped cut-offs represent minimum estimates of the true values where fault scarps have been eroded, buried, or fall below the spatial resolution of the DEM.

Manual interpretation introduces additional uncertainty. Parameters for hillshading, vertex spacing, and line continuity can vary between interpreters, and nontectonic features may be misidentified as fault scarps in low-relief terrain. All subsequent products inherit these uncertainties. Displacement-distance profiles depend on both the smoothing method and the choice of peak prominence and minimum spacing thresholds; Kernel Density Estimates depend on bandwidth; and rose diagrams depend on the number of bins and use (or not) of length weighting, which can under-represent very short traces.

The classification of linkage types (soft vs. hard) is determined solely from the surface geometry and does not necessarily indicate how connected the fault system is at depth. Cross-cutting relationships can be masked by resurfacing or burial; therefore, only clearly truncating and offsetting relationships were used. The minimum strain values calculated using the elongation method assume negligible ductile strain and no loss of layer area; thus, the calculated extension represents a true lower bound.

Finally, polygon boundaries representing geological units were used to compare fault maturity with surface geology at a scale of 1:3,100,000, generalise complex contacts, and polygon ages and boundaries were based on compiled sources. Therefore, mismatches between DEM-based fault scarps and local contacts are possible. These constraints are acknowledged alongside relevant figures; however, they do not affect the comparison of relative differences between zones, which is the primary aim of the analysis.

3.7 Data quality control (QC)

Ensuring that fault-geometry data are accurate and reliable is fundamental to structural or quantitative fault analyses. Therefore, a systematic quality control (QC) program was implemented throughout all stages of data processing to verify that the derived results were both consistent and reproducible. The QC procedures were designed to identify and minimise errors introduced during manual digitisation, spatial attribute assignment, data extraction, and automated computation of fault parameters.

The first stage involved the manual validation of digitised fault-sampling points. For each fault scarp, the footwall (top) and hanging wall (bottom) cut-off points were carefully inspected to confirm that they were correctly located and aligned along the mapped trace. In particular, each point along the footwall cut-off was checked to ensure that it corresponded vertically and laterally with its paired point on the hanging wall cut-off. Maintaining this geometric consistency was essential for the accurate measurement of apparent displacement and for preserving a coherent three-dimensional representation of each fault surface.

Following this validation, all digitized faults were checked for naming and indexing consistency. Each fault was assigned to a structured and unique identifier encoding the fault number, cut-off type (top or bottom), and location within the study area (for example, F001_t_E, where F001 denotes Fault 001, t represents the top cut-off, and E indicates the eastern part of the zone). This system ensured a one-to-one correspondence between the top and bottom data, prevented duplication, and allowed rapid cross-referencing within the QGIS and Python datasets. All identifiers were spatially verified to confirm that each tag corresponded to the correct mapped location.

Next, the coordinate datasets (*x, y, z*) were reviewed for internal consistency and completeness. Errors such as duplicate points, missing values, and reversed point sequences along fault traces were corrected. Each dataset was checked to ensure that the points were ordered from tip to tip and accurately represented the geometry of the mapped scarp. Fault traces were checked for discontinuities, duplicate vertices, incorrect point order, or anomalously large gaps between successive vertices that could result from digitising errors. Where identified, these errors were corrected before inclusion in the statistical analysis. Variable vertex spacing itself was not treated as an error, because vertices were positioned according to changes in fault-trace geometry rather than at fixed intervals.

To confirm the accuracy of the automated calculations performed in Python, a

representative subset of faults was independently recalculated using the same equations as those in the scripts. Parameters such as fault length, apparent displacement, and displacement–length ratios were manually recomputed and compared with the automated outputs. These redundancy checks confirmed that the scripting workflow produced consistent and unbiased results.

In the final step, the complete dataset was statistically screened for anomalies. Outliers in fault length, displacement, or D/L ratios were flagged and reassessed by cross-checking with the original Hillshade and DEM profiles. Values representing genuine geological variability were retained and documented, whereas values arising from measurement or mapping errors were corrected or removed.

This multistage QC process, comprising manual validation, standardised naming, independent verification, and statistical screening, provides a rigorous framework for maintaining data quality and reproducibility. By reducing uncertainty and ensuring consistency at every stage, the resulting fault database offers a reliable foundation for subsequent analyses of fault growth, segmentation, linkage, and strain accommodation across the Afar study zones.

The methodological framework outlined in this chapter establishes a foundation for the systematic mapping and quantitative analysis of normal faults across the Afar Depression and Main Ethiopian Rift. By integrating 30 m ASTER DEM data, geological maps, and statistical tools within QGIS and Python, the workflow ensures consistent measurements of fault geometry, segmentation, linkage, and strain. The quality control procedures and error assessments described above provide confidence that the extracted parameters are robust and reproducible. The following chapter applies these methods to Zone 1, the North Afar Depression (NAD), where fault characteristics are analysed in detail to describe the geometry, segmentation, linkage, and strain patterns of the northern part of the rift system. This analysis forms the first step in comparing fault growth and strain localisation through successive stages of rift evolution across the three study areas.

Chapter 4: Quantitative analysis of faulting geometries in the North Afar Depression (NAD)

4.1 Introduction

The Afar Depression, at the junction of the Red Sea, Gulf of Aden, and the Main Ethiopian Rift, is an exceptional natural laboratory for studying normal fault growth at actively extending plate boundaries (Wolfenden et al., 2004; Corti, 2009). Normal faulting related to Arabia–Africa divergence is well characterised at the regional scale; however, comparable quantitative analysis of fault geometry, segmentation, linkage, and strain at the scale of individual fault populations and across different rift sectors remains limited (Ebinger and Hayward, 1996; Manighetti et al., 1998; Agostini et al., 2011).

To address this, a three-zone approach was adopted based on surface topographic expression, because fault-scarp exposure, sedimentary burial, and DEM-based measurement accuracy all depend on surface relief and morphology. These topographic contrasts also reflect differences in rift maturity and magmatic construction across Afar (Ebinger, 2005; Wolfenden et al., 2004; Corti, 2009). The three zones are Zone 1 in the North Afar Depression (NAD), Zone 2 in the Northern Main Ethiopian Rift (NMER), and Zone 3 in the Eastern Afar Depression (EAD) (see the regional geological and study-area map presented earlier in the thesis).

This chapter aims to quantitatively evaluate the characteristics and evolution of normal fault systems in Zone 1 of the NAD to assess whether they conform to the established theoretical models of fault growth in extensional settings. To achieve this, the chapter sets out to: (1) analyse fault geometries by characterising apparent lengths and displacements and quantify displacement–length (D–L) scaling using regression analysis based on the relationship $D_{max} = cL^n$; (2) describe observed segmentation and linkage states for individual faults and for composite fault zones (overlaps, relays, throughgoing links); (3) assess the linkage relationships among fault segments by distinguishing between soft and hard linkages to infer connectivity and structural evolution, including comparison of segment lengths with the total lengths of hard-linked fault systems to assess the influence of linkage on D–L scaling; (4) quantify the minimum apparent extensional strain along eight cross-sectional profiles using elongation between undeformed (L_0) and extended (L_1) lengths, with summed heave used as a cross-check; and (5) compare fault maturity (via Dmax/L ratios) with mapped surface ages (Rime et al., 2022) and compare Dmax and D–L scaling between mapped geological units to assess the influence of lithology,

resurfacing or sedimentary burial on apparent fault development. These objectives were addressed using Digital Elevation Model (DEM) data with a resolution of 30 m, integrated with geological maps and age constraints derived from Rime et al. (2022), providing a comprehensive framework for understanding fault growth dynamics within this segment of the Afar Depression.

4.2 North Afar Depression (NAD; Zone 1)

The North Afar Depression (NAD) comprises Zone 1 of this study and is located at ~12.67° N, 41.09° E in the northern Afar region**.** The study area extends ~78 km from north to south and ~30 km from east to west, totalling ~2,305 km². Elevation ranges from ~926 m above sea level on ridge tops to ~−125 m in closed depressions (Figure 4.1). An abundance of predominantly north–south-striking normal faults characterises the area, varying from a few hundred metres to >15 km in length and typically spaced ~0.5–2 km apart. The fault patterns are highly segmented and dense, and there is clear morphological evidence of ongoing extensional deformation (Ebinger and Hayward, 1996; Manighetti et al., 2001).

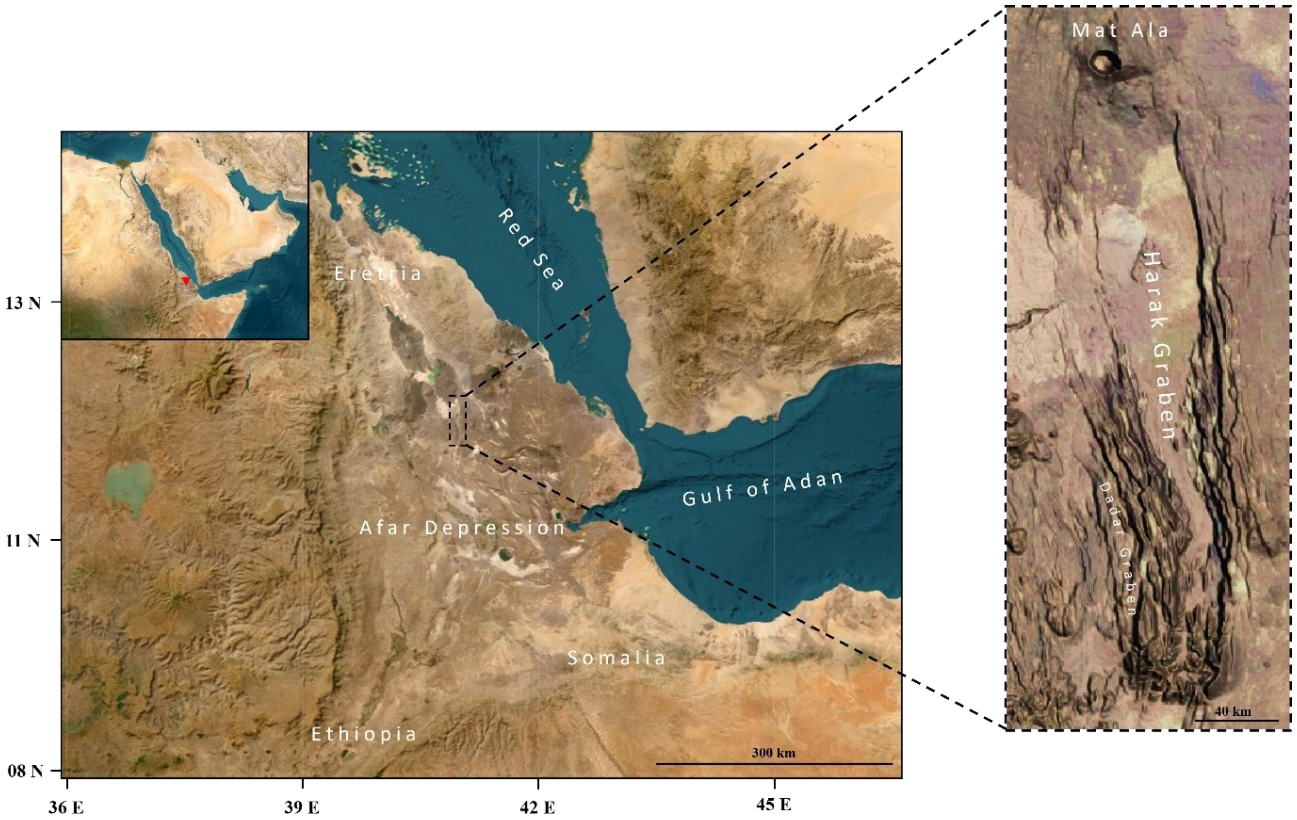


Figure 4.1 (a) Regional map of the Afar Depression showing its position relative to the Red Sea, Gulf of Aden, and East African Rift systems. The inset shows the broader location of the Afar Depression in the Horn of Africa**. (b)** Local map of Study Zone 1 in the North Afar Depression (NAD), highlighting key structural features including the Mat'Ala volcano, Harak Graben, and Dadar Graben (basemap derived from ASTER GDEM Version 3; NASA/METI/AIST/Japan Spacesystems and U.S./Japan ASTER Science Team, 2019).

Geologically, the North Afar Depression is heterogeneous, with both structural and volcanic elements. The Mat'Ala volcano lies near the northern boundary of the depression and represents an important Quaternary volcanic centre. The Harak Graben is the dominant structural feature, extending from the southern to the northern margin of the depression, and is ~50 km long and 3–10 km wide. The Harak Graben contains syn-rift sedimentary infill of Pleistocene to Holocene age, demonstrating ongoing subsidence and fault-controlled basin development. Rime et al. (2023) and Wolfenden et al. (2004) interpret the present geometry of the Harak Graben as evidence of active subsidence.

The south-eastern portion of the study area also contains the Dadar Graben, another structurally distinct depression aligned with the dominant regional fault trend (Ebinger and Hayward, 1996). The Harak Graben also includes a seasonally flooded plain, predominantly in its northern and central parts. This ephemeral standing water influences sediment deposition and locally buries or softens young scarps, which in turn reduces fault-scarp visibility in both field-based mapping and DEM-based analyses (Rime et al., 2023).

Collectively, these characteristics make the North Afar Depression an effective natural laboratory for examining spatial arrangement, linkage state, and evolution of normal faults along the northern sector of the Afar Rift. Extension associated with divergence between Arabia and Africa is localised into faulted grabens within the Afar triple-junction system. The exposed geology is dominated by Pleistocene–Holocene volcanics and Late Quaternary sediments, which provide a suitable temporal framework for comparing fault geometry, displacement, and apparent maturity across surfaces of different ages (Rime et al., 2023). The broader regional and stratigraphic context is discussed in Chapter 2 (Literature Review).

4.3 Results

In this chapter, all analyses are conducted within the methodological framework outlined in Chapter 3. This includes the classification of fault linkages, assessment of fault maturity, and calculation of the minimum apparent strain. Faults were manually mapped from ASTER Global DEM data with a 30 m resolution and then processed in QGIS. Geometric attributes including apparent fault length, maximum displacement (Dmax), and spatial relationships were extracted and analysed with a custom Python script (see Section 3.5.1). Fault linkage was classified using the soft- and hard-linkage categories defined in Section 3.5.3. Fault maturity was assessed using Dmax/L ratios, with comparisons made between mapped surface geological units from Rime et al. (2022),

with their tectonostratigraphic context following Rime et al. (2023) to evaluate the influence of lithology, volcanic resurfacing, and sedimentary burial on apparent fault development. Minimum apparent extensional strain was calculated along eight cross-rift profiles (Section 3.5.4) using elongation, $e = (L_1 - L_0)/L_0$, where L_0 is the undeformed baseline length, and L_1 is the current extended length. Cumulative heave was used as a cross-check for extension estimates. Together, these methods provide a quantitative framework for assessing fault growth behaviour, linkage state, strain localisation, and structural maturity in Zone 1 of the North Afar Depression within the context of active continental rifting.

4.3.1 Fault geometry analysis

The geometric properties of a fault system are crucial for identifying fault growth processes associated with extensional environments. Specific geometric characteristics, including fault type, geometric relationships between faults, fault length, and maximum displacement, allow the sequence of fault development to be evaluated from the initial stages of faulting through propagation and linkage. This section provides a detailed evaluation of fault geometry in the North Afar Depression (NAD) based on an assessment of the spatial distribution of faults, their length, and maximum displacements. Combined, these evaluations allow an integrated analysis of fault growth behaviour and, therefore, the structural evolution of NAD.

4.3.1.1 Fault Spatial Distribution

A total of 350 normal faults were mapped in the North Afar Depression (NAD) using a DEM dataset. The mapped traces indicate that the faults are heterogeneously distributed across the zone, resulting in clear spatial patterns in relation to both the orientation and density (Figure 4.2 a–d). Considering the orientation, most faults trend north–south, representing the dominant structural set in the area (Figure 4.2 c). The calculated dominant strike is ~167° (NNW–SSE), which closely coincides with the overall rift axis. Additionally, a smaller subset of faults trending northwest–southeast formed a secondary orientation with a more limited spatial extent (Figure 4.2 b). Although the rose diagram shows a strong overall NNW–SSE orientation, the mapped fault traces indicate systematic spatial variations in strike across the study area. Therefore, the dominant orientation shown by the rose diagram represents the zone-wide fault population and does not imply that fault strike is uniform throughout the NAD.

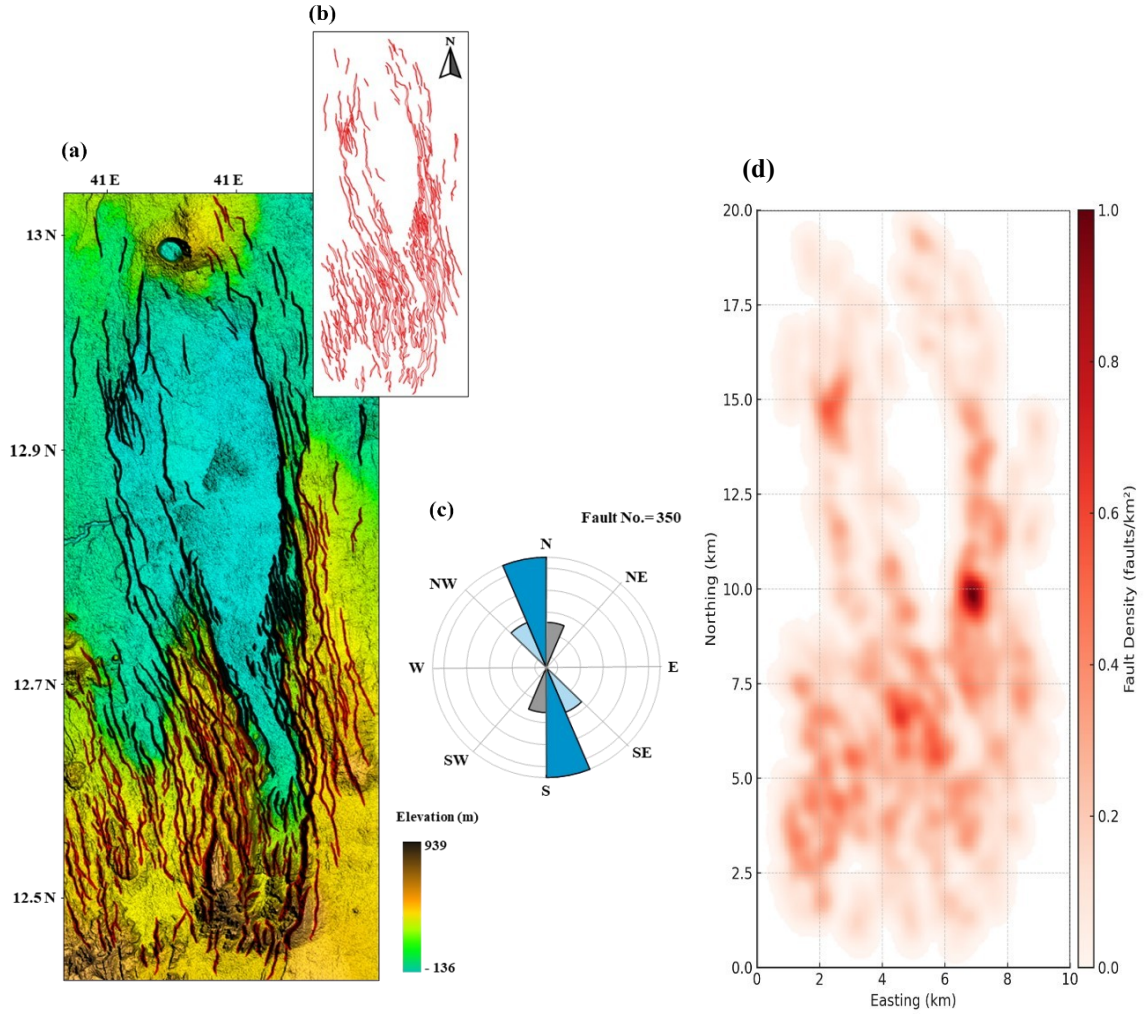


Figure 4.2: Spatial distribution of faults in Zone 1 (North Afar Depression [NAD]). **(a)** Digitised fault traces mapped from the DEM. (b) Line map highlighting structural trends. **(c)** Rose diagram showing the dominant NNW–SSE strike (~167°). **(d)** Kernel density map of fault traces, with the highest densities in the southern sector and lower values to the north ((basemap from ASTER GDEM Version 3; NASA/METI/AIST/Japan Spacesystems and U.S./Japan ASTER Science Team, 2019).

The spatial density analysis revealed systematic differences across the study area (Figure 4.2 d). Kernel density estimation (KDE) illustrated trace concentrations greater than five traces per km² in the southern sector of the zone, particularly in and around the Harak Basin. The central part of the NAD showed moderate densities that generally ranged from two to five traces per km², and the northern sector showed lower values that were generally < 2 traces per km². These values describe a density gradient from south to north, with the southern margin exhibiting a stronger clustering of fault traces and a more dispersed pattern in the northern portion of the zone. When averaged, the fault density for the entire area is ~0.56 km/km².

Parameter	Zone 1 (NAD)	Zone 2 (NMER)	Zone 3 (EAD)
Total area (km²)	2,305	29,163	17,550
Number of mapped faults	350	900	1,250
Mean fault length (m)	3,709	1,789	5,300
Mean D_{max} (m)	106 ±	77 ±	181 ±
Dominant fault strike (°)	~167° (NNW–SSE)	~152° (NW–SE)	~150° (NW–SE)
Average fault density (km/km²)	~ 0.56	~ 0.06	~ 0.38

Table 4.1: Summary of the key quantitative parameters for the three study areas. Zone 1 (NAD), Zone 2 (NMER), and Zone 3 (EAD) differ in mapped area, fault number, mean length, mean maximum displacement (Dmax), dominant strike, and average fault density. These values provide a descriptive overview of the structural characteristics of each zone; detailed interpretations are presented in Chapter 7.

It is important to note that these mapped density patterns are influenced by exposure and surface conditions. In the Harak Basin, seasonal flooding and syn-rift sedimentary infill can partially bury or soften young scarps. In the northern part of the depression, some scarps have been eroded or mantled by more recent deposits. These effects reduce surface relief at the scale of the 30 m DEM and can cause under-representation of small or low-relief faults in some areas. Therefore, the absolute density values reported here should be treated as the minimum expression of the exposed fault network, especially in areas with sediment cover or ephemeral standing water (Rime et al., 2023).

To provide context for the Zone 1 results, Table 4.1 compares the principal quantitative fault parameters across the three study zones. Zone 1 (NAD) contains 350 mapped faults, with a shorter mean fault length and lower mean displacement than Zones 2 (NMER) and 3 (EAD). Zone 2 has the shortest mean fault length (~1.8 km) but a higher mean displacement (~76 m), whereas Zone 3 contains the longest faults (maximum ~16.9 km) and the highest mean displacement (~181 m). In comparison, Zone 1 is characterised by an intermediate mean fault length (~3.7 km) and lower mean displacement (~59 m). These differences indicate that the three zones differ in the characteristic dimensions and displacement accumulated by their mapped fault populations, providing a quantitative basis for the more detailed comparison of fault scaling, linkage and rift evolution presented in Chapter 7.

4.3.1.2 Fault Length (L)

The measurements of fault length in Zone 1 (NAD) represent the apparent trace length of each individual fault that was manually mapped from tip to tip, including curvature and variation in orientation. Overall, the lengths of the 350 faults examined ranged from 487 to 16,859 m, with a cumulative mapped length of ~1,303 km. The summary statistics are presented in Table 4.2, which shows an overall mean length of ~3.7 km and a median length of ~2.8 km.

Parameter	Min. (m)	Max. (m)	Mean (m)
Fault Length (*L*)	487	16,859	3,709
Maximum Displacement (D_{max})	14	593	106

Table 4.2: Statistical summary of fault geometry in Zone 1 (NAD, N = 350). The values show the minimum, maximum, and mean fault lengths (L) and maximum displacement (Dmax) derived from manually mapped fault traces.

The frequency distribution (Figure 4.3) shows that short faults dominate this population. Approximately one-third of the dataset lies between 1,000 and 2,500 m, and another substantial proportion lies between 2,500 and 4,000 m. Faults longer than 10,000 m are rare, representing less than 5% of the total fault population.

The scaling relationship between fault length and maximum displacement is illustrated in Figure 4.4. Faults cluster predominantly between the D/L = 0.01 and D/L = 0.1 reference lines, with a smaller number of points approaching the D/L = 0.001 line; the D/L = 1 line is shown as an upper reference and is not approached by the dataset. Power-law regression of the Zone 1 fault population gives Dmax = 0.4909L^0.6395, with R^2 = 0.3011. The corresponding scaling exponent is n = 0.6395. The regression is statistically significant ($p < 0.001$).

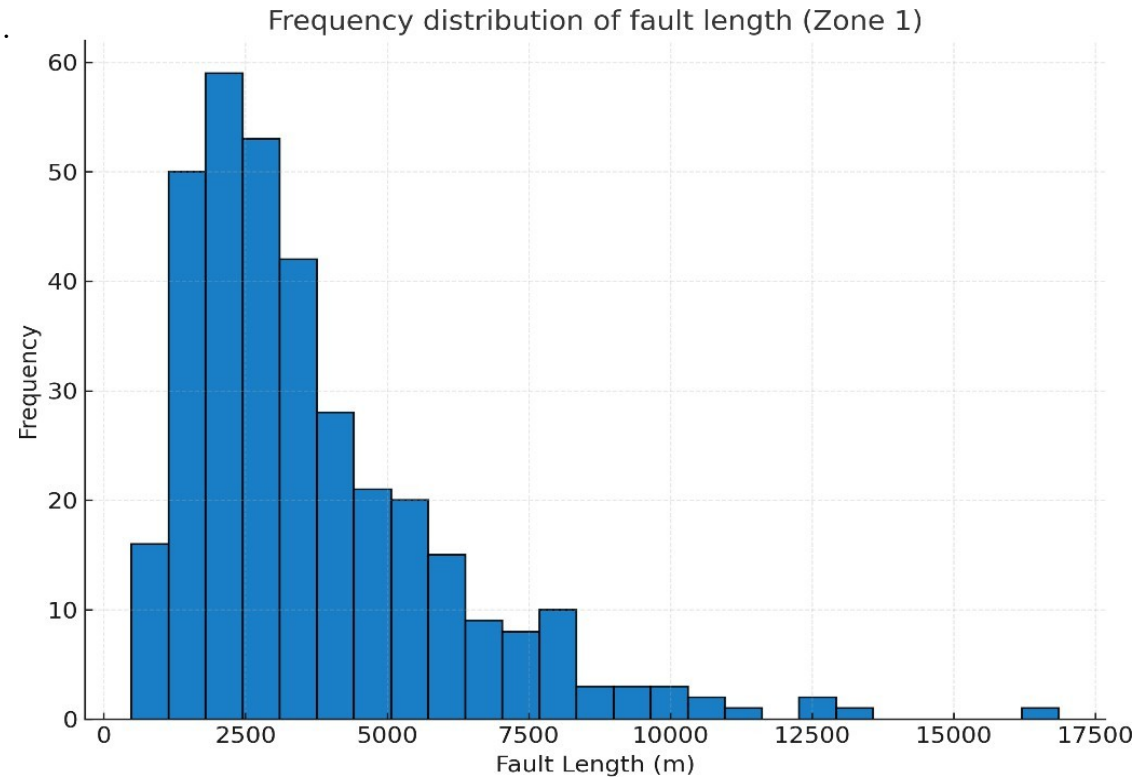


Figure 4.3: Frequency distribution of fault length in Zone 1 (NAD). The histogram shows that most faults are short to intermediate in length, with most values falling below 4 km in length.

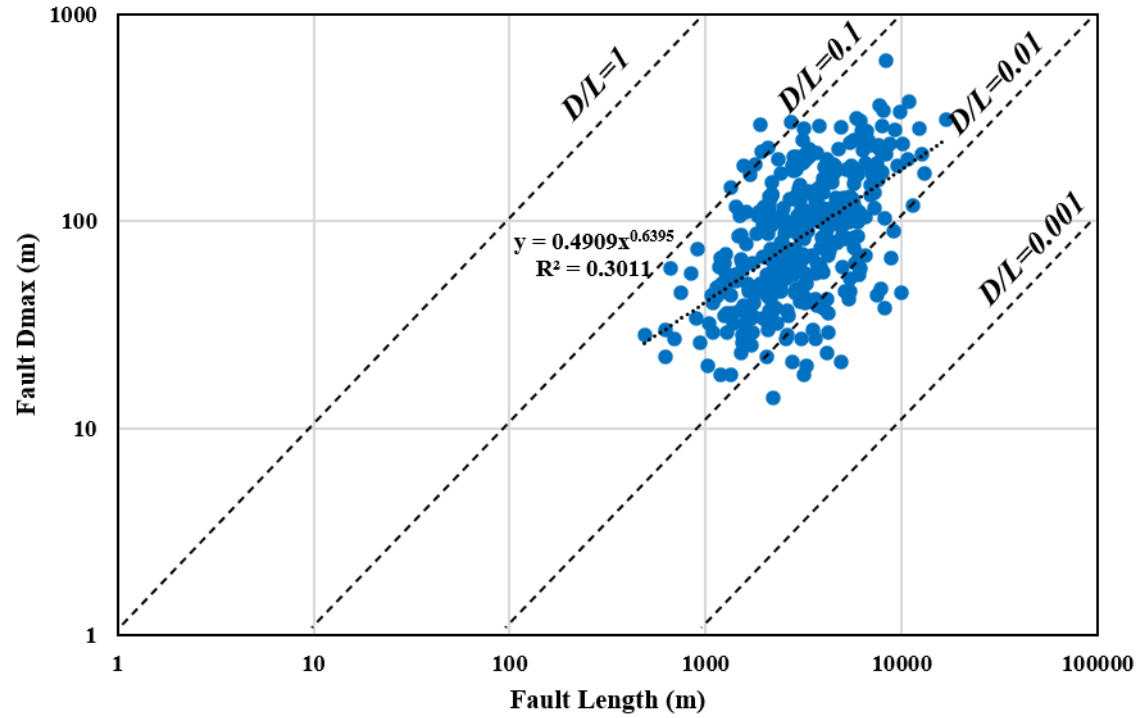


Figure 4.4 Log–log plot of maximum displacement (Dmax) versus fault length (*L*) for 350 faults in Zone 1 (NAD). Dashed lines represent constant displacement–length ratios (D/L = 1, 0.1, 0.01 and 0.001). The fitted power-law regression is Dmax = 0.4909L^0.6395 (R^2 = 0.3011, $p < 0.001$).

4.3.1.3 Fault Maximum Displacement (Dmax)

The maximum displacement (D_{max}) of a fault represents the maximum apparent displacement measured between paired top and bottom cut-off points across the fault scarp using the three-dimensional separation described in Chapter 3. Apparent Dmax was calculated for all 350 faults identified in Zone 1 using the mapped surface geometry, as described in Chapter 3. The Dmax values ranged from 14 to 593 m, with a mean value of 106 m (Table 4.2).

As illustrated by the frequency distribution of D_{max} (Figure 4.5), most faults in this dataset have relatively low D_{max} values. Approximately 45% of the faults have D_{max} values of 0–100 m, and a further ~30% have D_{max} values of 100–200 m, while fewer than 10% have Dmax values greater than 200 m.

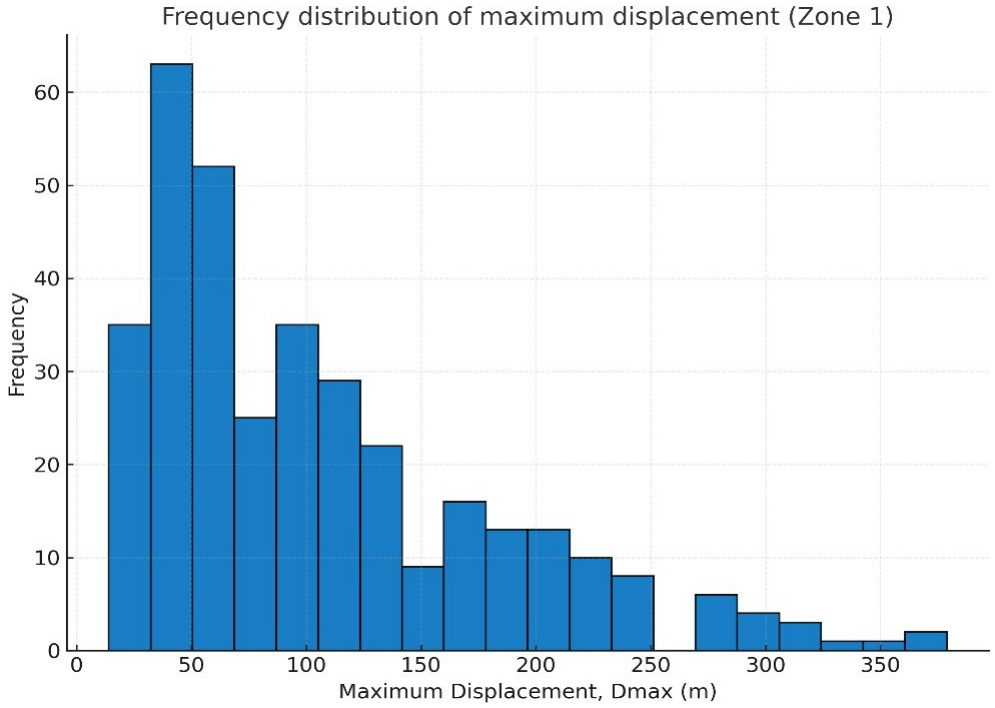


Figure 4.5: Frequency distribution of the maximum displacement (D_{max}) for 350 mapped faults in Zone 1 (NAD). The histogram shows that the dataset is strongly skewed towards small displacements, with most values below 200 m and relatively few faults exceeding this range.

The cumulative frequency plot of Dmax on log–log axes (Figure 4.4) depict the general trend of the displacement distribution as well as the relative proportions of faults with varying displacement magnitudes. At lower displacements, the slope of the curve is steep, whereas at higher displacements, the slope becomes less steep, reflecting the inherent statistical properties of fault populations and the tendency for fault populations to be skewed towards lower displacement magnitudes in Zone 1, similar to other normal-fault datasets.

4.3.2 Fault displacement profiles

Fault displacement profiles provide a quantitative description of how displacement varies along with the strike and are widely used to characterise fault geometry. In Zone 1, faults were grouped into three descriptive classes based on the number of peaks observed in their displacement–length (D–L) curves: (i) smooth profiles, defined by a single peak with a bell-shaped distribution and one maximum near the centre of the profile; (ii) multi-peak profiles, defined by two or three distinct maxima separated by intervening minima along the trace; and (iii) irregularly peaked profiles, defined by more than three distinct maxima with variable spacing and amplitude.

4.3.2.1 Single-peak profiles

Zone 1 contained 35 faults classified as smooth single-peak profiles, comprising ~10% of the fault population analysed for displacement profiles (n = 350). These faults exhibited continuous traces and did not show clear subdivisions into segments. Single-peak profiles are characterised by displacement increasing from the fault tips towards a single maximum (Dmax) before decreasing towards the opposite tip. Representative examples are faults F050 and F049, whose locations and displacement profiles are shown in Figure 4.6.

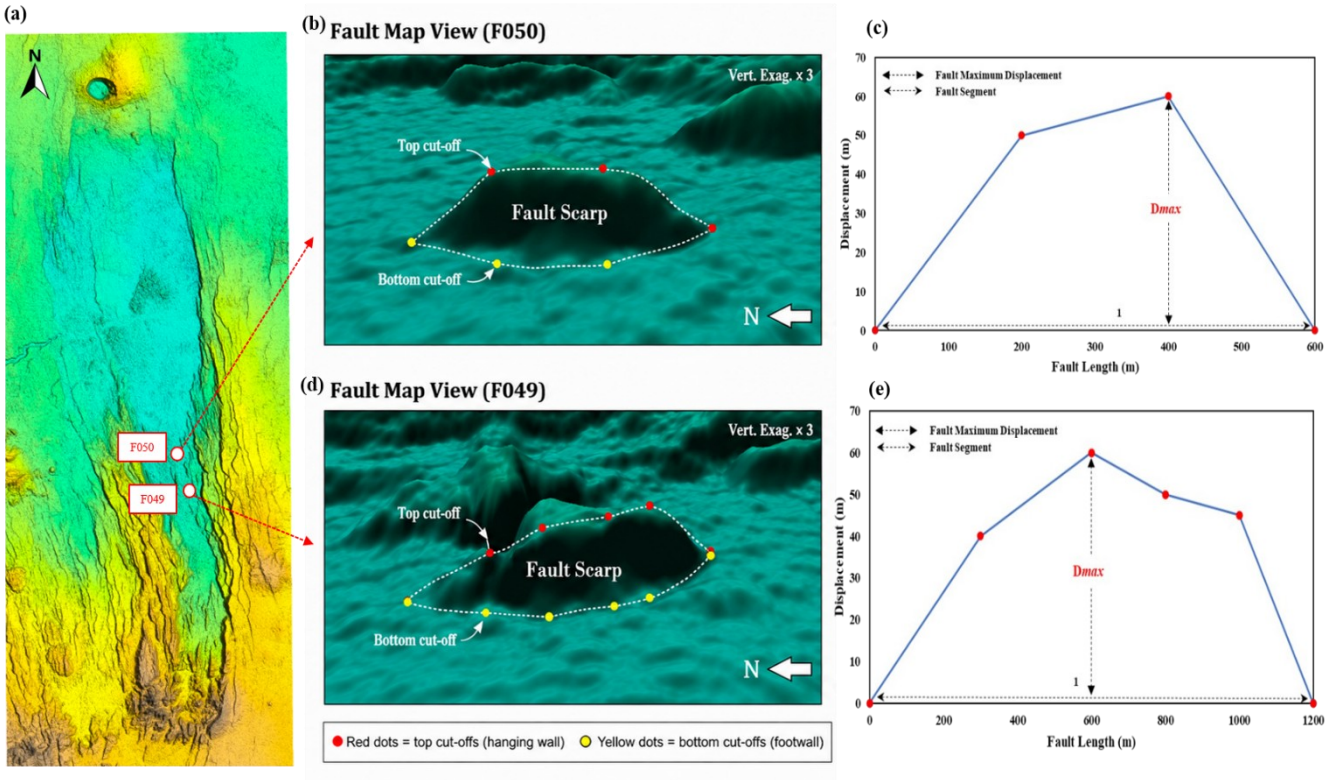


Figure 4.6: Location and displacement characteristics of representative single-peak faults F050 and F049 in Zone 1 of the North Afar Depression (NAD). (a) DEM showing the locations of faults F050 and F049 within Zone 1. (b) 3D DEM view of fault F050 showing the mapped top

and bottom cut-offs across the fault scarp. (c) Along-strike displacement–length (D–L) profile of F050, showing displacement increasing towards a single maximum displacement (Dmax) before decreasing towards the opposite fault tip. (d) 3D DEM view of fault F049 showing the mapped top and bottom cut-offs across the fault scarp. (e) Along-strike displacement–length (D–L) profile of F049, similarly showing a single displacement maximum. Red and yellow points in the 3D DEM views represent the mapped top and bottom cut-offs, respectively.

Across the 35 single-peak faults, fault lengths ranged from 487 to 3,371 m (mean 1,589 m), whereas maximum displacement (Dmax) ranged from 18 to 205 m (mean 65 m) (Table 4.3).

Parameter of Single Peak	Min. (m)	Max. (m)	Mean (m)
Fault Length (*L*)	487	3,371	1,589
Maximum Displacement (D_{max})	18	205	65

Table 4.3: Statistical summary of smooth single-peak faults in Zone 1 (NAD, n = 35). The values show the minimum, maximum and mean fault lengths (L) and maximum displacements (Dmax).

The displacement–length (D–L) scaling relationship for the single-peak fault population is shown in Figure 4.7. Power-law regression of the 35 single-peak faults yields Dmax = 0.1344L^0.8219, with $R^2 = 0.3869$. The positive scaling exponent (n = 0.8219) indicates that Dmax generally increases with increasing fault length, although the moderate R^2 indicates considerable scatter within the relationship. This positive scaling relationship is statistically significant ($p < 0.001$). Multi-peak and irregularly peaked faults are shown in grey for comparison.

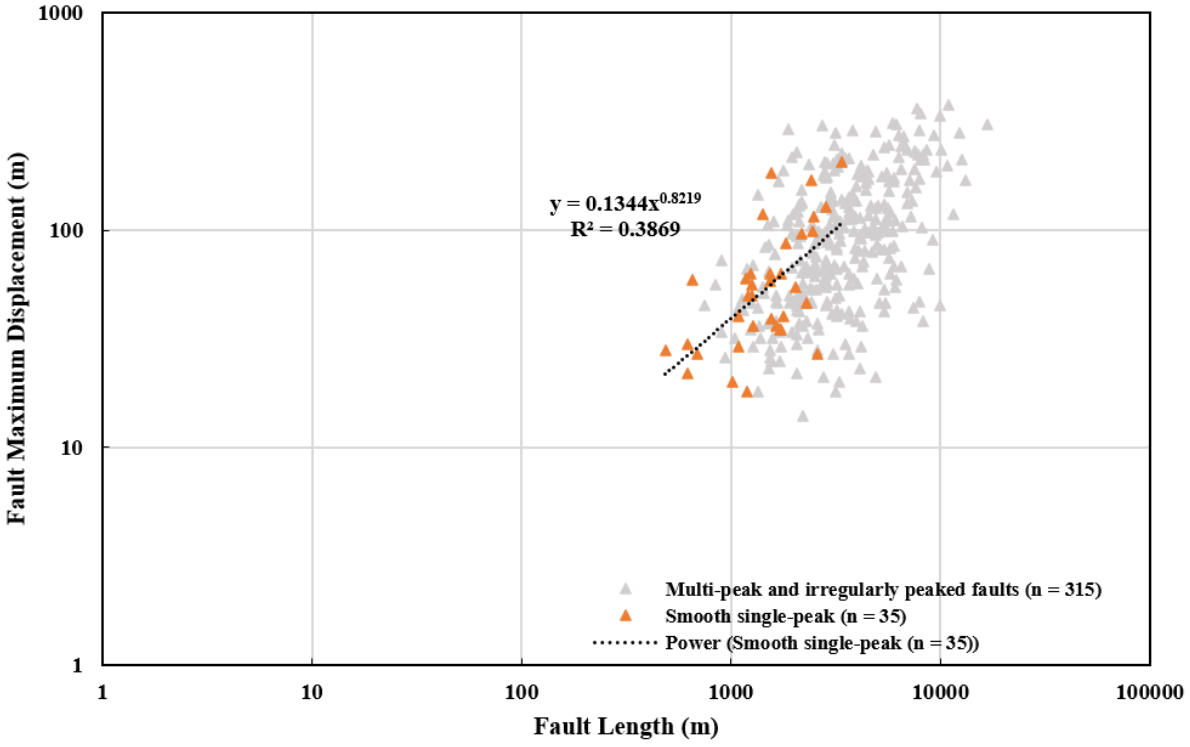


Figure 4.7: Log–log plot of maximum displacement (Dmax) versus fault length (L) for faults in Zone 1 (NAD). Smooth single-peak faults are shown by orange triangles (n = 35), with the power-law regression Dmax = 0.1344L^0.8219 (R^2 = 0.3869; $p < 0.001$). Multi-peak and irregularly peaked faults are shown by grey triangles (n = 315) for comparison.

4.3.2.2 Multi-peak profiles

A total of 71 faults were classified as having multi-peak profiles, representing approximately 20% of the fault population analysed for displacement profiles in Zone 1 (n = 350). These faults were identified from displacement–length (D–L) profiles containing two or three displacement maxima separated by intervening minima. In some profiles, neighbouring maxima form a broad zone of relatively high displacement, whereas in others the individual maxima remain clearly separated by displacement minima.

Representative examples are faults F011 and F094 (Figure 4.8). Fault F011 is approximately 2,300 m long, with a maximum displacement (Dmax) of 45 m, and its displacement profile contains three maxima separated by intervening minima. Fault F094 is approximately 3,300 m long, with a Dmax of 83 m, and similarly displays multiple clearly defined displacement maxima. In both examples, displacement generally decreases towards the fault tips, while the internal maxima and minima produce the characteristic multi-peak profile geometry.

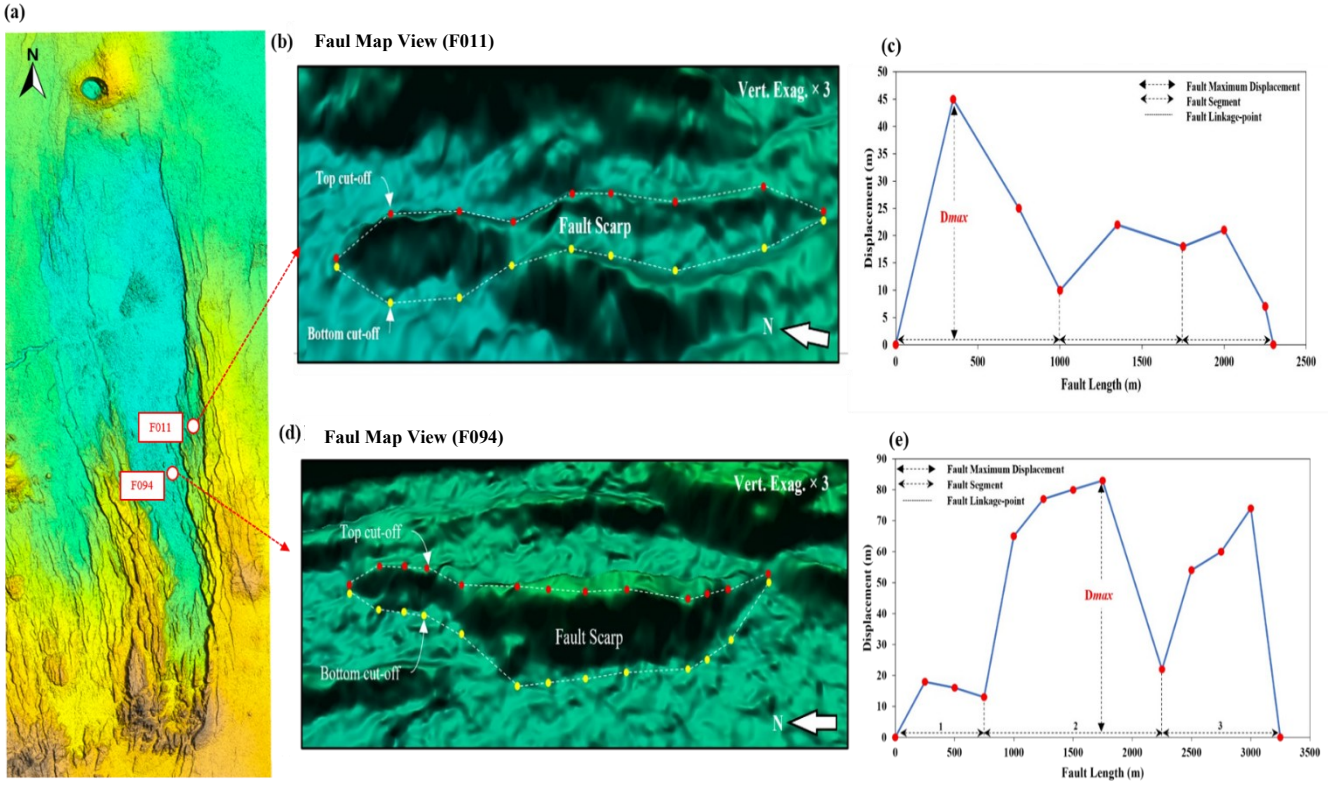


Figure 4.8: Location and displacement characteristics of representative multi-peak faults F011 and F094 in Zone 1 of the North Afar Depression (NAD). **(a)** DEM showing the locations of faults F011 and F094 within Zone 1. **(b)** Three-dimensional DEM view of fault F011 showing the

mapped top and bottom cut-offs across the fault scarp. **(c)** Along-strike displacement–length (D–L) profile of F011, showing multiple displacement maxima separated by intervening minima. **(d)** Three-dimensional DEM view of fault F094 showing the mapped top and bottom cut-offs across the fault scarp. **(e)** Along-strike displacement–length (D–L) profile of F094, similarly showing multiple displacement maxima separated by intervening minima. Red and yellow points represent the mapped top and bottom cut-offs, respectively.

Across the 71 multi-peak faults, fault lengths ranged from 845 to 5,674 m, with a mean of 2,344 m. Maximum displacement (Dmax) ranged from 18 to 288 m, with a mean of 86 m (Table 4.4).

Parameter of multi-peak	Min. (m)	Max. (m)	Mean (m)
Fault Length (*L*)	845	5,674	2,344
Maximum Displacement (D_{max})	18	288	86

Table 4.4: Statistical summary of multi-peak profiles in Zone 1 (NAD, n = 71). Values show the minimum, maximum, and mean fault length (L) and maximum displacement (Dmax).

The displacement–length (D–L) scaling relationship for the multi-peak fault population is shown in Figure 4.9. Multi-peak faults (blue triangles) predominantly occupy the intermediate part of the Zone 1 D–L population, although their length and displacement ranges overlap with those of the smooth single-peak and irregularly peaked faults (grey triangles). Power-law regression of the 71 multi-peak faults yields Dmax = 0.0284L^1.0088, with $R^2 = 0.3823$. The positive scaling exponent (n = 1.0088) indicates that Dmax generally increases with increasing fault length, although the moderate R^2 value indicates considerable scatter within the relationship. The relationship is statistically significant ($p < 0.001$).

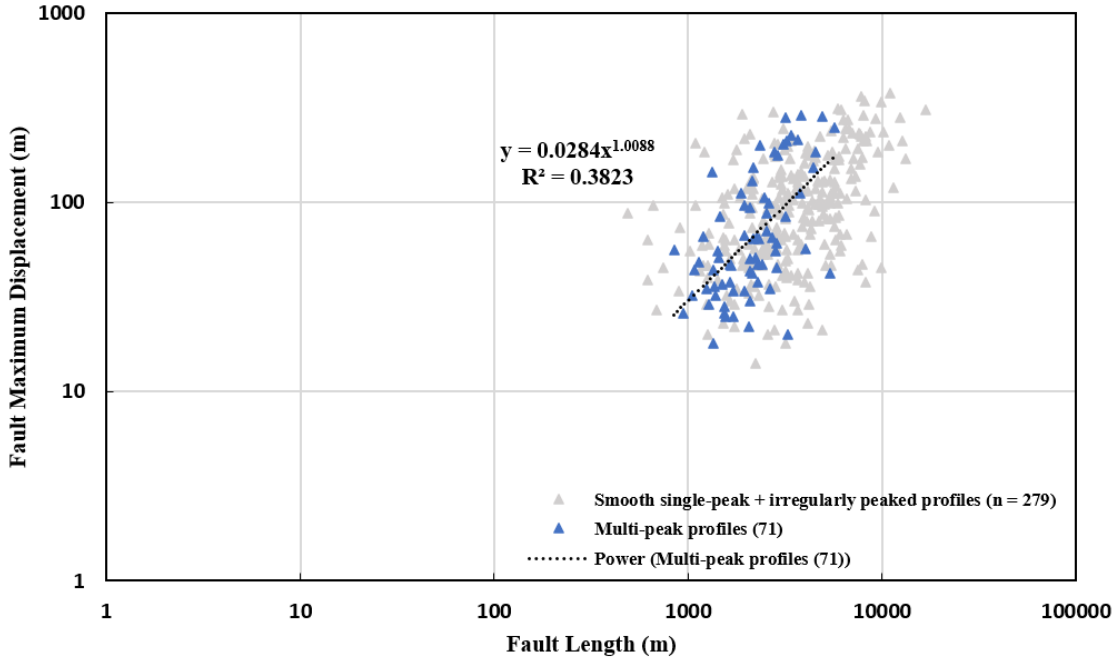


Figure 4.9: Log–log plot of maximum displacement (Dmax) versus fault length (L) for faults in Zone 1 (NAD). Multi-peak faults are shown by blue triangles (n = 71), with the power-law regression Dmax = 0.0284L^1.0088 (R^2 = 0.3823; p < 0.001). Smooth single-peak and irregularly peaked faults are shown by grey triangles (n = 279) for comparison.

4.3.2.3 Irregular-peak profiles

A total of 244 faults were classified as having irregularly peaked profiles, representing approximately 70% of the fault population analysed for displacement profiles in Zone 1 (n = 350). These faults were identified from displacement–length (D–L) profiles containing more than three distinct displacement maxima separated by intervening minima**.** No fixed displacement threshold was applied to identify individual maxima or minima; rather, classification was based on the number and distribution of distinct peaks and intervening minima observed along each mapped displacement profile. The repeated maxima and minima produce more complex along-strike displacement patterns than those observed for the smooth single-peak and multi-peak populations.

Representative examples are faults F108 and F076 (Figure 4.10). Both faults display multiple displacement maxima and intervening minima along their traces. In each case, displacement generally decreases towards the fault tips, whereas the internal parts of the fault contain repeated peaks and troughs. These examples illustrate the irregularly peaked profiles characteristic of this population.

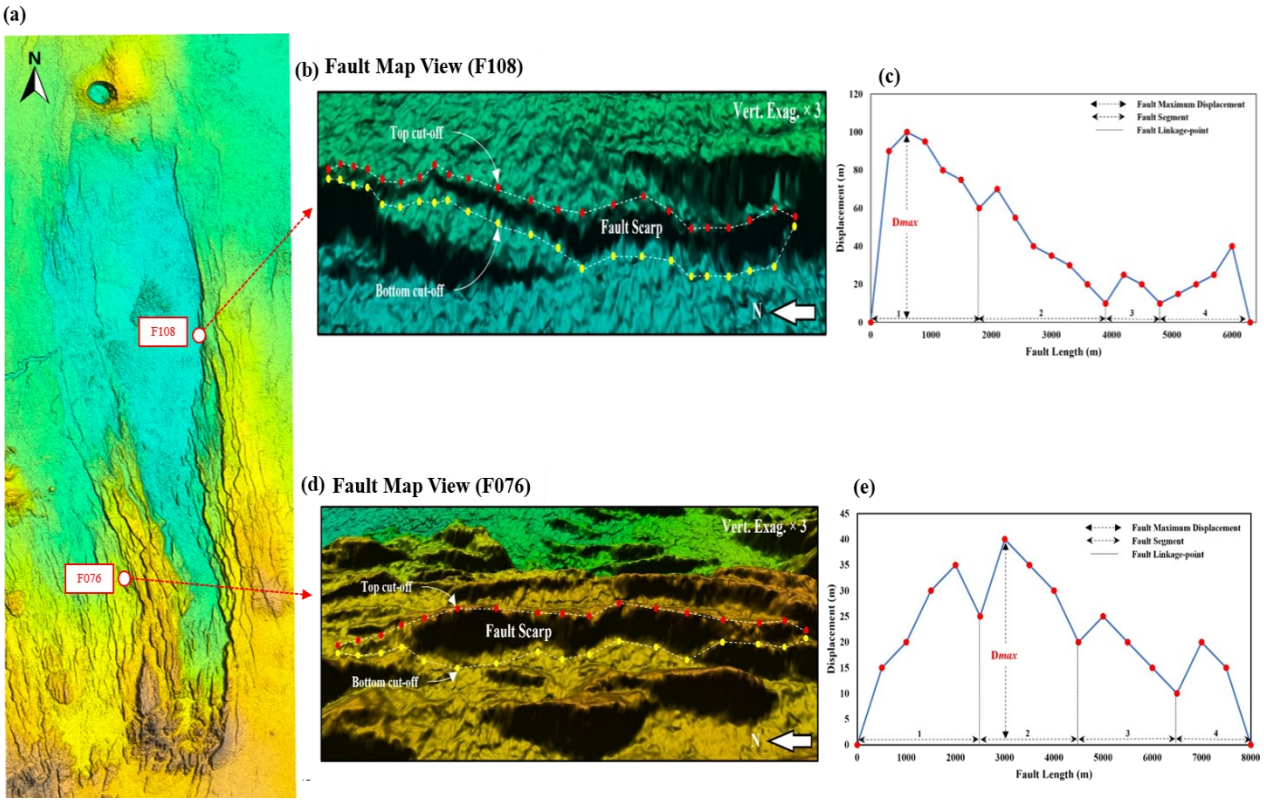


Figure 4.10: Location and displacement characteristics of representative irregularly peaked faults F108 and F076 in Zone 1 of the North Afar Depression (NAD). **(a)** DEM showing the locations

of faults F108 and F076 within Zone 1. **(b)** Three-dimensional DEM view of fault F108 showing the mapped top and bottom cut-offs along the fault scarp. **(c)** Along-strike displacement–length (D–L) profile of F108, showing more than three displacement maxima separated by intervening minima. **(d)** Three-dimensional DEM view of fault F076 showing the mapped top and bottom cut-offs along the fault scarp. **(e)** Along-strike displacement–length (D–L) profile of F076, similarly showing multiple displacement maxima and intervening minima characteristic of an irregularly peaked profile. Red and yellow points represent the mapped top and bottom cut-offs, respectively.

Across the 244 irregularly peaked faults, fault lengths ranged from 748 to 16,859 m, with a mean of 4,430 m. Maximum displacement (Dmax) ranged from 14 to 593 m, with a mean of 119 m (Table 4.5).

Parameter of Irregular	Min. (m)	Max. (m)	Mean (m)
Fault Length (*L*)	748	16,859	4,430
Maximum Displacement (D_{max})	14	593	119

Table 4.5: Statistical summary of irregularly peaked faults in Zone 1 (NAD, n = 244). Values show the minimum, maximum and mean fault length (*L*) and maximum displacement (Dmax**).**

The displacement–length (D–L) scaling relationship for the irregularly peaked fault population is shown in Figure 4.11. Irregularly peaked faults occupy a relatively broad range of the Zone 1 D–L population, extending to greater fault lengths and maximum displacements than many of the smooth single-peak and multi-peak faults. Most irregularly peaked faults have lengths of approximately 2,000–8,000 m and Dmax values of approximately 50–200 m, although considerable scatter is present. Overall, the data shows a positive relationship between fault length and maximum displacement.

Power-law regression of the irregularly peaked fault population yields Dmax = 1.0712*L*^0.5443 (R^2 = 0.1959; p < 0.001). The positive scaling exponent (*n* = 0.5443) indicates that maximum displacement generally increases with increasing fault length. However, the relatively low R^2 value indicates considerable scatter within the relationship. Despite this scatter, the positive D–L relationship is statistically significant ($p < 0.001$).

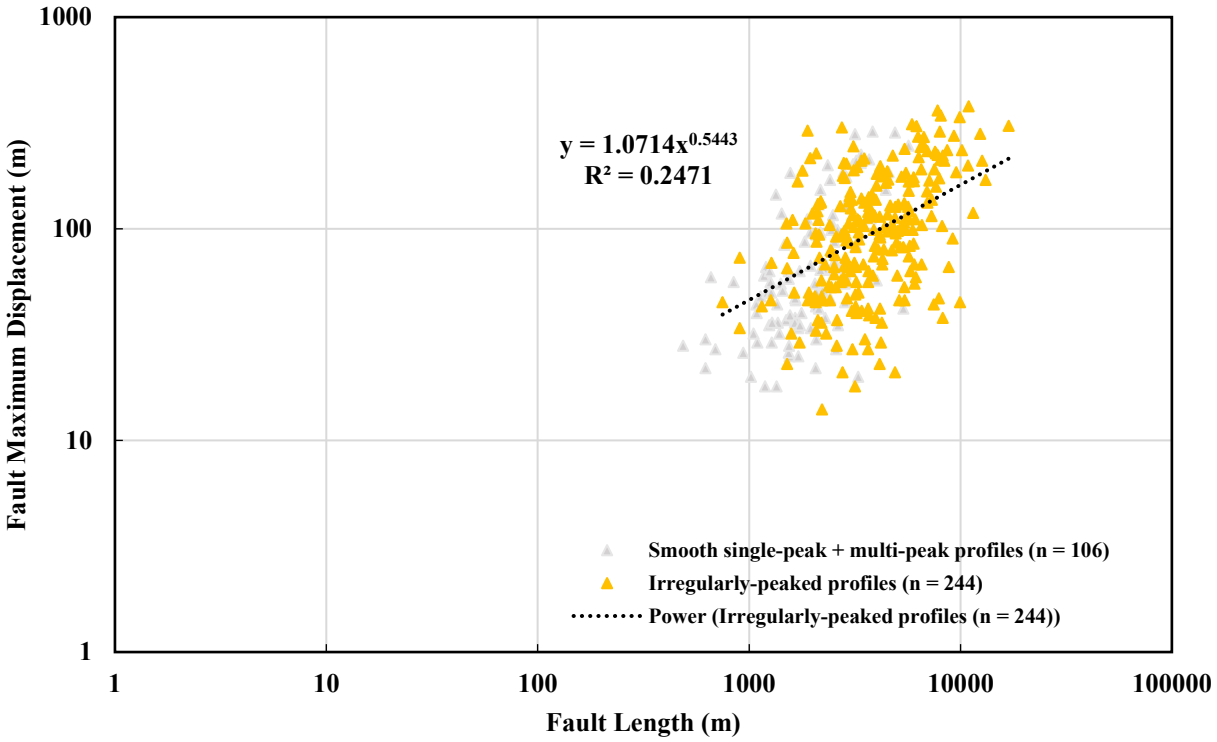


Figure 4.11: Log–log plot of maximum displacement (Dmax) versus fault length (*L*) for faults in Zone 1 (NAD). Irregularly peaked faults (orange triangles, n = 244) are compared with smooth single-peak and multi-peak faults (grey triangles, n = 106). The power-law regression for the irregularly peaked population is Dmax = 1.0712*L*^0.5443 (R^2 = 0.1959; $p < 0.001$).

4.3.3 Fault linkage analysis

Fault linkage is critical in the structural development of rift-related fault systems because it controls fault geometry, connectivity, and the organisation of strain within the rift (Peacock and Sanderson, 1991; Walsh et al., 2003). In extensional settings, faults rarely initiate as long, continuous structures. Instead, they begin as discrete segments that propagate, overlap and interact. With progressive displacement, some segments connect and begin to transfer displacement between each other (Childs et al., 1995). These interactions redistribute the extensional strain, modify the propagation pathways, and progressively determine which structures accommodate most of the slip within the network (Cartwright et al., 1995).

In Zone 1, the linkage between neighbouring segments was classified into two observational categories based on surface geomorphology: soft linkage (SL) and hard linkage (HL). Soft linkage refers to overlapping or en echelon segments separated by a relay zone or gap, where displacement is transferred across the relay, but the segments do not form a single throughgoing scarp at the surface. Hard linkage refers to locations where the tips of adjacent segments breach the intervening relay and form a continuous surface

trace that behaves as a single longer fault. In this study, these categories were used as indicators of immature (soft) versus more mature (hard) stages of linkage.

Each mapped fault was assigned a linkage state to provide a quantitative record of the linkage maturity across the network. Of the 350 mapped faults, 190 (~54%) were soft-linked, 96 (~27%) were hard-linked, and the remaining 64 (~19%) showed no clear surface interaction with neighbouring segments and were classified as non-linked.

These proportions are based on the surface morphology in the 30 m DEM and therefore represent only the surface expression of connectivity. Some structures identified as soft-linked may already be hard-linked at shallow depths below the DEM resolution, and some non-linked segments may interact structurally at depth. Therefore, the values reported here should be considered as minimum estimates of the linkage maturity at the surface.

4.3.3.1 Soft Linked (SL)

In Zone 1, 190 fault segments (approximately 54% of the analysed fault population, n = 350) exhibited soft-linkage characteristics. Soft linkage was identified where adjacent fault segments overlap or are arranged en echelon but remain physically separated at the surface by an intervening relay zone. These geometries indicate interaction between neighbouring fault segments without the development of a continuous throughgoing fault scarp.

Soft-linked fault zones are distributed across the study area but are most frequent in the southern sector, where fault density is highest, and are less common in the central and northern sectors, where faults are more widely spaced. Mapped examples occur at different scales, from relay zones between two overlapping fault segments to larger en echelon arrays involving several segments.

Figure 4.12 presents a representative example of soft linkage in Zone 1. The two overlapping fault segments (Faults 1 and 2) remain physically separated by an intervening relay zone. The mapped top and bottom cut-offs define the surface expression of each fault scarp. The associated along-strike displacement profiles show variations in displacement along the interacting fault segments and provide additional evidence for their segmented geometry.

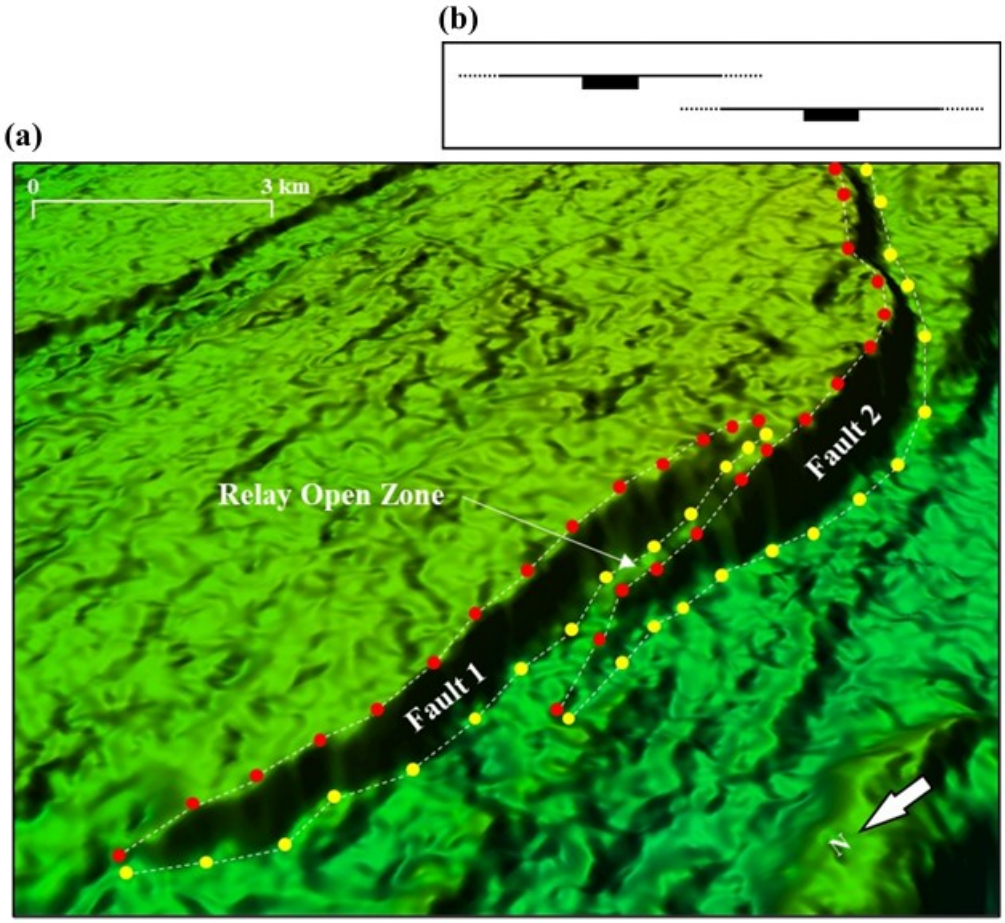


Figure 4.12: Example of soft linkage between overlapping normal-fault segments in Zone 1 (NAD). **(a)** Three-dimensional DEM view showing Faults 1 and 2 separated by an intervening relay zone. Red and yellow points indicate the mapped top and bottom cut-offs, respectively. (b–c) Along-strike displacement–length (D–L) profiles of Faults 1 and 2, showing displacement variations along the interacting fault segments. **(d)** Schematic representation of the soft-linkage geometry.

4.3.3.2 Hard Linked (HL)

Hard-linked faults accounted for approximately 27% of the fault population analysed in Zone 1 (96 of 350 faults). Hard linkage was identified where previously separate fault segments are physically connected at the surface across a breached relay zone, forming a continuous fault trace. Hard-linked faults are therefore less abundant than the soft-linked population within Zone 1.

The principal characteristic of hard linkage is the structural continuity produced by the breaching of an intervening relay zone. Previously separate fault segments become physically connected to form a longer composite fault. Despite this connection, the resulting fault may retain geometric evidence of its former segmentation, including changes in fault orientation and irregularities around the linkage zone.

Figure 4.13 shows a representative example of hard linkage in Zone 1. The 3D DEM illustrates two fault segments that are physically connected across a breached relay ramp, producing a continuous surface fault trace. The mapped top and bottom cut-offs delineate the fault scarp and show the geometry of the linkage zone. The schematic in Figure 4.13b illustrates the geometric configuration of the linked segments and is not a displacement–length (D–L) profile.

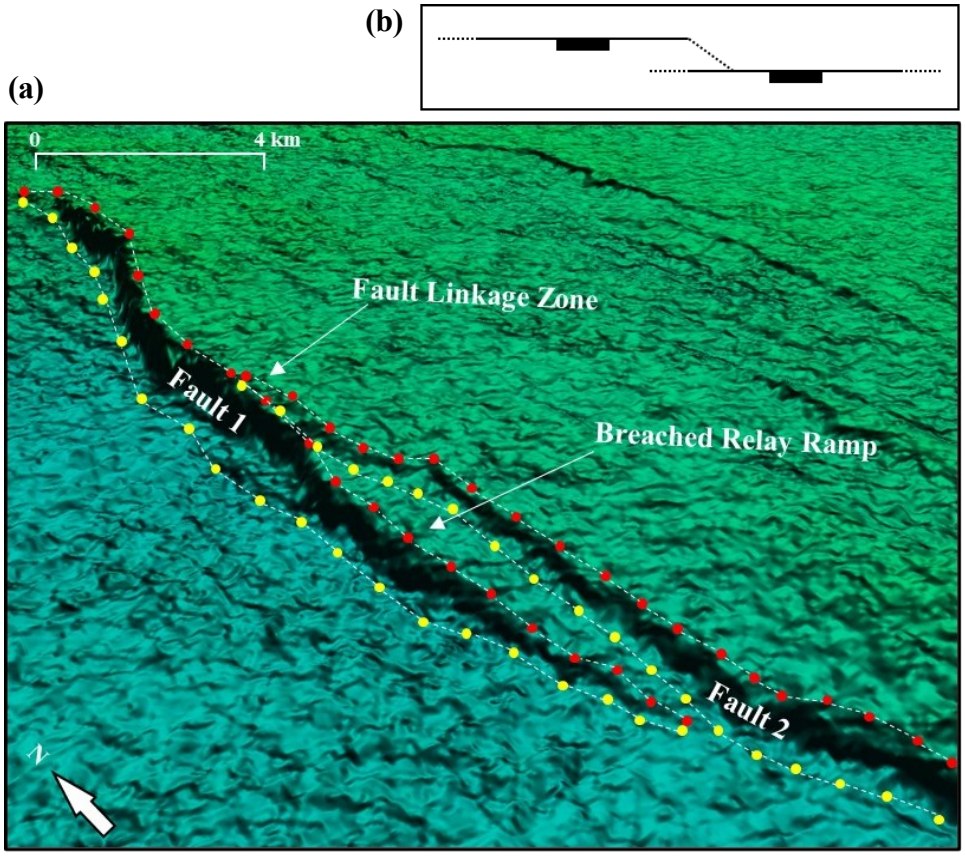


Figure 4.13: shows a representative example of hard linkage in Zone 1. The 3D DEM illustrates two fault segments that are physically connected across a breached relay ramp, producing a continuous surface fault trace. The mapped top and bottom cut-offs delineate the fault scarp and show the geometry of the linkage zone. The schematic in Figure 4.13b illustrates the geometric configuration of the linked segments and is not a displacement–length (D–L) profile.

To examine the effect of hard linkage on fault displacement–length scaling, an additional D–L analysis was undertaken in which the total length of each hard-linked fault was used rather than the lengths of the individual constituent segments (Figure 4.14). For comparison, non-hard-linked faults, comprising the non-linked (NL) and soft-linked (SL) populations, are also shown. This allows the position of hard-linked composite faults within the overall Zone 1 D–L population to be evaluated after accounting for their total linked length.

When plotted using their total linked lengths, hard-linked faults generally occupy the longer-length part of the Zone 1 D–L population. The hard-linked population shows a positive relationship between total fault length and maximum displacement, described by the power-law regression D*max* = 2.2351L^0.4478 (R^2 = 0.138). The positive scaling exponent (*n* = 0.4478) indicates that maximum displacement generally increases with

increasing total linked fault length. However, the relatively low R^2 value indicates considerable scatter in Dmax among hard-linked faults of similar total length.

The distribution of hard-linked faults towards the longer-length part of D–L space is consistent with the physical connection of previously separate fault segments to form longer composite structures. However, the relatively low R^2 value indicates that greater total linked length is not associated with a proportionate or uniform increase in D*max*. This suggests that linkage contributes to variability in the D–L scaling relationship, because the development of a longer composite fault does not necessarily result in an equivalent increase in maximum displacement.

Fault linkage may also influence the form of a long-strike displacement profile. Individual fault segments may initially possess separate displacement maxima. Following interaction and physical linkage, these segments form a longer composite structure, while the displacement distribution may retain multiple maxima and intervening minima associated with the constituent segments. Therefore, hard linkage can be associated with longer composite fault traces and more complex displacement profiles rather than a single smooth displacement maximum.

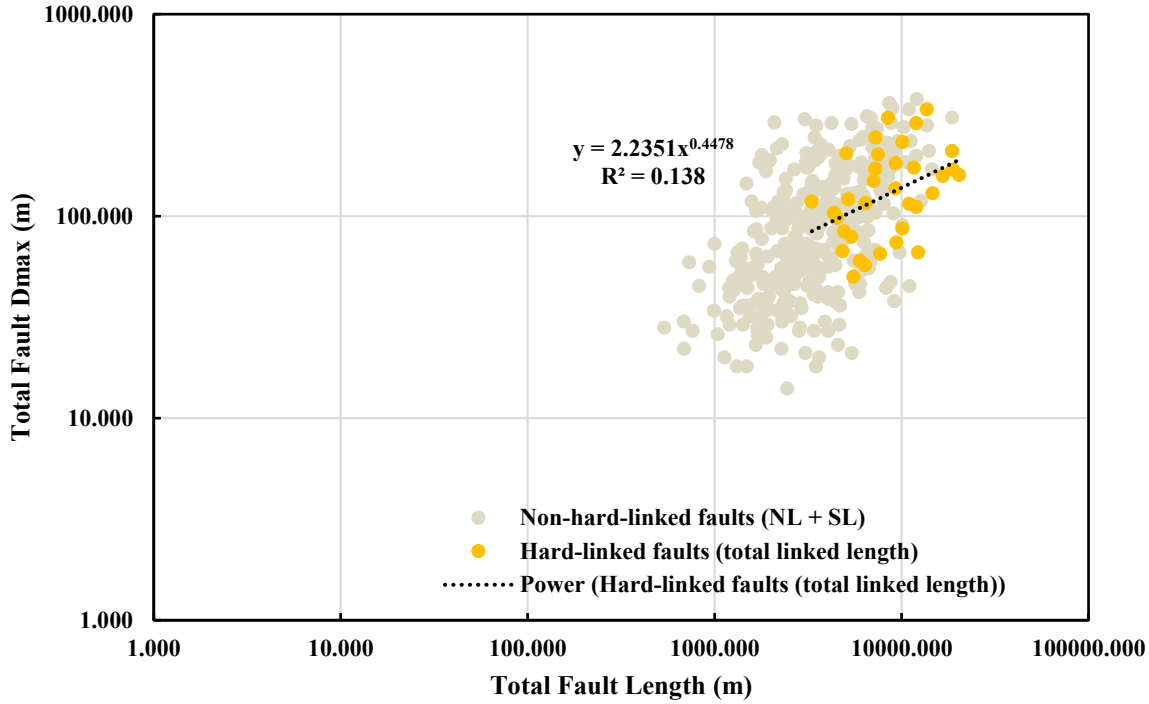


Figure 4.14: Log–log plot of maximum displacement (Dmax) versus fault length (L) for hard-linked and non-hard-linked faults in Zone 1 (NAD). Hard-linked faults are plotted using the total length of the linked fault structure, rather than the lengths of the individual constituent segments. Non-hard-linked faults comprise the non-linked (NL) and soft-linked (SL) populations. The power-law regression for the hard-linked population is Dmax = 2.2351L^0.4478 (R^2 = 0.138).

4.3.4 Minimum strain analysis of NAD (Zone 1)

Measuring strain accommodation during rifting is essential for understanding how deformation is distributed between faults and how they grow and interact (Peacock and Sanderson, 1991). Therefore, establishing spatial variations in strain is important for evaluating fault behaviour along the rift axis in the North Afar Depression. In Zone 1, strain was calculated from eight systematically located cross-sections (profiles A–A′ to H–H′) using elongation, $e = (L_1 - L_0)/L_0$, where L_0 is the undeformed baseline length and L1 is the current extended length. Cumulative heaves were used only to check the extent ofeach section, and not as the primary strain measure. These data allow the evaluation of fault density (number of faults per unit area), total offset, and spatial arrangement of fault segments that contribute to extensional strain across the rift. All values represent minimum estimates because surface-based measurements can underestimate the true strain owing to the DEM resolution and the burial or resurfacing of volcanic and sedimentary deposits.

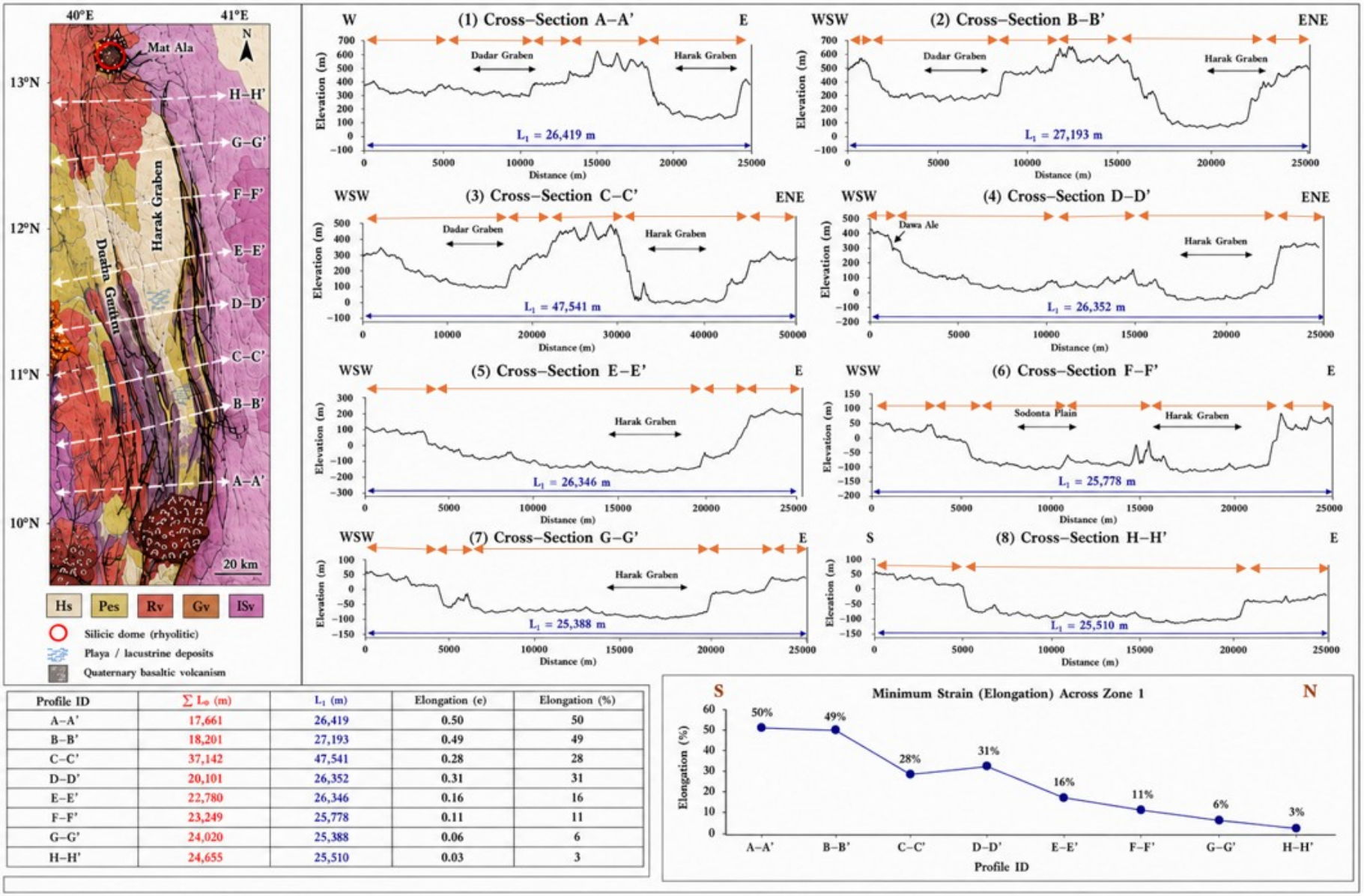
4.3.4.1 Cross-section Profiles

Eight cross-sections (A–A′ to H–H′) were constructed across Zone 1 to examine along-strike variations in rift geometry and to provide the geometric basis for calculating minimum apparent extensional strain (Figure 4.15). The profiles extend across the principal faulted zone and were oriented approximately perpendicular to the local fault strike, following the procedure described in Chapter 3. Where fault strike varies, the profile orientations were adjusted to remain approximately orthogonal to the mapped fault traces. The locations of the eight cross-sections are shown on the geological map in Figure 4.15.

The cross-sections illustrate the principal fault-controlled topographic features intercepted by each profile, including the Dadar and Harak grabens and their major fault-bounded escarpments. Several profiles show asymmetric graben geometries. In particular, parts of the Harak Graben are characterised by a pronounced topographic step across a major bounding fault and a comparatively subdued opposing margin, producing an effective half-graben geometry at the surface. However, the ASTER DEM records only surface elevation and therefore does not constrain the depth to the base of the sedimentary fill within the hanging wall. As no subsurface geophysical or borehole data were used in this analysis, the thickness of the sedimentary fill and the subsurface geometry of the bounding faults cannot be determined from these data.

For each profile, the present-day cross-profile length (L_1) and the reconstructed pre-extension surface segments (L_0) used in the elongation calculation are shown in Figure 4.15. The individual L_0 segments represent reconstructed surface lengths separated at the major fault offsets identified along each topographic profile, following the reconstruction method described in Chapter 3 and illustrated in Figure 3.9 and 3.10. Their summed length ($\sum L_0$) represents the reconstructed pre-extension surface length, whereas L_1 represents the present-day length of the complete cross-section. Displaying the L_0 segments and major fault-related breaks directly on the profiles distinguishes the reconstructed pre-extension surface segments from the present-day faulted topography and explicitly shows the measurements used to calculate minimum apparent elongation.

Because this reconstruction considers the measurable surface expression of major fault-related extension and does not account for unresolved small faults, fault dip at depth, distributed deformation, sediment thickness or buried structures, the calculated values are treated as minimum apparent extensional strain, rather than estimates of total crustal extension.



Profile ID	∑ L_0 (m)	L_1 (m)	Elongation (e)	Elongation (%)
A–A'	17,661	26,419	0.50	50
B–B'	18,201	27,193	0.49	49
C–C'	37,142	47,541	0.28	28
D–D'	20,101	26,352	0.31	31
E–E'	22,780	26,346	0.16	16
F–F'	23,249	25,778	0.11	11
G–G'	24,020	25,388	0.06	6
H–H'	24,655	25,510	0.03	3

Figure 4.15: Geological map and cross-sectional profiles used to calculate minimum apparent extensional strain across Zone 1 of the Northern Afar Depression. The map shows the locations of profiles A–A′ to H–H′, arranged from south to north. The cross-sections show the present-day surface topography and principal fault-controlled features intercepted by each profile. Reconstructed pre-extension surface segments (L_0) are separated at the major fault offsets identified along each profile, and their summed length ($\sum L_0$) represents the reconstructed pre-extension surface length. The present-day cross-profile length (L_1) is also shown for each profile. The accompanying plot summarises the resulting minimum apparent elongation values from south to north. Cross-sections were derived from ASTER GDEM Version 3; geological units are from the geological map of Rime et al. (2022), with tectonostratigraphic interpretation following Rime et al. (2023).

4.3.4.2 Analysis of Elongation (e)

Minimum apparent elongation was calculated for each of the eight cross-sections using the reconstruction described above in Chapter 3. The resulting elongation values and their spatial variation from south to north are presented in Figure 4.15.

The highest minimum apparent elongation values occur in the southern part of Zone 1, with A–A′ and B–B′ recording 50% and 49%, respectively. Farther north, C–C′ records 28%, followed by a small increase to 31% at D–D′. Elongation then decreases northwards to 16% at E–E′, 11% at F–F′, 6% at G–G′ and 3% at H–H′ (Figure 4.15).

Although the profile-to-profile variation is not strictly monotonic, particularly between C–C′ and D–D′, the overall pattern shows a pronounced decrease in minimum apparent elongation from south to north, from approximately 50% in the southern profiles to 3% at the northernmost profile. This demonstrates substantial along-strike variability in the minimum surface extension recorded by the mapped fault system across Zone 1.

4.3.5 Fault maturity and geological surface units

Fault maturity in Zone 1 was evaluated using fault length, maximum displacement (Dmax), and the displacement–length ratio (Dmax/L). The 350 faults for which these measurements were available were classified according to the geological surface units shown on the geological map (Figure 4.15). To maintain consistency between the geological map and the quantitative analysis, the unit identifiers used here follow those displayed on the map**:** Rv, Gv, Gv?, ISv, ISv?, Pes and Hs. Units labelled with a question mark represent areas where the geological attribution is uncertain on the source geological map.

Each fault was assigned to its mapped geological surface unit, producing 111 faults in Rv, 2 in Gv, 61 in Gv?, 22 in ISv, 97 in ISv?, 31 in Pes and 26 in Hs (Figure 4.16). The number of faults therefore varies substantially between the mapped geological units, with Rv and ISv? containing the largest fault populations and Gv containing the smallest.

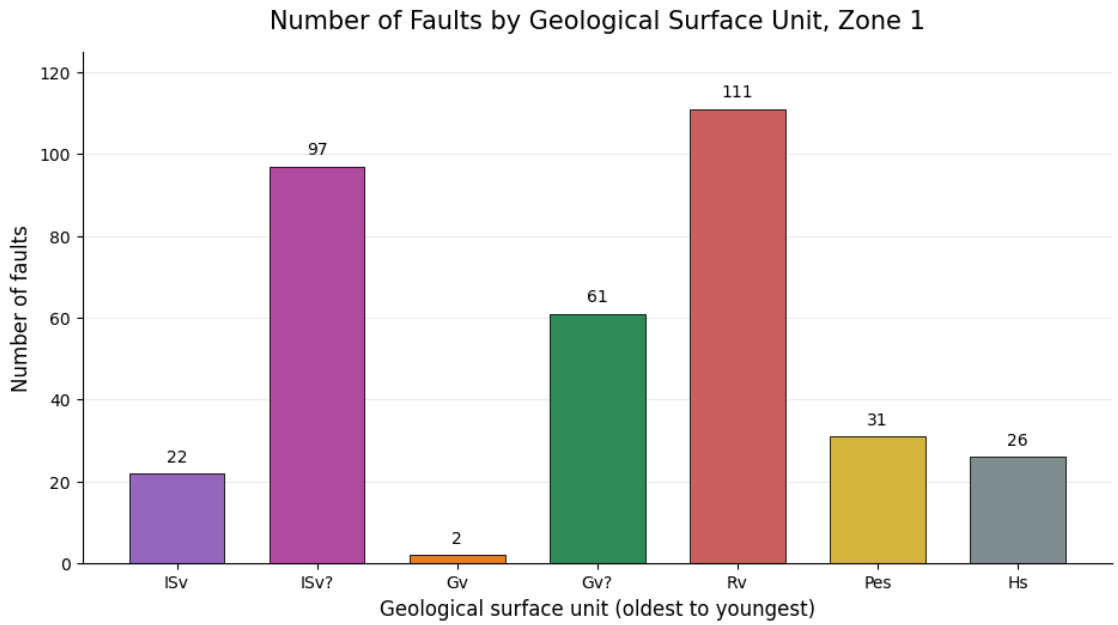


Figure 4.16: Number of faults classified within each mapped geological surface unit in Zone 1 (n = 350), arranged from older to younger surface units. Unit identifiers correspond to those shown on the geological map in Figure 4.15. Question marks indicate uncertain geological attribution on the source geological map.

The relationship between fault length (L) and maximum displacement (Dmax) is shown in Figure 4.17, with individual faults symbolised according to their mapped geological surface unit. The geological-unit populations show substantial overlap in Dmax–L space, although Dmax generally increases with increasing fault length. Rv, Gv?, ISv, ISv?, Pes and Hs span broad ranges of fault length and displacement, whereas Gv contains only two observations and should therefore be interpreted with caution.

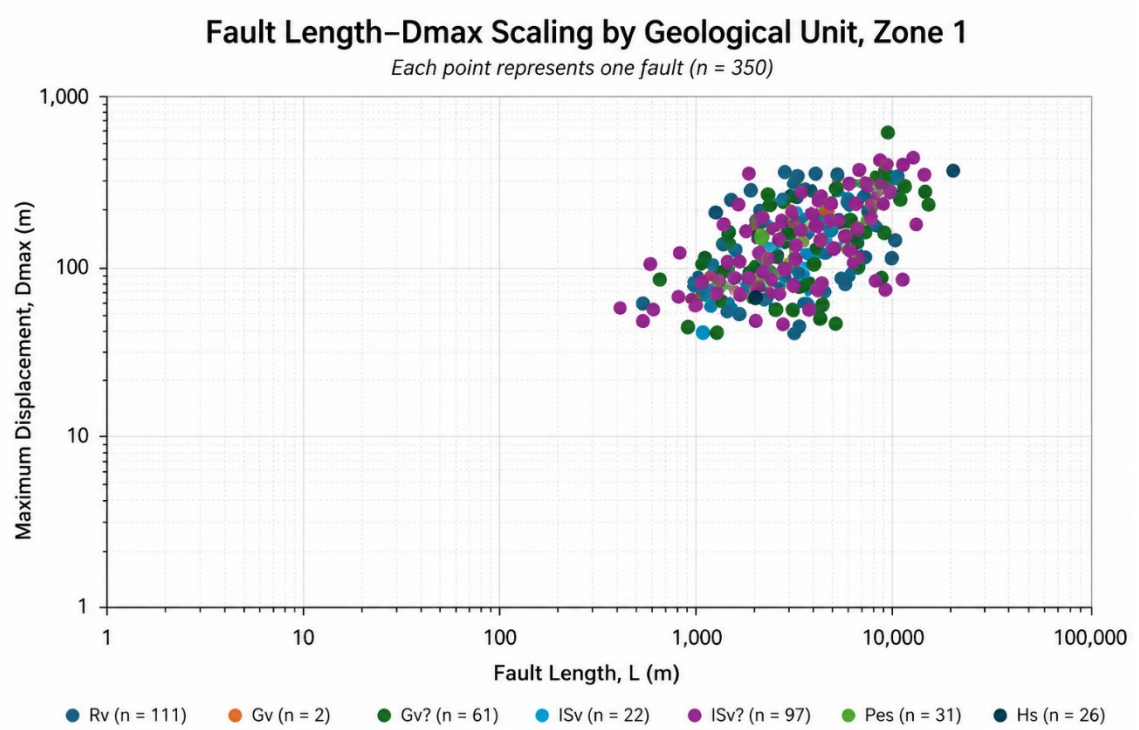


Figure 4.17: Log–log plot of maximum displacement (Dmax) versus fault length (L) for faults classified according to mapped geological surface unit in Zone 1 (n = 350). Each point represents

an individual fault and is coloured according to its mapped geological surface unit. Pes and Hs represent sedimentary units, whereas Rv, Gv, Gv?, ISv and ISv? represent volcanic units. The geological-unit populations show substantial overlap in Dmax–L space.

Maximum displacement (Dmax) also varies within and between the mapped geological surface units (Figure 4.18). The distributions show considerable overlap between units, although differences occur in their median values and overall spread. ISv has the lowest median Dmax, whereas the remaining units generally show higher median values and broader distributions. Gv contains only two faults and should therefore be interpreted with caution.

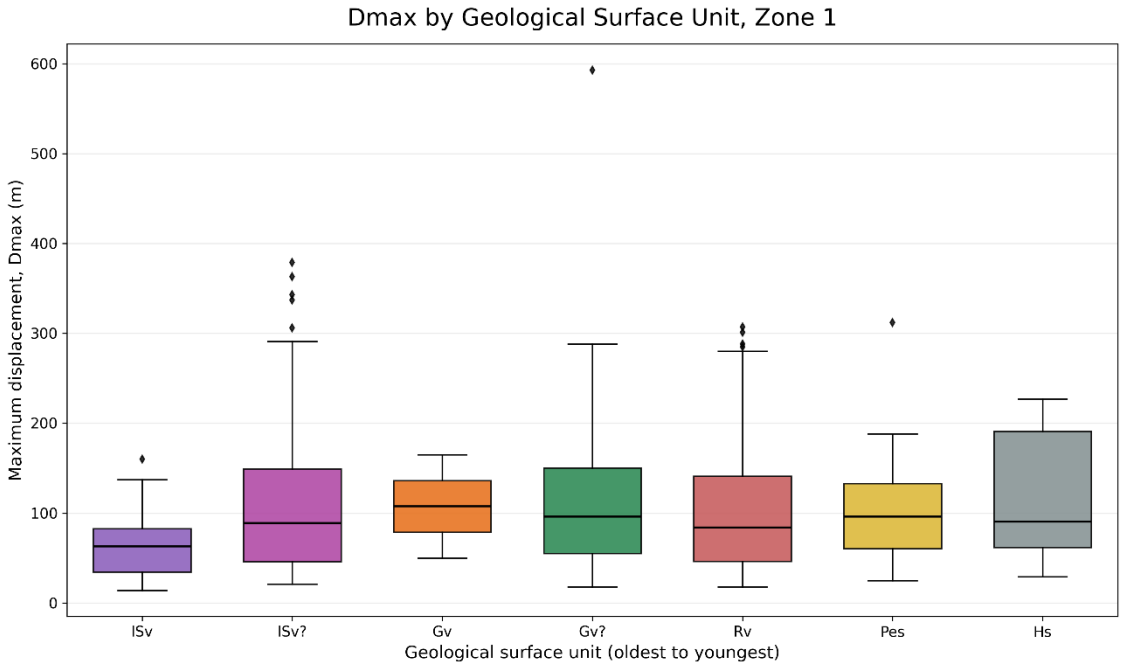


Figure 4.18: Boxplots of maximum displacement (Dmax) for faults classified according to mapped geological surface unit in Zone 1 (n = 350), arranged from older to younger surface units. Boxes represent the interquartile range (IQR), horizontal lines indicate median values, whiskers extend to 1.5 × IQR, and points beyond the whiskers represent outliers. Geological-unit identifiers correspond to those shown on the geological map in Figure 4.15. Question marks indicate uncertain geological attribution on the source geological map.

The Dmax/L distributions are shown in Figure 4.19. The values vary both within and between the mapped geological units, with differences in their median values, interquartile ranges and overall spread. Rv, Gv?, ISv, ISv?, Pes and Hs contain sufficient numbers of faults for comparison, whereas Gv contains only two faults and is therefore not suitable for meaningful statistical comparison.

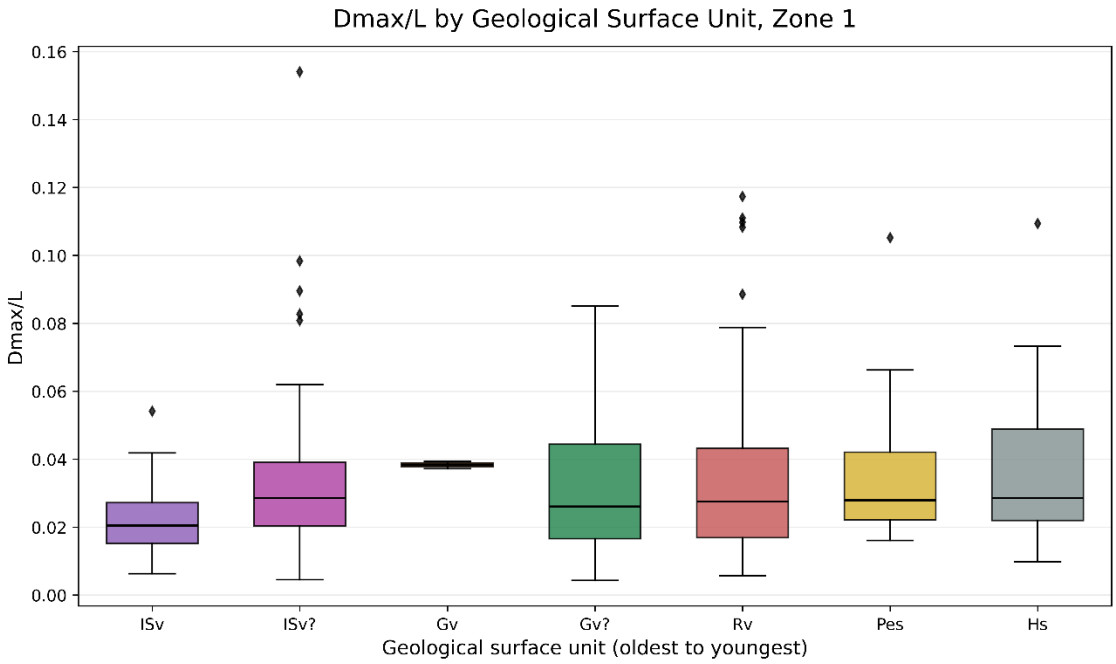


Figure 4.19: Boxplots of Dmax/L for faults classified according to mapped geological surface unit in Zone 1 (n = 350), arranged from older to younger surface units. Boxes represent the interquartile range (IQR), horizontal lines indicate median values, whiskers extend to 1.5 × IQR, and points beyond the whiskers represent outliers. Geological-unit identifiers correspond to those shown on the geological map in Figure 4.15. Question marks indicate uncertain geological attribution on the source geological map.

4.4 Discussion

This discussion combines the findings from each of the sections related to geometry, segmentation, linkage, minimum strain, and maturity in Zone 1 (the North Afar Depression) to assess faulting in a young continental rift system. This was achieved by evaluating how the measured quantitative relationships between faults are compared with the fault growth models defined in Chapter 3. Specifically, this assessment evaluates how the processes of segmentation and linkage affect fault propagation, how faults accommodate strain along the strike, and how surface age affects the apparent maturity of faults. The results also allow Zone 1 to be placed in context within the larger-scale evolution of the Afar Rift and to serve as a baseline for assessing and comparing the properties of other segments of the rift system, particularly those that are further evolved than Zone 1, in the next chapter.

4.4.1 Fault size and scaling (NAD)

The geometric properties of the faults in Zone 1 are broadly consistent with published displacement–length scaling relationships for normal faults. The Zone 1 D–L plot (Figure 4.4) shows a statistically significant positive power-law relationship, described by Dmax = 0.4909L^0.6395 (R^2 = 0.3011, $p < 0.001$). The scaling exponent (n = 0.6395) indicates

that maximum displacement increases with fault length, although the relatively low R^2 indicates substantial scatter within the fault population. Most faults cluster between reference ratios of Dmax/L ~ 10^{-2} and 10^{-1}, with a smaller number approaching Dmax/L ~ 10^{-3}. The Dmax/L = 1 reference line is included only as an upper-limit guide and is not approached by the dataset. The observed Dmax/L values fall within the broad range reported for normal-fault populations (Walsh and Watterson, 1988; Cowie and Scholz, 1992; Kim and Sanderson, 2005; Lathrop et al., 2022).

The fault-length distribution for Zone 1 is strongly skewed towards short to intermediate lengths, with most structures between ~1 and 4 km and only a small number of longer faults extending to ~17 km. The relatively large population of short faults, together with the smaller number of long faults, is consistent with a fault population containing structures at different stages of growth and interaction (Nicol et al., 1996; Childs et al., 2017). The mean Dmax of ~106 m and the predominance of relatively low-displacement faults similarly indicate considerable variability in displacement accumulation across the mapped fault population.

The spatial patterns further demonstrate that fault development is heterogeneous across Zone 1. The highest fault densities and cumulative fault lengths occur in the southern Harak Basin, where closely spaced faults define narrow grabens, whereas the northern part of the zone contains fewer and more widely spaced faults. This south–north gradient in fault density is comparable with along-axis variations in strain localisation documented elsewhere in the Afar Depression and Main Ethiopian Rift, where extension can become concentrated within narrower zones of deformation (Ebinger and Casey, 2001; Corti, 2009). Within Zone 1, the concentration of faults in the southern Harak Basin therefore indicates greater localisation of surface faulting relative to the northern part of the study area.

These observations can also be considered in the context of fault-growth models. Propagating or isolated-fault models describe growth through synchronous increases in fault length and displacement, whereas constant-length models involve relatively rapid establishment of fault length followed predominantly by displacement accumulation. Natural fault-growth histories may combine these behaviours, with an early lengthening stage involving tip propagation, segment interaction and linkage followed by a displacement-dominated stage with limited additional lengthening (Rotevatn et al., 2019; Lathrop et al., 2022). The Zone 1 fault population shows characteristics consistent with such mixed growth behaviour. The presence of numerous short, relatively low-

displacement faults is consistent with continued development of individual structures, while longer faults with greater displacement represent structures that have accumulated greater displacement and/or experienced interaction and linkage.

Overall, the Dmax–L scaling relationship, broad scatter in fault dimensions and spatial variability across Zone 1 indicate a heterogeneous fault population. The sub-linear scaling exponent (n = 0.6395) shows that Dmax increases with fault length across the population, while the relatively low R^2 (0.3011) demonstrates that fault length alone does not account for much of the observed variation in maximum displacement. This variability provides a basis for examining the additional influence of fault interaction, linkage and geological surface units in the following sections

4.4.2 Segmented faults and linkage (NAD)

Segmentation controls the displacement–length behaviour of the faults in Zone 1. The displacement profiles in Zone 1 were dominated by irregularly peaked faults (244 faults; ~70 %), followed by multi-peak faults (71 faults; ~20%), whereas single-peak faults accounted for 35 faults (~10%) of the analysed population (n = 350; Table 4.6).

Irregularly peaked faults are typically long and have high maximum displacements (Dmax); multi-peaked faults fall into an intermediate range of both length and displacement; and single-peaked faults are generally shorter and exhibit lower maximum displacements (Dmax). This hierarchy indicates that many of the larger scarps in Zone 1 are composite fault zones created through the interaction of two or more segments rather than a single mechanically coherent fault. The existence of multiple displacement maxima along the strike of faults is expected because overlapping segments retain their peak displacement magnitudes until the linkage is complete (Peacock and Sanderson, 1991; Trudgill and Cartwright, 1994; Childs et al., 1995; Cartwright et al., 1995; Kim and Sanderson, 2005).

The high proportion of multi-peaked and irregular displacement profiles in Zone 1 suggests that most of the fault network is at an intermediate stage of mechanical integration, in which many faults are composed of several partially linked segments. Step-like D–L relationships with repeated peaks, particularly on the longest faults, are indicative of growth through sequential segment interaction, overlap across relay zones, and time-dependent reactivation, rather than the simple propagation of a single segment (Cowie and Scholz, 1992; Childs et al., 2017). Single-peaked faults with relatively smooth displacement profiles are likely to represent individual segments that have developed

largely in isolation and, therefore, have more internally consistent displacement distributions. The average D–L scaling in Zone 1 lies within the bounds established for normal faults in Section 4.3, but the scatter at short lengths and the abundance of irregular profiles reflect ongoing mechanical integration and localisation of slip at fault tips and relay zones (Kim and Sanderson, 2005; Walsh et al., 2003).

The classification of fault linkages at the map scale supports this interpretation. Linkages were categorised based on overlapping fault tips and en-échelon segments connected by relay ramps (soft linkages) or complete connections across a relay ramp forming a single continuous scarp (hard linkages). Of the mapped segments, approximately 54% exhibited soft linkages, 27% exhibited hard linkages, and the remaining ~19% showed no apparent linkage. Soft linkages are most abundant in the southern Harak Basin, where the fault density is greatest, and become less common northward. This pattern supports the view that many surface-level interactions between faults in Zone 1 remain incomplete and that deformation is still largely transferred across relay zones rather than being fully localised onto continuous, integrated strands (Peacock and Sanderson, 1991; Walsh et al., 2003). Hard linkages, although fewer than soft linkages, are concentrated along the more linear axial and graben-bounding faults in the southern part of the depression. Their distribution suggests that these sectors have reached a higher degree of strain focus and that thecomposite faults locally behave as single structures, even though the overall fault population remains dominated by relatively small, partly linked segments, similar to the early to intermediate stages of more mature rifts (Cartwright et al., 1995; Trudgill and Cartwright, 1994; Mansfield and Cartwright, 2001).

Collectively, the high frequency of irregular and multi-peaked displacement profiles, dominance of soft linkages, and spatially restricted occurrence of hard linkages indicate different degrees of mechanical integration within the Zone 1 fault network. Many faults remain segmented and interact across relay zones, whereas a smaller subset, particularly in the southern Harak Basin, forms hard linked, more laterally continuous structures. In Zone 1, this process appears to be most advanced in the southern part of the zone, where the high fault density, coexistence of soft and hard linkages, and complex displacement profiles indicate a greater degree of fault integration than in the northern part of the zone, where the fault network remains more segmented.

Finally, the segmentation and linkage characteristics identified from the DEM should be regarded as minimum estimates of the true fault network structure. The 30 m DEM resolution is too coarse to resolve narrow relay-damage zones, and volcanic resurfacing plus syntectonic sedimentation in the Harak Basin can obscure parts of fault zones while

leaving individual displacement peaks where the scarps remain exposed. These effects may obscure low-relief fault tips and narrow relay-zone structures, leading to underestimation of fault length and displacement and potentially causing interacting segments to appear as separate surface traces (Kim and Sanderson, 2005; Lathrop et al., 2022). Nevertheless, the combined evidence from displacement profiles, linkage statistics, and map-scale geometries provides strong support for spatial variation in the degree of fault integration across Zone 1, from relay-dominated, segmented faults to more integrated fault structures, with implications for rift evolution discussed in Chapter 7.

Segment Pattern	Fault Numbers	Fault Length (m)			Fault D_{max} (m)		
		Min.	Max.	Mean.	Min.	Max.	Mean.
Single	35	487	3,371	1,589	18	205	65
Multi	71	845	5,674	2,344	18	288	86
Irregular	244	748	16,859	4,430	14	593	119

Table 4.6: Statistical summary of displacement-profile classes in Zone 1 of the North Afar Depression (NAD; n = 350). Faults were classified as single-peak, multi-peak and irregularly peaked according to the shapes of their displacement–length (D–L) profiles. The table reports the minimum, maximum and mean fault length (L) and maximum displacement (Dmax) for each profile class.

4.4.3 Minimum strain distribution (NAD)

The minimum (apparent) strain calculated from the eight cross-rift profiles shows a clear south–north variation across Zone 1 (Figure 4.15). The highest apparent extension values occur across the southern profiles A–A′ and B–B′, where values are approximately 50%. The central profiles C–C′ and D–D′ record intermediate values of approximately 30%, whereas the northern profiles E–E′ to H–H′ record substantially lower values, decreasing from approximately 16% to 3% (Figure 4.15). Overall, these measurements show a systematic decrease in minimum apparent strain from the southern to the northern part of the North Afar Depression.

When considered alongside the structural framework and surface geology, the elongation pattern suggests spatial variation in how extension is accommodated across Zone 1. In the southern Harak Basin, high apparent strain coincides with a narrow basin width, dense clusters of faults, and a mixture of soft- and hard-linked structures, many of which cut

Late Quaternary volcanic and syn-rift sedimentary units (Rv, Gv, Gv?, ISv, ISv?, Pes and Hs; after Rime et al., 2023). This combination favours efficient accommodation of extension and higher localised elongation. In the central part of Zone 1, where the basins widen and individual segments begin to coalesce into larger composite fault systems, the elongation values are intermediate, implying that extension is shared between several fault zones across a broader deformation belt. In the northernmost profiles, the calculated apparent elongation is lower, but the structural pattern includes a prominent basin-bounding fault towards the Danakil Block. Therefore, the lower apparent elongation in the northern profiles does not necessarily indicate a diffuse or structurally immature fault system but instead reflects a different fault architecture in which deformation is associated with a major bounding structure.

The south–north gradient in the minimum strain is consistent with observations from other parts of Afar and the Main Ethiopian Rift, where the maximum extension tends to be concentrated in narrow axial grabens and decreases along the strike and towards the rift margins and transfer zones (Ebinger and Hayward, 1996; Ebinger and Casey, 2001; Corti, 2009; Agostini et al., 2011; Rime et al., 2023). In this context, the southern Harak Basin behaves like a locally more mature axial segment within an overall young rift, with strong localisation, whereas the northern NAD marks a sector where faulting is more distributed and the rift has not yet reorganised into a small number of major through-going structures. The absolute elongation values in Zone 1 should be interpreted as minimum apparent surface strain because the DEM-based reconstruction does not account for unresolved small faults, buried structures or distributed deformation. Direct quantitative comparison with extension estimates derived using different methods and spatial scales should therefore be made cautiously.

A 30 m DEM cannot fully resolve small scraps or distributed strain; therefore, numerous minor offsets may be missed or smoothed. Volcanic resurfacing and syn-rift sedimentation, particularly in the Harak Basin, can bury older scarps or drape parts of fault zones, thereby reduce the measured heaves and shorten the effective faulted length along the profile. In addition, any local obliquity between a profile and the mean fault strike tends to underestimate the true extension unless fully corrected. Together, these factors imply that the true strain may be higher than the mapped values, especially in areas with thick cover or complex fault geometry.

Despite these limitations, the relative patterns were robust. The combination of high apparent elongation, high fault density, and advanced linkage in the southern Harak Basin, and progressively lower elongation, reduced density, and weaker linkage towards

the north, supports the interpretation that Zone 1 is a structurally transitional rift sector. The southern part of the NAD appears closer to a locally mature, strongly localised axial segment, whereas the northern part remains in a more distributed, mechanically immature state, where strain has not yet been fully focused on major through-going faults. This south–north maturity and strain localisation gradient provides an important reference for comparing how Zone 1 evolves relative to the more advanced rift sectors discussed in later chapters.

However, the fault size distributions, segmentation and linkage patterns, and minimum strain estimates together suggest that Zone 1 (NAD) forms part of a structurally transitional, relatively young rift sector, where deformation is still shared among numerous short- to medium-length faults with only partial linkage, and where strain is most strongly focused on the southern Harak Basin. The next chapter turns to Zone 2 in the Northern Main Ethiopian Rift (NMER), a more advanced rift segment with a better-developed axial graben, higher fault densities, and a different balance between fault growth, linkage, and accumulated displacement. The same workflow for fault geometry, displacement profiles, linkage classification, and minimum strain analysis was applied in Zone 2, allowing a direct comparison of how fault systems evolve from the relatively immature configuration in Zone 1 to the more integrated, displacement-efficient architecture observed in Zone 2.

4.4.4 Influence of geological surface units on fault scaling (NAD)

The comparison of fault populations across the mapped geological surface units indicates that lithology does not exert a simple first-order control on Dmax–L scaling in Zone 1. The volcanic and sedimentary units show substantial overlap in Dmax–L space (Figure 4.17), although differences are present in their Dmax and Dmax/L distributions (Figures 4.18 and 4.19). This suggests that lithology may contribute to the observed variability but cannot alone explain the scaling relationships. Previous compilations have similarly shown that host-rock properties can influence fault D–L scaling, but that scaling is also affected by fault size, growth history, segmentation, linkage and maturity (Cowie and Scholz, 1992; Kim and Sanderson, 2005; Lathrop et al., 2022). In particular, Lathrop et al. (2022) found systematic differences between faults hosted in relatively stiff igneous rocks and those in more compliant sedimentary rocks. The substantial overlap between the volcanic and sedimentary populations in Zone 1 therefore suggests that any lithological influence is superimposed on other controls, particularly fault growth and linkage, rather than producing distinct lithology-dependent scaling populations.

Differences are nevertheless apparent in the distributions of Dmax and Dmax/L between geological units (Figures 4.18 and 4.19). ISv displays a relatively low median Dmax, whereas several of the other volcanic and sedimentary units show broader displacement distributions. However, these differences should not be interpreted solely as lithological control because the mapped units also differ in surface age, exposure, preservation and sample size. In particular, Gv contains only two mapped faults and therefore cannot provide a statistically representative comparison with the more extensively sampled units.

The substantial overlap between geological units is consistent with the broad scatter commonly reported in displacement–length compilations for normal faults, where Dmax–L relationships can be influenced by factors in addition to host-rock properties, including fault interaction, segmentation, linkage and the stage of fault growth (Cowie and Scholz, 1992; Kim and Sanderson, 2005). In Zone 1, the widespread occurrence of segmented and linked faults provides an additional source of variability, as demonstrated by the different displacement-profile geometries and linkage states described above.

Therefore, the Zone 1 results do not indicate a simple separation in Dmax–L scaling between volcanic and sedimentary units. Instead, lithology and geological surface characteristics appear to contribute to the observed scatter, together with differences in fault growth, segmentation, linkage and surface preservation. This interpretation is consistent with the broad variability observed in previous normal-fault D–L compilations.

4.5 Conclusion

The principal findings from Zone 1 of the North Afar Depression (NAD) are summarised as follows:

- The 350 mapped faults show a statistically significant positive relationship between maximum displacement (Dmax) and fault length (L), described by Dmax = 0.4909L^0.6395 (R^2 = 0.3011; $p < 0.001$). The considerable scatter indicates substantial variability in fault growth across the population.
- Irregularly peaked displacement profiles dominate the fault population (244 faults; ~70%), followed by multi-peak profiles (71 faults; ~20%) and single-peak profiles (35 faults; ~10%). Irregularly peaked faults are generally longer and have higher maximum displacements than the other profile classes.
- Soft-linked faults are the dominant linkage state (~54%), compared with hard-linked faults (~27%) and non-linked faults (~19%). The coexistence of these linkage states, together with the predominance of complex displacement profiles, indicates variable degrees of fault interaction and mechanical integration across

Zone 1.

- Minimum apparent elongation shows a pronounced south–north variation, decreasing from approximately 50% in the southern profiles to approximately 3% in the northernmost profile. The highest apparent strain occurs in the southern Harak Basin, where fault density and fault interaction are greatest.
- Volcanic and sedimentary geological units show substantial overlap in Dmax–L space. Lithology therefore does not appear to exert a simple first-order control on fault scaling in Zone 1; instead, the observed variability is also associated with fault growth, segmentation, linkage and surface preservation.

Chapter 5: Analysis of Scaling Properties of Normal Fault Growth in the North Main Ethiopian Rift (NMER)

5.1 Introduction

The North Main Ethiopian Rift (NMER), the northern sector of the Main Ethiopian Rift within the East African Rift System, records a transition from long Miocene border faults that define the rift shoulders to younger, closely spaced axial faults that accommodate much of the present-day deformation (Wolfenden et al., 2004; Mackenzie et al., 2005; Corti, 2009; Agostini et al., 2011). Many of the earliest border faults initiated after ~11 Ma and developed into long-lived structures that now form broad, eroded escarpments along the rift margins (Corti, 2009; Agostini et al., 2011). Younger faults are buried or lie at the base of the slope, leaving little discrete surface-scarp expression while continuing to control subsurface basin architecture (Wolfenden et al., 2004; Mackenzie et al., 2005). Geological, geophysical, and geomorphic studies indicate that extensional strain has progressively migrated from these border faults into a narrow sub-axial zone, implying progressive deactivation or reduced activity on many border structures and localisation onto intra-rift faults (Corti, 2009; Agostini et al., 2011; Keir et al., 2015).

Within the NMER, the Wonji Fault Belt (WFB) forms an axial to sub-axial zone of Quaternary faulting and volcanism along the rift floor, where much of the younger deformation is concentrated. Within this zone, normal faulting, steep asymmetric grabens, and axial volcanism are closely linked to each other. These intra-rift faults are typically right-stepping, en-echelon, and interact with magmatic segments, making the NMER an important natural laboratory for rift evolution and fault–magmatism feedback (Corti, 2009; Agostini et al., 2011; Keir et al., 2006, 2015). In this chapter, a distinction is made between the older, partly buried border-fault framework and the younger axial faults that are clearly expressed in the surface morphology. DEM-based measurements primarily capture the latter, whereas the former are incorporated from published stratigraphic and geophysical constraints and are considered explicitly when drawing cross-sections (Wolfenden et al., 2004; Mackenzie et al., 2005; Agostini et al., 2011).

This chapter quantitatively evaluates the characteristics and development of normal fault systems in Zone 2 of the NMER (Figure 5.1) and tests their compatibility with extensional fault growth models. The specific objectives are as follows: (i) map and quantify fault geometries, including apparent fault length (L) and apparent maximum displacement (Dmax); (ii) classify displacement–length (D–L) profiles (single-peak, multi-peak, and irregularly peaked) to describe along-strike displacement organisation; (iii) document

segmentation and linkage styles (soft-linked versus hard-linked) to infer connectivity and along-strike slip transfer, noting that "immature" (soft-linked) and "mature" (hard-linked) linkage states are defined from surface geomorphology and may not represent full continuity at depth; (iv) quantify minimum apparent extensional strain from cross-rift sections drawn approximately perpendicular to fault strike, using elongation as defined in Chapter 3, Section 3.5.4 (Minimum Strain Elongation); and (v) evaluate how fault maturity and strain localisation vary with surface geology by comparing Dmax/L across mapped volcanic and sedimentary units, while accounting for resurfacing, erosion, and burial effects on surface expression (Peacock and Sanderson, 1991; Corti, 2009; Agostini et al., 2011; Rime et al., 2022). All mapping and measurements used a 30 m DEM and published surface age information (Rime et al., 2022).

5.2 The North Main Ethiopian Rift (NMER; Zone 2)

Zone 2 is located in the North Main Ethiopian Rift (NMER), between the Main Ethiopian Rift to the southwest and the northeastern Afar Depression to the northeast. The study area covers ~28,900 km² between latitudes 8°30′N–10°30′N and longitudes 38°50′E–40°30′E, with the spatial extent of Zone 2 shown in Figure 5.1. Elevations range from 3,509 m on the Ethiopian Plateau to 707 m along the axial valley floor. At present, tectonic and volcanic activity are concentrated in an axial region less than ~20 km wide, which contains normal faults with relatively small offsets, fissure systems, and lava fields. In this part of the rift, extension is increasingly taken up by magmatic intrusion and closely spaced axial faulting, whereas the high rift-border escarpments show eroded flanks and more subdued topography (Ebinger and Hayward, 1996; Keir et al., 2006; Corti, 2009; Shmela, 2018).

Faulting in Zone 2 includes structures associated with two major volcano-tectonic segments, Kone and Fantale, which are contemporaneous and form part of the inward migration of deformation from pre-existing border-fault systems to the axial segments (Agostini et al., 2011). This physiographic and structural context provides a well-constrained setting for examining fault length, maximum displacement (Dmax), and strain distribution in a relatively evolved continental rift (Corti, 2009; Agostini et al., 2011; Shmela, 2018).

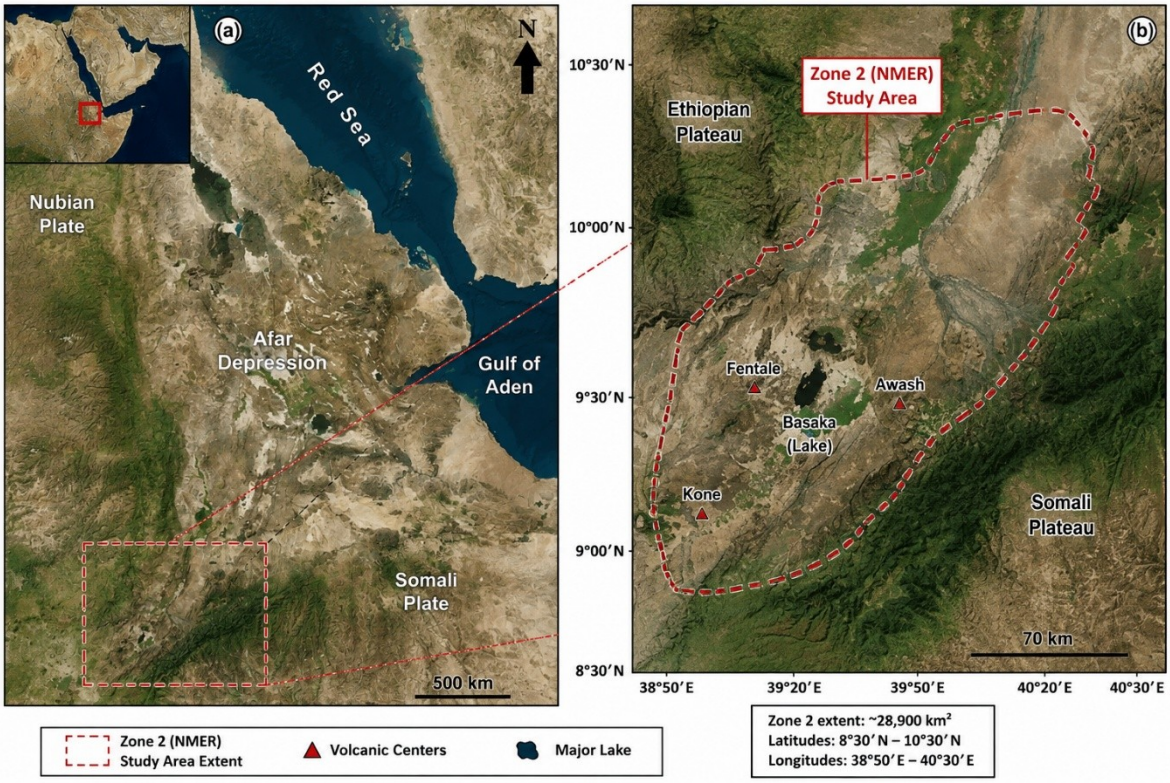


Figure 5.1: Regional and local settings of the North Main Ethiopian Rift (NMER). **(a)** Regional context of the Afar Depression and adjoining rifts within the northern East African Rift System. Major plates and margins are indicated (Nubian, Somali), with the Red Sea and Gulf of Aden shown; the dashed box outlines the enlarged area in the panel**. (b)** Close-up of the NMER axial zone between the Ethiopian and Somali plateaus, highlighting the key physiographic and volcanic features, including Kone, Fantale, Awash, and Lake Basaka. The base map is derived from ASTER GDEM Version 3 (NASA/METI/AIST/Japan Spacesystems and U.S./Japan ASTER Science Team, 2019).

5.3 Results

This section presents the quantitative results for normal faults in Zone 2 (NMER) in terms of fault geometry, displacement–length (D–L) profiles, fault zone segmentation and linkage, and minimum apparent extensional strain. Faults are characterised by their apparent length (L), apparent maximum displacement (Dmax), D–L profile type (single-peak, multi-peak, or irregularly peaked), linkage style (soft or hard), and contribution to the minimum apparent extension across the rift. All measurements were derived from the manual mapping of fault scarps on 30 m DEM data, integrated with the tectonostratigraphic framework and surface age information from previous studies.

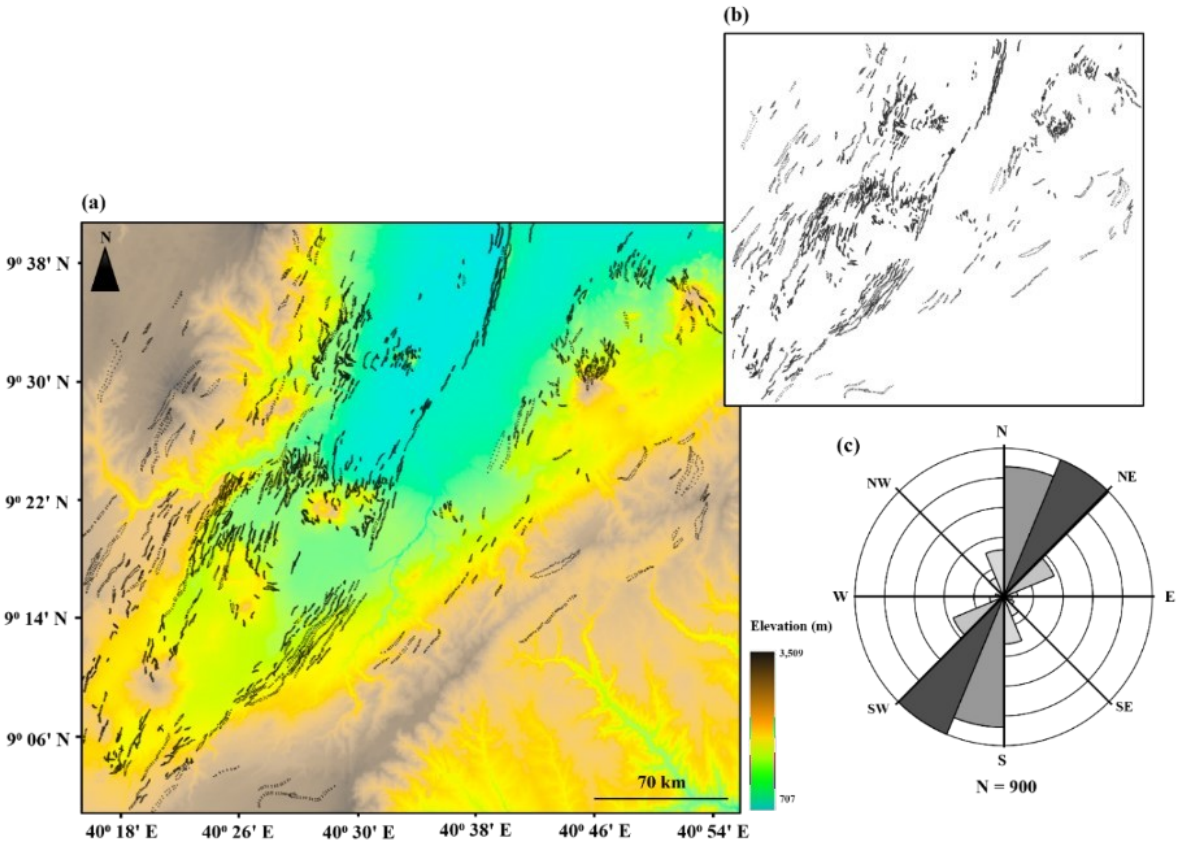


Figure 5.2: Spatial distribution and orientation of faults in Zone 2 of the North Main Ethiopian Rift (NMER). **(a)** Fault traces mapped from DEM data draped on shaded topography. **(b)** Extracted linework showing the mapped fault traces. **(c)** Rose diagram showing the dominant NW–SE fault orientation (~030°) with a subordinate NE–SW set (basemap from ASTER GDEM v3; NASA/METI/AIST/Japan Spacesystems and U.S./Japan ASTER Science Team, 2019).

5.3.1 Fault geometry analysis

5.3.1.1 Fault spatial distribution

A total of 900 normal faults were mapped manually. The traces were heterogeneously distributed, forming clusters based on orientation and density (Figure 5.2). Most faults trend NE-SW, with a dominant strike of ~ 030°, broadly aligned with the rift axis (Figure 5.2c), and a subordinate NE–SW set (Figure 5.2b). Fault density is assessed using kernel density estimation (KDE), which shows systematic differences between the axial valley and flanks (Figure 5.3): the highest concentrations (>2.5 faults km^{-2}) occur along the central rift axis, coincident with DEM topographic lows, whereas the margins show lower values (< 0.5 faults km^{-2}) with widely spaced or isolated traces of faults. The mean fault density for the study area was ~0.06 faults km^{-2}.

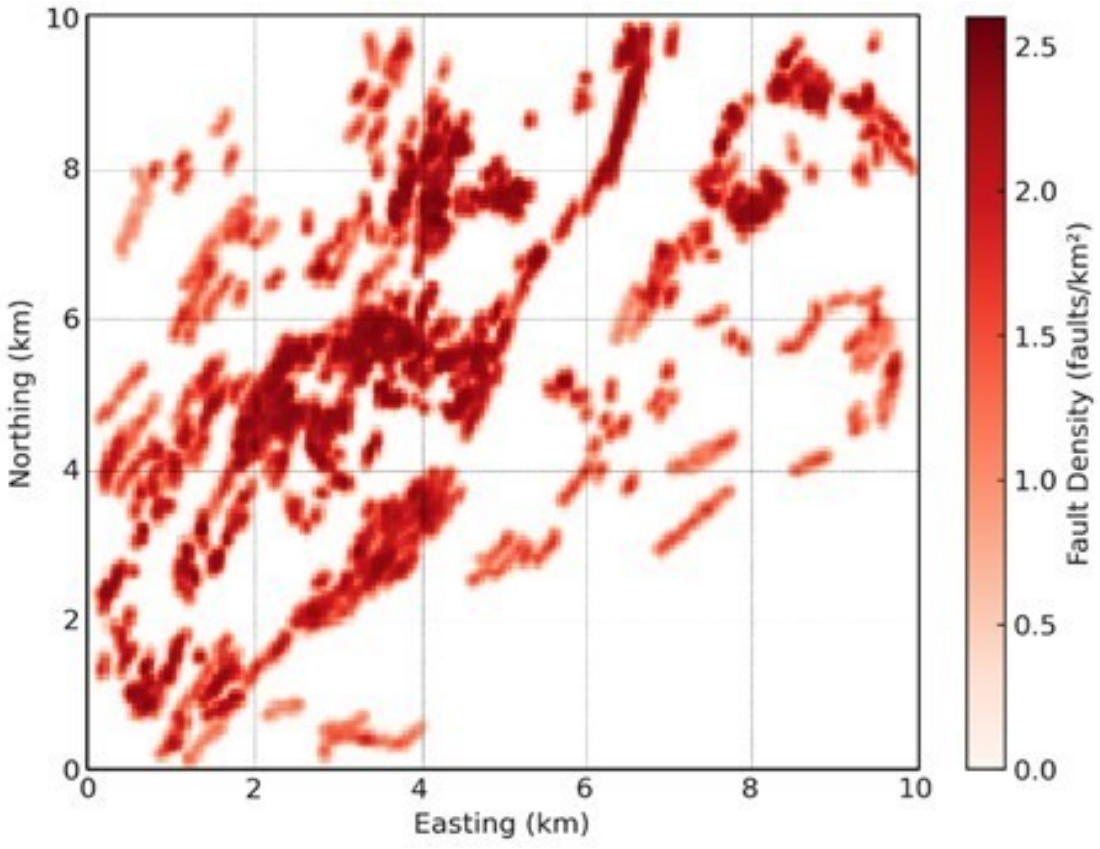


Figure 5.3: Kernel density map of mapped normal fault traces in Zone 2 (NMER). Colours show fault density (faults/km²) estimated from kernel density analysis, plotted against local easting and northing (km). High-density clusters along the central part of the map correspond to the axial rift zone, whereas lower densities occur towards the margins.

5.3.1.2 Fault Length (L)

In the North Main Ethiopian Rift (NMER), 900 normal faults were mapped within Zone 2 using DEMs with a 30 m grid resolution. Across the entire DEM-mapped fault population (n = 900), fault lengths range from 303 to 20,851 m, with an average length of 1,789 m. These measurements represent the faults identified and measured from their surface morphological expression within Zone 2 and do not include the major rift-border faults. The major border faults located on the flanks of the rift have been strongly eroded and/or buried and may reach lengths of ~50 km. Geological and geophysical studies indicate that the Mio-Pliocene border faults form the original rift boundaries, but are now largely dormant or only weakly active in the NMER, and control the overall geometry of the rift basins via broad escarpments where faults occur at the base of the slope, even though very little surface faulting is expressed (Wolfenden et al., 2004; Mackenzie et al., 2005; Corti, 2009; Agostini et al., 2011).

The literature-derived border-fault traces shown in previous studies are included only to provide structural context and are not included in the statistical analysis of the 900 DEM-

mapped faults reported here. Summary statistics for the axial faults identified in the DEM mapping are given in Table 5.1 (minimum, maximum, and mean values for length (L) and apparent maximum displacement (Dmax)).

Parameter	Min. (m)	Max. (m)	Mean (m)
Fault Length (*L*)	303	20,851	1,789
Maximum Displacement (D_{max})	10	1,045	77

Table 5.1: Statistical summary of fault geometry in zone 2 (NMER, n = 900). The table reports the minimum, maximum, and mean values for fault length (*L*) and maximum displacement (D*max*), derived from manually mapped fault traces digitised from the DEM.

The length–frequency distribution (Figure 5.4) shows that short faults dominate the population, with more than half of the 900 mapped faults measuring < 2,500 m. The modal bin lies between 1,000 and 2,000 m. Faults > 10,000 m are rare, representing < 3 % of the population.

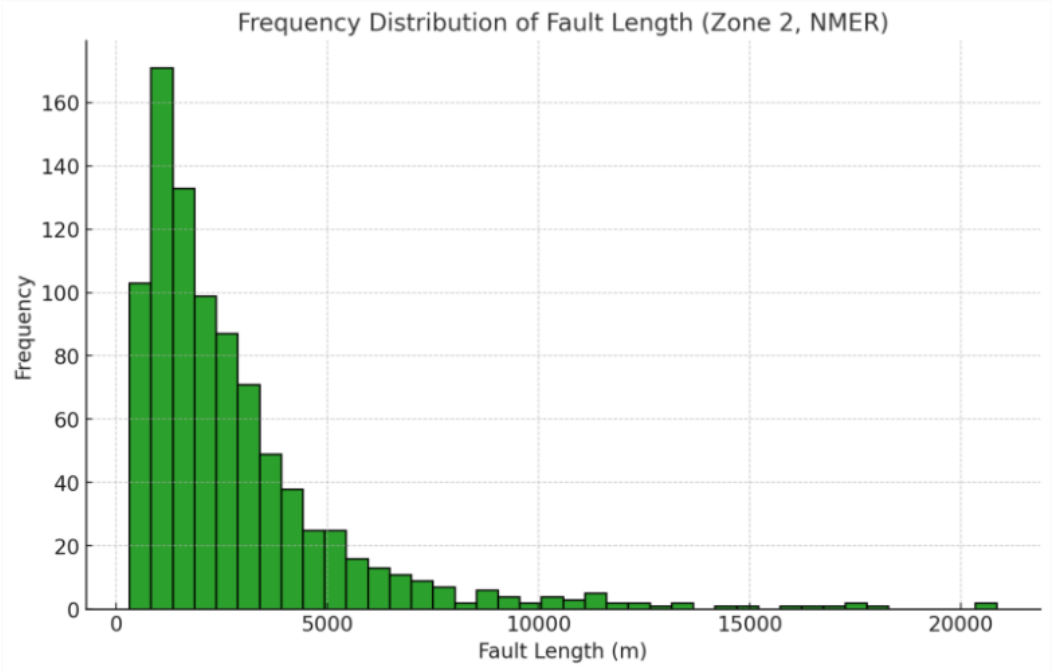


Figure 5.4: Frequency distribution of fault length in Zone 2 (NMER; n = 900). The distribution is strongly skewed towards shorter fault lengths, with more than half of the mapped faults measuring < 2.5 km. Fault frequency decreases progressively with increasing length, and faults >10 km are rare.

The scaling relationship between fault length and maximum displacement is shown in Figure 5.5. Faults cluster predominantly between the D/L = 0.01 and D/L = 0.1 reference lines, with a smaller number of points approaching the D/L = 0.001 line; the D/L = 1 line is shown as an upper reference and is not approached by the dataset. Power-law regression of the Zone 2 fault population gives Dmax = 0.7698L^0.6007, with R^2 = 0.2614. The corresponding scaling exponent is n = 0.6007. The relatively low R^2 indicates

considerable scatter in maximum displacement for faults of similar length.

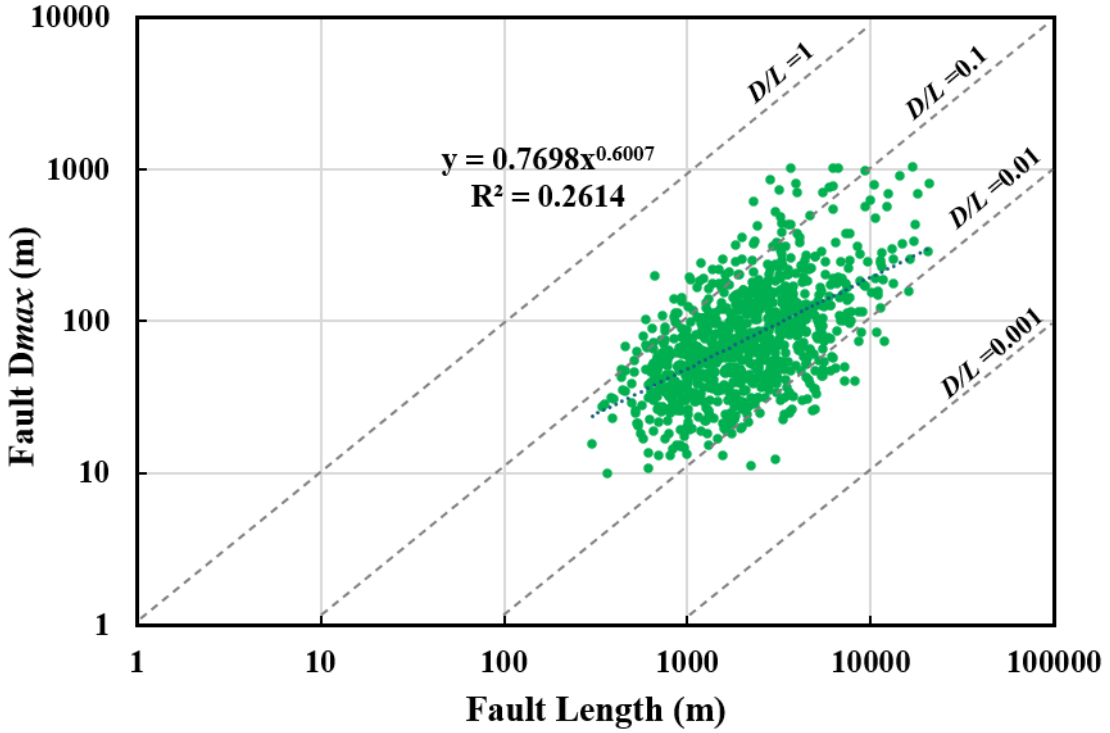


Figure 5.5: Log–log plot of maximum displacement (Dmax) versus fault length (*L*) for 900 faults in Zone 2 (NMER). Dashed lines represent constant displacement–length ratios (D/L = 1, 0.1, 0.01 and 0.001). The fitted power-law regression is Dmax = 0.7698L^0.6007 (R^2 = 0.2614).

5.3.1.3 Fault maximum displacement (Dmax)

The apparent maximum displacement (Dmax) of the 900 mapped faults in Zone 2 ranges from 10 to 1,045 m, with a mean of 77 m (Table 5.1). The frequency distribution of Dmax for the complete mapped fault population is shown in Figure 5.6. The distribution is strongly skewed towards lower displacement values, with nearly half of the mapped faults having Dmax values below 100 m. Displacements above 200 m are relatively rare, and only a few faults exceed 1,000 m.

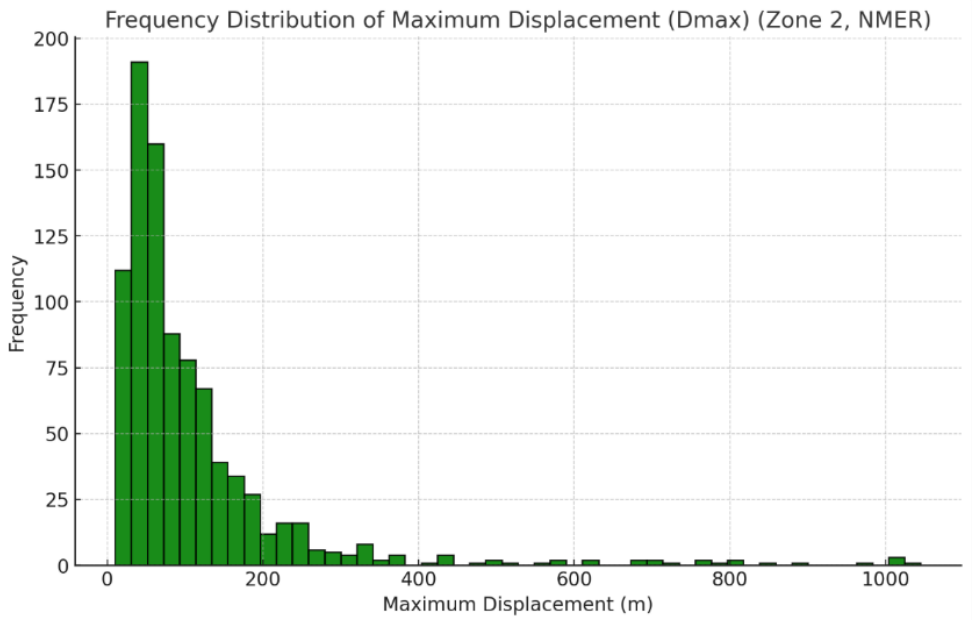


Figure 5.6: Frequency distribution of maximum displacement (Dmax) for the 900 mapped faults in Zone 2 of the North Main Ethiopian Rift (NMER). Dmax ranges from 10 to 1,045 m, with the distribution strongly skewed towards lower displacement values. Nearly half of the mapped faults have Dmax values below 100 m, whereas displacements above 200 m are relatively rare and only a few faults exceed 1,000 m.

The distribution of apparent Dmax is strongly skewed towards small values (Figure 5.6). Nearly all of the DEM-mapped faults fall within the 0–100 m and 100–200 m bins, with a smaller number of larger values (>200 m) that together account for ~18% of the population. On the log–log axes, the cumulative Dmax curve shows a rapid rise at low displacements and a reduced rate of increase at higher values, indicating a population dominated by small-displacement faults identified from surface fault geomorphology. As described in Section 5.3.1.2, the quantitative analyses presented in this chapter are based on the 900 DEM-mapped faults. The major rift-border faults are not included in these statistical analyses because their surface expression is commonly degraded by erosion and/or burial and is therefore not consistently resolved in the DEM. Literature-derived border-fault traces and published geological and geophysical observations are used only to provide structural context for these older rift-margin structures (Wolfenden et al., 2004; Mackenzie et al., 2005; Maguire et al., 2006; Corti, 2009; Keir et al., 2015).

5.3.2 Fault displacement profiles

This section characterises the internal geometry and segmentation of faults mapped based on preserved surface fault scarp morphologies in Zone 2 (NMER) using displacement–length (D–L) profiles from the mapped traces. The number, amplitude, and spacing of the displacement maxima along the strike describe each fault type. The profiles were grouped into single-, multi-, and irregular-peak classes. This taxonomy summarises how displacement is distributed along faults, independent of process/maturity. The following

subsections outline the traits of each class and provide typical examples.

5.3.2.1 Smooth single-peak profiles

A total of 280 faults (~31% of the mapped population, n = 900) displayed smooth single-peak displacement–length (D–L) profiles. These profiles are characterised by a single displacement maximum, with displacement generally increasing towards the central part of the fault and decreasing towards both fault tips. Fault lengths ranged from 303 to 3,319 m, with a mean length of 1,211 m, whereas maximum displacement (Dmax) ranged from 10 to 245 m, with a mean of 57 m (Table 5.2).

Parameter of Smooth Profile	Min. (m)	Max. (m)	Mean (m)
Fault Length (*L*)	303	3,319	1,211
Maximum Displacement (D_{max})	10	245	57

Table 5.2: Statistical summary of single-peak faults in Zone 2 (NMER, n = 280). Values show the minimum, maximum, and mean for fault length (*L*) and maximum displacement (D_{max}).

All faults in this category exhibited along-strike displacement profiles characterised by a single displacement maximum (Dmax), with displacement decreasing towards both fault tips. The Dmax–L scaling relationship for the 280 smooth single-peak faults is shown in Figure 5.7, with the remaining multi-peak and irregularly peaked faults shown in grey for comparison.

Power-law regression of the smooth single-peak population gives Dmax = 0.8772L^0.5727, with $R^2 = 0.2157$ and $p < 0.001$. The positive scaling exponent (n = 0.5727) indicates that maximum displacement generally increases with increasing fault length. However, the relatively low R^2 value indicates considerable scatter within the single-peak population, showing that fault length alone explains only a limited proportion of the variation in maximum displacement. Representative examples of individual smooth single-peak displacement profiles are presented separately in Figure 5.8.

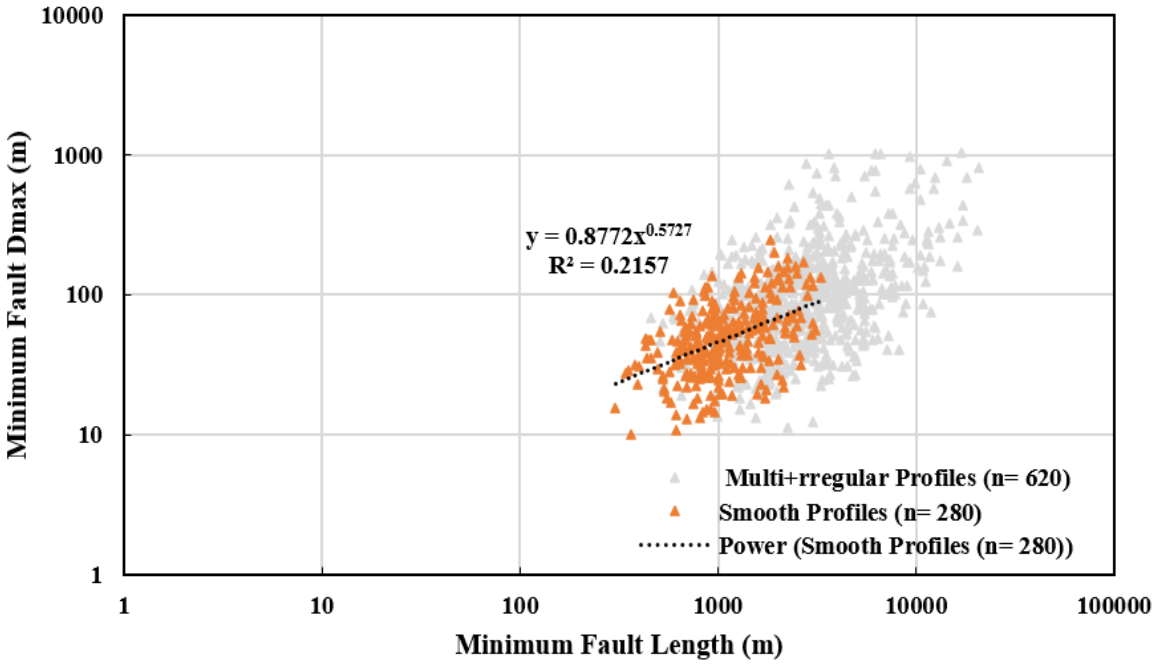


Figure 5.7: Log–log plot of maximum displacement (Dmax) versus fault length (L) for faults in Zone 2 of the North Main Ethiopian Rift (NMER). Smooth single-peak faults are highlighted in orange (n = 280), whereas multi-peak and irregularly peaked faults are shown in grey (n = 620) for comparison. The fitted power-law regression for the smooth single-peak population is Dmax = 0.8772L^0.5727 (R^2 = 0.2157, $p < 0.001$).

Representative examples of smooth single-peak faults are shown in Figure 5.8. Faults F049 and F026 display broadly continuous fault traces with a single dominant displacement maximum and no pronounced secondary maxima. In both examples, displacement increases towards a single maximum within the fault trace and decreases towards the fault tips.

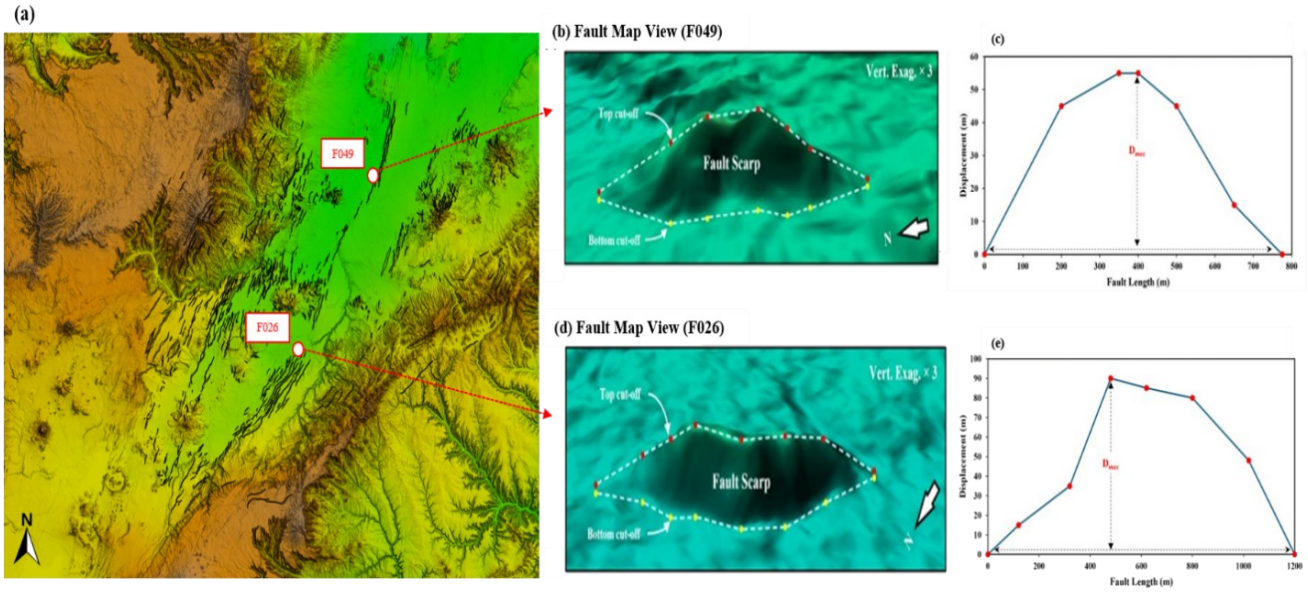


Figure 5.8: Examples of smooth single-peak fault displacement profiles in Zone 2 (NMER). **(a)** DEM showing the locations of the two example faults, F049 and F026. **(b, d)** Three-dimensional views of the fault scarps F049 and F026, respectively (vertical exaggeration ×3), showing the mapped top and bottom cut-offs used to calculate displacement along the fault traces. (c, e) Corresponding along-strike displacement–length (D–L) profiles for F049 and F026, respectively,

showing the location of maximum displacement (Dmax).Both examples display broadly single-peaked displacement profiles, with displacement increasing towards a maximum within the fault trace and decreasing towards the fault tips.

5.3.2.2 Multi-peak profiles

A total of 382 faults in Zone 2 displayed multi-peak displacement–length (D–L) profiles containing two or three distinct displacement maxima separated by intervening minima. These faults represent approximately 42% of the mapped fault population (n = 900). Fault lengths ranged from 456 to 4,690 m, with a mean of 2,069 m, whereas maximum displacement (Dmax) ranged from 11 to 1,011 m, with a mean of 106 m (Table 5.3).

Parameter of Multi Profile	Min. (m)	Max. (m)	Mean (m)
Fault Length (*L*)	456	4,690	2,069
Maximum Displacement (D_{max})	11	1,011	106

Table 5.3: Statistical summary of multi-peak faults in Zone 2 (NMER, n = 382). The table reports the minimum, maximum, and mean values for the fault length (*L*) and maximum displacement (D_{max}) derived from manually mapped fault traces.

All faults in this category exhibited along-strike displacement profiles characterised by two or three distinct displacement maxima separated by intervening minima. The Dmax–L scaling relationship for the 382 multi-peak faults is shown in Figure 5.9, with the remaining single-peak and irregularly peaked faults shown in grey for comparison.

Power-law regression of the multi-peak population gives Dmax = 1.2183L^0.5517, with $R^2 = 0.0892$ and $p < 0.001$. The positive scaling exponent (n = 0.5517) indicates that maximum displacement generally increases with increasing fault length. However, the low R^2 value indicates substantial scatter and a relatively weak relationship between fault length and maximum displacement within the multi-peak population. This scatter is consistent with displacement being distributed between several local maxima along interacting fault segments, rather than being concentrated into a single smooth maximum. Representative examples of individual multi-peak displacement profiles are presented separately in Figure 5.10.

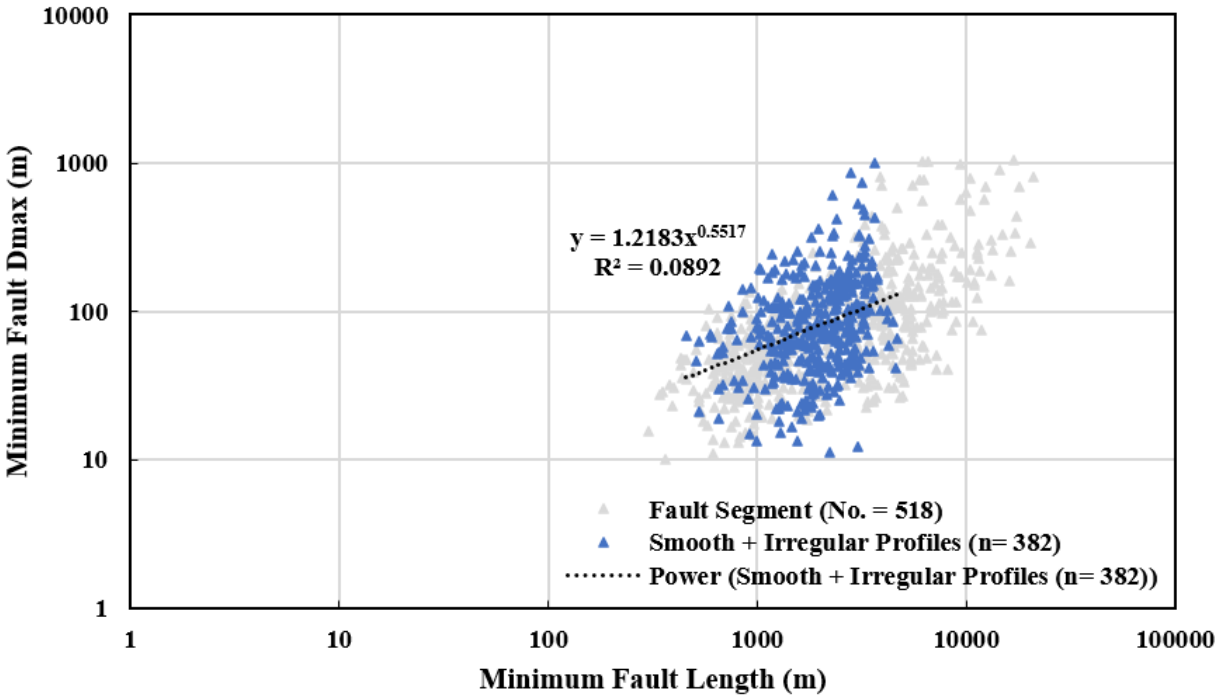


Figure 5.9: Log–log plot of maximum displacement (Dmax) versus fault length (L) for faults in Zone 2 of the North Main Ethiopian Rift (NMER). Multi-peak faults are highlighted in blue (n = 382), whereas single-peak and irregularly peaked faults are shown in grey (n = 518) for comparison. The fitted power-law regression for the multi-peak population is Dmax = 1.2183L^0.5517 (R^2 = 0.0892, $p < 0.001$).

Representative examples of multi-peak faults are shown in Figure 5.10. Faults F249 and F453 both display more than one displacement maximum separated by intervening minima along strike. In both examples, displacement decreases progressively towards the fault tips, while the central parts of the faults contain repeated local maxima characteristic of the multi-peak profile class.

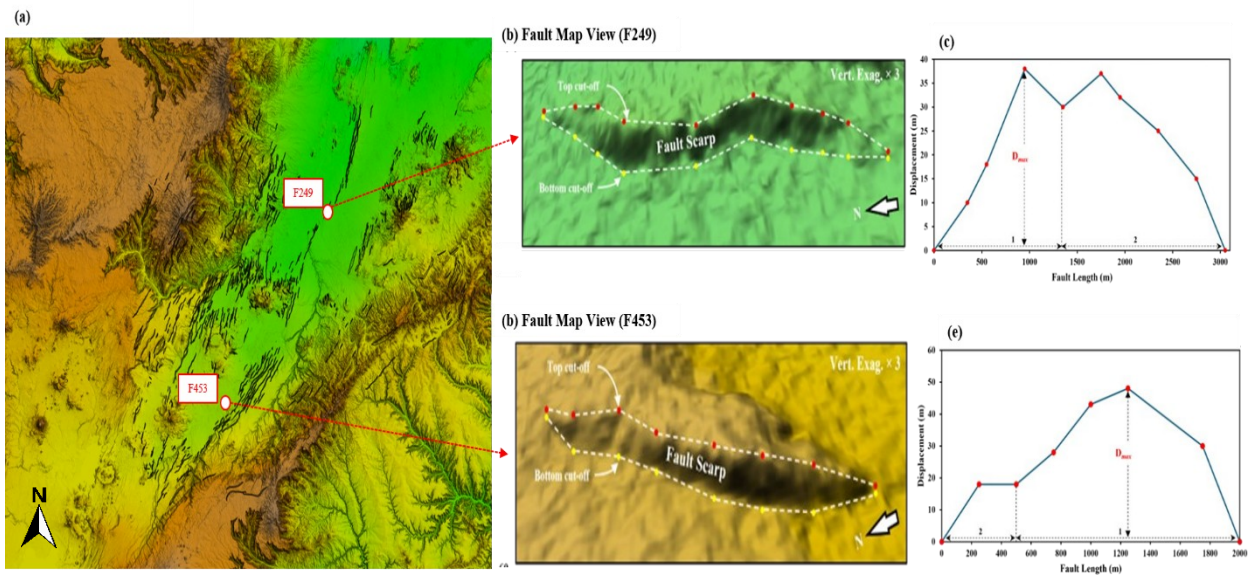


Figure 5.10: Examples of multi-peak displacement–length (D–L) profiles from Zone 2 of the North Main Ethiopian Rift (NMER). **(a)** DEM showing the locations of the two representative faults, F249 and F453. **(b, d)** Three-dimensional views of the fault scarps F249 and F453, respectively (vertical exaggeration ×3), showing the mapped top and bottom cut-offs used to calculate displacement along the fault traces. **(c, e)** Corresponding along-strike D–L profiles for

F249 and F453, respectively. Both faults display multiple displacement maxima separated by intervening minima, characteristic of the multi-peak displacement-profile class.

5.3.2.3 Irregular-peak profiles

A total of 238 faults (~26% of the mapped population, n = 900) displayed irregularly peaked displacement–length (D–L) profiles characterised by multiple local displacement maxima and intervening minima along strike. Fault lengths ranged from 735 to 20,851 m, with a mean of 6,088 m, whereas maximum displacement (Dmax) ranged from 23 to 1,045 m, with a mean of 186 m (Table 5.4).

Parameter of Irregular Profile	Min. (m)	Max. (m)	Mean (m)
Fault Length (*L*)	735	20,851	6,088
Maximum Displacement (D_{max})	23	1,045	186

Table 5.4: Statistical summary of irregular faults in zone 2 (NMER, n = 238). The table reports the minimum, maximum, and mean values for fault length (*L*) and maximum displacement (D_{max}) derived from manually mapped fault traces.

All faults in this category exhibited irregular along-strike displacement profiles with repeated displacement maxima and intervening minima. The Dmax–L scaling relationship for the 238 irregularly peaked faults is shown in Figure 5.11, with the remaining single-peak and multi-peak faults shown in grey for comparison.

Power-law regression of the irregularly peaked population gives Dmax = 0.0743L^0.8644, with $R^2 = 0.1972$ and $p < 0.001$. The positive scaling exponent (n = 0.8644) indicates that maximum displacement generally increases with increasing fault length. The exponent is higher than those calculated for the single-peak and multi-peak populations, indicating a stronger increase in displacement with increasing length within the irregularly peaked group. However, the relatively low R^2 value indicates substantial scatter, showing that fault length alone explains only a limited proportion of the variation in maximum displacement. Irregularly peaked faults nevertheless extend to greater lengths and higher displacements than the other profile classes, consistent with a structurally more complex population affected by repeated segment interaction and linkage.

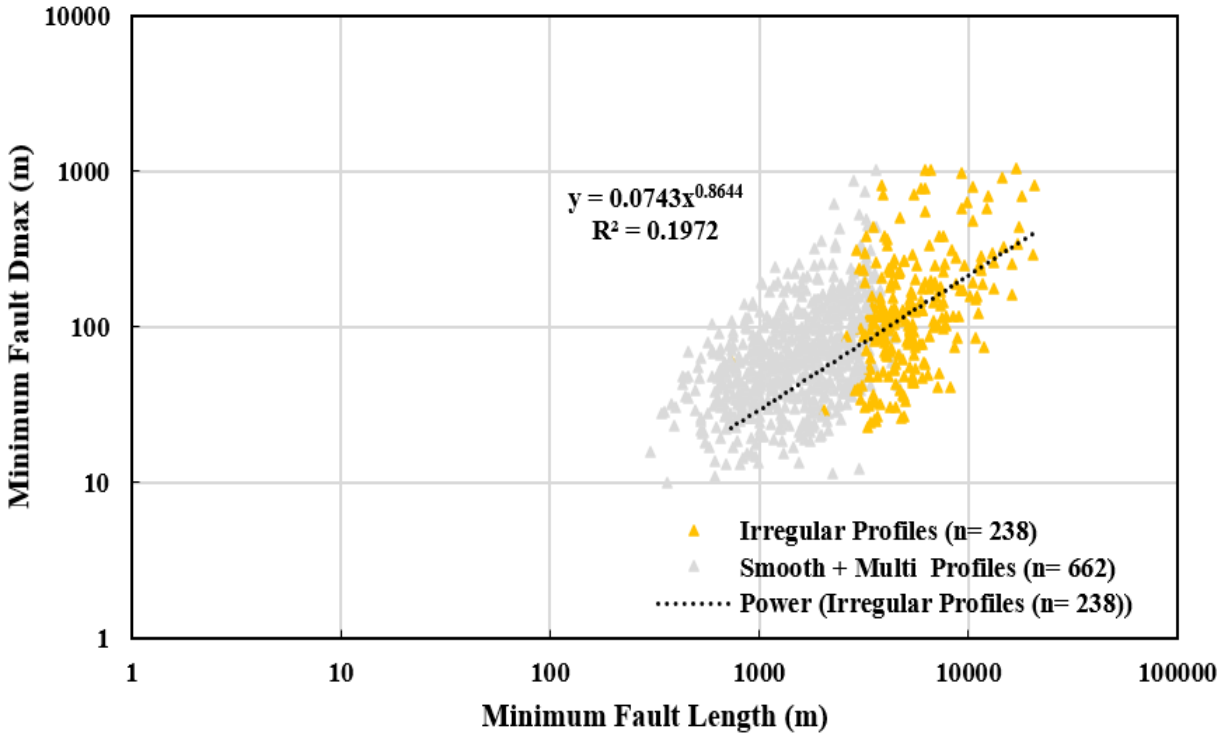


Figure 5.11: Log–log plot of maximum displacement (Dmax) versus fault length (L) for faults in Zone 2 of the North Main Ethiopian Rift (NMER). Irregularly peaked faults are highlighted in yellow (n = 238), whereas single-peak and multi-peak faults are shown in grey (n = 662) for comparison. The fitted power-law regression for the irregularly peaked population is Dmax = 0.0743L^0.8644 (R^2 = 0.1972, $p < 0.001$).

Comparison of the three displacement-profile classes shows differences in their D–L scaling relationships. Single-peak faults have a scaling exponent of n = 0.5727 (R^2 = 0.2157), multi-peak faults have n = 0.5517 (R^2 = 0.0892), and irregularly peaked faults have the highest exponent, n = 0.8644 (R^2 = 0.1972). All three relationships are statistically significant ($p < 0.001$). The broadly similar exponents of the single-peak and multi-peak populations indicate comparable increases in maximum displacement with fault length, although the multi-peak population shows greater scatter. In contrast, the higher exponent of the irregularly peaked population indicates a stronger increase in maximum displacement with increasing fault length. Together with their greater average lengths and displacements, this suggests that irregularly peaked faults represent more structurally integrated fault systems in which repeated segment interaction and linkage have contributed to the development of longer composite structures and more complex displacement distributions. Nevertheless, the relatively low R^2 values for all three groups indicate that displacement-profile type alone does not explain the full variability in D–L scaling.

Representative examples of irregularly peaked faults are shown in Figure 5.12. Faults F006 and F028 both display repeated displacement maxima separated by intervening

minima along strike. In both examples, displacement generally decreases towards the fault tips, whereas the central parts of the faults retain complex, irregular displacement patterns.

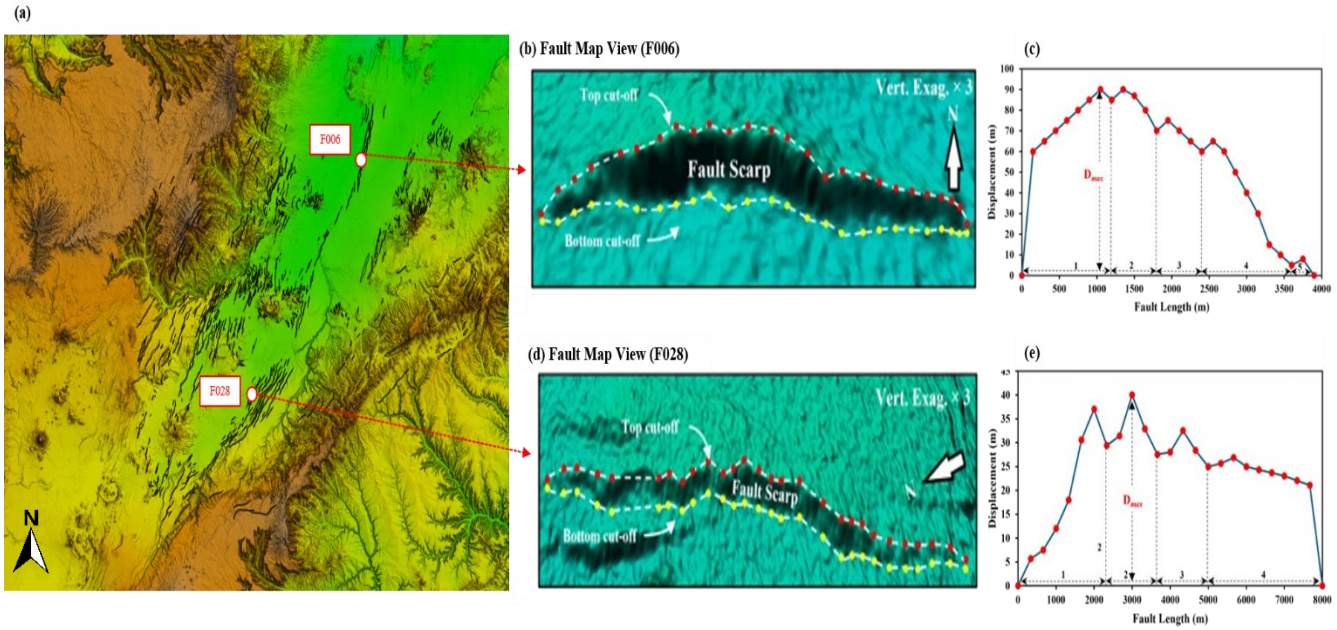


Figure 5.12: Examples of irregularly peaked displacement–length (D–L) profiles from Zone 2 of the North Main Ethiopian Rift (NMER). **(a)** DEM showing the locations of the two representative faults, F006 and F028. **(b, d)** Three-dimensional views of the fault scarps F006 and F028, respectively (vertical exaggeration ×3), showing the mapped top and bottom cut-offs used to calculate displacement along the fault traces. **(c, e)** Corresponding along-strike D–L profiles for F006 and F028, respectively. Both faults display irregular displacement profiles characterised by multiple local displacement maxima and intervening minimum along strike.

5.3.3 Fault-zone segmentation and linkage

Linkage patterns in Zone 2 of the North Main Ethiopian Rift (NMER) were mapped and classified into two types of fault linkage: soft linkage (SL) and hard linkage (HL)**.** Soft linkage was recorded where fault tips overlap or underlap and displacement is transferred across a relay ramp or deformation zone, whereas hard linkage was recorded where fault segments are physically connected to form a continuous surface trace. A total of 228 linked fault segments were mapped within the study area.

5.3.3.1 Soft linked (SL)

A total of 152 fault segments (~67% of the linked population and ~16% of the total mapped fault population) were classified as soft-linked features, where overlapping or underlapping fault tips are separated by relay ramps or deformation zones. The relay-zone widths range from several hundred metres to several kilometres. The corresponding displacement profiles show displacement variations towards the interacting fault tips and across the relay zone, consistent with displacement transfer between neighbouring fault segments.

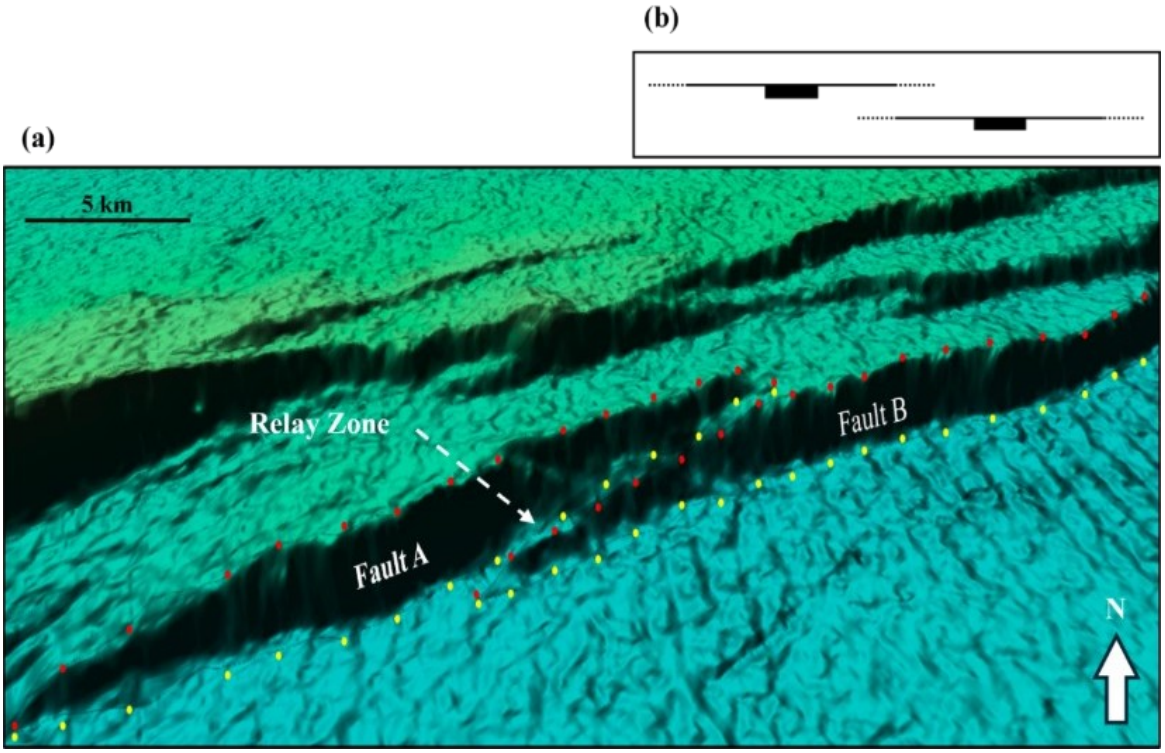


Figure 5.13: Example of soft linkage between two normal-fault segments in Zone 2 (NMER). **(a)** DEM view showing Faults A and B arranged in an overlapping en-echelon geometry and separated by an intervening relay zone. **(b)** Corresponding along-strike displacement profiles for Faults A and B, showing displacement variations towards the interacting fault tips. The faults remain physically separated at the surface and are therefore classified as soft linked.

5.3.3.2 Hard linked (HL)

Hard-linked cases constitute ~33% of the observed linkages, representing ~8% of all mapped faults. Hard-linked faults occur on both rift flanks and within the central graben, with some traces extending for several kilometres. Figure 5.14 illustrates two contiguous faults that are hard-linked across a breached relay ramp, producing a through-going surface trace.

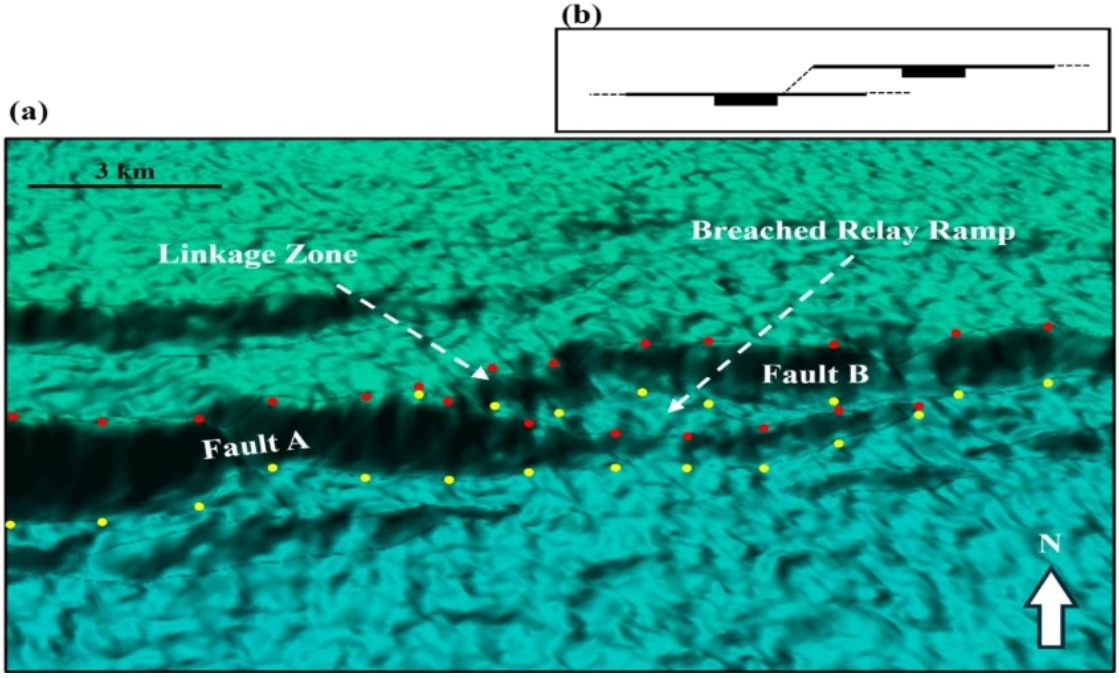


Figure 5.14: Hard linkage across a breached relay ramp in Zone 2 (NMER). Faults A and B merged across a breached relay ramp to form a continuous, through-going scarp, illustrating the transition from independent segments to a hard-linked fault. Linkage-zone location.

To examine the effect of hard linkage on displacement–length (D–L) scaling in Zone 2, the constituent faults belonging to each physically connected hard-linked system were combined and treated as a single composite fault structure. The total linked fault length was calculated as the sum of the lengths of the constituent faults, while Dmax was taken as the maximum displacement recorded within each composite structure. This produced 63 hard-linked composite structures for the scaling analysis. Non-hard-linked faults, comprising the non-linked (NL) and soft-linked (SL) populations, are shown for comparison in Figure 5.15.

When plotted using their total linked lengths, the hard-linked structures show a statistically significant positive relationship between total fault length and maximum displacement, described by Dmax = 0.6552L^0.6021 (R^2 = 0.2834, $p < 0.001$). The positive scaling exponent (n = 0.6021) indicates that maximum displacement generally increases with increasing total linked fault length. However, the sub-linear exponent and moderate R^2 indicate that the increase in Dmax is not proportional to the increase in total fault length and that considerable variability remains among composite hard-linked

structures.

The sub-linear exponent (n < 1) indicates that Dmax increases at a lower rate than total fault length, while the moderate R^2 value indicates considerable variability in maximum displacement among hard-linked structures of similar total length. Compared with the non-hard-linked population, the hard-linked faults extend towards the longer-length part of the Zone 2 D–L distribution.

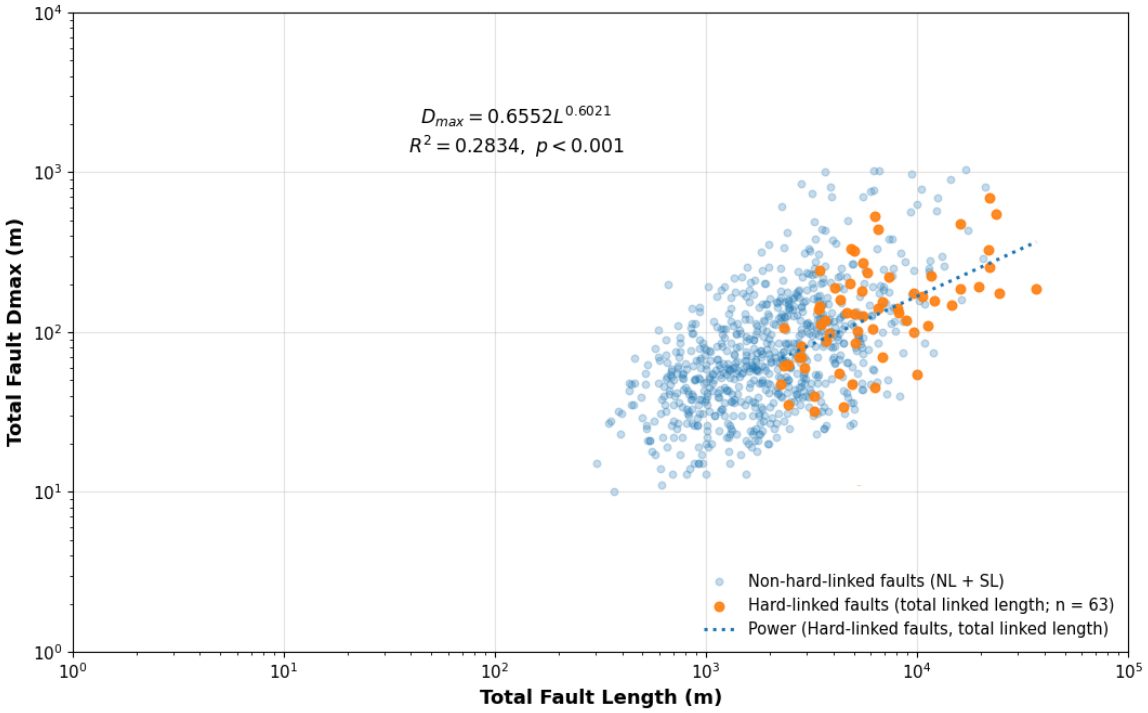


Figure 5.15: Log–log plot of maximum displacement (Dmax) versus total fault length (L) for hard-linked and non-hard-linked faults in Zone 2 of the North Main Ethiopian Rift (NMER). Hard-linked faults are plotted using the total length of each connected hard-linked structure rather than the lengths of the individual constituent segments. Non-hard-linked faults comprise the non-linked (NL) and soft-linked (SL) populations. The fitted power-law regression for the hard-linked composite population Dmax = 0.6552L^0.6021 (R^2 = 0.2834, p < 0.001; n = 63).

5.3.4 Fault distribution across surface units

The spatial distribution and geometric characteristics of faults in Zone 2 (NMER) were assessed relative to the mapped geological surface units. The geological framework used in this study was derived from a modified compilation of the geological mapping of Rime et al. (2022) and Persits et al. (1997), allowing the mapped faults to be classified according to the volcanic and sedimentary units exposed at the surface across the study area. The geological-unit codes, lithological classifications and approximate age ranges used in the analysis are summarised in Table 5.5.

In total, 900 faults were mapped in Zone 2, of which 807 (~90%) occur within volcanic units and 93 (~10%) within sedimentary units. Among the volcanic units, the post-Stratoid Pliocene volcanic unit (Pov; ~2.5–5 Ma) contains the largest number of mapped

faults (n = 304), followed by the Early Pleistocene volcanics (Q1v; ~1.1–2.5 Ma; n = 195), Late Miocene volcanics (M3v; ~5–8 Ma; n = 154), Mid-Pleistocene–Recent volcanics (Q3v; <~0.6 Ma; n = 70), Early–Mid Pleistocene volcanics (Q2v; ~0.6–1.1 Ma; n = 51), Late Oligocene–Early Miocene volcanics (O2M1v; ~28–19 Ma; n = 24), and Early–Late Miocene volcanics (M2v; ~19–8 Ma; n = 9). Within the sedimentary units, most mapped faults occur in Pleistocene sediments (Pes; 0.0117–2.58 Ma; n = 72) and Holocene sediments (Hs; 0–0.0117 Ma; n = 16), whereas only five faults are mapped across the older Miocene (Ms; ~23–5.33 Ma; n = 1) and Jurassic (Js; ~201–145 Ma; n = 4) sedimentary units.

When the geological units are arranged in approximate chronological order from oldest to youngest (Figure 5.16), the number of mapped faults does not show a simple monotonic relationship with geological surface age. Instead, fault frequency is highest within the intermediate-age volcanic units Pov, Q1v and M3v. Some of the oldest units, including Js, O2M1v and M2v, contain comparatively few mapped faults, while the youngest sedimentary units, Pes and Hs, also contain substantially fewer faults than Pov and Q1v. The observed distribution therefore indicates that geological surface age alone does not explain the number of faults preserved and identified in the DEM. Differences in the mapped area of individual geological units, their position within the rift, volcanic and sedimentary resurfacing, erosion, burial and the preservation of fault scarps may all influence the observed fault frequencies.

Type of Rocks	Code	Unit (concise)	Age range (Ma)
Volcanic	Q_3v	Mid-Pleistocene–Recent volcanics	< ~0.6
	Q_2v	Early Mid Pleistocene volcanics	~0.6–1.1
	Q_1v	Early Pleistocene volcanics	~1.1–2.5
	Pov (post-Stratoid)	Pliocene volcanics	~2.5–5
	M_3v	Late Miocene volcanics	~5–8
	M_2v	Early Late Miocene volcanics	~19–8
	O_2M_1v	Late Oligocene–Early Miocene volcanics	~28–19
Sedimentary	Hs	Holocene sediments	0–0.0117
	Pes	Pleistocene sediments	0.0117–2.58
	Ms	Miocene sediments	~23–5.33
	Js	Jurassic sediments	~201–145

Table 5.5: Summary of the principal volcanic and sedimentary surface units used to classify mapped faults in Zone 2, showing geological-unit codes, concise unit descriptions and approximate age ranges. Age assignments follow the geological and tectonostratigraphic framework used in this study, based on Rime et al. (2022, 2023) and Persits et al. (1997).

.

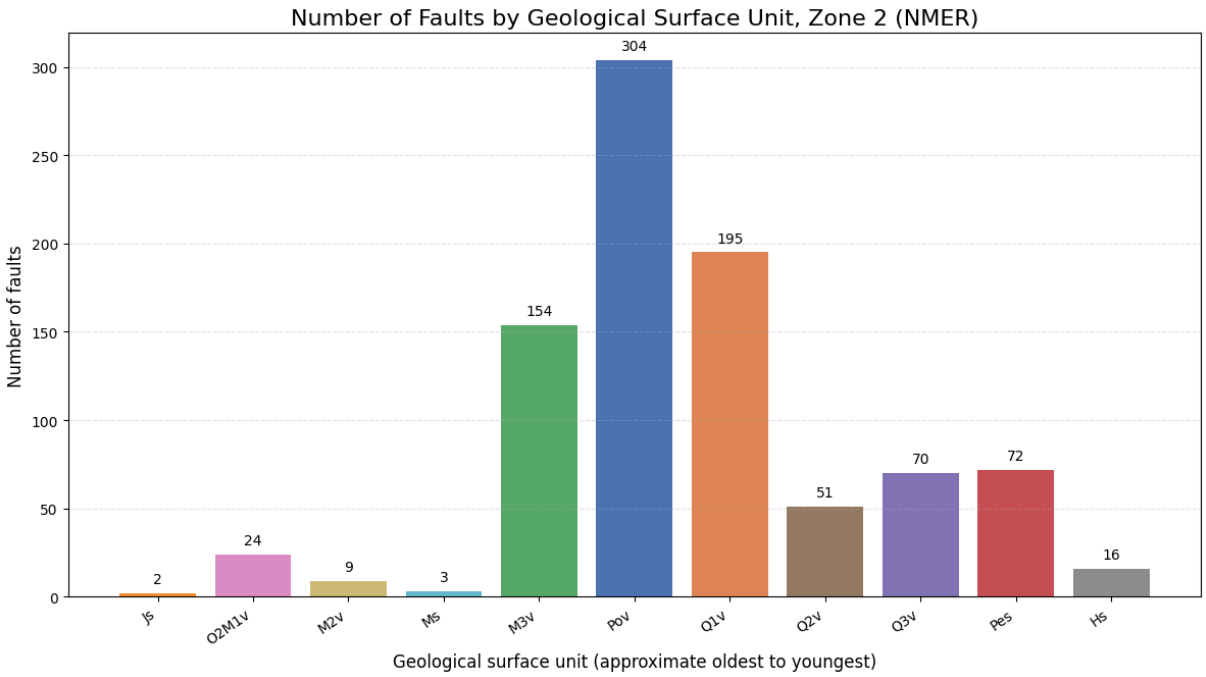


Figure 5.16: Bar chart showing the number of mapped faults per geological surface unit in Zone 2 of the North Main Ethiopian Rift (NMER), arranged in approximate chronological order from oldest to youngest. Volcanic units contain ~90% of the mapped faults, with Pov, Q1v and M3v recording the highest frequencies, whereas sedimentary units contain ~10%. The distribution does not show a simple monotonic relationship between the number of mapped faults and geological surface age. Geological-unit codes and corresponding approximate age ranges are defined in Table 5.5.

Fault size also varies between geological surface units. The relationship between fault length (L) and maximum displacement (Dmax) is shown for individual faults in Figure 5.17. Faults mapped within the volcanic units span a broad range of lengths and maximum displacements and include many of the longest and highest-displacement structures in Zone 2. In comparison, faults mapped within the sedimentary units Pes and Hs are concentrated mainly within shorter to intermediate fault lengths and lower to moderate Dmax values. However, substantial overlap occurs between the volcanic and sedimentary fault populations. The observed pattern therefore represents a tendency rather than a distinct lithological separation and indicates that geological surface age or lithology alone does not explain the variation in fault size.

The comparatively restricted surface expression of faults within some sedimentary units may partly reflect preservation effects. Sedimentation and burial can obscure pre-existing fault scarps, while erosion may modify their surface expression and reduce their detectability in the DEM. Volcanic resurfacing can similarly bury or modify older structures. Consequently, the fault populations associated with individual geological surface units reflect both tectonic fault development and the subsequent preservation or modification of fault-related topography.

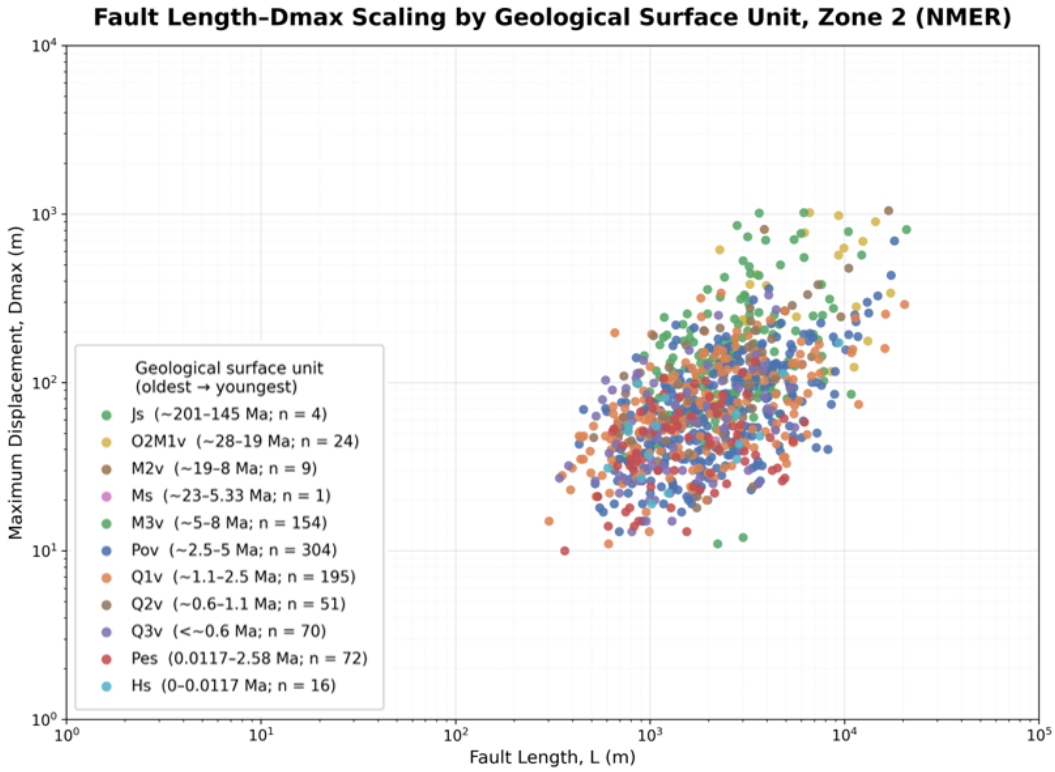


Figure 5.17: Log–log plot of fault length (L) against maximum displacement (Dmax) for faults classified according to mapped geological surface unit in Zone 2 of the North Main Ethiopian Rift (NMER). Each point represents an individual mapped fault, with colours indicating geological surface units. Units are listed in approximate chronological order from oldest to youngest, with approximate age ranges and the number of mapped faults (*n*) shown in the legend. Faults within the volcanic units span a broad range of lengths and maximum displacements and include many of the longest and highest-displacement structures, whereas faults mapped within the sedimentary units Pes and Hs are concentrated mainly within shorter to intermediate fault lengths and lower to moderate Dmax values. Considerable overlap occurs between geological units, indicating that geological surface age and lithology alone do not explain the observed variation in fault size.

Maximum displacement provides a further comparison of fault size between geological surface units (Figure 5.18). The Dmax distributions show substantial variation both within and between units. Several volcanic units contain faults with relatively high maximum displacements and broad Dmax distributions, whereas Pes and Hs are concentrated predominantly at lower to moderate Dmax values. However, the distributions overlap considerably, and when the units are considered in approximate chronological order, there is no simple monotonic increase or decrease in Dmax with geological surface age. The results therefore do not support an interpretation in which older geological surfaces necessarily contain larger faults, or younger surfaces necessarily contain smaller faults.

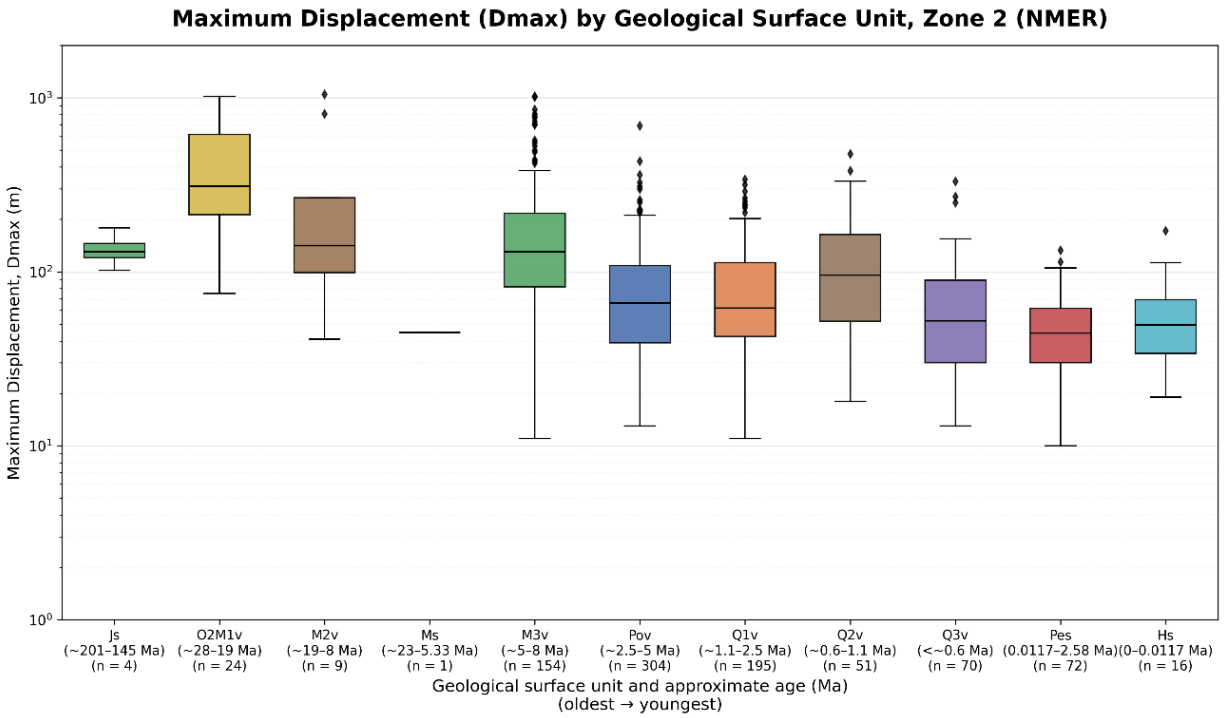


Figure 5.18: Boxplots of maximum displacement (Dmax) for faults classified according to mapped geological surface unit in Zone 2 of the North Main Ethiopian Rift (NMER). Geological surface units are arranged in approximate chronological order from oldest to youngest, with approximate age ranges and the number of mapped faults (*n*) shown beneath each unit. Dmax is plotted on a logarithmic scale. Volcanic units span a broad range of maximum displacements and include many of the highest-displacement faults, whereas faults mapped within the sedimentary units Pes and Hs are concentrated predominantly at lower to moderate Dmax values. Considerable overlap occurs between geological units, indicating that maximum fault displacement does not show a simple monotonic relationship with geological surface age.

The Dmax/L distributions provide an additional measure of the relationship between fault displacement and length across the geological surface units (Figure 5.19). Considerable variability and overlap occur between units. The older Js and O2M1v units display relatively high median Dmax/L values, although these units contain comparatively small fault populations and should therefore be interpreted cautiously. M3v and Pov show relatively lower median Dmax/L values, whereas Q1v, Q2v and Q3v occupy broadly overlapping intermediate ranges. The sedimentary units Pes and Hs also overlap substantially with the volcanic populations and do not form a distinct Dmax/L population.

When considered in approximate chronological order, the Dmax/L distributions therefore do not define a simple monotonic relationship with geological surface age (Figure 5.19). In particular, the results do not support interpreting Dmax/L as a direct proxy for fault maturity based solely on the age of the mapped surface. Instead, the observed variability is likely to reflect the combined effects of fault growth and linkage, geological setting, volcanic and sedimentary resurfacing, erosion, burial and the preservation of fault scarps. These factors should therefore be considered together

when interpreting differences in fault geometry between geological surface units in Zone 2.

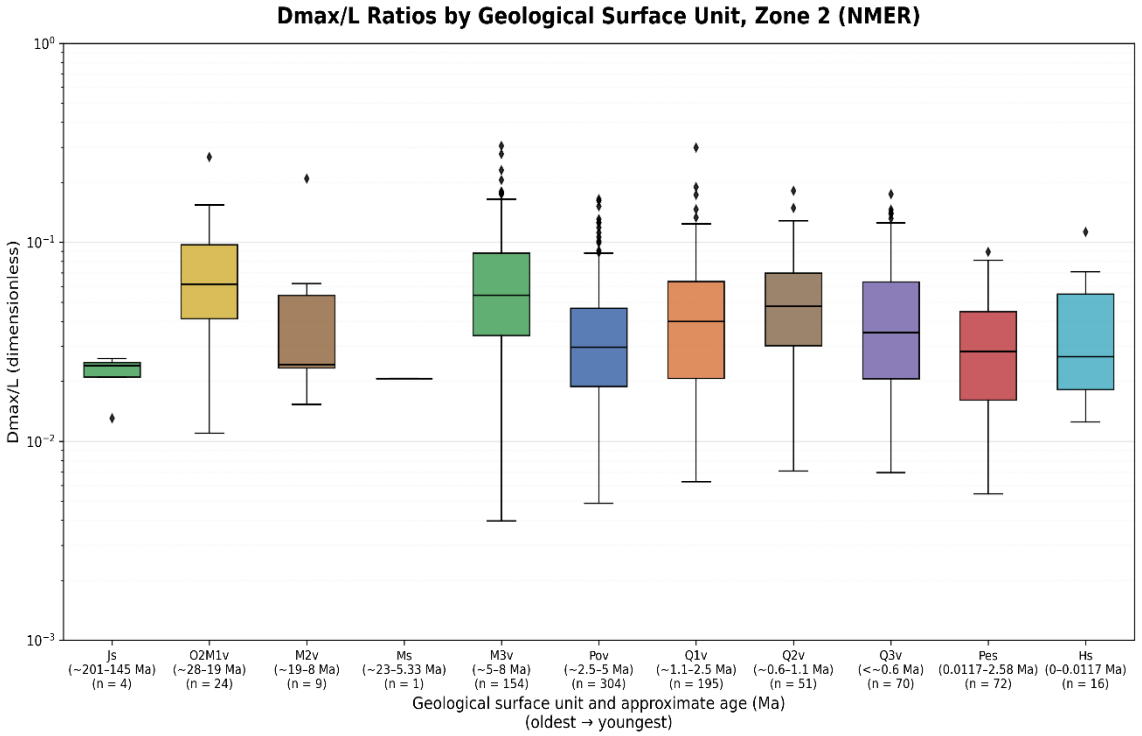


Figure 5.19: Boxplots of Dmax/L ratios for faults classified according to mapped geological surface unit in Zone 2 of the North Main Ethiopian Rift (NMER). Geological surface units are arranged in approximate chronological order from oldest to youngest, with approximate age ranges and the number of mapped faults (*n*) shown beneath each unit. Dmax/L is dimensionless and plotted on a logarithmic scale. The distributions show substantial variability and overlap between geological units and do not define a simple monotonic relationship between Dmax/L and geological surface age. Geological unit codes and approximate age ranges are summarised in Table 5.5.

5.3.5 Minimum strain analysis of NMER (Zone 2)

The apparent extensional strains (elongations) that developed owing to strain accommodation across Zone 2 were assessed by evaluating the minimum elongation using the three cross-rift sections constructed approximately perpendicular to the dominant fault strike. For each cross-section, elongation was calculated from the original baseline length (L_0) and the current length (L_1) using $e = (L_1 - L_0)/L_0$. The elongation is expressed as a percentage as well as Zone 1 (Section 4.3.4). These elongation values are an underestimation of the actual strain because they reflect only the minimum elongation that occurred as a result of mapping surface fault scarps from DEM data. These elongation values represent minimum apparent estimates because only fault scarps resolved in the 30 m ASTER GDEM are included; degraded, buried or low-relief scarps may therefore be omitted. In addition, ASTER GDEM elevation data are subject to terrain- and land-cover-dependent vertical uncertainty (Gesch et al., 2016).

5.3.5.1 Cross-section profiles

The topographic cross-sections for Zone 2 span the deforming width of the North Main Ethiopian Rift (NMER) at three representative positions, represented by sections A–A′ (south-west), B–B′ (central) and C–C′ (north-east) (Figure 5.20a–b). The three cross-sections trend approximately north-west to south-east (NW–SE) across the rift and intersect the principal structural elements, including the Ankober Border Fault, the axial rift valley and the Arboye Border Fault. They extend from the western highlands, across the rift floor, towards the eastern plateau. The cross-sections vary in length according to the structural width and topographic relief of the rift at each location; however, all extend beyond the outermost mapped faults to capture the deforming zone represented in the DEM.

Each cross-section was positioned approximately perpendicular to the dominant strike of the normal faults mapped from the DEM (Figures 5.2 and 5.20a). Where fault strike varies along a cross-section, gentle bends were introduced to maintain an approximately fault-normal orientation. This approach was used to estimate the horizontal heaves accommodated by the mapped surface faults and therefore to calculate minimum apparent extensional strain, rather than to reconstruct the complete regional extension vector.

The use of bent cross-sections introduces an important geometric limitation. Bending changes the measured cross-section lengths (L_0 and L_1), while the horizontal heave measured across individual faults represents only the component of displacement resolved along the orientation of the cross-section. Where fault slip is oblique to the section, part of the displacement may therefore not be represented by the measured horizontal heave. Similarly, maintaining a locally fault-normal cross-section does not necessarily imply that displacement occurred entirely perpendicular to the fault, particularly where local fault orientations differ from the regional extension direction. Consequently, the calculated elongation values are treated as minimum apparent estimates of extension and are dependent on fault geometry, cross-section orientation and the assumption that the measured horizontal heave provides a first-order representation of fault-related extension.

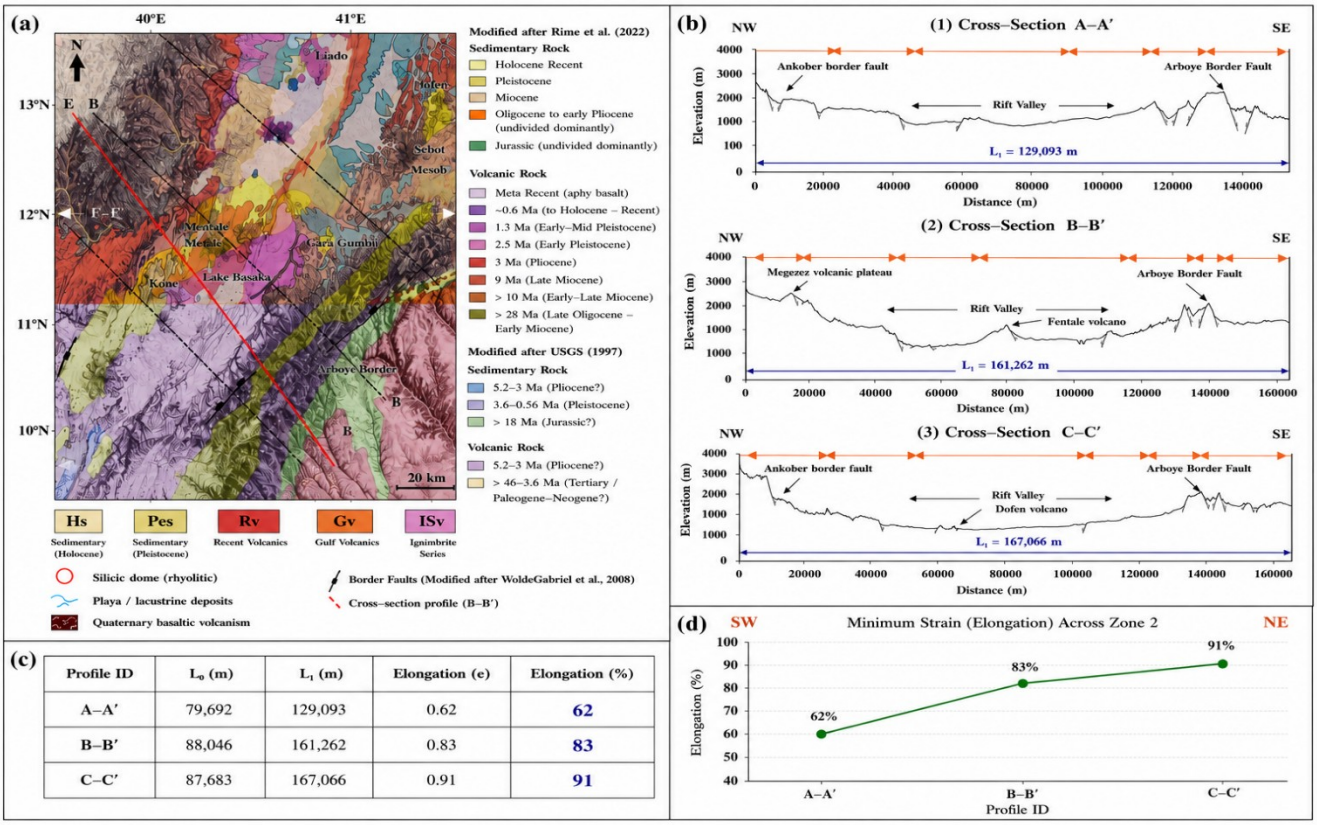
This limitation is relevant in the NMER because the orientations of individual faults vary locally relative to the regional plate-motion direction. The present-day kinematics of the rift reflect divergence between the Nubian and Somalian plates, and the regional extension direction therefore provides an important reference against which the locally fault-normal cross-sections should be considered. Where fault slip contains an oblique component, the horizontal heave measured along the cross-section may underestimate the

complete displacement vector. The strain values calculated here should therefore not be interpreted as estimates of total plate-scale extension, but rather as a consistent measure of the minimum apparent extension accommodated by the mapped surface faults across the three cross-section locations.

The topographic profiles presented in Figure 5.20b are vertically exaggerated to improve the visibility of fault-related topographic relief and the morphology of the rift. This vertical exaggeration was applied for visualisation only and was not used to derive the horizontal measurements employed in the strain calculations. The cross-section lengths and horizontal fault-heave measurements used to calculate elongation were determined from the DEM-derived map geometry using the procedure described in Chapter 3. Therefore, the vertical exaggeration of the displayed topographic profiles does not affect the calculated minimum apparent extensional strain.

For each cross-section, the original cross-section length before accounting for fault-related horizontal heave (L_0) and the reconstructed length after incorporating the cumulative horizontal heave of the faults intersected by the section (L_1) were determined, as described in Chapter 3. Minimum apparent extensional strain (elongation) was subsequently calculated from L_0 and L_1. The results are summarised in Figure 5.20c. Cross-section A–A′ has an L_0 of 79,692 m and an L_1 of 129,093 m, corresponding to an elongation of 0.62 (62%). Cross-section B–B′ has an L_0 of 88,046 m and an L_1 of 161,262 m, corresponding to an elongation of 0.83 (83%). Cross-section C–C′ has an L_0 of 87,683 m and an L_1 of 167,066 m, giving the highest calculated elongation of 0.91 (91%).

The calculated minimum apparent extensional strain therefore increases from A–A′ to B–B′ and C–C′, from 62% to 83% and 91%, respectively (Figure 5.20d). This variation indicates that the apparent extension accommodated by the mapped surface faults is not uniform across Zone 2. However, because these values are derived from DEM-mapped fault heave along cross-sections with varying orientations, they should not be interpreted as representing the complete regional extension. Instead, they provide a comparative measure of the minimum apparent extension expressed by the mapped fault population at the three cross-section locations.



Profile ID	L_0 (m)	L_1 (m)	Elongation (e)	Elongation (%)
A–A′	79,692	129,093	0.62	62
B–B′	88,046	161,262	0.83	83
C–C′	87,683	167,066	0.91	91

Figure 5.20: Cross-section analysis and minimum apparent extensional strain across Zone 2 of the North Main Ethiopian Rift (NMER). **(a)** Geological map and shaded-relief DEM of Zone 2 showing the locations of cross-sections A–A′, B–B′ and C–C′ and the principal geological and structural features of the study area. **(b)** NW–SE topographic cross-sections A–A′, B–B′ and C–C′, extending across the rift and showing the Ankober Border Fault, axial rift valley, Arboye Border Fault and the Fentale and Dofen volcanic centres. The orange markers indicate fault-related horizontal heave along each cross-section, and the blue lines show the reconstructed cross-section length (L_1). **(c)** Summary of the original cross-section length (L_0), reconstructed length (L_1), and calculated minimum apparent extensional strain (elongation) for each profile. **(d)** Variation in minimum apparent extensional strain across Zone 2, increasing from 62% along A–A′ to 83% along B–B′ and 91% along C–C′. The topographic profiles in (b) are vertically exaggerated for visualisation only; horizontal measurements used to calculate minimum apparent extensional strain were derived from the DEM/map geometry rather than from the vertically exaggerated profiles. DEM basemap from ASTER GDEM Version 3 (NASA/METI/AIST/Japan Spacesystems and U.S./Japan ASTER Science Team, 2019); geological mapping modified after Persits et al. (1997) and Rime et al. (2022); major border faults modified after Wolfenden et al. (2004).

5.4 Discussion

This section presents the results from Zone 2 (NMER) on fault geometry, displacement–length scaling, along-strike displacement profiles, linkage styles, unit-based variations, and minimum apparent strain to evaluate how deformation is organised within the Late Pliocene–Quaternary axial segment of the rift relative to established models of fault growth and strain localisation. The analysis tests whether the observed length–displacement statistics, the prevalence of multi-peak and irregularly peaked displacement profiles, and the balance of soft versus hard linkages are consistent with progressive segment interaction and linkage (Peacock and Sanderson, 1991; Walsh et al., 2003), and with the documented inward migration of deformation towards axial magma-assisted belts in the NMER (Wolfenden et al., 2004; Corti, 2009; Agostini et al., 2011; Keir et al., 2015).

In this chapter, "mature" refers specifically to hard-linked, surface-expressed faults that remain visible in the 30 m DEM and therefore represent the younger intra-rift structures of the Wonji Fault Belt. This usage does not include the older, deeply eroded Miocene border-fault systems, which are mechanically mature but lack discrete surface scarps and are only captured in published geological and geophysical datasets (Wolfenden et al., 2004; Mackenzie et al., 2005). Accordingly, the classifications of "mature" and "immature" describe surface geomorphology rather than full subsurface continuity. The minimum strain values were treated as lower-bound estimates because DEM-based mapping may omit degraded, buried or low-relief scarps and is subject to the spatial and vertical limitations of ASTER GDEM (Gesch et al., 2016).

5.4.1 Fault size characteristics

The Zone 2 fault population is dominated by relatively short faults and low to moderate maximum displacements. More than half of the mapped faults are shorter than approximately 2.5 km, whereas faults exceeding 10 km constitute only a small proportion of the population. The D*max* distribution is similarly skewed towards lower values, with most D*max* values between 0 and 200 m and only a limited number of larger structures approaching 1 km. Together, these distributions indicate that the DEM-mapped fault population in Zone 2 is dominated by short, low-displacement faults, with a relatively small number of larger structures forming the upper tail of the distribution.

This distribution partly reflects the nature of the fault population captured by the DEM-based mapping. The 900 faults analysed in Zone 2 predominantly represent structures

preserved within the rift, particularly within the axial fault system. Older border faults are less completely represented because their surface expression may have been modified by erosion, burial, sedimentation or subsequent volcanic activity. Consequently, the mapped Zone 2 fault population should not be considered a complete representation of faulting throughout the structural evolution of the NMER, but rather the population of surface faults that can be consistently identified using the DEM-based mapping approach.

Fault length and maximum displacement show an overall positive power-law relationship in Zone 2, described by Dmax = 0.7698L^0.6007 (R^2 = 0.2614). The positive scaling exponent (n = 0.6007) indicates that maximum displacement generally increases with increasing fault length. However, the relatively low R^2 value indicates considerable scatter, showing that fault length alone explains only part of the variation in Dmax across the mapped fault population. Most faults occupy Dmax/L ratios of approximately 10^{-3}–10^{-1}, with the main population concentrated around ~10^{-2}. The observed scatter is likely to reflect several interacting controls, including fault segmentation and linkage, variations between geological surface units, volcanic resurfacing, sedimentary burial, erosion and differences in fault-scarp preservation.

The geological unit analysis further demonstrates this variability (Figures 5.16 and 5.17). Most mapped faults occur within volcanic units, with Pov, Q1v and M3v containing the largest numbers of faults. However, the number of mapped faults does not show a simple relationship with geological surface age (Figure 5.16). Fault frequency cannot therefore be interpreted solely in terms of the duration available for fault development because the mapped area of each geological unit, its position within the rift, subsequent volcanic or sedimentary burial, erosion and the preservation of fault scarps can all influence the number of faults identified from the DEM.

The D*max*/L distributions also vary between geological surface units but show substantial overlap (Figure 5.19). Pov and Q1v display relatively low dispersion, whereas Q2v and Q3v show broader distributions and several outliers, and the sedimentary units Pes and Hs also display considerable variability. Importantly, these distributions do not define a simple monotonic relationship between D*max*/L and geological surface age. The results therefore do not support interpreting D*max*/L alone as a direct measure of fault maturity in Zone 2. Instead, the differences between geological units are likely to reflect a combination of fault growth and linkage, geological setting, volcanic resurfacing, sedimentation, erosion and preservation of fault scarps.

Preservation is particularly important when interpreting these differences. Erosion can

reduce and modify the topographic expression of fault scarps, while sedimentation and volcanic resurfacing may partly or completely bury pre-existing structures. Conversely, better-preserved scarps may be more readily identified in the DEM. The small number of mapped faults within some of the older sedimentary units may therefore reflect degradation, burial and subsequent resurfacing rather than an absence of earlier faulting. Similarly, the greater variability observed in some younger sedimentary units may partly reflect differences in surface preservation rather than differences in fault growth alone. The geological-unit comparisons therefore record both tectonic fault development and the subsequent preservation or modification of fault-related topography.

Overall, the Zone 2 fault-size distribution is characterised by predominantly short, low-displacement faults, a small population of larger structures, substantial scatter in the D–L relationship and overlapping D*max*/L distributions between geological surface units. These observations do not support a simple progression in fault size or D*max*/L with geological surface age. Instead, the mapped fault population reflects the combined influence of fault growth and linkage, geological setting, volcanic and sedimentary resurfacing, erosion and preservation. These factors must therefore be considered together when interpreting fault development and strain localisation within the NMER.

5.4.2 Segmentation and linkage of fault zones

The displacement–length (D–L) profiles in Zone 2 show that segmentation exerts strong control on fault geometry and maturity. Smooth single-peak profiles form only approximately one-third of the population, whereas multi-peak and irregularly peaked profiles together account for roughly two-thirds of the mapped faults. Single-peak profiles are generally short (mean ~1.2 km) and have relatively low apparent Dmax, consistent with mechanically discrete and weakly interacting segments in the early growth stage. In contrast, multi-peak and irregularly peaked profiles are longer and accommodate higher apparent displacements, reflecting zones where several segments overlap, interact, and, in places, have already been linked along the strike.

The regression results support these differences in displacement-profile geometry. Smooth single-peak faults have a scaling exponent of $n = 0.5727$ ($R^2 = 0.2157$), whereas multi-peak faults have a similar exponent of $n = 0.5517$ ($R^2 = 0.0892$). In contrast, irregularly peaked faults have a higher exponent of $n = 0.8644$ ($R^2 = 0.1972$). All three relationships are statistically significant ($p < 0.001$). The similar exponents of the single-peak and multi-peak populations indicate broadly comparable increases in displacement

with increasing fault length, although the lower R^2 of the multi-peak population reflects greater scatter associated with segment interaction. The higher exponent of the irregularly peaked population, together with its greater average fault length and displacement, is consistent with a more structurally integrated population in which repeated interaction and linkage have contributed to the development of longer composite structures. Nevertheless, the relatively low R^2 values for all three groups indicate that displacement-profile type alone does not account for the full variability in D–L scaling.

These observations fit well with general models of normal-fault growth, where faults begin as short, separate segments and lengthen by tip propagation, overlap, and relay interaction before merging into larger composite zones (Peacock and Sanderson, 1991; Walsh et al., 2003; Childs et al., 2017). In Zone 2, the multiple displacement maxima on many faults are typical of partially linked systems, in which each segment preserves its own Dmax until the intervening relay ramps are breached. The high proportion of multi-peak and irregularly peaked profiles shows that segment interaction is already advanced within parts of the axial belt, even though many individual scarps are still relatively short.

The map-scale linkage patterns were consistent with this interpretation. Soft linkages, where overlapping or underlapping tips are separated by relay ramps or deformation zones, are more common than hard linkages and are widespread within dense axial fault clusters. Hard-linked faults are fewer but tend to coincide with the longest, highest-displacement structures in Pov and Q1v, where continuous surface scarps define the through-going fault zones. This dual population of numerous soft-linked segments plus a smaller number of hard-linked zones suggests that Zone 2 is in a transitional state, with extension increasingly transferred from many short, immature segments to fewer, longer, and more efficient axial faults.

The additional D–L analysis of hard-linked faults provides direct evidence that linkage modifies the scaling behaviour of the fault population. When each physically connected hard-linked system is treated as a single composite structure, the total linked length and maximum displacement define a statistically significant positive relationship described by $Dmax = 0.6552L^{0.6021}$ ($R^2 = 0.2834$, $p < 0.001$; $n = 63$). The sub-linear exponent ($n = 0.6021$) indicates that maximum displacement increases more slowly than total linked fault length. This suggests that structural integration through hard linkage can substantially increase the effective length of a fault system without producing a proportional increase in Dmax. The remaining scatter is consistent with linked structures retaining geometric and displacement heterogeneity inherited from their constituent

segments. This behaviour helps explain why hard-linked faults may preserve multiple displacement maxima and irregular along-strike displacement profiles even after physical connection.

All segmentation and linkage interpretations are limited by the 30 m DEM resolution, resurfacing, and burial. Some faults mapped as soft-linked at the surface may already be continuous at shallow depths, whereas volcanic or sedimentary cover may fragment a truly continuous structure into several discrete scarps. Therefore, the linked faults and composite profiles described here should be regarded as the minimum expressions of fault-zone integration. However, the high proportion of multi-peak and irregularly peaked profiles, combined with the presence of hard-linked axial faults, supports the view that Zone 2 represents an intermediate stage between a distributed, segment-dominated rift and a more mature axial system in which strain is concentrated on a limited number of composite fault zones.

5.4.3 Apparent strain localisation

The three cross-sectional profiles A–A′, B–B′ and C–C′ show a clear south-west to north-east increase in minimum apparent extensional strain across Zone 2 (Figure 5.20). Profile A–A′ records an original length (L_0) of 79,692 m and a reconstructed length (L_1) of 129,093 m, corresponding to an elongation of 0.62 (62%). Profile B–B′ records L_0 = 88,046 m and L_1 = 161,262 m, corresponding to an elongation of 0.83 (83%). The highest value occurs along C–C′, where L_0 = 87,683 m and L_1 = 167,066 m, corresponding to an elongation of 0.91 (91%). These profiles therefore indicate an increase in the minimum apparent extension accommodated by the mapped surface faults towards the north-east of Zone 2. As discussed in Section 5.3.5.1, these values represent minimum apparent strain and do not include deformation associated with small, buried or poorly resolved faults.

The observed increase should not, however, be interpreted as direct evidence that dyke intrusion produces greater calculated extension towards the north-east. Under the method applied here, the strain estimate is derived from the difference between L_0 and L_1 associated with mapped fault heave. Dyke intrusion is not independently resolved as fault-related horizontal extension in this calculation; where dyke width contributes to both measured section lengths, it does not generate an equivalent increase in the calculated fault-related elongation and may reduce the proportional strain estimate. The north-eastward increase from 62% to 91% therefore primarily reflects differences in the apparent extension expressed by the mapped fault population rather than a direct measurement of magmatic extension.

The spatial pattern nevertheless occurs within the broader structural evolution of the NMER, where deformation has progressively shifted from older border-fault systems towards younger axial fault and volcanic systems. Geological and geochronological studies indicate that Miocene extension was initially accommodated by major border faults, including the Ankober and Asela–Sire systems, whereas Quaternary deformation became increasingly concentrated within axial fault and magmatic systems on the rift floor (Ebinger and Hayward, 1996; Wolfenden et al., 2004; Corti, 2009; Agostini et al., 2011). Wolfenden et al. (2004) similarly distinguished the older border-fault systems bounding the rift from younger fault belts and volcanic chains within the Koka, Boset and Fentale–Dofan magmatic segments. The increase in calculated minimum apparent strain towards the north-east may therefore reflect spatial differences in the amount of extension expressed by mapped surface faulting within this evolving axial system. However, the present cross-sections alone do not demonstrate that the rift systematically becomes narrower from south-west to north-east, and the calculated strain values should not be used independently to infer changes in total rift width or the contribution of magmatic extension.

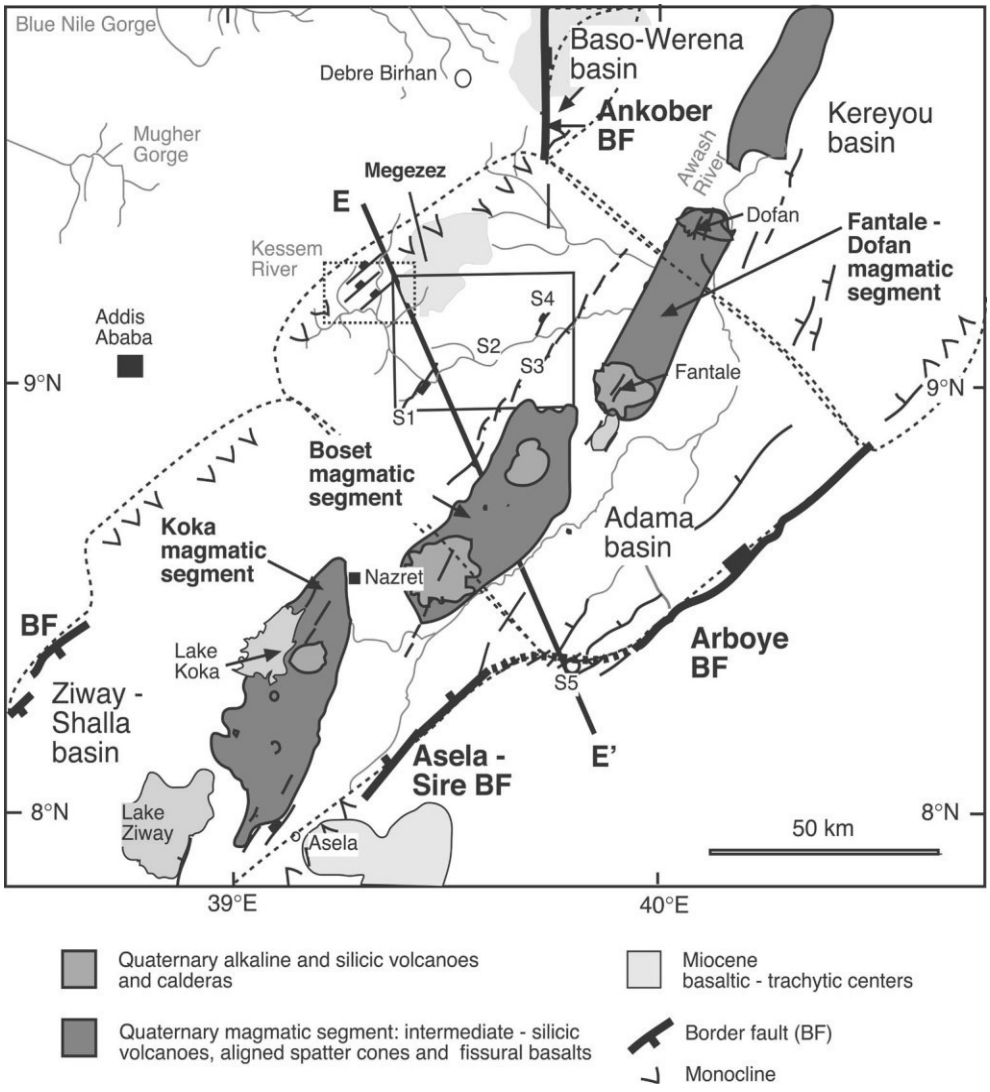


Figure 5.21: Summary tectonic map of the northern Main Ethiopian Rift (NMER), showing the Quaternary Koka, Boset and Fentale–Dofan magmatic segments, the major Miocene border faults (Ankober, Asela–Sire and Arboye) and the adjacent Baso–Werena, Adama, Ziway–Shalla and Kerayou basins. The map also shows the distribution and orientation of faults and volcanic centres within the axial magmatic segments relative to the older border-fault systems. S1–S5 indicate field sample locations in the original study, and E–E′ marks the location of the geological cross-section presented in Figure 3 of Wolfenden et al. (2004). Map simplified and modified after Wolfenden et al. (2004).

Within this structural framework, profiles B–B′ and C–C′ record higher minimum apparent elongation values (83% and 91%, respectively) than A–A′ (62%). B–B′ and C–C′ intersect the central and north-eastern parts of the NMER, where mapped faulting is associated with the axial volcanic and fault systems, including the Fentale–Dofan sector. In contrast, A–A′ crosses the southern part of the study area, where the mapped structural configuration differs in fault spacing, orientation and distribution. These spatial differences indicate that the amount of minimum apparent extension expressed by mapped surface faulting varies along the NMER. However, the cross-section results alone do not demonstrate that differences in rift width, fault spacing or magmatic activity directly cause the observed variation in elongation.

The Fentale and Dofan areas, together with faults associated with the axial Wonji Fault Belt, are characterised by numerous relatively short, closely spaced NNE-striking faults that are broadly subparallel to volcanic vent alignments within the Boset, Kone, Fentale and Dofan magmatic segments. Previous studies have demonstrated a close spatial relationship between faulting, volcanic centres and dyke intrusion within these magmatic segments (Casey et al., 2006; Keir et al., 2006, 2015). Geodetic and seismic observations also indicate that present-day deformation in the NMER is strongly localised within the axial magmatic system and that regional extension is accommodated by both faulting and magmatic intrusion (Keir et al., 2006, 2015).

This regional magmatic contribution must, however, be distinguished from the minimum apparent strain calculated in this study. The L_0–L_1 reconstruction primarily quantifies extension expressed by mapped surface-fault heave and does not independently resolve extension accommodated by dyke opening. Where dyke intrusion contributes to the measured section geometry without being reconstructed as fault heave, it would not produce a corresponding increase in calculated fault-related elongation and could reduce the proportional strain estimate. Consequently, the higher values along B–B′ and C–C′ should be interpreted as greater minimum apparent extension expressed by the mapped surface faults, rather than as evidence that dyke intrusion directly produced the higher calculated strain.

The spatial association between the mapped faults and axial magmatic segments is nevertheless consistent with the broader evolution of the NMER from deformation dominated by major border faults towards increasing localisation of Quaternary faulting and magmatism within the rift axis (Wolfenden et al., 2004; Corti, 2009; Acocella, 2014). The differences between A–A′, B–B′ and C–C′ therefore demonstrate along-rift variability in the amount of extension preserved by mapped surface faults. They do not, on their own, demonstrate a systematic south-west to north-east decrease in rift width or quantify the contribution of magmatic extension.

Taken together, the cross-section results and regional structural framework indicate that Zone 2 forms part of an evolving magma-rich continental rift in which deformation has become increasingly concentrated within axial fault and volcanic systems. However, the calculated elongation values represent minimum apparent fault-related extension and should not be interpreted as measurements of total regional strain or magmatic extension. These limitations are important when comparing Zone 2 with the more strongly magma-influenced rift setting examined in Chapter 6.

5.5 Conclusion

The principal findings from Zone 2 of the North Main Ethiopian Rift (NMER) are summarised as follows:

- A total of 900 surface-expressed normal faults were mapped in Zone 2. The overall fault population shows a positive displacement–length relationship described by Dmax = 0.7698L^0.6007 (R^2 = 0.2614), although substantial scatter indicates that fault length alone does not explain the full variation in maximum displacement.
- Displacement-profile analysis identified 280 smooth single-peak faults (~31%), 382 multi-peak faults (~42%) and 238 irregularly peaked faults (~26%). All three populations show statistically significant D–L relationships, with irregularly peaked faults displaying the highest scaling exponent and generally greater lengths and displacements.
- Fault segmentation and linkage are widespread within the axial fault system. Soft-linked faults are more common than hard-linked structures, while analysis of 63 hard-linked composite structures using total linked fault length gives Dmax = 0.6552L^0.6021 (R^2 = 0.2834, $p < 0.001$). The sub-linear relationship indicates that linkage can substantially increase total fault length without a proportional increase in Dmax.
- Fault frequency, Dmax and Dmax/L vary between geological surface units but do

not show a simple monotonic relationship with geological surface age. The observed variability reflects the combined influence of fault growth and linkage, geological setting, resurfacing, burial, erosion and preservation.

- Minimum apparent extensional strain increases from 62% along A–A′ to 83% along B–B′ and 91% along C–C′. These values represent minimum apparent extension expressed by the mapped surface faults and do not quantify total regional strain or magmatic extension.
- Overall, Zone 2 records rift-scale localisation of deformation within the axial fault and volcanic system, while individual faults retain a range of segmentation and linkage states. This indicates that rift-scale strain localisation can occur while fault-scale structural integration remains incomplete.

Chapter 6: Quantitative Analysis of the Spatial and Temporal Evolution of Normal Faults during an Advanced Stage of Rifting: The Eastern Afar Depression (EAD) and Ethiopia–Djibouti Transition Zone.

6.1 Introduction

The Eastern Afar Depression (EAD) within the Ethiopia–Djibouti transition zone, here defined as the border region between Ethiopia and Djibouti in eastern Afar, where continental rifting approaches incipient oceanic (Makris and Ginzburg, 1987; Moore et al., 2021; Rime et al., 2023), represents one of the most advanced rift sectors in the East African Rift System. The rift is characterised by stepping, overlapping grabens, systematic variations in fault orientation, and well-defined magmatic segments, which together reflect strong along-axis segmentation and late-stage rift development approaching incipient seafloor spreading (Corti, 2009; Bastow and Keir, 2011; Rime et al., 2023). At a broader scale, the EAD lies at the junction between the Afar and Gulf of Aden rift systems and accommodates the relative motion between the Nubian, Somali, and Arabian plates. A key kinematic control on rift geometry, fault orientations, and strain localisation in this region is the anticlockwise rotation of the Danakil Block (McClusky et al., 2010).

The magma-assisted character of the EAD is recognised from the spatial association between axial volcanic centres, fissure systems, dyke-related deformation and closely spaced normal faults within narrow magmatic segments (Kendall et al., 2005; Bastow and Keir, 2011; Moore et al., 2021; Rime et al., 2023). In such systems, extension may be accommodated by both brittle faulting and magma intrusion, particularly through dyke emplacement. Magmatic activity can therefore influence the location, orientation, segmentation and displacement of surface faults by modifying the local stress field and concentrating deformation around active volcanic and intrusive centres. Consequently, fault geometry and displacement in the EAD may record the combined effects of tectonic extension and magma-assisted deformation rather than purely tectonic fault growth.

This chapter analyses the spatial and temporal evolution of normal faults in Zone 3 of the EAD to evaluate how magma-assisted rifting and Danakil Block rotation are expressed in the fault geometry. Specifically, the chapter (i) maps and quantifies fault spatial distribution, apparent length (L), and maximum displacement (Dmax); (ii) classifies along-strike displacement–distance profiles into single-peak, multi-peak, and irregularly peaked types to describe how displacement is organised along individual scarps; and (iii)

documents fault segmentation and linkage style (soft versus hard) to assess connectivity and potential slip transfer at the surface, while recognising that subsurface linkage cannot be resolved directly from DEM morphology alone.

Cross-cutting relationships are also used to constrain relative fault timing and identify possible reorganisation of local stress fields that may be associated with plate-boundary kinematics and Danakil Block rotation. Finally, Dmax/L ratios were compared between mapped geological surface units to test whether fault scaling varies systematically with surface age. These ratios are not treated as direct measures of fault maturity because geological surface age may differ from fault age, while volcanic resurfacing, erosion and burial can modify the preserved fault morphology. Mapping and quantitative measurements were performed using a 30 m-resolution DEM and published surface age information for Afar (Rime et al., 2022).

6.2 East afar depression study zone 3

Zone 3 is located on the eastern flank of the Eastern Afar Depression (EAD), between the Tendaho–Goba'ad rift to the southwest and the Danakil Block to the northwest (Figure 6.1). The study area extends from approximately 11°15′ to 12°15′ N and 41°30′ to 42°30′ E and spans a pronounced topographic range, from elevations of more than 1,700 m along the Danakil Escarpment to areas below sea level along the rift axis (approximately −116 m below sea level, ~5 km west of Lake Karum). The regional setting of Zone 3, including its position relative to the Danakil Block, Afar Depression, Red Sea and Gulf of Aden rift systems, is shown in Figure 6.1a.

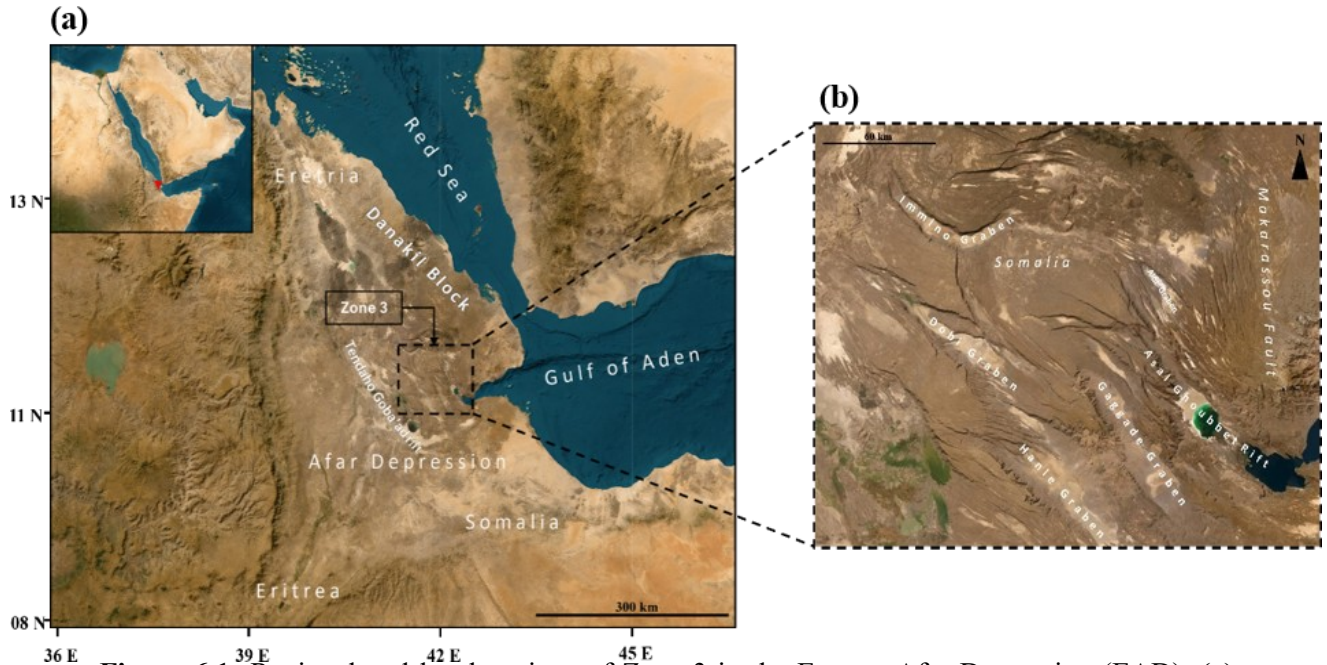


Figure 6.1: Regional and local settings of Zone 3 in the Eastern Afar Depression (EAD). **(a)** Regional map of the Afar Depression and Gulf of Aden showing the position of Zone 3 (dashed

box) on the eastern flank of the EAD between the Tendaho–Goba'ad Rift and the Danakil Block. **(b)** Enlarged view of Zone 3 showing the main grabens (Immino, Dobi, Hanlé, and Gaggadé) and the Asal–Ghoubbet basin, bounded to the east by the Makarrassou Fault. Country boundaries and coastlines are shown for reference purposes ((basemap from ASTER GDEM Version 3; NASA/METI/AIST/Japan Spacesystems and U.S./Japan ASTER Science Team, 2019).

Magma-assisted extension in Afar is characterised by the spatial association of axial volcanic centres, fissure systems, dyke-related deformation and closely spaced normal faults within narrow zones of extension (e.g. Kendall et al., 2005; Bastow and Keir, 2011). Dyke intrusion can modify the local stress field, promote fault initiation or reactivation and concentrate surface deformation around magmatic segments. Consequently, the geometry, segmentation and displacement of faults preserved at the surface may reflect the combined influence of tectonic extension and magmatic intrusion rather than purely tectonic fault growth.

Within this regional framework, the anticlockwise rotation of the Danakil Block provides an important kinematic context for deformation in Zone 3 (McClusky et al., 2010). Rotation of the block relative to the surrounding Nubian, Somali and Arabian plates may contribute to spatial variations in extension direction and local stress orientation across eastern Afar. This provides a potential kinematic framework for interpreting variations in fault orientation, cross-cutting relationships and strain localisation within Zone 3. The physiographic and structural configuration of Zone 3 therefore provides a suitable natural laboratory for investigating fault length, maximum displacement, displacement-profile characteristics and segmentation/linkage within an advanced magma-rich rift. However, the tectonic evolution of eastern Afar remains debated. Some studies interpret the region as representing an advanced stage of continental breakup in which strongly thinned continental lithosphere is progressively replaced or modified by magma-assisted extension, but where continental crust may still persist beneath parts of the rift. Other interpretations emphasise the oceanic-like character of the axial crust and suggest that parts of eastern Afar may represent an incipient form of seafloor spreading, with extension increasingly accommodated through magmatic intrusion and axial faulting rather than through distributed continental faulting (e.g. Ebinger and Casey, 2001; Bastow and Keir, 2011; Hammond et al., 2011; Chauvet et al., 2023).

These alternative models are important when interpreting the fault patterns quantified in this chapter. If Zone 3 represents highly thinned but persisting continental crust, the mapped fault geometries may principally record continued continental extension modified by increasing magmatic intrusion. Conversely, if the region is approaching an oceanic-style spreading regime, localisation of short, closely spaced and segmented axial

faults may reflect a greater contribution of magma-assisted extension and dyke-related deformation. The fault geometry and displacement data presented here cannot independently determine whether the underlying crust is continental, transitional or oceanic. Instead, they are used to evaluate how surface deformation is organised within this debated continental–oceanic transition and whether the mapped fault population is consistent with increasingly localised, magma-assisted rifting. Accordingly, interpretations of fault length, displacement, segmentation, linkage and orientation in Zone 3 are considered in the context of both tectonic extension and magmatic modification.

6.3 Results

6.3.1 Fault geometric analysis

A total of 1,250 normal faults were mapped in Zone 3 of the Eastern Afar Depression (EAD) from the 30 m DEM using geomorphological and structural criteria. The dataset was evaluated for spatial distribution and density, apparent fault length (L), and maximum displacement (D_{max}) to summarise the mapped fault characteristics.

6.3.1.1 Fault spatial distribution

Zone 3 fault traces have an irregular distribution and are organised into a series of overlapping grabens and intervening elevated blocks (Figure 6.2a). Large numbers of overlapping and intersecting normal faults occur along the margins of the main graben systems and on several high-standing footwalls, whereas few mapped fault scarps occur in the intervening basins and on the more gently sloping flanks, many of which are veneered by recent volcanic flows.

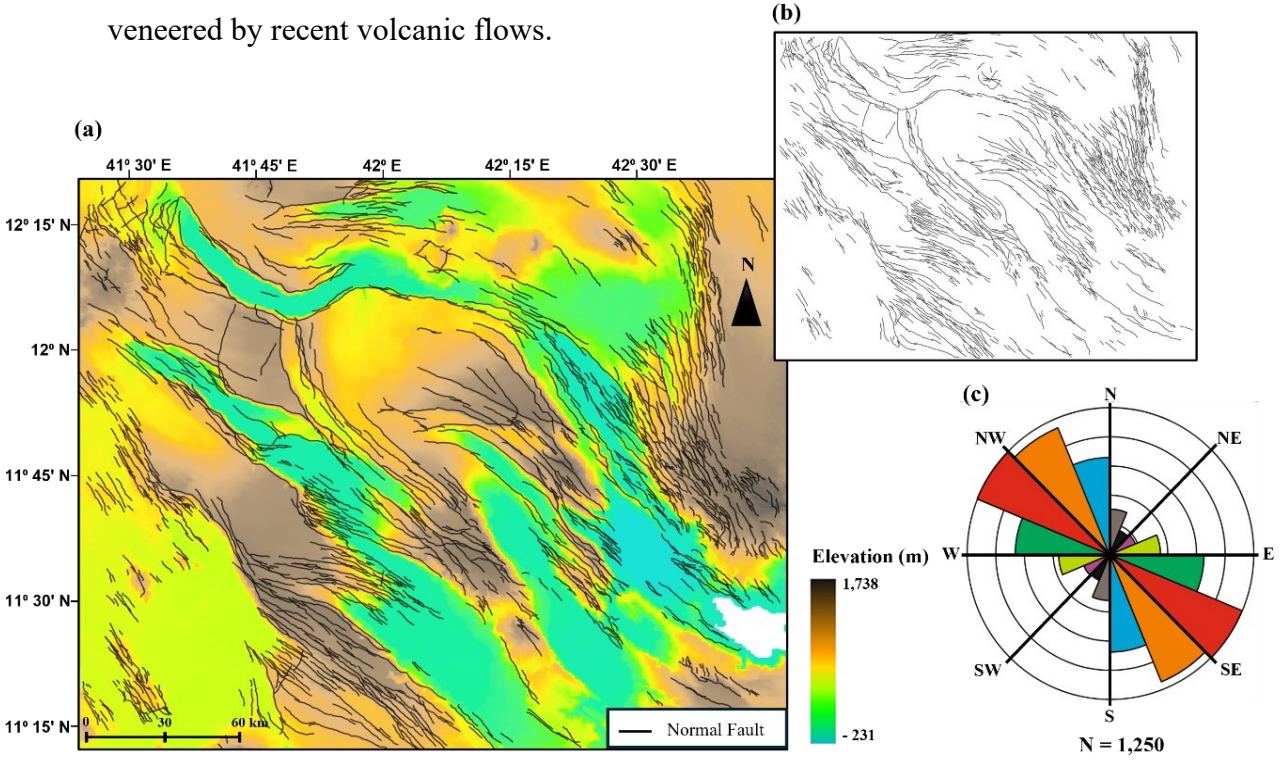


Figure 6.2 (a) Map of manually digitised normal fault traces from the 30 m-resolution DEM, showing the distribution of faults across Zone 3 in the Eastern Afar Depression (EAD). **(b)** Simplified line drawing of the mapped fault network. **(c)** Rose diagram showing the principal fault-orientation populations, dominated by NW–SE and NE–SW trends (n = 1,250). Basemap from ASTER GDEM v3 (NASA/METI/AIST/Japan Spacesystems and U.S./Japan ASTER Science Team, 2019).

The spatial relationship between mapped faults and surface geology was assessed using geological-unit classifications assigned to the mapped fault population. Detailed comparisons between fault characteristics and geological surface units are presented in Section 6.3.4. Fault density is spatially variable across Zone 3, with the highest

concentrations occurring along the principal graben margins and structurally complex fault corridors (Figure 6.3).

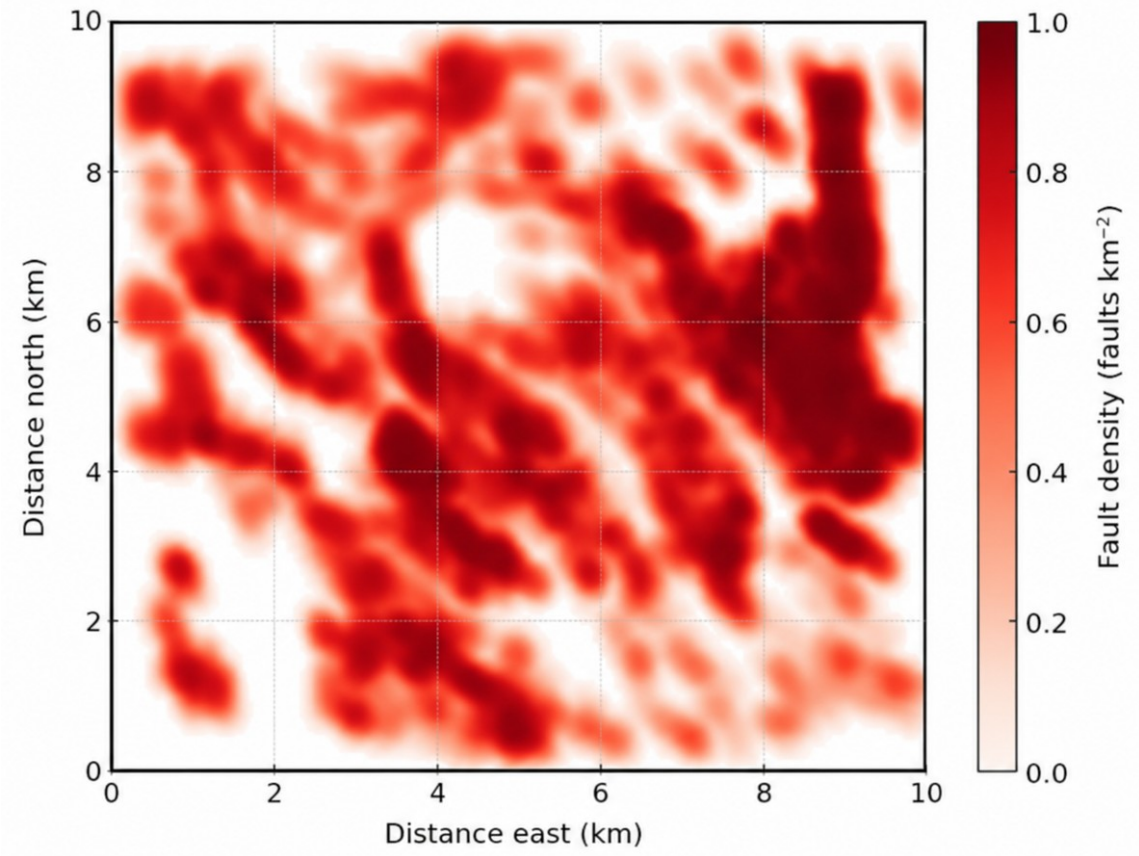


Figure 6.3: Fault-density map of Zone 3 showing spatial variation in mapped fault density (faults km^{-2}). Darker red areas represent zones of higher mapped fault concentration. Fault traces were manually mapped from the 30 m-resolution DEM, and the density surface was generated in QGIS.

The rose diagram for all faults in Zone 3 (Figure 6.2c) shows that NW–SE-trending faults represent the largest population and define the main structural trend in the region. Secondary populations of faults strike NE–SW, and smaller numbers of NNW–SSE, N–S and E–W faults are also present. In the map view (Figures 6.2a, b), NW–SE faults are particularly common along the Dobi, Hanle, and Gaggade grabens, whereas NE–SW to NNE–SSW faults are more widely spaced and locally link adjacent grabens or cut obliquely across their boundaries.

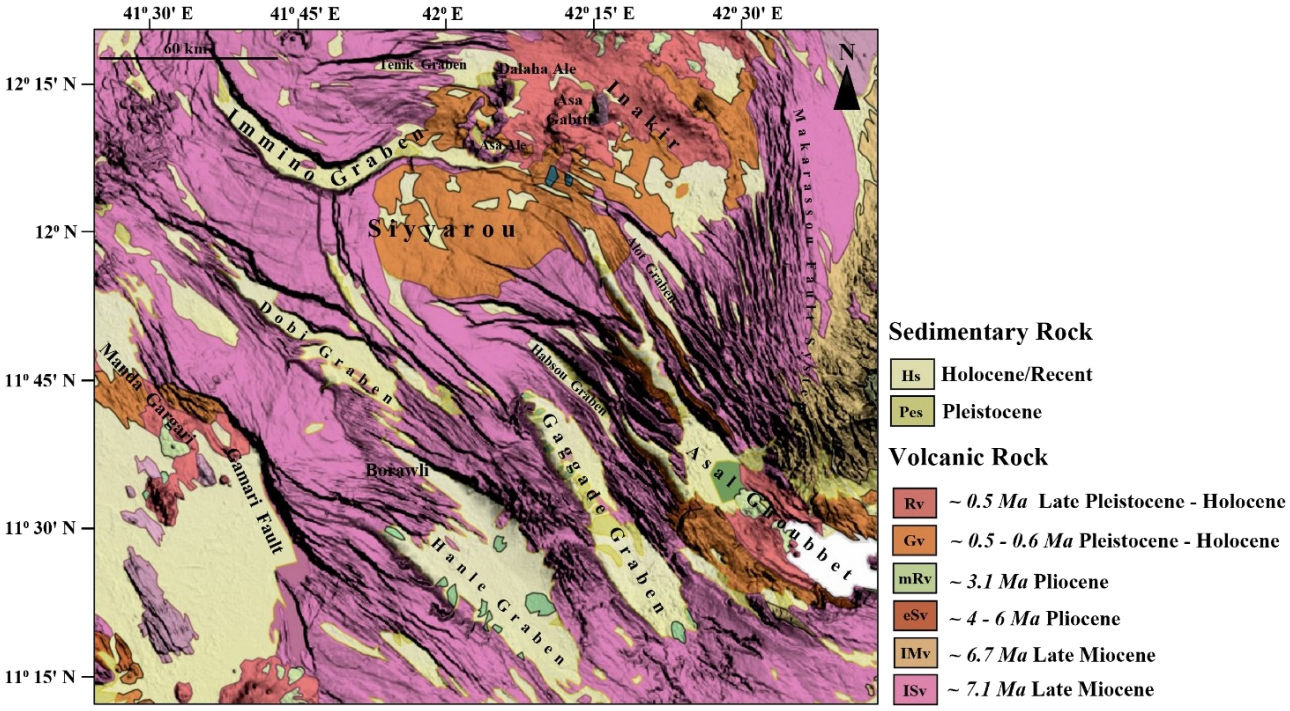


Figure 6.4: Geological and structural map of Zone 3 in the Eastern Afar Depression (EAD), showing the principal grabens (Immino, Dobi, Hanlé, Gaggadé and Asal–Ghoubbet), the Makarrassou and Gamari border faults, and intervening uplifted blocks. Volcanic and sedimentary surface units are colour-coded according to mapped age (Hs, Pes, Rv, Gv, mRv, eSv, IMv and ISv), with mapped normal fault traces shown in black. Basemap from ASTER GDEM v3 (NASA/METI/AIST/Japan Spacesystems and U.S./Japan ASTER Science Team, 2019); geology modified after Rime et al. (2022).

6.3.1.2 Fault Length (L)

Apparent fault length (*L*) ranges from 399 to 41,556 m, with a mean of 5,300 m across the mapped Zone 3 faults (Table 6.1). The longest mapped faults occur within the major graben systems (Figure 6.2a). The length–frequency distribution (Figure 6.6) is positively skewed, with most faults measuring ~2,000–7,500 m and a modal class of ~4,000–5,000 m. Faults longer than 20 km are uncommon and form the upper tail of the distribution.

Parameter	Min. (m)	Max. (m)	Mean (m)
Fault Length (*L*)	399	41,556	5,300
Maximum Displacement (D_{max})	13	1,215	181

Table 6.1: Summary statistics (*min–max–mean*) for apparent fault length (*L*) and apparent maximum displacement (D_{max}) of 1,250 normal faults in Zone 3 (EAD).

The log–log plot of apparent fault length (L) against apparent maximum displacement (Dmax) (Figure 6.5) shows a clear positive trend, with Dmax increasing systematically with L. Most data points plot between reference displacement–length envelopes of Dmax/L = 0.001 and 0.1, with the main cluster close to Dmax/L ≈ 0.01; the Dmax/L = 1

line is shown as an upper reference envelope. These reference lines are defined by Dmax = cL, where c = 1, 0.1, 0.01, and 0.001, and bracket the displacement–length ratios reported for normal faults in the published compilations (Walsh and Watterson, 1988; Cowie and Scholz, 1992; Kim and Sanderson, 2005; Lathrop et al., 2022).

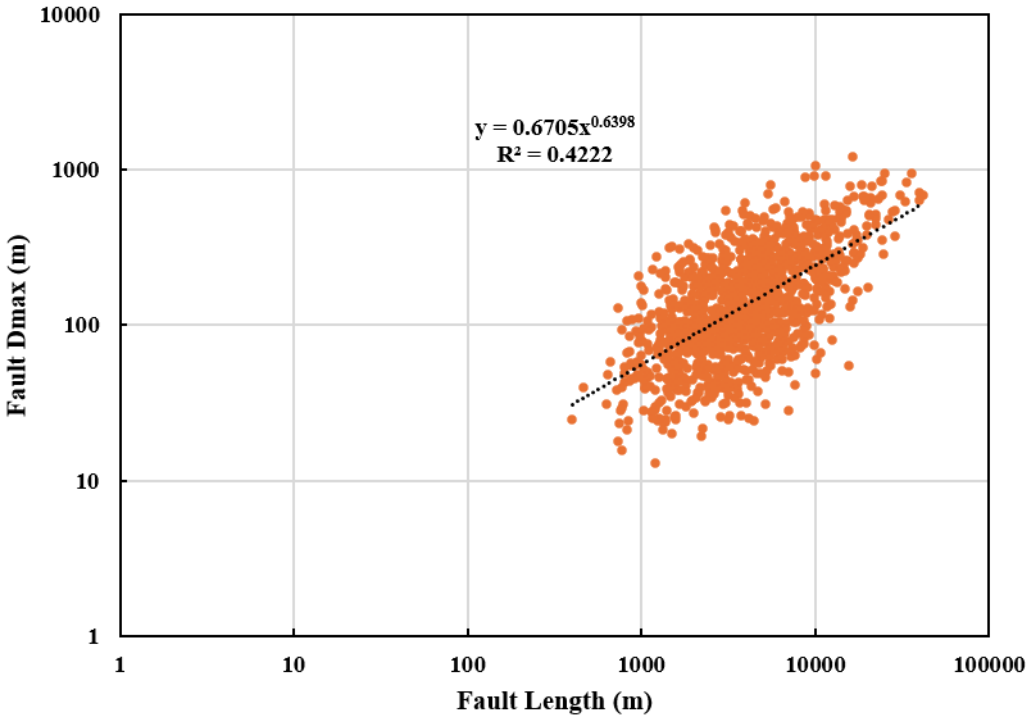


Figure 6.5: Log–log plot of apparent maximum displacement (Dmax) versus apparent fault length (L) for mapped normal faults in Zone 3. The data show an overall positive relationship described by the power-law regression Dmax = 0.6705L^0.6398 (R^2 = 0.4222). Most faults plot between the reference envelopes Dmax/L = 0.01–0.1, with fewer approaching Dmax/L = 0.001; the Dmax/L = 1 line is shown as an upper reference envelope. The reference lines follow Dmax = cL, where c = 1, 0.1, 0.01 and 0.001. (Walsh and Watterson, 1988; Cowie and Scholz, 1992; Kim and Sanderson, 2005; Lathrop et al., 2022).

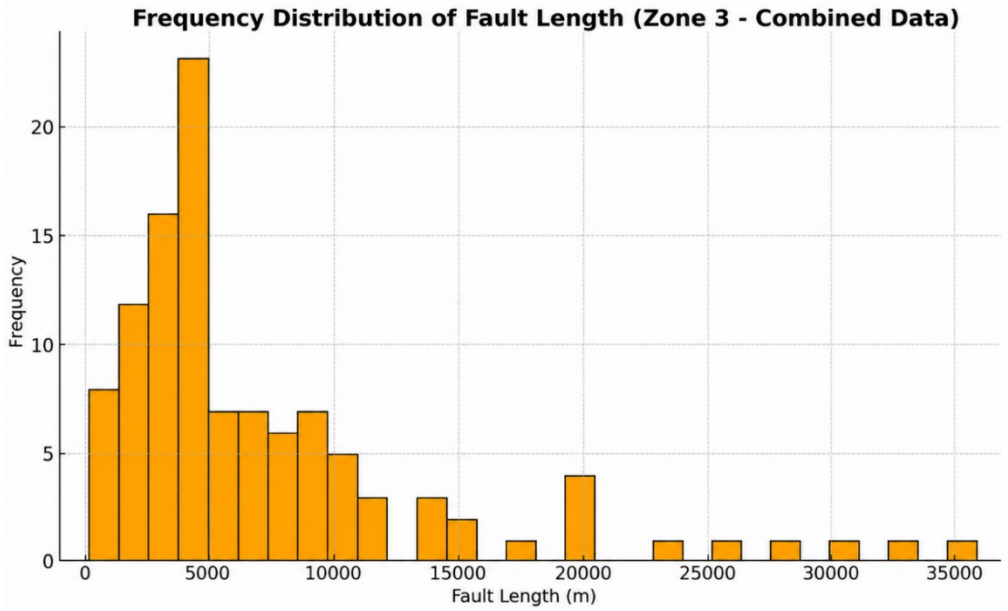


Figure 6.6: Frequency distribution of fault lengths in zone 3 of the EAD. The histogram shows a positively skewed distribution, with most faults between 2,000–7,500 m, and relatively few long faults exceeding 20,000 m.

6.3.1.3 Fault Maximum Displacement (D_{max})

Apparent maximum displacement (Dmax) ranges from 13 to 1,215 m, with a mean of 181 m (Table 6.1). The frequency distribution was positively skewed (Figure 6.7), with most faults having Dmax < 200 m and a smaller concentration at ~200–400 m. Displacements > 600 m are uncommon, and only a few faults reach Dmax ≥ 1,000 m, occurring within major graben systems.

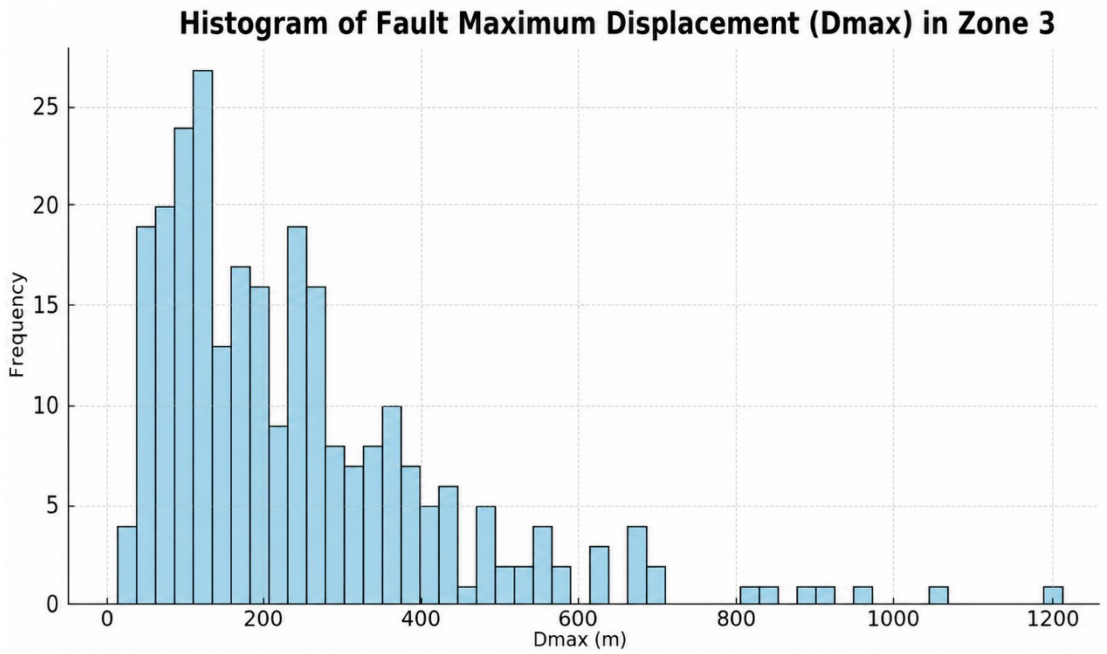


Figure 6.7: Histogram showing the frequency distribution of the apparent maximum displacement (D_{max}) for 1,250 normal faults in Zone 3 (EAD).

6.3.2 Fault displacement profile

This section describes the internal geometry of the faults in Zone 3 (EAD) based on the displacement–length (D–L) profiles derived from the mapped traces. Each fault is characterised by the number, amplitude, and spacing of the displacement maxima along the strike. The profiles were grouped into single, multi, and irregular peaks classes based on observable local maxima. This classification summarises the distribution of displacement along faults, independent of the process or maturity.

6.3.2.1 Single-peak profiles

In total, 112 faults (~9% of n = 1,250) exhibited a single-peak displacement profile, characterised by a broadly bell-shaped D–L curve with a continuous surface trace and no identified internal segmentation. Displacement reaches a single maximum approximately near the centre of the fault trace and generally decreases towards both ends. Fault lengths range from 399 to 5,142 m (mean = 1,625 m), and Dmax ranges from 22 to 307 m (mean = 84 m) (Table 6.2). Single-peak relationships are shown in Figure 6.8 relative to the

remaining fault-segment population, whereas two representative single-peak examples with no secondary maxima are illustrated in Figure 6.9.

Faults number (n=112)	Min. (m)	Max. (m)	Mean (m)
Fault Length (L)	399	5,142	1,625
Maximum Displacement (D_{max})	22	307	84

Table 6.2: Summary statistics (*min–max–mean*) for fault length (L) and D_{max} of single-peak displacement profiles in Zone 3 (n = 112).

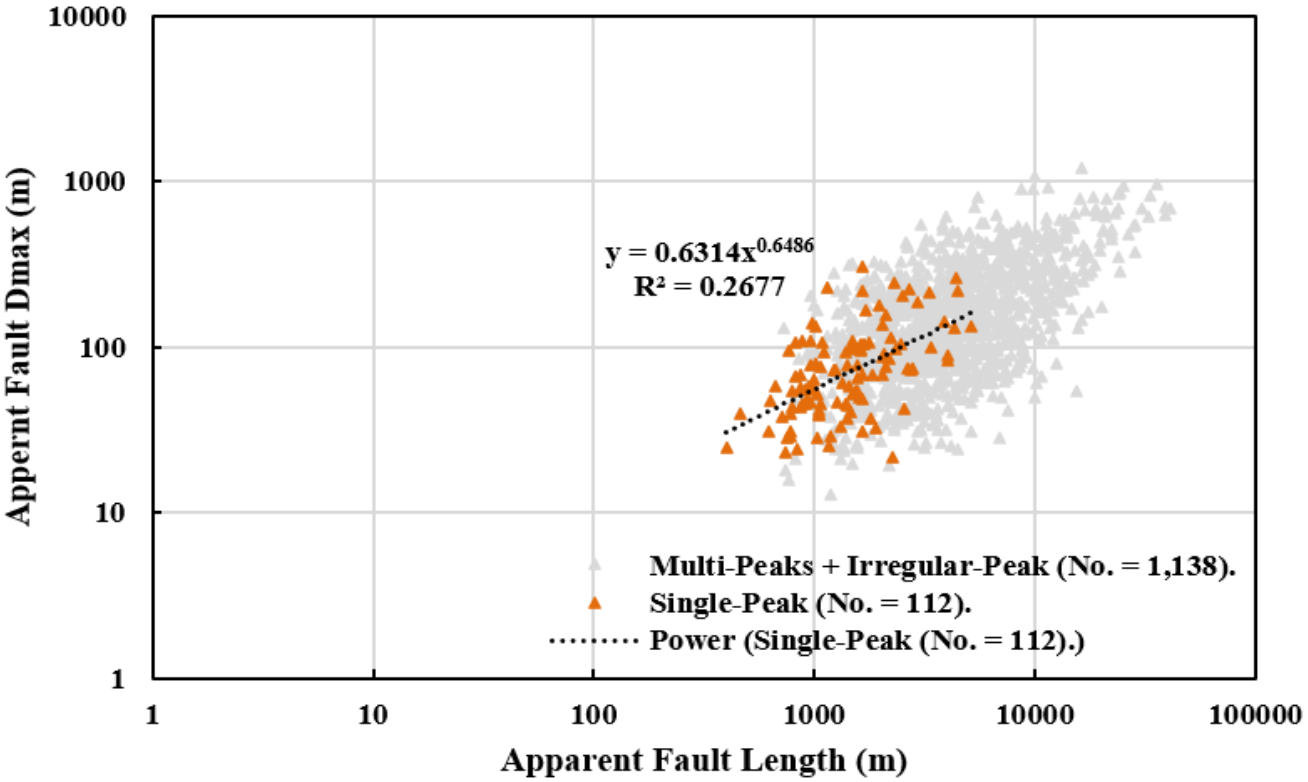


Figure 6.8: Log–log plot of apparent maximum displacement (Dmax) versus apparent fault length (L) for Zone 3, showing the remaining fault-segment population (grey; n = 1,138) and the single-peak fault population (orange; n = 112). The dotted line shows the power-law regression fitted to the single-peak faults Dmax = 0.6314L^0.6486 (R^2 = 0.2677, $p < 0.001$)..

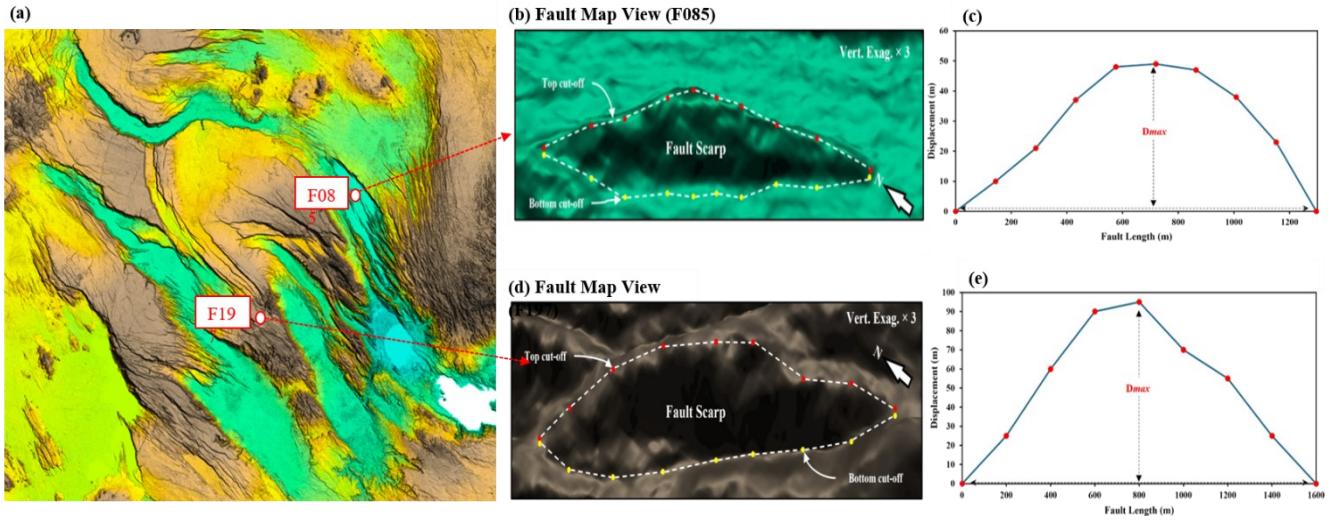


Figure 6.9: Examples of single-peak (bell-shaped) displacement profiles in Zone 3. **(a)** DEM showing the locations of representative faults F085 and F191. **(b)** Oblique DEM view of F085 showing the digitised top and bottom cut-offs and fault scarp (vertical exaggeration ×3). **(c)** Corresponding along-strike displacement–distance profile for F085, showing a single displacement maximum (Dmax). **(d)** Oblique DEM view of F191 showing the digitised top and bottom cut-offs and fault scarp (vertical exaggeration ×3). **(e)** Corresponding along-strike displacement–distance profile for F191, showing a single displacement maximum (Dmax).

6.3.2.2 Multi-peak profiles

Of the 1,250 faults, 542 (~43%) displayed multi-peak displacement–length (D–L) profiles, characterised by two or three prominent displacement peaks along strike. These faults range in length from 729 to 9,925 m (mean = 3,021 m), and their maximum displacements (Dmax) range from 13 to 701 m (mean = 139 m) (Table 6.3). Multi-peak faults occur primarily near the margins of the major grabens within the study area. In the log–log plot (Figure 6.10), multi-peak faults are highlighted relative to the remaining fault population. Representative faults F075 and F073 illustrate profiles containing two to three displacement peaks separated by intervening troughs (Figure 6.11).

Faults number (*n*=542)	**Min. (m)**	**Max. (m)**	**Mean (m)**
Fault Length (*L*)	729	9,925	3,021
Maximum Displacement (D_{max})	13	701	139

Table 6.3: Summary statistics (*min–max–mean*) for apparent fault length (*L*) and apparent maximum displacement (Dmax) of multi-peak displacement profiles in Zone 3 (*n* = 542).

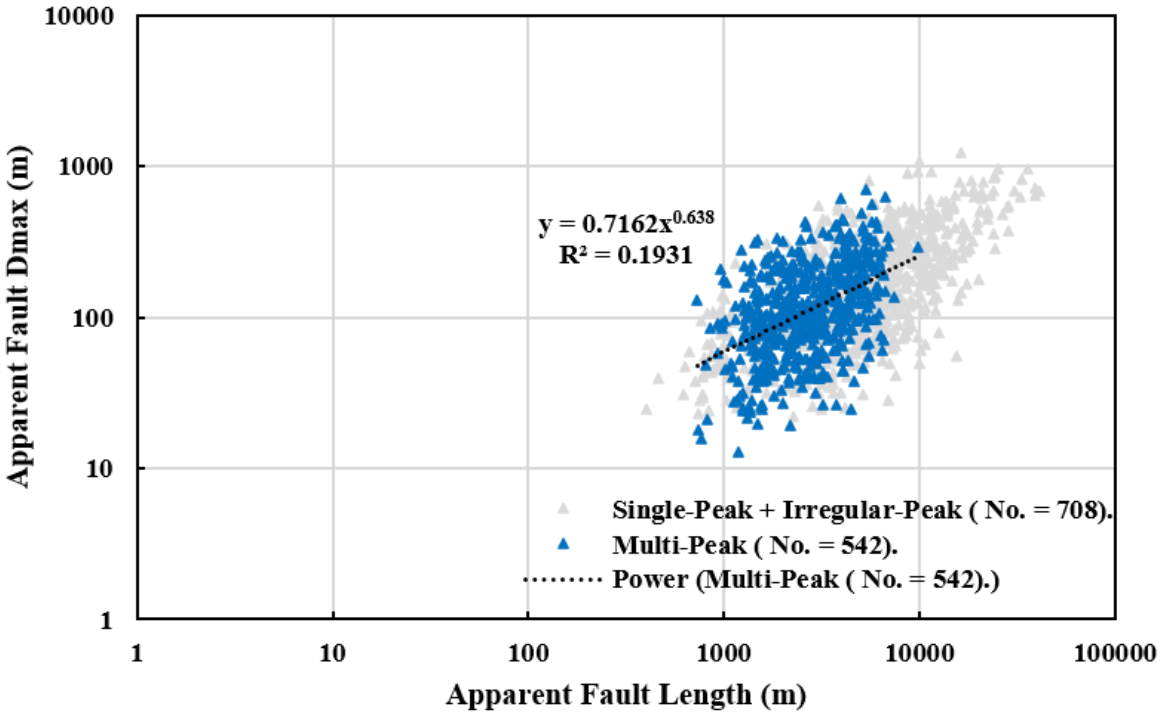


Figure 6.10: Log–log plot of apparent maximum displacement (Dmax) versus apparent fault length (L) for Zone 3, highlighting multi-peak faults (blue; *n* = 542) relative to faults with single-peak and irregular-peak displacement profiles (grey; *n* = 708). The dotted line shows the power-law regression fitted to the multi-peak population (Dmax = 0.7162L^0.638; R^2 = 0.1931).

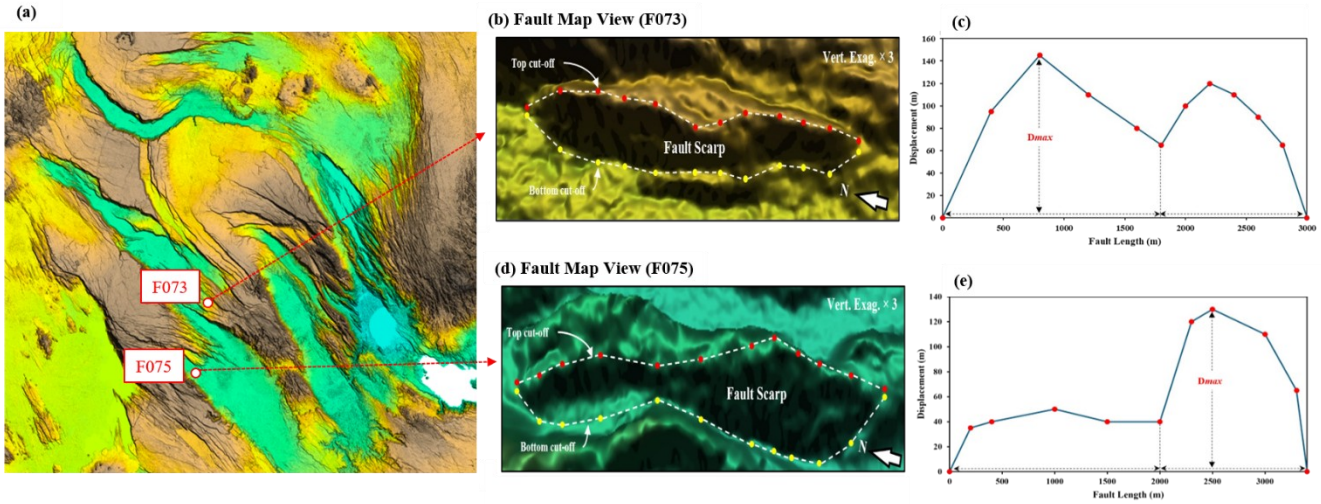


Figure 6.11: Examples of multi-peak displacement–distance profiles in Zone 3. **(a)** DEM showing the locations of representative faults F073 and F075. **(b)** Oblique DEM view of F073 showing the digitised top and bottom cut-offs and fault scarp (vertical exaggeration ×3). **(c)** Corresponding along-strike displacement–distance profile for F073, showing multiple displacement peaks separated by an intervening trough and the position of Dmax. **(d)** Oblique DEM view of F075 showing the digitised top and bottom cut-offs and fault scarp (vertical exaggeration ×3). **(e)** Corresponding along-strike displacement–distance profile for F075, showing multiple displacement peaks separated by intervening troughs and the position of Dmax.

6.3.2.3 Irregular-peak profiles

A total of 596 faults (~48% of n = 1,250) exhibit irregular-peak displacement–distance profiles, defined by four or more along-strike local maxima. This group includes the longest mapped faults in Zone 3. Apparent fault lengths range from 1,629 to 41,556 m (mean = 8,062 m), and Dmax ranges from 24 to 1,215 m (mean = 237 m) (Table 6.4). Irregular-peak profiles occur predominantly within and adjacent to the major graben systems and mapped subsidence corridors in Zone 3 (Figure 6.2a). In log–log space (Figure 6.12), this subset shows an overall positive relationship, with larger Dmax values generally associated with longer faults.

Faults number (n=596)	Min. (m)	Max. (m)	Mean (m)
Fault Length (L)	1,629	41,556	8,062
Maximum Displacement (D_{max})	24	1,215	237

Table 6.4: Summary statistics (*min–max–mean*) for apparent fault length (L) and apparent maximum displacement (Dmax) of irregular-peak displacement profiles in Zone 3 (n = 596).

Irregularly peaked profiles occur predominantly within and adjacent to the major graben systems and mapped subsidence corridors in Zone 3 (Figure 6.13a). In the log-log space (Figure 6.12), this subset follows an overall positive trend, with larger D_{max} values generally associated with longer faults.

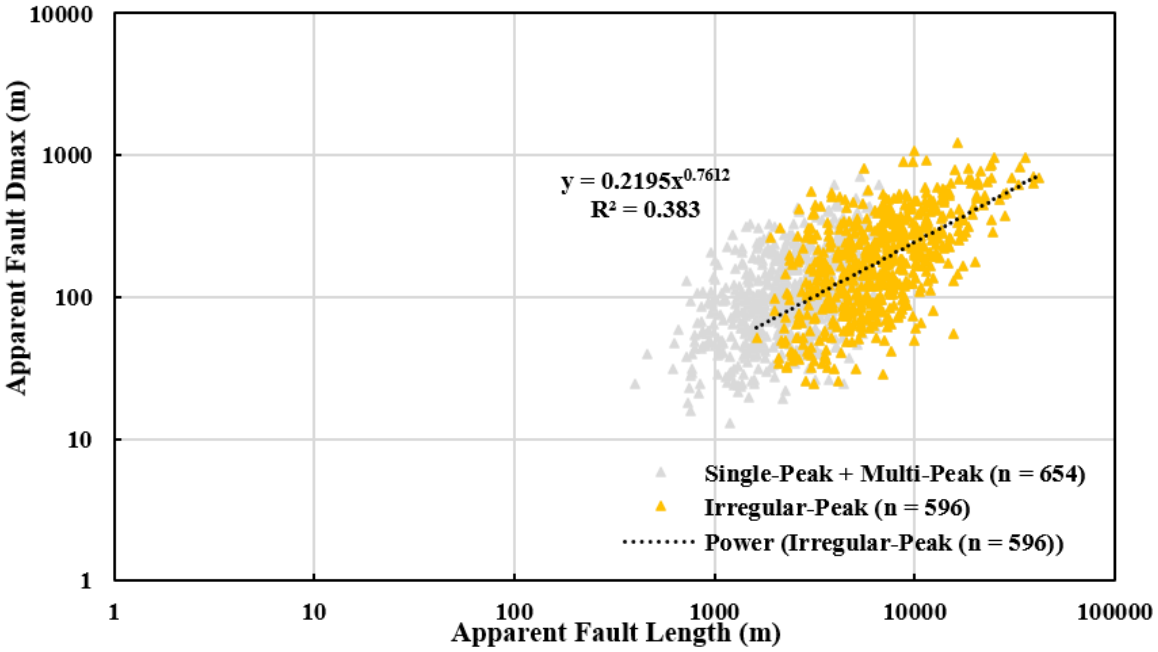


Figure 6.12: Log–log plot of apparent maximum displacement (Dmax) versus apparent fault length (*L*) for Zone 3 faults, highlighting irregular-peak profiles (yellow; *n* = 596) relative to the combined single-peak and multi-peak population (grey; *n* = 654). The dotted line shows the power-law regression fitted to the irregular-peak population (Dmax = 0.2195*L*^0.7612; R^2 = 0.383).

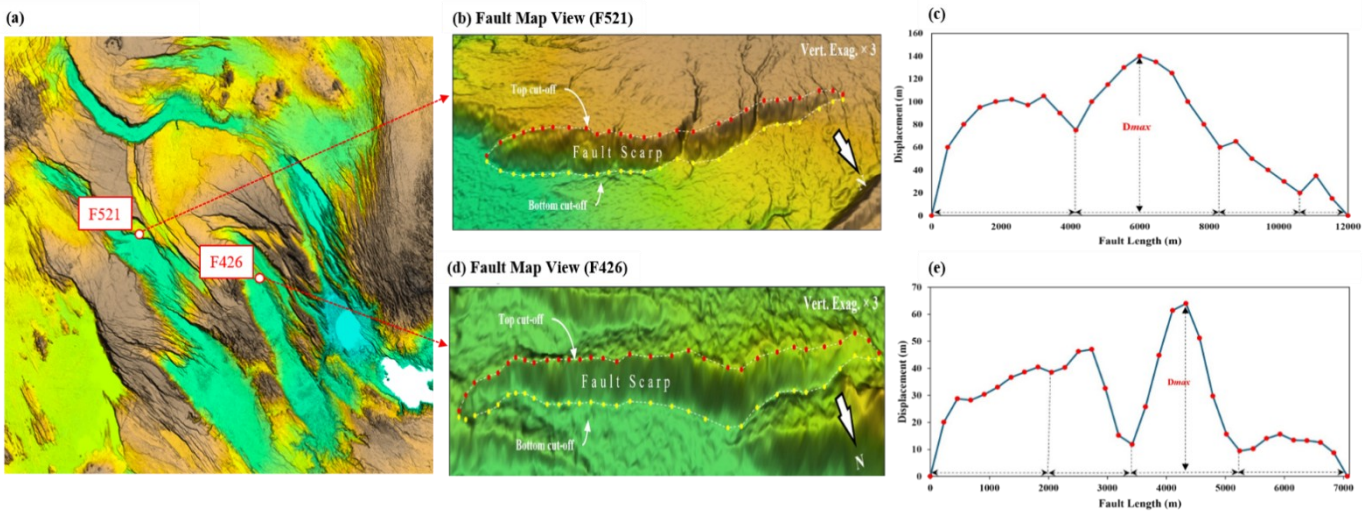


Figure 6.13: Examples of irregular-peak displacement–distance profiles in Zone 3. **(a)** DEM showing the locations of representative faults F521 and F426. **(b)** Oblique DEM view of F521 showing the digitised top and bottom cut-offs and fault scarp (vertical exaggeration ×3). **(c)** Corresponding along-strike displacement–distance profile for F521, showing multiple local displacement maxima and the position of Dmax. **(d)** Oblique DEM view of F426 showing the digitised top and bottom cut-offs and fault scarp (vertical exaggeration ×3). **(e)** Corresponding along-strike displacement–distance profile for F426, showing multiple local displacement maxima and the position of Dmax.

6.3.3 Fault segmentation and linkage

In Zone 3, linkage relationships were mapped from DEM surface traces and classified as soft or hard, based on the geometry of the adjacent mapped fault traces. In this section, a *fault trace* refers to an individual mapped surface scarp, and the term *segment* is avoided for single, isolated traces and is reserved for strands that form part of a larger fault zone in the linkage literature. Soft linkage is identified where neighbouring fault traces overlap or step but remains discontinuous, separated by a relay zone/relay ramp or a narrow deformation corridor. Hard linkage is identified where neighbouring traces are physically connected at the surface, producing a continuous, through-going scarp (e.g. Peacock and Sanderson, 1991; Peacock, 2002; Fossen and Rotevatn, 2016).

6.3.3.1 Soft linkage (SL)

A total of 298 mapped fault traces were classified as soft-linked (~ 24% of n = 1,250), where overlapping or closely spaced tips were separated by a relay zone or narrow deformation corridor. Soft-linked geometries occur throughout the study area and are common along the mapped graben margins and in areas of higher fault density. Displacement–distance profiles were extracted for these faults, and they commonly showed more than one along-strike local maximum.

6.3.3.2 Hard linkage (HL)

A total of 97 mapped fault traces were classified as hard linked (~8% of n = 1,250), forming continuous surface scarps with no observable gaps between adjacent traces. These hard-linked scarps occur mainly within the principal graben systems and align with the dominant rift-related fault trends in map view.

To examine the effect of hard linkage on displacement–length (D–L) scaling in Zone 3, the constituent faults belonging to each physically connected hard-linked system were combined and treated as a single composite fault structure. Total linked fault length was calculated as the sum of the lengths of the constituent faults, while Dmax was taken as the maximum displacement recorded within each composite structure. This produced 65 complete hard-linked composite structures for the scaling analysis.

When plotted using total linked length, the hard-linked composite structures show a statistically significant positive relationship between total fault length and maximum displacement, described by Dmax = 1.2422L^0.5623 (R^2 = 0.3977, $p < 0.001$; n = 65). The sub-linear exponent (n = 0.5623) indicates that Dmax increases with total linked fault

length, but at a lower rate than fault length itself. The moderate R^2 value indicates that substantial variability remains among composite hard-linked structures of similar total length. Compared with the non-hard-linked population, the hard-linked structures extend towards the longer-length part of the Zone 3 D–L distribution, indicating that structural linkage increases the effective length of the fault system without a proportional increase in maximum displacement.

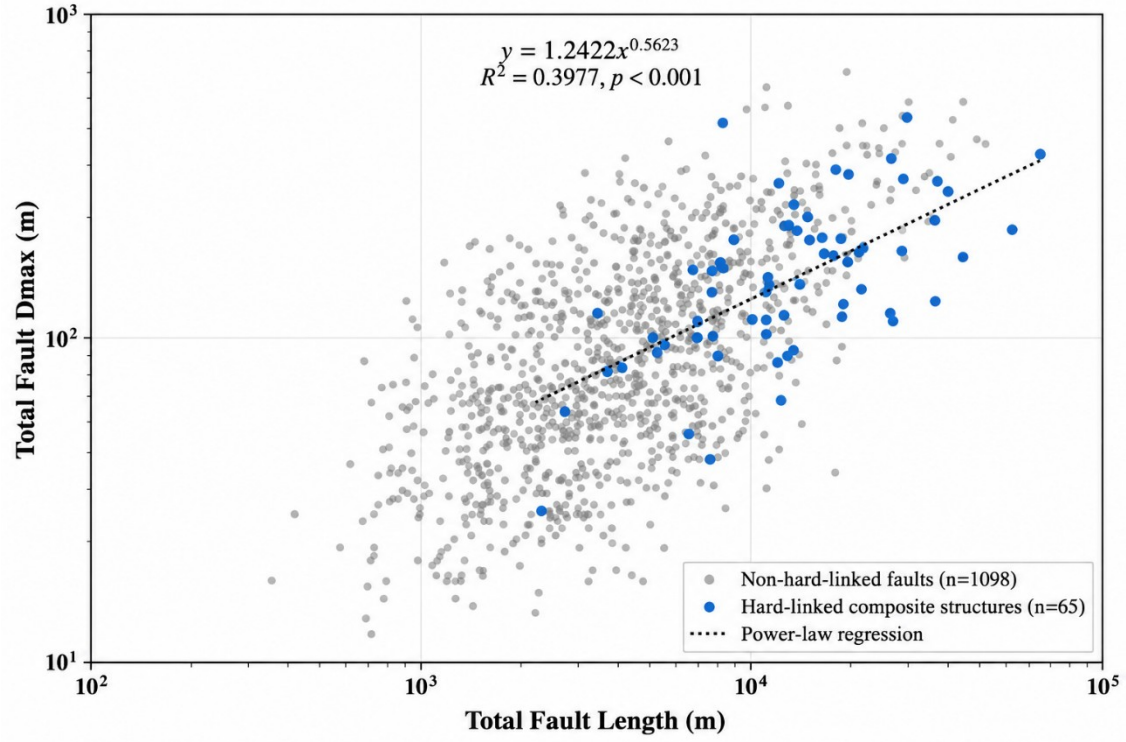


Figure 6.14: Log–log plot of maximum displacement (Dmax) versus total fault length (L) for hard-linked and non-hard-linked faults in Zone 3 of the Eastern Afar Depression (EAD). Hard-linked faults are plotted using the total length of each connected hard-linked structure rather than the lengths of individual constituent segments. Non-hard-linked faults are shown for comparison. The fitted power-law regression for the hard-linked composite population is Dmax = 1.2422L^0.5623 (R^2 = 0.3977, p < 0.001; n = 65).

6.3.4 Fault distribution across surface units

The mapped fault dataset (n = 1,250) was classified according to the surface geological units exposed across Zone 3 using the geological map of Rime et al. (2022) and the tectonostratigraphic framework of Rime et al. (2023). The mapped units comprise volcanic and sedimentary rocks ranging from Miocene to Holocene age (Table 6.5). To investigate whether fault characteristics vary systematically with geological surface age, fault abundance, apparent fault length (*L*), apparent maximum displacement (Dmax), and the normalised displacement-to-length ratio (Dmax/*L*) were compared between geological units.

Type of rock	Code	Geological unit (concise)	Approximate age range (Ma)
Volcanic	**M2v**	Manda Rift Volcanics	~19–8
	Pov	Pliocene volcanics	~5–2.5
	Q1v	Early Pleistocene volcanics	~2.5–1.1
	Q2v	Early Mid Pleistocene volcanics	~1.1–0.6
	Q3v	Mid-Pleistocene–Recent volcanics	<~0.6
Sedimentary	**Pes**	Pleistocene sediments	~2.58–0.0117
	Hs	Holocene sediments	~0.0117–0

Table 6.5: Summary of the volcanic and sedimentary geological surface units used to classify faults in Zone 3 of the Eastern Afar Depression (EAD). Units within each rock-type group are arranged in approximate chronological order from oldest to youngest. Geological-unit codes, concise descriptions and approximate age ranges are shown to clarify the classifications used in the fault-frequency, L–Dmax and Dmax/L analyses.

The geological-unit terminology used in Zone 3 was reviewed to reconcile differences with the unit nomenclature used elsewhere in the thesis. In particular, the ISv label shown on the Zone 3 geological map (Figure 6.4) refers to a volcanic unit assigned an age of approximately 7.1 Ma in the geological framework used for eastern Afar. This unit should not be directly equated with the younger volcanic unit labelled ISv in Zone 1, which was assigned an age of approximately 2.5 Ma. The identical abbreviation therefore represents different age assignments in the geological source frameworks used for the two study areas. To avoid interpreting the abbreviation itself as indicating equivalent stratigraphic age, the Zone 3 fault–surface-unit analysis uses the harmonised geological-unit codes and age ranges listed in Table 6.5.

The distribution of mapped faults is strongly uneven between geological units (Figure 6.15). Q1v contains the largest proportion of the mapped fault population, whereas substantially fewer faults occur within the remaining surface units. When the units are

considered in approximate chronological order, however, fault abundance does not show a simple monotonic relationship with geological surface age. Fault frequency therefore cannot be interpreted solely as a function of the age of the exposed geological surface.

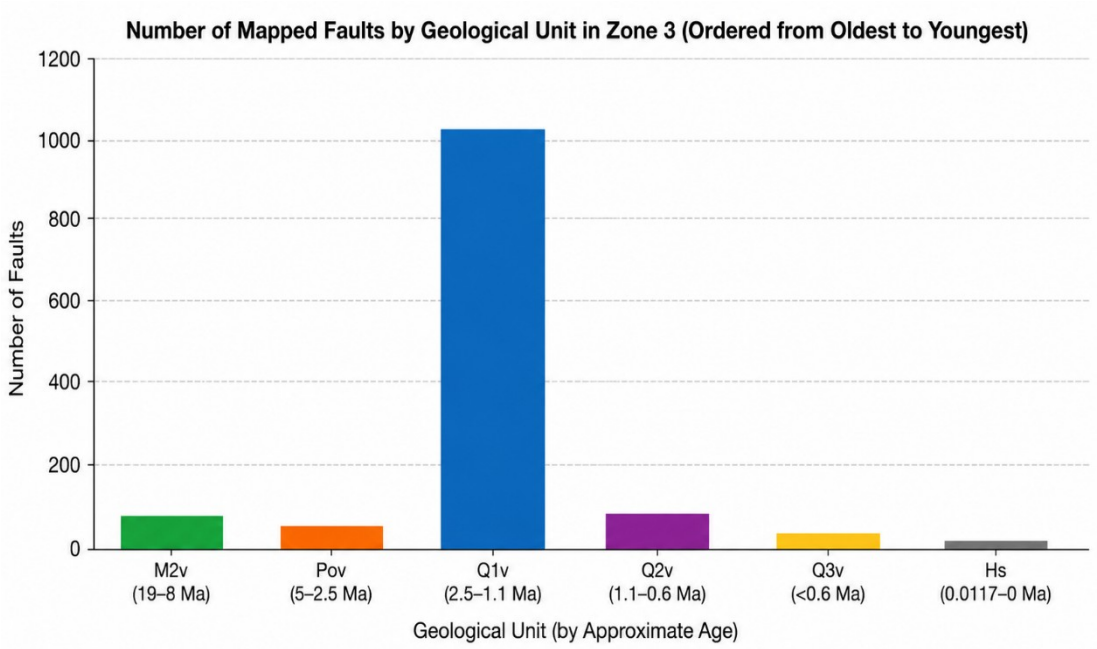


Figure 6.15: Number of mapped faults classified according to geological surface unit in Zone 3 of the Eastern Afar Depression (EAD). Geological units are arranged in approximate chronological order from old to young based on their mapped age ranges. The Early Pleistocene volcanic unit (Q1v) contains the largest proportion of the mapped fault population. Fault abundance does not show a simple monotonic relationship with geological surface age.

Apparent fault length and Dmax show an overall positive relationship, but considerable overlap occurs between geological units (Figure 6.16). Q1v spans a broad range of fault lengths and maximum displacements, while the other units occupy overlapping regions of *L*–Dmax space. This indicates that geological surface age alone does not account for the observed variation in fault size.

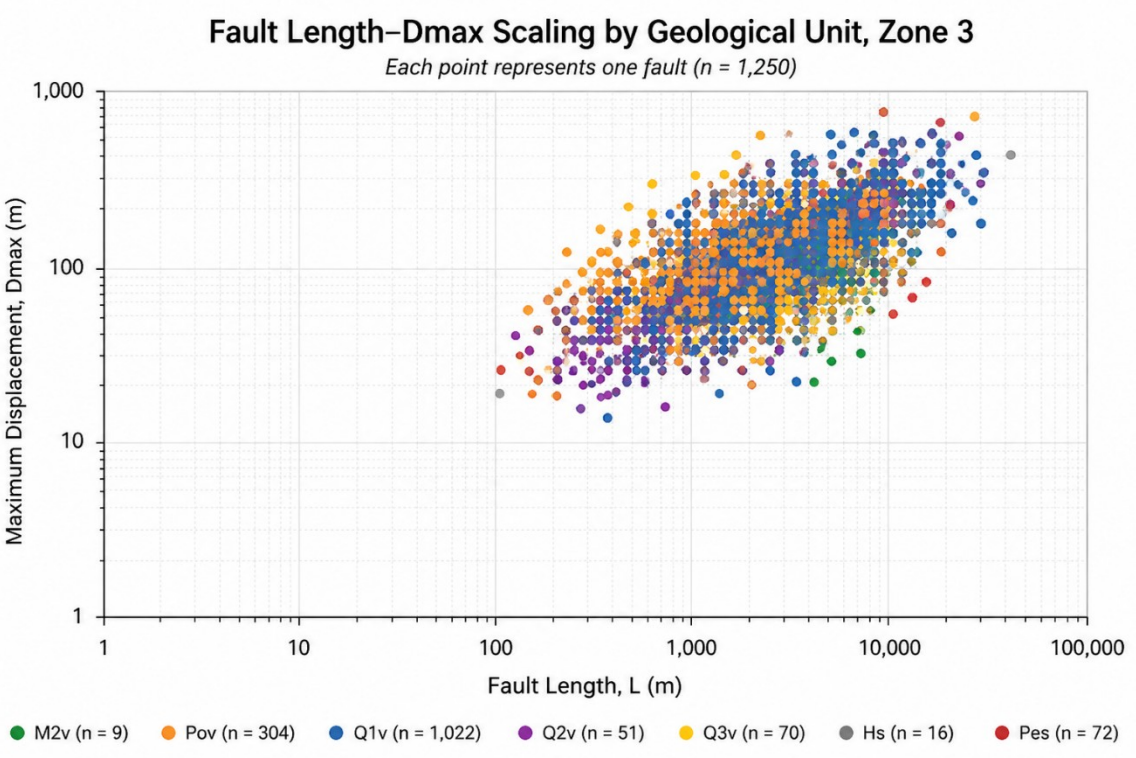


Figure 6.16: Log–log plot of apparent fault length (*L*) against apparent maximum displacement (Dmax) for faults classified according to mapped geological surface unit in Zone 3 of the Eastern Afar Depression (EAD). Each point represents an individual mapped fault (n = 1,250), with colours indicating the geological surface units. The Q1v unit contains the largest mapped fault population and spans a broad range of fault lengths and maximum displacements. Considerable overlap occurs between the geological units, indicating that fault size does not show a simple systematic relationship with geological surface age.

Maximum displacement also varies substantially within and between geological units (Figure 6.17). Although several volcanic units contain faults with relatively large Dmax values, their distributions overlap considerably. The age-ordered comparison therefore does not define a simple monotonic relationship between maximum fault displacement and geological surface age. Consequently, older geological surfaces do not systematically contain faults with greater maximum displacement than younger surfaces.

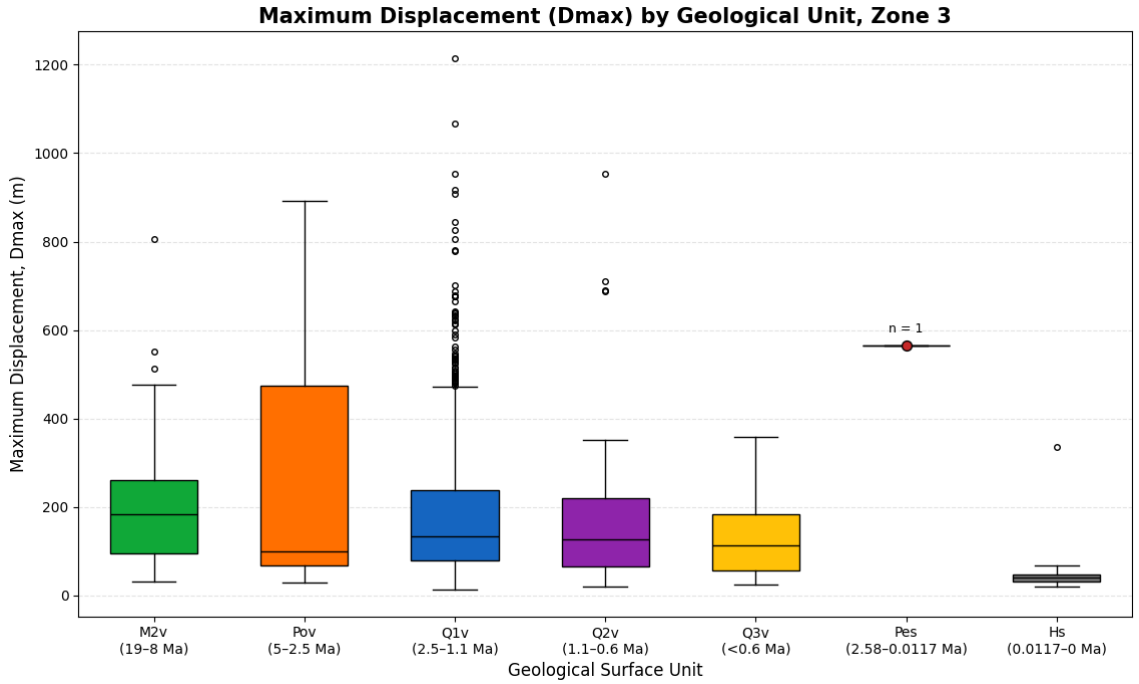


Figure 6.17: Boxplots of apparent maximum displacement (Dmax) for faults classified according to mapped geological surface unit in Zone 3 of the Eastern Afar Depression (EAD). Volcanic units are arranged in approximate chronological order from oldest to youngest, followed by the sedimentary units. The distributions show substantial variability and overlap between geological units and do not define a simple monotonic relationship between maximum fault displacement and geological surface age. The Pleistocene sedimentary unit (Pes) contains only one mapped fault ($n = 1$) and is therefore represented by a single observation.

Similarly, Dmax/L varies between geological units (Figure 6.18). M2v displays a comparatively broad range of Dmax/L values, whereas substantial overlap occurs between the remaining geological units. When considered together with fault abundance, L–Dmax scaling and Dmax, the Dmax/L distributions do not define a simple systematic progression with geological surface age. The observed variations therefore indicate that geological surface age alone does not explain differences in fault geometry across Zone 3.

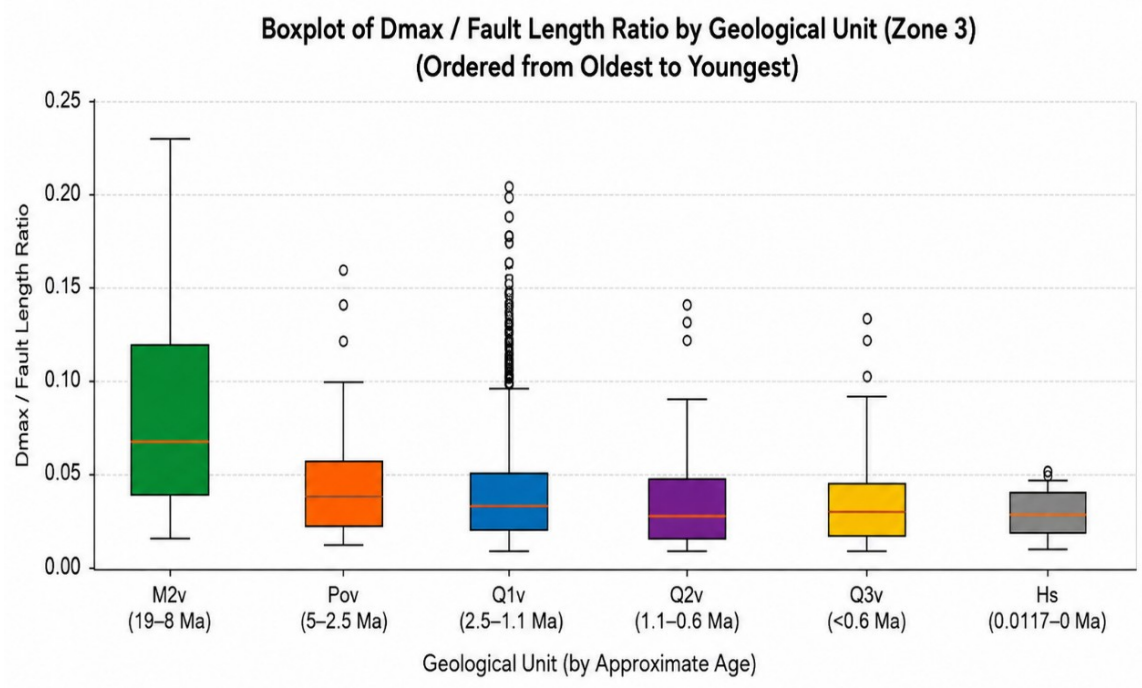


Figure 6.18: Boxplot showing the distribution of Dmax/fault length (D_{max}/L) ratios for faults within different geological units in Zone 3 of the Eastern Afar Depression (EAD). Faults in the Manda Rift Volcanics (M_2v) display the widest range of values, whereas younger volcanic and sedimentary units (Q_3v, Q_2v, Pov, and Hs) exhibit narrower distributions. The Early Pleistocene volcanic unit (Q_1v) contains the largest fault population with a moderate central tendency and numerous outliers.

6.3.5 Cross-cutting analysis

Fault orientation and cross-cutting relationships in Zone 3 were characterised by digitising all scarps on the 30 m DEM and checking their geometry against orthorectified Google Earth imagery in both plan view and oblique 3-D perspective (Figure 6.18). This mapping defines four main orientation sets: Set A, broadly E–W faults; Set B, NW–SE faults; Set C, NNW–SSE faults; and Set D, N–S to NNE–SSW faults. These sets were unevenly distributed, with Set A dominant in the north and centre, Set B forming dense swarms in the central and southern parts, Set C extending across much of the area, and Set D concentrated along the eastern side of the zone. Where these sets meet, they commonly overlap and crosscut.

In the western part of Zone 3, a prominent Set A E–W scarp forms the southern edge of the graben, and several shorter Set D N–S scarps intersect the scarp. On the DEM, the E–W scarp is a single continuous feature, whereas none of the N–S scarps continue beyond their intersection with this structure. The N–S scarps lose relief at the intersections, whereas the E–W scarp maintains a pronounced relief along its length, indicating that the E–W fault formed before the N–S faults in this area (Figure 6.20).

In the central part of the zone, Set A E–W scarps are cut by Set B NW–SE faults. The DEM shows E–W scarps truncated or slightly displaced at the intersection points, whereas

the NW–SE faults remain straight and continuous across the earlier topography in both 2-D and 3-D views. Therefore, the E–W faults predate the NW–SE faults (Figure 6.21). In the eastern part of Zone 3, Set D N–S scarps were intersected by Set C NNW–SSE faults. At the intersections, the N–S scarps terminated or broke into short segments, whereas the NNW–SSE faults maintained continuous linear traces across them in both datasets. These relationships show that in this sector, the N–S faults formed before the NNW–SSE faults (Figure 6.22). Relative timing is only assigned where these termination and continuity patterns are clear and consistent in both DEM and Google Earth imagery.

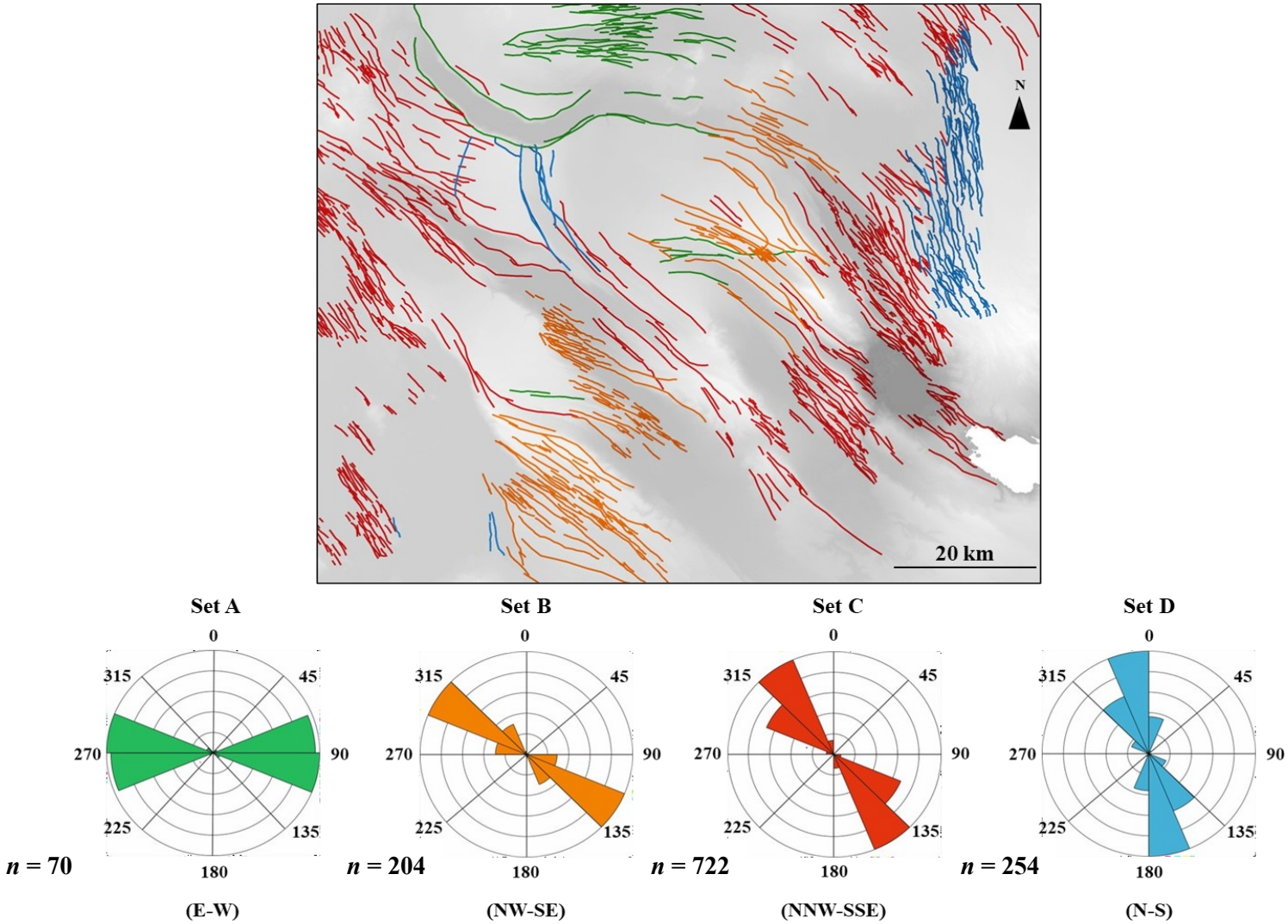


Figure 6.19: Fault orientation sets in Zone 3. Faults were digitised from the DEM map (Hillshade) and colour-coded by orientation: Set A (green; broadly E–W), Set B (orange; NW–SE), Set C (red; NNW–SSE) and Set D (blue; N–S to NNE–SSW). The map shows the spatial distribution of each set and the zones where differently oriented faults overlap, particularly in the central and eastern parts of the study area. The rose diagrams below the map summarise the dominant strike of each orientation set using the same colour scheme (ASTER GDEM v3; NASA/METI/AIST/Japan Spacesystems and U.S./Japan ASTER Science Team, 2019).

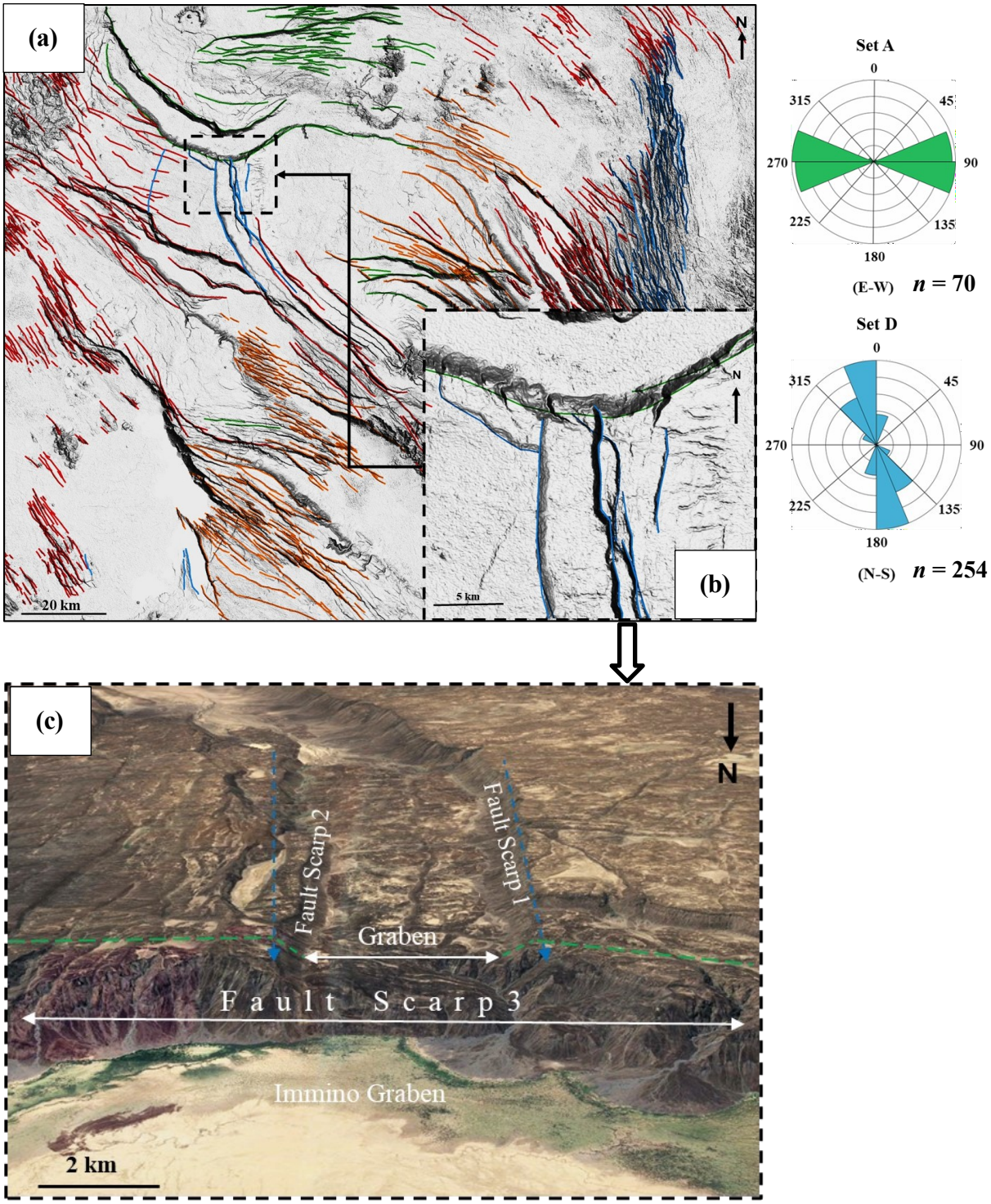


Figure 6.20: (**a)** The map shows Set A (green) and Set D (blue) faults in the western part of Zone 3, with rose diagrams indicating their dominant orientations. **(b)** Enlarged DEM view of the Immino Graben margin, where a continuous E–W scarp (Set A) is intersected by several shorter N–S scarps (Set D) that terminate against it. **(c)** Google Earth oblique perspective of the same area. The long E–W escarpment (Fault Scarp 3) forms the main graben margin, whereas two shorter N–S scarps (Fault Scarps 1 and 2) die out against it, confirming the mapped cross-cutting geometry (DEM basemap from ASTER GDEM v3; NASA/METI/AIST/Japan Spacesystems and U.S./Japan ASTER Science Team, 2019; imagery from Google Earth™, accessed 2025).

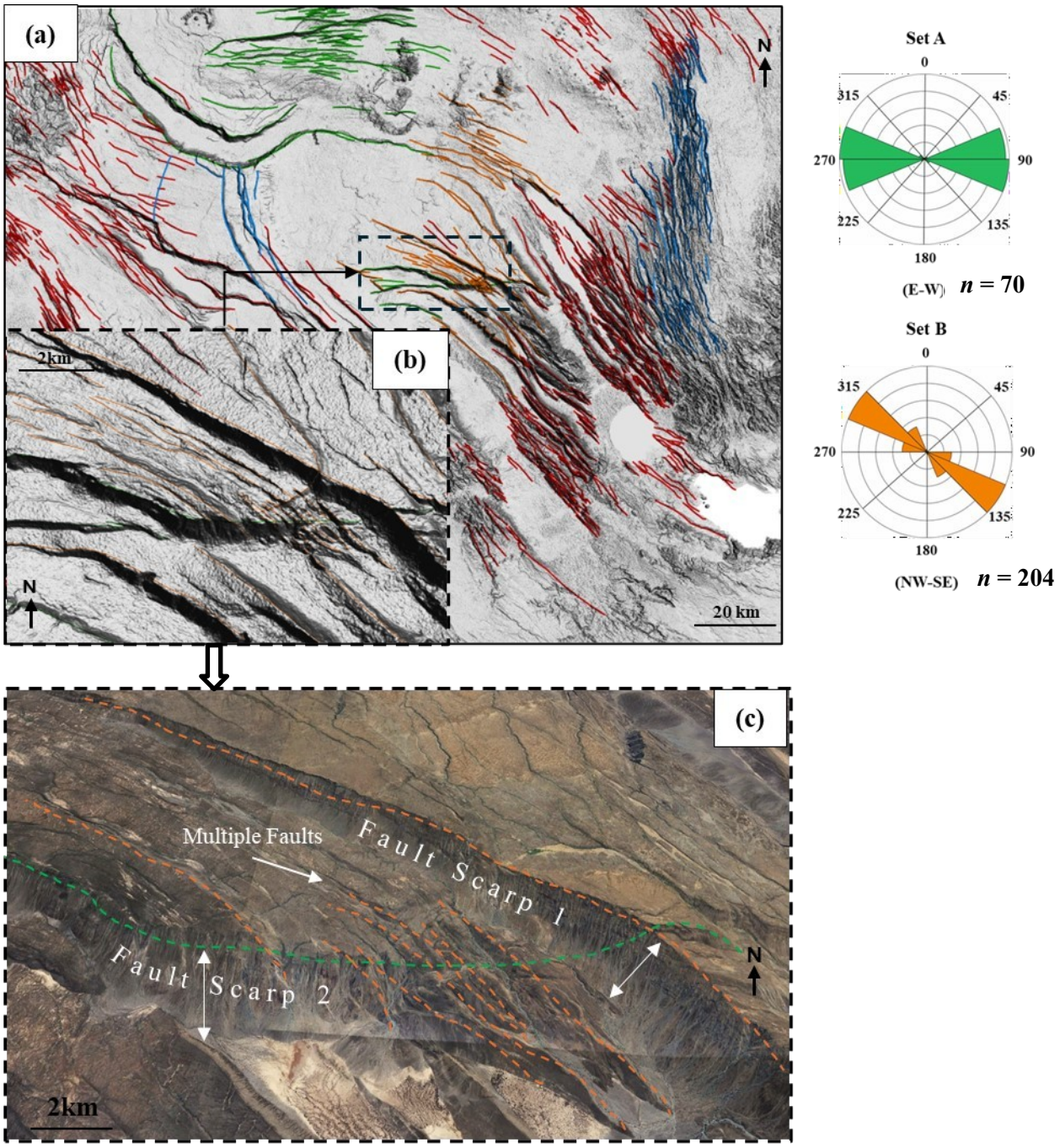


Figure 6.21: (a) Map showing Set A (green) and Set B (orange) faults, with rose diagrams illustrating their strike ranges. **(b)** Zoomed DEM panel highlighting a zone where sub-parallel E–W scarps are truncated or slightly offset at intersections with NW–SE faults that remain straight and continuous. **(c)** Google Earth oblique view of the same sector showing a long E–W escarpment (Fault Scarp 1) overprinted by multiple NW–SE scarps (Fault Scarp 2 and associated faults), confirming the cross-cutting relationship (DEM basemap from ASTER GDEM v3; NASA/METI/AIST/Japan Spacesystems and U.S./Japan ASTER Science Team, 2019; imagery from Google Earth™, accessed 2025).

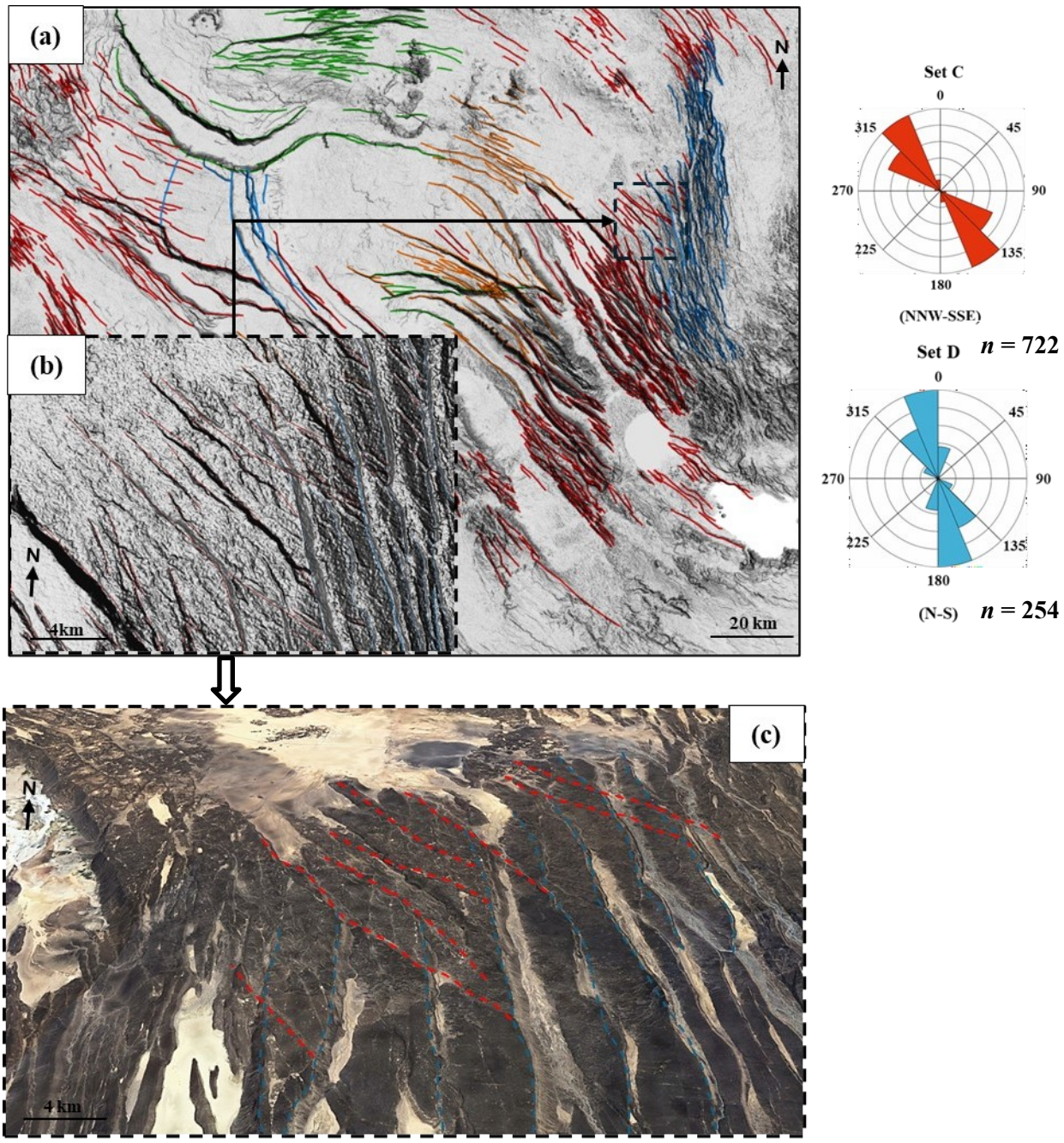


Figure 6.22: (a) Map showing Set C (red) and Set D (blue) faults, with rose diagrams summarising their strike distributions. **(b)** Enlarged DEM view of a fault zone where N–S scarps are intersected by NNW–SSE faults; the N–S scarps become discontinuous or fragment into shorter segments at the intersections. **(c)** Google Earth oblique perspective of the same area. NNW–SSE scarps (dashed red lines) form long, continuous ridges that cut across a series of N–S faults (blue), confirming the mapped cross-cutting geometry (DEM basemap from ASTER GDEM v3; NASA/METI/AIST/Japan Spacesystems and U.S./Japan ASTER Science Team, 2019; imagery from Google Earth™, accessed 2025).

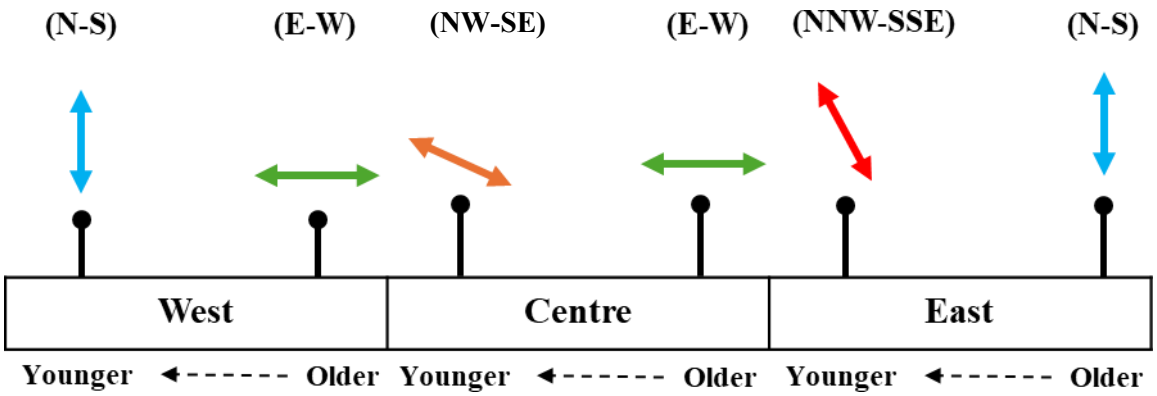
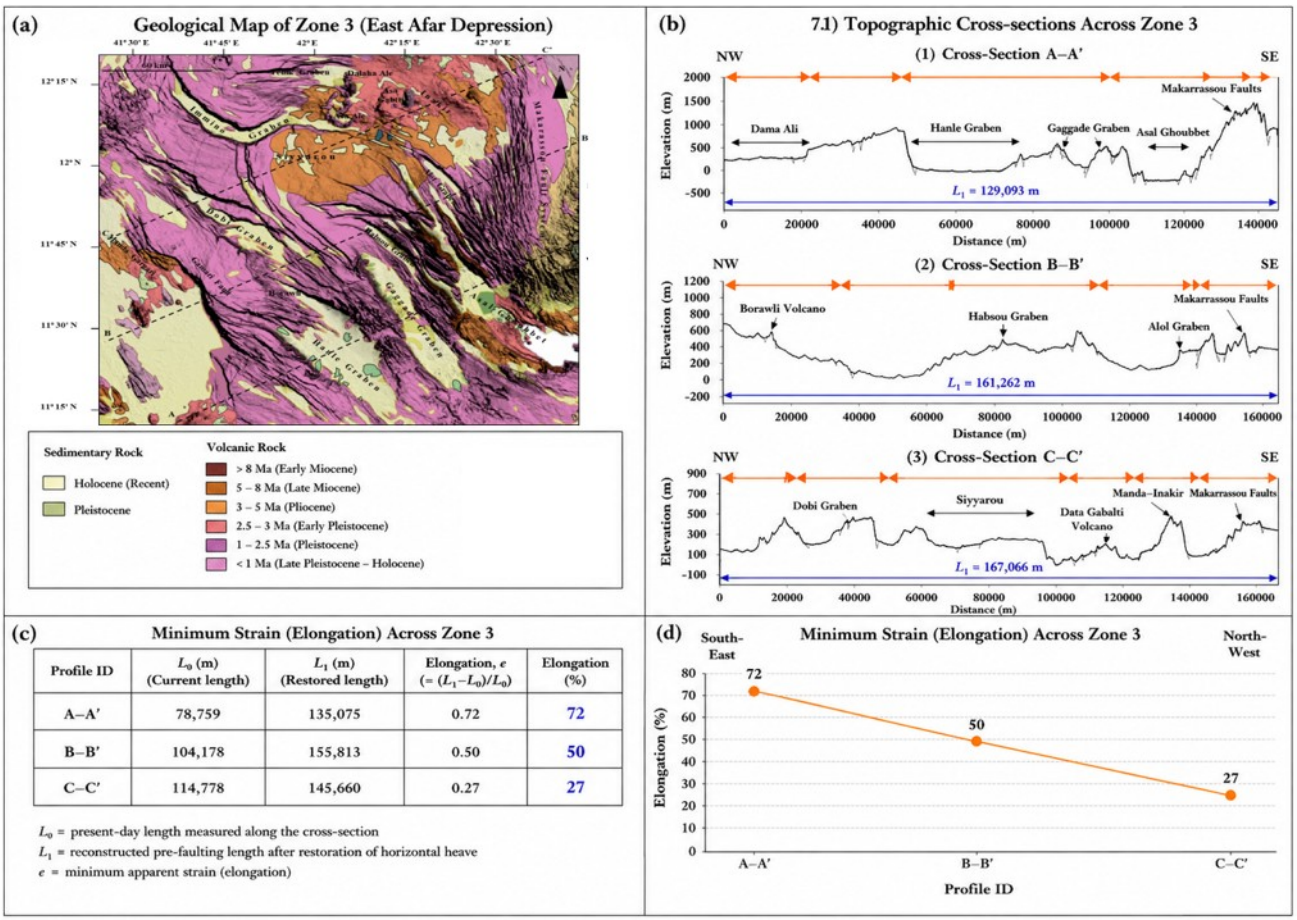


Figure 6.23: Schematic summary of the relative cross-cutting relationships between the principal fault-orientation sets identified in Zone 3. In the western part of the study area, E–W-oriented faults locally predate N–S-oriented faults; in the central part, E–W-oriented faults locally predate NW-SE-oriented faults; and in the eastern part, N–S-oriented faults locally predate NNW–SSE-oriented faults. These relationships represent local relative-age constraints derived from mapped fault intersections and should not be interpreted as demonstrating a uniform temporal rotation of fault orientations across the whole of Zone 3. Arrow orientations and positions are schematic and not to scale.

6.3.6 Minimum strain analysis of EAD (Zone 3)

Three separate cross-rift profiles were used to estimate the minimum apparent extensional strain across Zone 3. Profiles A–A′, B–B′ and C–C′ are shown on the geological map, together with their corresponding topographic profiles (Figure 6.24). The profiles extend continuously across the mapped faulted corridor and were constructed approximately orthogonal to the dominant strike of the mapped normal faults. Where local variations in fault orientation occur, minor bends were introduced to maintain an approximately fault-normal profile while preserving continuity of the cross-section. Consequently, the calculated values represent extension resolved along each profile rather than the total regional extension where fault slip is oblique to the section.



Profile ID	L_0 (m) (Current length)	L_1 (m) (Restored length)	Elongation, e $(= (L_1-L_0)/L_0)$	Elongation (%)
A–A′	78,759	135,075	0.72	72
B–B′	104,178	155,813	0.50	50
C–C′	114,778	145,660	0.27	27

L_0 = present-day length measured along the cross-section
L_1 = reconstructed pre-faulting length after restoration of horizontal heave
e = minimum apparent strain (elongation)

Figure 6.24: Cross-section analysis and minimum apparent extensional strain across Zone 3 of the Eastern Afar Depression (EAD). (a) Geological map of Zone 3 showing the main geological units and structural framework of the study area. (b) Topographic cross-sections A–A′, B–B′ and C–C′ across Zone 3, showing the principal grabens, volcanic centres and Makarrassou Fault system. Orange markers indicate mapped fault-related offsets along each profile, while the blue arrows show the reconstructed profile length (L_1). (c) Summary of the reconstructed pre-faulting length (L_0), present-day extended profile length (L_1), calculated elongation $e = (L_1 - L_0)/L_0$, and corresponding minimum apparent extensional strain.. (d) Variation in minimum apparent extensional strain across Zone 3, decreasing from 72% along A–A′ to 50% along B–B′ and 27% along C–C′ from the south-east towards the north-west. These values represent minimum apparent fault-related extension because unresolved, buried or volcanically obscured faults are not included in the surface-based reconstruction.

Minimum apparent extensional strain decreases systematically across Zone 3, from 72% along A–A′ to 50% along B–B′ and 27% along C–C′ (Figure 6.24 c–d). These values represent minimum apparent fault-related strain rather than total regional extension. Small faults below the resolution of the DEM, degraded or buried fault scarps, and structures obscured by volcanic or sedimentary resurfacing may not be represented in the reconstruction.

This limitation may be particularly important along C–C′, where younger volcanic rocks locally cover parts of the faulted terrain and may obscure older structures. The

comparatively low apparent strain of 27% along C–C′ may therefore partly reflect reduced preservation or surface expression of earlier faulting rather than necessarily indicating a proportionally lower amount of cumulative extension. In addition, extension accommodated by dyke intrusion is not independently resolved by this fault-heave approach and is therefore not included in the calculated values.

6.4 Discussion

This section discusses the principal findings from Zone 3 of the Eastern Afar Depression (EAD) in the context of fault growth and late-stage magma-assisted rifting. Fault-size and Dmax/*L* relationships are first evaluated together with variations between geological surface units. Fault segmentation and linkage are then considered to assess patterns of surface fault interaction and connectivity. The spatial distribution of minimum apparent fault-related strain and the relative timing of selected fault-orientation sets are subsequently examined. These observations are interpreted in the context of regional plate-boundary kinematics, magmatic modification, structural inheritance and preservation, while recognising the limitations of the DEM-based dataset.

6.4.1 Fault size distributions

The Zone 3 fault population shows an overall positive relationship between apparent fault length (*L*) and maximum displacement (Dmax), although considerable scatter occurs around the fitted relationship (Figure 6.5). Most faults plot within the broad Dmax/*L* range reported for natural normal-fault populations, while the Dmax/*L* = 1 line is retained only as an upper reference envelope (Walsh and Watterson, 1988; Cowie and Scholz, 1992; Kim and Sanderson, 2005; Lathrop et al., 2022). The observed scatter indicates that fault length alone does not account for the full variation in displacement across Zone 3 and is consistent with variability in fault segmentation, linkage, geological setting and preservation.

Classification by geological surface unit reveals a strongly uneven distribution of the mapped fault population (Figures 6.14–6.17). Q1v contains the largest proportion of mapped faults and spans a broad range of fault lengths and Dmax values. However, the age-ordered comparison shows that neither fault abundance nor fault size varies systematically from older to younger geological surfaces. Similarly, the Dmax/*L* distributions overlap substantially between units. M2v displays a comparatively broad range of Dmax/*L* values, but its smaller fault population means that this distribution should not be interpreted as evidence of systematically greater fault maturity.

The lack of a simple age-dependent trend is particularly important in the magma-rich setting of Eastern Afar. Surface geological age does not necessarily represent the duration of fault activity because younger lava flows and sedimentary deposits may bury or obscure older fault scarps, while faults may continue to propagate through, or

be reactivated beneath, younger volcanic cover. Magmatic intrusion may also modify the local stress field and redistribute deformation between faults and intrusive structures. Consequently, the fault population preserved in the DEM reflects both tectonic fault development and subsequent modification of the surface by volcanic and sedimentary processes.

Contrasts in lithology, competence and mechanical layering can influence fault propagation, segmentation and linkage (Gudmundsson, 2011; Lathrop et al., 2022). Repeated volcanic resurfacing can additionally modify the preservation and surface expression of fault scarps (Rime et al., 2023). However, the present data does not demonstrate that older geological units systematically contain longer-lived or more mature faults than younger units. In particular, the overlapping Dmax, *L*–Dmax and Dmax/*L* distributions indicate that geological surface age alone is insufficient to infer fault maturity.

The cross-cutting relationships described in Section 6.3.5 provide local relative-age constraints between selected fault-orientation sets, but they do not establish a region-wide sequence of fault initiation or repeated reactivation. Therefore, the concentration of faults within Q1v should not be interpreted as direct evidence that these structures initiated earlier or experienced more episodes of slip than faults in other units. Instead, the combined fault-size and geological-unit analyses indicate that the present-day fault population reflects the interacting effects of fault growth and linkage, magmatic modification, geological setting, resurfacing and preservation.

This interpretation is consistent with the advanced magma-assisted character of Zone 3: extension is distributed between brittle faulting and magmatic processes, while repeated volcanic resurfacing can modify which generations of faults remain visible at the surface. The large overlap between geological units therefore suggests that fault evolution in Zone 3 cannot be represented by a simple progression from young, immature faults to old, mature faults.

6.4.2 Fault-zone segmentation and linkage

The Zone 3 displacement profiles indicate that fault growth is strongly influenced by segmentation and interaction between neighbouring fault traces. Single-peak profiles form only a small proportion of the mapped population, whereas multi-peak and irregular profiles are substantially more common. The repeated displacement maxima observed along these faults is consistent with composite fault zones in which

individual segments have interacted and, in some cases, become linked. Local displacement lows between adjacent peaks may preserve the positions of former segment boundaries or relay zones (Trudgill and Cartwright, 1994; Childs et al., 1995; Cartwright et al., 1995; Kim and Sanderson, 2005).

The mapped linkage relationships show that fault connectivity is spatially variable across Zone 3. Soft-linked geometries, characterised by overlapping or closely spaced fault tips, are more common than fully hard-linked structures. Hard linkage is nevertheless present within some of the principal axial and graben-related fault systems, where individual segments have developed more continuous surface traces. These observations suggest that the Zone 3 fault network contains faults at different stages of interaction rather than representing a single, uniform stage of fault development.

This mixed linkage pattern is particularly relevant to the magma-assisted setting of eastern Afar. Fault interaction occurs within narrow grabens and axial zones that are also affected by volcanic and intrusive activity. Magmatic deformation may modify local stress conditions and influence where faults initiate, propagate or interact, while volcanic resurfacing can obscure earlier segment boundaries and relay structures. Consequently, the mapped linkage patterns represent the preserved surface expression of fault interaction and should not be interpreted as a complete record of subsurface connectivity.

Interpretation is also limited by the 30 m spatial resolution of the DEM. Closely spaced scarps may be mapped as a single continuous structure, whereas locally subdued or resurfaced sections of the same fault may appear discontinuous. These effects are particularly important in Zone 3, where lava emplacement, sedimentation and erosion can modify fault-scarp continuity. The soft- and hard-linkage classifications are therefore used here primarily to describe surface-scale fault interaction and connectivity, rather than to assign individual faults to a specific maturity stage. Their implications for fault-growth models and the broader evolution of the three study zones are considered further in Chapter 7.

6.4.3 Minimum strain localisation

The minimum apparent strain analysis identifies a clear spatial variation across Zone 3, with elongation decreasing from 72% along A–A′ to 50% along B–B′ and 27% along C–C′ (Figure 6.24). This pattern indicates that the southern profile records substantially greater cumulative surface-resolved fault-related extension than the northern profile. However, these values should not be interpreted as the complete regional extension budget because the calculation is based only on horizontal heave associated with faults that can be resolved at the surface.

The contrast between the three profiles therefore primarily reflects differences in the cumulative mapped fault heaves intersected by each cross-section. A–A′ records the greatest reconstructed extension, whereas C–C′ records the least. The present data demonstrates this spatial variation but do not, by themselves, establish why strain localisation differs between the profiles. In particular, the geological-unit and Dmax/*L* analyses do not show a simple systematic relationship between geological surface age and fault development and therefore cannot independently explain the observed decrease in apparent strain.

Preservation may contribute to the comparatively low value recorded along C–C′. Younger volcanic rocks locally cover parts of the faulted terrain along this profile and may obscure older fault scarp or reduce their preserved surface expression. Consequently, the calculated **27%** may partly underestimate earlier fault-related extension. This interpretation remains cautious because the DEM data cannot directly resolve faults buried beneath younger volcanic cover.

Several methodological limitations also affect the calculated values. The 30 m DEM may not resolve small-displacement faults or distributed deformation, while sedimentation, erosion and volcanic resurfacing can reduce the surface expression of fault scarps. In addition, although the profiles were constructed approximately orthogonal to the dominant fault strike, residual local obliquity means that only the component of fault-related extension resolved along each profile is measured. Extension accommodated by dyke intrusion is also not independently represented in the fault-heave reconstruction.

The Zone 3 values are therefore interpreted as minimum apparent fault-related strain. The decrease from A–A′ to C–C′ is a clear feature of the mapped surface dataset, but

its cause cannot be attributed uniquely to differences in fault maturity, geological surface age or magmatic activity. Instead, it probably reflects a combination of spatial variations in mapped fault displacement, structural organisation and preservation. The broader significance of this strain pattern for the evolution of Zone 3 is considered together with the other datasets in Chapter 7.

6.4.4 Cross-cutting relationships

The cross-cutting relationships mapped across Zone 3 indicate spatial variation in the relative timing and orientation of fault sets. Rather than defining a single chronological sequence applicable to the entire study area, individual fault intersections provide local relative-age constraints that differ between the western, central and eastern parts of Zone 3. These relationships therefore indicate local reorganisation of faulting through time, but do not independently demonstrate a uniform progressive rotation of the regional stress field.

In the western part of Zone 3, approximately E–W-oriented faults are locally cross-cut by N–S-oriented structures, indicating that the E–W-oriented faults predate the N–S-oriented set at these intersections. In the central part, E–W-oriented faults are locally cross-cut by NW–SEoriented structures, suggesting relatively younger NW–SE faulting. Farther east, N–S-oriented structures are locally cross-cut by NNW–SSE-oriented faults, indicating that the NNW–SSE set is relatively younger at the mapped intersections. These local relationships are summarised schematically in Figure 6.22.

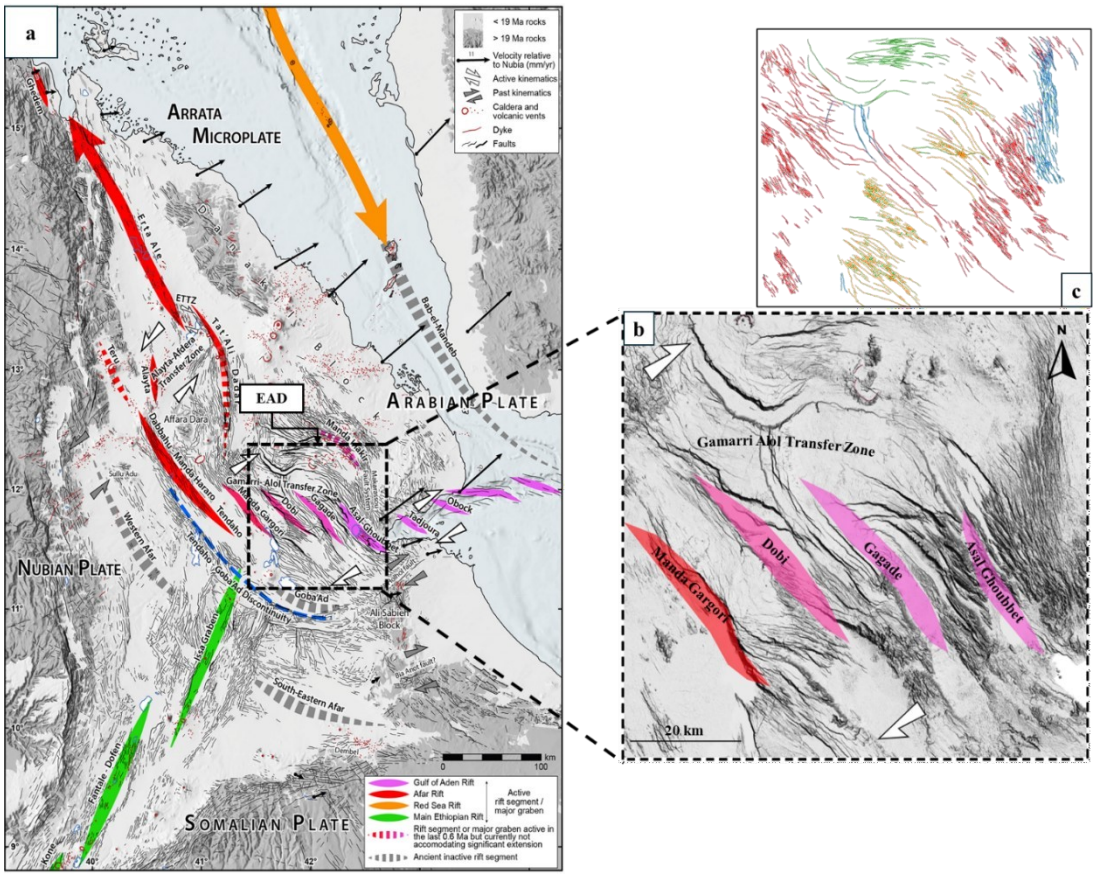


Figure 6.25: (a) Regional rift dynamics of the Afar Depression, showing the interaction between the Afar, Red Sea, Gulf of Aden and Main Ethiopian Rift systems, together with the location of

the Eastern Afar Depression (EAD) and the Gamarri–Abli Transfer Zone (modified after Rime et al., 2023). (b) Hill-shaded DEM of the Gamarri–Abli Transfer Zone showing the principal grabens, including Manda, Dobi, Gaggade and Asal–Ghoubbet. (c) Colour-coded fault traces in Zone 3 illustrating spatial variations in fault orientation across the transfer zone, with older blue–green fault sets preserved predominantly in the northern part of the transfer zone and younger red–orange NW–SE to NNW–SSE-oriented fault sets occurring farther south and east.

The spatial variation in these relationships is consistent with the structurally complex setting of eastern Afar. At the regional scale, Zone 3 lies within an area where several oblique grabens and rift segments interact, including the Gamarri–Abli Transfer Zone shown in the regional structural framework (Figure 6.25). This transfer zone provides an important structural context for the observed variations in fault orientation because it links neighbouring graben and rift systems with different structural trends. Consequently, local variations in fault orientation and cross-cutting relationships may partly reflect deformation associated with interaction between adjacent rift segments rather than a single regional fault-generation sequence.

The broader kinematic setting may also contribute to this structural variability. Eastern Afar accommodates deformation associated with the interaction of the Red Sea, Gulf of Aden and Main Ethiopian Rift systems, together with anticlockwise rotation of the Danakil Block (McClusky et al., 2010). These regional processes provide a plausible framework for changes in extension direction and fault orientation. However, the cross-cutting relationships documented here do not independently demonstrate that Danakil Block rotation caused the observed changes in fault orientation. Instead, the mapped relationships are consistent with deformation occurring within a complex plate-boundary setting in which regional extension, block rotation, structural inheritance and interaction between neighbouring rift segments may all contribute.

Magmatic processes provide an additional possible local control. Dyke intrusion and volcanic activity can perturb the local stress field and influence the location and orientation of fault initiation or reactivation within magma-assisted rifts (Kendall et al., 2005; Bastow and Keir, 2011; Moore et al., 2021). This may be particularly relevant where fault systems occur close to axial volcanic centres and magmatic segments. Nevertheless, the present cross-cutting dataset cannot distinguish uniquely between fault reorientation caused by regional plate kinematics, Danakil Block rotation, transfer-zone deformation or local magmatic stress perturbations. These mechanisms are therefore considered as possible controls, rather than demonstrated causes of individual cross-cutting relationships.

Individual fault intersections must also be interpreted cautiously because apparent cross-cutting relationships can be affected by fault reactivation, incomplete preservation and volcanic or sedimentary resurfacing. A younger structure may exploit or reactivate part of an older fault, while subsequent lava emplacement or sedimentation may obscure the original geometry of an intersection. For this reason, the relative chronology inferred from individual mapped intersections is considered more robust than attempting to construct a continuous region-wide sequence of fault rotation from the DEM alone.

Overall, the cross-cutting relationships indicate that Zone 3 contains multiple locally interacting generations of fault orientations. The western, central and eastern sectors preserve different relative-age relationships, demonstrating spatial and temporal reorganisation of surface faulting. These observations are consistent with the complex structural setting of eastern Afar, including interaction across the Gamarri–Alol Transfer Zone and the broader influence of plate-boundary kinematics and Danakil Block rotation. However, the data do not support a simple progressive rotation from one fault orientation to another across the entire study area. The implications of these relationships for the broader tectonic evolution of Zone 3 are considered together with the fault-size, segmentation, linkage and strain results in Chapter 7.

6.5 Conclusion

The quantitative analysis of 1,250 mapped normal faults in Zone 3 of the Eastern Afar Depression (EAD) shows that fault geometry, displacement distribution, linkage and surface expression are strongly variable across this advanced magma-rich rift sector. The principal findings are:

- Faults in Zone 3 range from 399 to 41,556 m in apparent length, with a mean length of 5,300 m, while apparent maximum displacement (Dmax) ranges from 13 to 1,215 m, with a mean of 181 m. The overall fault population shows a positive displacement–length relationship described by Dmax = 0.6705L^0.6398 (R^2 = 0.4222), indicating that displacement generally increases with fault length, although substantial scatter remains.

- Displacement-profile geometry varies systematically across the mapped fault population. Single-peak faults account for 112 faults (~9%), multi-peak faults for 542 faults (~43%), and irregularly peaked faults for 596 faults (~48%). Irregularly

peaked faults include the longest and highest-displacement structures and display the highest scaling exponent among the three profile classes, consistent with a greater degree of structural complexity and segment interaction.

- Fault linkage is an important control on the effective length of fault systems. Soft-linked faults are common throughout the main graben margins and high-density fault corridors, whereas 97 mapped fault traces (~8%) were classified as hard linked. When physically connected hard-linked structures are treated as composite faults, 65 complete systems define a statistically significant relationship of Dmax = 1.2422L^0.5623 (R^2 = 0.3977, $p < 0.001$). The sub-linear exponent indicates that total linked fault length increases more rapidly than maximum displacement during linkage.

- Fault abundance, Dmax, fault length and Dmax/L vary between geological surface units, but none shows a simple monotonic relationship with surface age. This indicates that geological surface age alone does not control the preserved fault population. Instead, the observed distributions reflect the combined effects of fault growth, linkage, volcanic resurfacing, sedimentation, erosion, burial and preservation of fault scarps.

- The EAD is characterised by a close spatial association between normal faults, volcanic centres, fissure systems and dyke-related deformation. This supports interpretation of Zone 3 as a magma-assisted extensional system, in which brittle faulting and magmatic intrusion jointly influence fault location, orientation, segmentation and displacement.

- The fault patterns are compatible with an advanced stage of continental–oceanic transition, but the surface fault data alone cannot distinguish uniquely between highly thinned continental crust and an incipient oceanic-spreading regime. The mapped structures are therefore interpreted within a transitional framework in which tectonic extension, magmatic intrusion and Danakil Block rotation collectively influence strain localisation and fault organisation.

Chapter 7: Discussion and conclusion

This chapter synthesises the results from the three study areas (Zone 1: North Afar Depression, NAD; Zone 2: North Main Ethiopian Rift, NMER; Zone 3: East Afar Depression, EAD) to examine how normal faults grow, interact, and accommodate extension across the northern East African Rift System and the wider Afro–Arabian rift domain. The synthesis integrates four linked strands of evidence developed in the zone-specific chapters: (1) fault-size relationships, using apparent fault length (L) and apparent maximum displacement (Dmax), including the regression relationships and associated statistical measures calculated for the different fault populations; (2) fault segmentation and linkage, evaluated using displacement–distance profiles and map-scale geometries, including assessment of how fault linkage influences Dmax–L scaling relationships; (3) minimum (apparent) strain, estimated from cross-rift elongation profiles to assess variations in the distribution and localisation of extension between the three study areas; and (4) lithological and surface-age relationships, using the mapped surface-unit framework to assess whether lithology and relative surface age influence fault geometry and Dmax–L scaling relationships.

Bringing these datasets together (total n = 2,500 faults) allows the combined Afar–MER fault population to be evaluated against established displacement–length scaling relationships and fault-growth concepts. The regression analyses, together with observations of fault segmentation and linkage, provide a basis for evaluating the evidence for different fault-growth models and for assessing how linkage modifies Dmax–L scaling relationships. The synthesis also considers the role and age of magmatism, informed by published GPS, InSAR and other relevant geodetic observations, to assess how magmatic and tectonic processes may influence the distribution and localisation of extension. Together, these analyses provide a basis for determining whether variations in fault scaling, segmentation, linkage, lithology and strain localisation between the three study areas reflect differences in fault-growth history and progressive rift development, or reorganisation between neighbouring rift segments through time (Walsh and Watterson, 1988; Cowie and Scholz, 1992; Ebinger and Casey, 2001; Kim and Sanderson, 2005; Corti, 2009; Rime et al., 2023).

A key assumption is that fault scarps and displaced landforms mapped from the 30 m DEM provide a consistent regional-scale measure of apparent fault geometry that can be compared between zones. However, because the DEM captures only the surface

expression of faulting, both Dmax and elongation should be treated as minimum (apparent) estimates. Variations in apparent elongation may therefore reflect real differences in how extension is distributed, but they may also be influenced by the completeness of scarp preservation and detection on surfaces with different lithologies and exposure histories. This limitation is particularly important when comparing volcanic terrains with sedimentary basins, where fault scarps may be muted or buried, and when relating present-day fault patterns to longer-term rift-evolution models. These uncertainties are explicitly addressed throughout the chapter so that interpretations remain grounded in what can be demonstrated from the mapped fault scarps (Walsh and Watterson, 1988; Lathrop et al., 2022; Rime et al., 2023).

7.1 Fault size distribution

This section discusses the relationship between fault length (L) and apparent maximum displacement (Dmax) across the three zones studied in this thesis (Zones 1 and 2: NAD and NMER, and Zone 3: EAD) and what these differences imply for fault growth. The descriptive statistics and basic D–L plots for each zone are presented in the Results chapters; here, the emphasis is on how the three fault populations occupy displacement–length space and how these patterns compare with published fault growth models. A summary of the fault numbers, lengths, and maximum displacements is presented in Table 7.1, which shows that Zone 2 in the central part of the NMER is dominated by short, low-displacement faults, Zone 3 (EAD) contains the longest and highest-displacement faults identified in the DEM data, and Zone 1 (NAD) lies between these two zones in terms of mean L and Dmax.

Study Zone	Faults (*n*)	Fault Length (m)			Fault D*max* (m)		
		Min.	Max.	Mean	Min.	Max.	Mean
NAD	350	487	16,859	3,709	14	379	106
NMER	900	303	20,851	1,789	10	1,045	77
EAD	1,250	399	41,556	5,300	13	1,215	181

Table 7.1: Summary statistics of fault geometries for the three study zones. The table lists the number of mapped faults, minimum, maximum, and mean fault lengths (L), and minimum and maximum displacements (Dmax) for Zones 1 (NAD), 2 (NMER), and 3 (EAD). For the NMER, these statistics refer only to intra-rift faults resolved in the DEM and do not include the older, highly eroded rift-margin border faults, which are likely to form hard-linked fault sets with some longer than 50 km (after Ebinger and Casey, 2001).

Previous studies have shown that normal faults usually display a positive correlation between length and maximum displacement and lie within a broad displacement–length (D–L) envelope where Dmax/L is typically of the order 10^{-2}–10^{-1} (Walsh and Watterson, 1988; Cowie and Scholz, 1992; Kim and Sanderson, 2005; Lathrop et al., 2022). Although power-law relationships often summarise this trend, large compilations also show substantial scatters in D at any given L, reflecting differences in lithology, tectonic setting, and fault maturity. When the combined Afar–NMER dataset (n = 2,500) is plotted together with a global compilation of normal faults (Figure 7.1), the faults from all three zones fall within this established field. The lower limits of Dmax and L are governed by the resolution of the DEM data. In Figure 7.1, four reference lines of constant Dmax/L (1, 10^{-1}, 10^{-2}, and 10^{-3}) are shown, of which the latter three define the upper, middle, and lower fault displacement envelopes, as illustrated schematically in the inset displacement profiles. The Afar Depression and

NMER faults plot mainly between the upper and middle envelopes (Dmax/L ≈ 10^{-1}–10^{-2}), with only a small number of points approaching the lower envelope (10^{-3}) or highest line (Dmax/L ≈ 1). This agreement indicates that, despite being mapped from 30 m DEMs using apparent vertical separation, the faults follow the same overall scaling behaviour as normal faults in other extensional settings. This means that the Afar Depression and NMER datasets can be used to examine how the range and frequency of fault lengths and displacements change from one rift segment to another along strike, while still lying within this global displacement envelope, and to test end-member and hybrid fault-growth models.

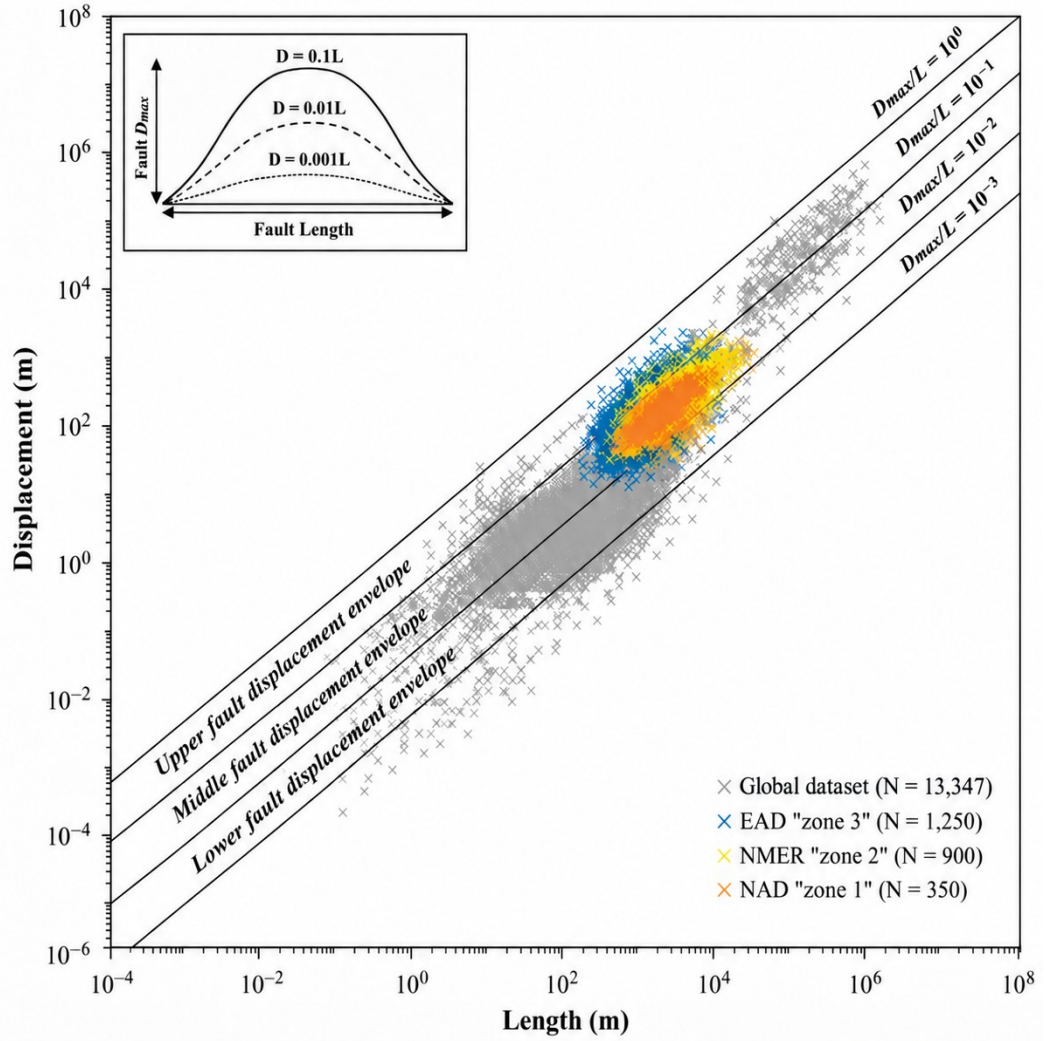


Figure 7.1: Log–log plot of fault displacement versus fault length for faults from the Afar–NMER study areas, together with previously published global fault displacement–length data from Gillespie et al. (1992) and Bailey et al. (2005). Grey crosses represent the global dataset ($N = 13{,}347$), while coloured crosses represent EAD (Zone 3; $N = 1{,}250$), NMER (Zone 2; $N = 900$) and NAD (Zone 1; $N = 350$). Solid diagonal lines indicate constant $D_{\max}/L$ratios of 10^{0}, 10^{-1}, $10^{-2}$and 10^{-3}, defining the upper, middle and lower fault-displacement envelopes. The inset illustrates idealised displacement–distance profiles for different $D_{\max}/L$ratios.

In the D–L plot that shows only the study areas (Figure 7.2), the three fault populations are displayed as overlapping clouds superimposed on the same displacement envelopes defined by constant Dmax/L lines (1, 10^{-1}, 10^{-2}, and 10^{-3}). This representation highlights two key aspects. First, the zones do not form three separate fields; instead, the NAD, NMER, and EAD clouds overlap strongly and all lie within the same part of the global D–L envelope, confirming that the same basic growth processes operate throughout the system. Second, within this overall overlap, the centres and upper limits of the clouds are systematically shifted relative to each other and to the three main envelopes (upper, middle, and lower). Most NAD faults occupy the lower–central part of the combined cloud. They are short to moderately long, have modest Dmax values, and show low to intermediate Dmax/L ratios with considerable scatter, clustering close to and just below the middle displacement envelope. This pattern is typical of a population in which many faults are still relatively small and extensional strain is shared between numerous structures (Cowie and Scholz, 1992; Kim and Sanderson, 2005). The high surface fault density and presence of several subparallel grabens in the NAD are consistent with a distributed fault system dominated by relatively immature faults.

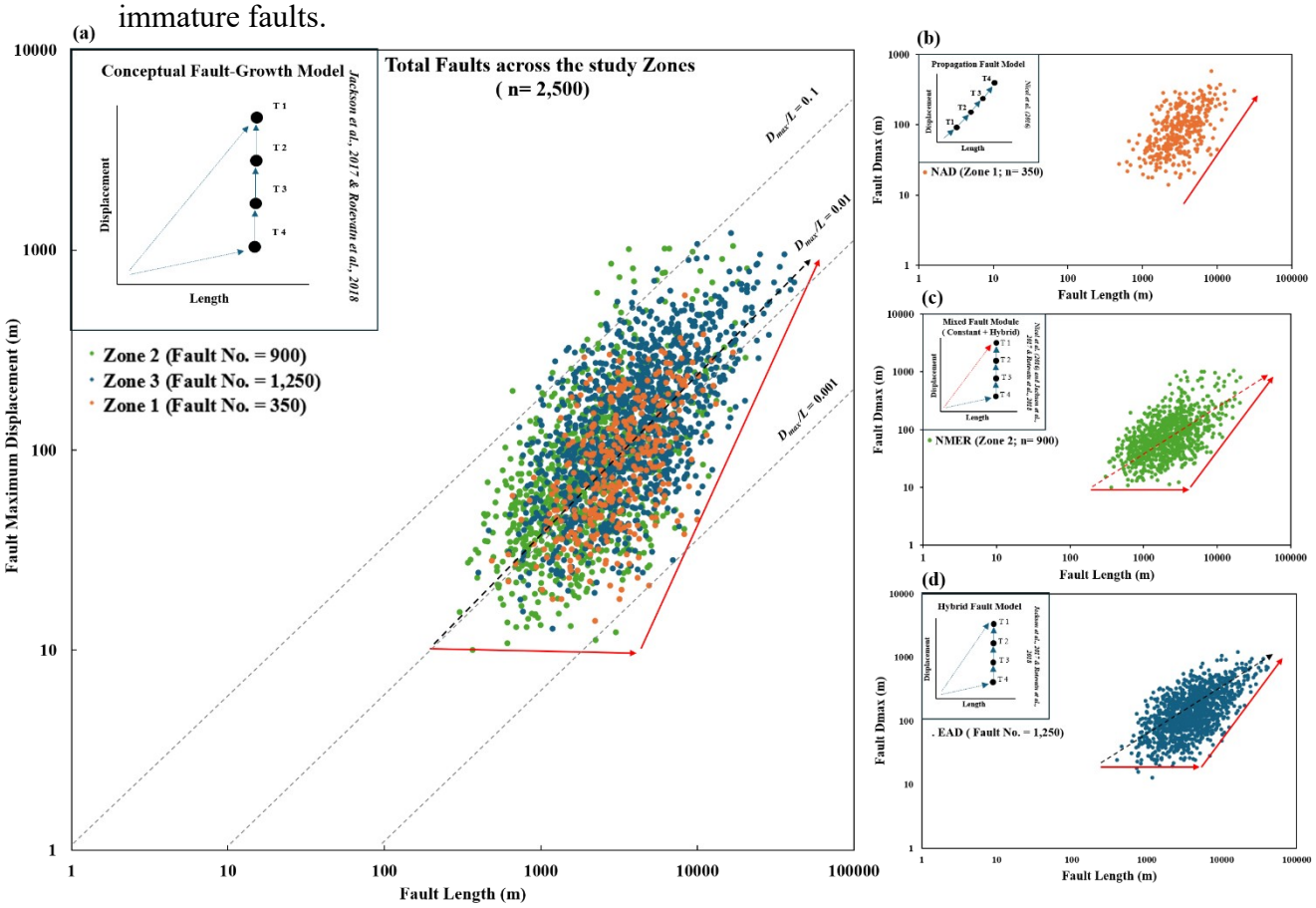


Figure 7.2: Log–log displacement–length (D–L) plots for mapped faults across the three study zones (n = 2,500). **(a)** Combined D–L distribution for all faults from NAD (Zone 1; n = 350), NMER (Zone 2; n = 900) and EAD (Zone 3; n = 1,250), together with a conceptual

fault-growth model used for comparison with the observed distributions. **(b)** D–L distribution for NAD (Zone 1; $n = 350$), shown alongside the propagation fault-growth model. **(c)** D–L distribution for NMER (Zone 2; $n = 900$), shown alongside the mixed fault-growth model (constant-length and hybrid growth). **(d)** D–L distribution for EAD (Zone 3; $n = 1{,}250$), shown alongside the hybrid fault-growth model. Dashed reference lines indicate constant $D_{\max}/L$ratios of 0.1, 0.01 and 0.001. The conceptual fault-growth models are modified after Nicol et al. (2017), Jackson et al. (2017) and Rotevatn et al. (2018).

In contrast, the NMER data are distributed across a wider part of D–L space. A large group of NMER faults overlaps with the NAD population, sharing similar lengths, displacements and $D_{\max}/L$ratios. However, the NMER also includes a clear subset of longer faults that extend further upwards and to the right on the D–L plot and lie closer to the upper displacement envelope. This combination indicates that Zone 2 contains many relatively small faults, similar to those in the NAD, together with a smaller but significant group of longer, higher-displacement faults that plot closer to the upper displacement envelope. Geometrically, Zone 2 therefore records a transitional D–L distribution, in which many short faults coexist with a smaller population of longer, higher-displacement structures.

The EAD (Zone 3) forms the upper part of the Afar–NMER D–L distribution. Its population overlaps with those of the NAD and NMER at low-to-moderate $L$and $D_{\max}$values but also extends to the greatest fault lengths and displacements in the study dataset and lies closest to the upper displacement envelope. For a given length, EAD faults generally record greater displacement than faults in the NAD or central NMER, and many have $D_{\max}/L$ratios approaching the upper part of the global normal-fault field. These characteristics indicate that Zone 3 contains a greater proportion of long, high-displacement faults. The spatial coincidence between these faults and the main axial grabens of the East Afar Depression is consistent with deformation being concentrated onto a smaller number of major structures.

These size-distribution patterns can be evaluated against the conceptual fault-growth models illustrated in Figure 7.2. In the propagating fault model, growth is dominated by simultaneous increases in fault length and displacement, producing an approximately diagonal trajectory through log–log D–L space (Nicol et al., 2017). In contrast, the constant-length model involves limited tip propagation after an initial phase of fault-length growth, with subsequent displacement accumulation occurring at approximately fixed length and producing a near-vertical trajectory in D–L space (Nicol et al., 2017).

Studies of normal-fault growth have shown that these end-member behaviours may occur sequentially during the lifetime of an individual fault, producing a hybrid growth trajectory (Jackson et al., 2017; Rotevatn et al., 2019). In this model, the initial lengthening stage occupies approximately 20–30% of the fault lifespan and involves fault-tip propagation, segment linkage and displacement accumulation. This is followed by a longer displacement-accrual stage, occupying approximately 70–80% of the fault lifespan, during which relatively little additional fault-length growth occurs (Rotevatn et al., 2019).

When compared with these conceptual growth trajectories, the Afar–NMER D–L distributions are consistent with, but do not independently demonstrate, hybrid fault growth. NAD faults are concentrated mainly at shorter lengths and lower displacements, whereas the NMER distribution spans a broader range and includes a subset of longer, higher-displacement faults. EAD faults extend towards the greatest lengths and displacements and occupy the upper part of the study-area D–L distribution. These systematic differences may therefore represent different stages or expressions of fault growth, although D–L position alone cannot uniquely distinguish between propagating, constant-length and hybrid growth histories. This interpretation is tested further below using the independent evidence provided by fault segmentation, linkage and displacement-profile geometries.

.

7.2 Fault segmentation and linkage

This section examines how fault segmentation and linkage vary between the North Afar Depression (Zone 1), North Main Ethiopian Rift (Zone 2), and East Afar Depression (Zone 3), and what these variations imply for fault maturity and growth mechanisms along the rift system. The discussion draws on two complementary analyses derived from the same DEM-based fault dataset. First, displacement–distance profiles along individual scarps are used to describe the internal segmentation of faults. Second, the surface geometry of neighbouring segments is used to classify soft versus hard linkages at the scale of fault zones.

The displacement profiles were classified into three types (smooth single-peak, multi-peak, and irregular-peak), following the definitions given in the Results chapters for Zones 1–3. In this chapter, these profile families are used to test a modified three-stage segmentation and linkage model based on Kim and Sanderson's (2005) model. In this framework, smooth single-peak profiles represent Stage-1 isolated segments, multi-peak profiles represent Stage-2 soft-linked segment arrays, and irregular-peak profiles represent Stage-3 composite fault zones formed by the breaching of relay ramps.

The linkage style was characterised from the 30 m DEM by examining the relationships between neighbouring fault traces. Soft-linked faults were identified where overlapping tips or en echelon steps were connected by a relay ramp or deformation corridor; these represent immature linkages where displacement is transferred across the relay, but the surface traces remain geometrically separate (Peacock and Sanderson, 1991; Trudgill and Cartwright, 1994; Cartwright et al., 1995). Hard-linked faults were mapped where adjacent segments formed a single continuous scarp, indicating breaching of the intervening relay and the development of a mechanically unified structure. These linkages are considered mature. The terms "immature" and "mature" refer to observable surface morphology rather than subsurface continuity.

Profile Pattern	Metric	NAD (Zone 1)			NMER (Zone 2)			EAD (Zone 3)		
		Min.	Max.	Mean	Min.	Max.	Mean	Min.	Max.	Mean
Single peak	Fault length (m)	487	3,371	1,589	303	3,319	1,211	399	5,142	1,625
	Fault D_{max} (m)	18	205	65	10	245	57	22	307	84
Multi-peak	Fault length (m)	845	5,674	2,344	456	4,690	2,069	729	9,925	3,021
	Fault D_{max} (m)	18	288	86	11	1,011	106	13	701	139
Irregular-peak	Fault length (m)	748	16,859	4,430	735	20,851	6,088	1,629	41,556	8,062
	Fault D_{max} (m)	14	593	119	23	1,045	186	24	1,215	237

Table 7.2: Summary of minimum, maximum and mean fault length (L) and maximum displacement (D_{max}) for each displacement-profile type in the three study zones (NAD, NMER and EAD).

The updated displacement–length (D–L) patterns show a consistent progression from the NAD through the NMER to the EAD, as illustrated in the revised Figure 7.3. The fault length (L) and maximum displacement (Dmax) both increased systematically eastward, accompanied by clear shifts in the displacement profile type and linkage style. Single-peak faults were the shortest and least displaced, whereas multi-peak faults increased in both L and Dmax, and irregular-peak faults reached the highest values, including maximum lengths >40 km and displacements >1 km in Zone 3.

In the revised D–L plot (Figure 7.3a), the three profile types of plots along a continuum bounded by constant $D_{\max}/L$reference lines of 1, 0.1, 0.01 and 0.001. Most NAD faults occupy the lower part of the D–L distribution, predominantly within the $D_{\max}/L =$ 0.1–0.01field (Figure 7.2), whereas the longest and highest-displacement faults in the NMER, and particularly the EAD, extend upwards towards $D_{\max}/L \approx 0.1$. These trends are consistent with global normal-fault scaling fields reported in previous studies (Walsh and Watterson, 1988; Cowie and Scholz, 1992; Kim and Sanderson, 2005; Lathrop et al., 2022). The constant $D_{\max}/L$reference lines shown in Figure 7.3 provide a clearer basis for comparing the relative positions of the fault populations within D–L space.

The linkage statistics followed the same spatial progression (Table 7.2). Zone 1 contains the highest proportion of soft-linked segments (~54%), Zone 2 shows a more balanced mixture of soft and hard linkages, and Zone 3 contains the greatest number and proportion of through-going hard-linked scarps. This pattern mirrors the distribution of displacement profile types: Zones 1 and 2 are dominated by single-peak and multi-peak faults, whereas Zone 3 contains the highest frequency of irregular-peak faults.

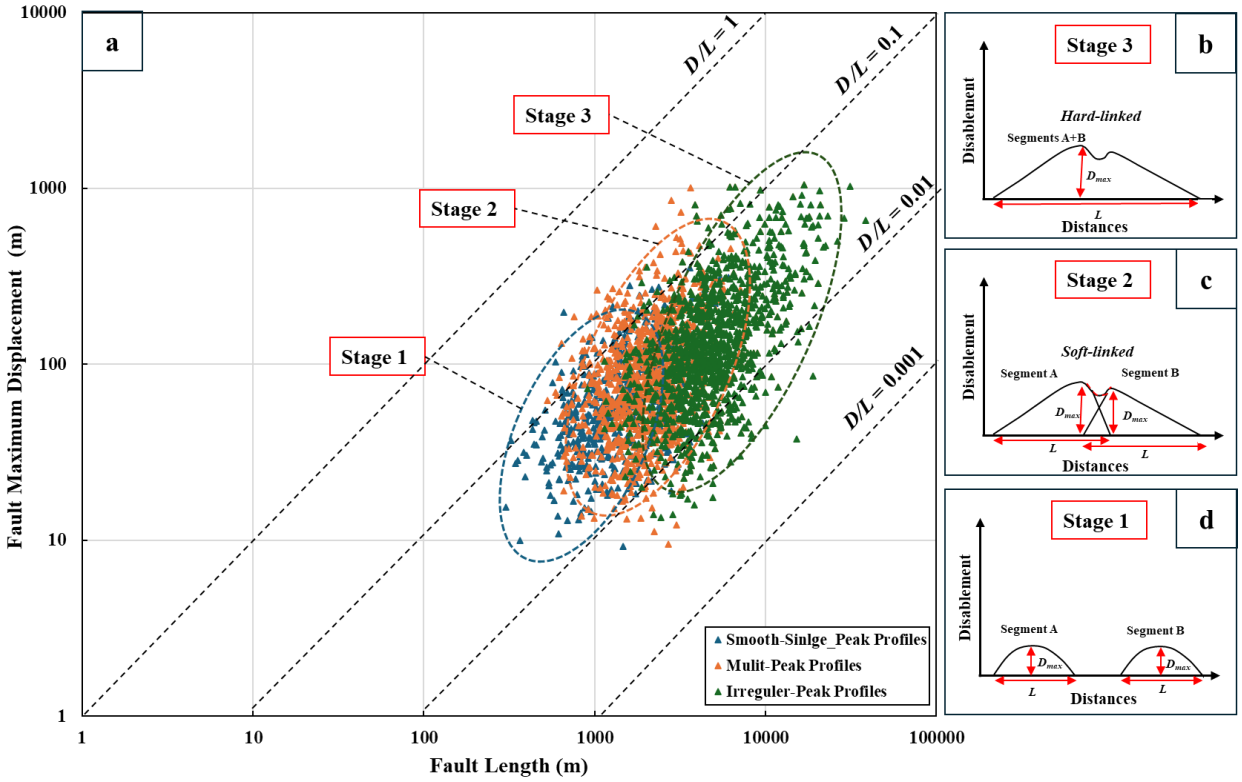


Figure 7.3: Log–log plot of apparent fault length (L) versus apparent maximum displacement (Dmax) for all mapped faults in Zones 1–3, coloured by displacement-profile type (smooth single-peak, multi-peak, and irregular-peak). Dashed lines show constant D/L ratios (1, 0.1, 0.01, and 0.001), and the three dashed fields mark the Stage-1, Stage-2, and Stage-3 domains in the segmentation–linkage model. The cartoons on the right illustrate the corresponding geometries: isolated single-peak segments (Stage 1), soft-linked multi-segment arrays (Stage 2), and hard-linked composite fault zones (Stage 3), modified from Kim and Sanderson (2005).

When all faults are plotted together by profile type (Figure 7.3a), the Stage-1, Stage-2, and Stage-3 fields defined in the new figure discriminate the observed profile groups, despite overlap of the groups Smooth single-peak faults occupy a generally lower D/L range and correspond to Stage-1 isolated segments. Multipeak faults form an intermediate band consistent with Stage-2 soft-linked arrays, whereas irregular-peak faults cluster in the highest D/L field corresponding to Stage-3 composite fault zones. This distribution closely agrees with the three-stage model of segmentation and linkage described by Kim and Sanderson (2005) and subsequent studies. The zone-by-zone comparison reinforces this interpretation. In Zone 1, most faults remain in Stage-1 or early Stage-2, consistent with extensive soft linkage and weak strain localisation. In Zone 2, an increasing number of Stage-2 segments evolve toward Stage-3 behaviour as relay ramps are breached and displacement is redistributed along longer scarps. In Zone 3, the dominance of irregular peak profiles and mature hard-linked scarps indicates that many earlier segments have already amalgamated into long, through-going composite faults, consistent with advanced rift development in this part of the system.

As before, uncertainties arise from the DEM resolution and surface-based nature of linkage mapping. Small-scale segmentation may be unresolved, and some soft-linked traces may already be hard-linked at shallow depths. This will explain some of the overlap between the three groups. And therefore, these classifications represent the minimum observable segmentation and linkage states. Overall, the combined segmentation, linkage, and D–L data show a coherent evolutionary pattern from isolated segments in the NAD through intermediate soft-linked arrays in the NMER to mature hard-linked composite faults in the EAD. These patterns reflect increasing fault maturity and progressive localisation of deformation along the rift, and they form the basis for linking fault geometry to strain accommodation in the next section.

7.3 Minimum strain localization

The minimum apparent elongation values indicate that the surface expression of fault-related extension varies between the three rift sectors rather than changing smoothly along a single continuous rift axis. In Zone 1 (NAD), minimum apparent elongation decreases northwards from approximately 50% in profiles A–A′ and B–B′ to approximately 3% in profile H–H′. In contrast, Zone 2 (NMER) shows a north-eastward increase from approximately 62% in A–A′ to approximately 90% in C–C′. Zone 3 (EAD) shows a north-westward decrease from approximately 72% in A–A′ to approximately 27% in C–C′. These contrasting gradients indicate that the surface expression of fault-related extension varies spatially between the Afar Rift/Danakil domain (NAD), the Main Ethiopian Rift (NMER), and the Afar–Gulf of Aden linkage zone (EAD). The spatial relationships between the transects and their corresponding elongation values are summarised in Figure 7.4. These contrasting patterns are consistent with the triple-junction geometry and with previous interpretations that deformation is reorganised between adjacent rift sectors rather than progressing uniformly along strike (Ebinger and Casey, 2001; Wolfenden et al., 2004; Corti, 2009; Rime et al., 2023).

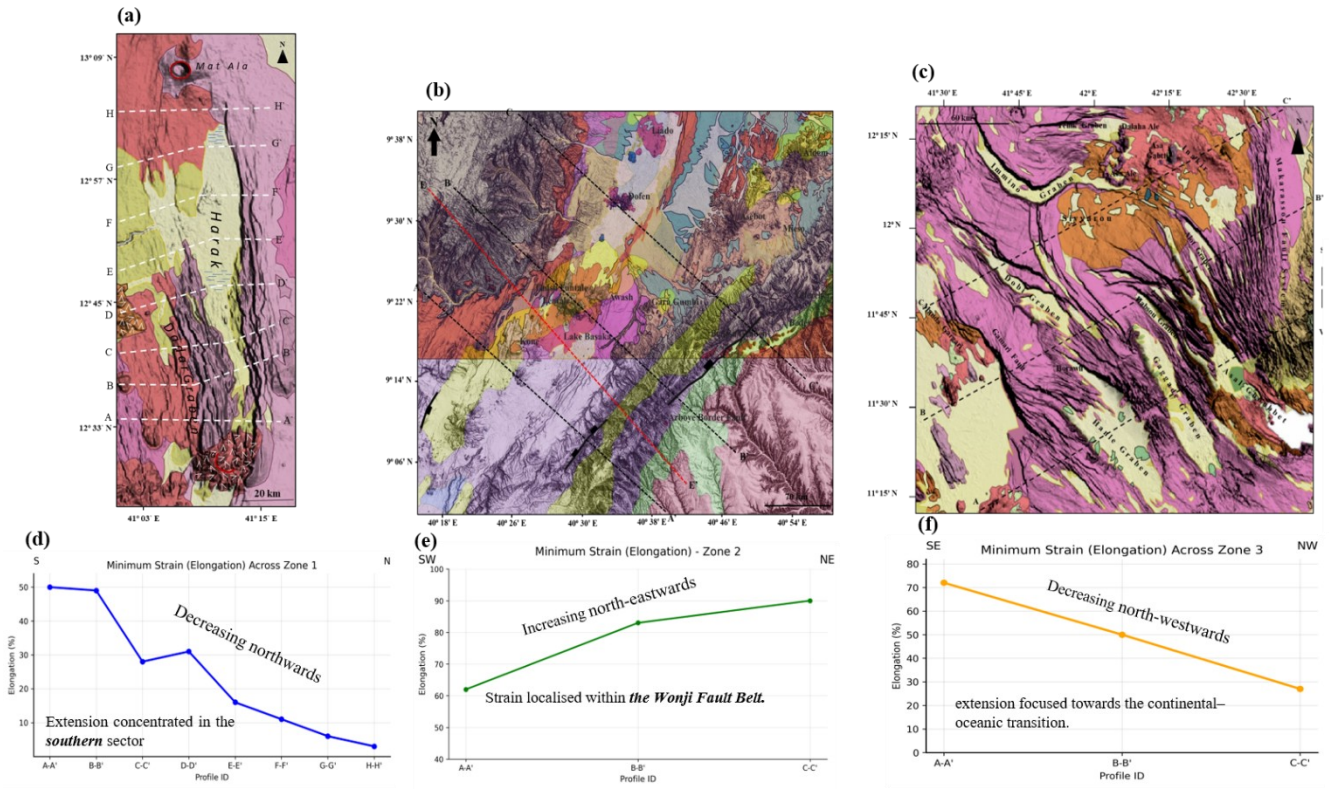


Figure 7.4: Summary of the spatial variation in minimum apparent fault-related elongation across the three study zones. The upper panels show the geological setting and locations of the cross-rift transects used for the minimum-strain analysis, and the lower panels show the corresponding elongation values along the transect directions. (a) Zone 1 (NAD), where minimum apparent elongation decreases overall northwards from approximately 50% in the southern profiles to approximately 3% in the northernmost profile. (b) Zone 2 (NMER), where minimum apparent elongation increases north-eastwards from approximately 62% to approximately 90%. (c) Zone 3 (EAD), where minimum apparent elongation decreases north-westwards from approximately 72% to approximately 27%. These values were derived from DEM-based line-length balancing and represent minimum apparent fault-related strain rather than total tectonic extension.

The DEM-derived elongation values should, however, be interpreted as minimum apparent fault-related strain rather than as measurements of total tectonic extension. The calculation assumes that the mapped fault scarps represent the principal surface expression of fault-related extension along each transect. However, the detectability and measured displacement of scarps depend on their preservation and topographic expression. Small scarps may be unresolved in the 30 m DEM, while erosion, sedimentary burial and volcanic resurfacing may degrade or obscure their surface expression. The calculated values therefore represent minimum estimates of the extension accommodated by the mapped surface-fault population. This limitation means that variations between transects may reflect both genuine spatial differences in fault-related extension and differences in preservation and detectability.

Surface age provides an additional control on the number of mapped faults and must

therefore be considered separately from preservation bias. Younger volcanic or sedimentary surfaces provide a shorter post-emplacement interval over which surface-breaking faulting can accumulate and be preserved and may therefore contain fewer mapped faults than older surfaces even where faulting rates are comparable. Conversely, older surfaces have potentially recorded deformation over a longer period but may also have experienced greater erosion, burial or resurfacing. Consequently, fault abundance cannot be interpreted solely as a measure of mapping completeness or tectonic strain. In Zone 2, approximately 90% of the 900 mapped faults occur within volcanic units, but fault frequency does not vary monotonically with surface age. Intermediate-age volcanic units contain the largest fault populations, whereas both some older units and the youngest units contain fewer faults. Geological surface age alone therefore does not explain the mapped fault frequency, because mapped area, rift position, resurfacing, erosion, burial and scarp preservation may also influence the observed distribution.

In Zone 1 (NAD), mapped faults occur predominantly on volcanic surfaces, whereas fewer faults are preserved on younger sedimentary surfaces. The northward decrease in minimum apparent elongation may therefore reflect a combination of genuine along-strike differences in surface fault-related extension and variations in the duration and preservation of the geological surface record. The elongation gradient should consequently not be interpreted from fault abundance alone.

Regional GPS observations provide an independent constraint on the present-day kinematics of the NAD–Danakil region. McClusky et al. (2010) showed that extension is progressively transferred southwards from the Red Sea rift into the Danakil Depression and that this transfer is associated with anticlockwise rotation of the Danakil Block relative to Nubia. Their GPS model indicates that the partitioning of Arabia–Nubia extension between the Red Sea and Danakil rift branches changes markedly along strike. These observations provide independent regional evidence that deformation in the northern Afar–Danakil region is spatially variable, consistent with the along-strike variation recorded by the DEM-derived minimum apparent elongation profiles. However, the GPS observations measure present-day plate-boundary deformation and should not be expected to reproduce directly the longer-term cumulative extension recorded by the mapped fault scarps. The regional GPS-derived kinematic framework and the locations of Zones 1 and 3 are illustrated in Figure 7.5. McClusky et al. report a present-day Danakil–Nubia rotation rate of $1.9° \pm 0.1^{\circ}\text{Myr}^{-1}$,

with extension transferred progressively from the Red Sea branch into the Danakil Depression

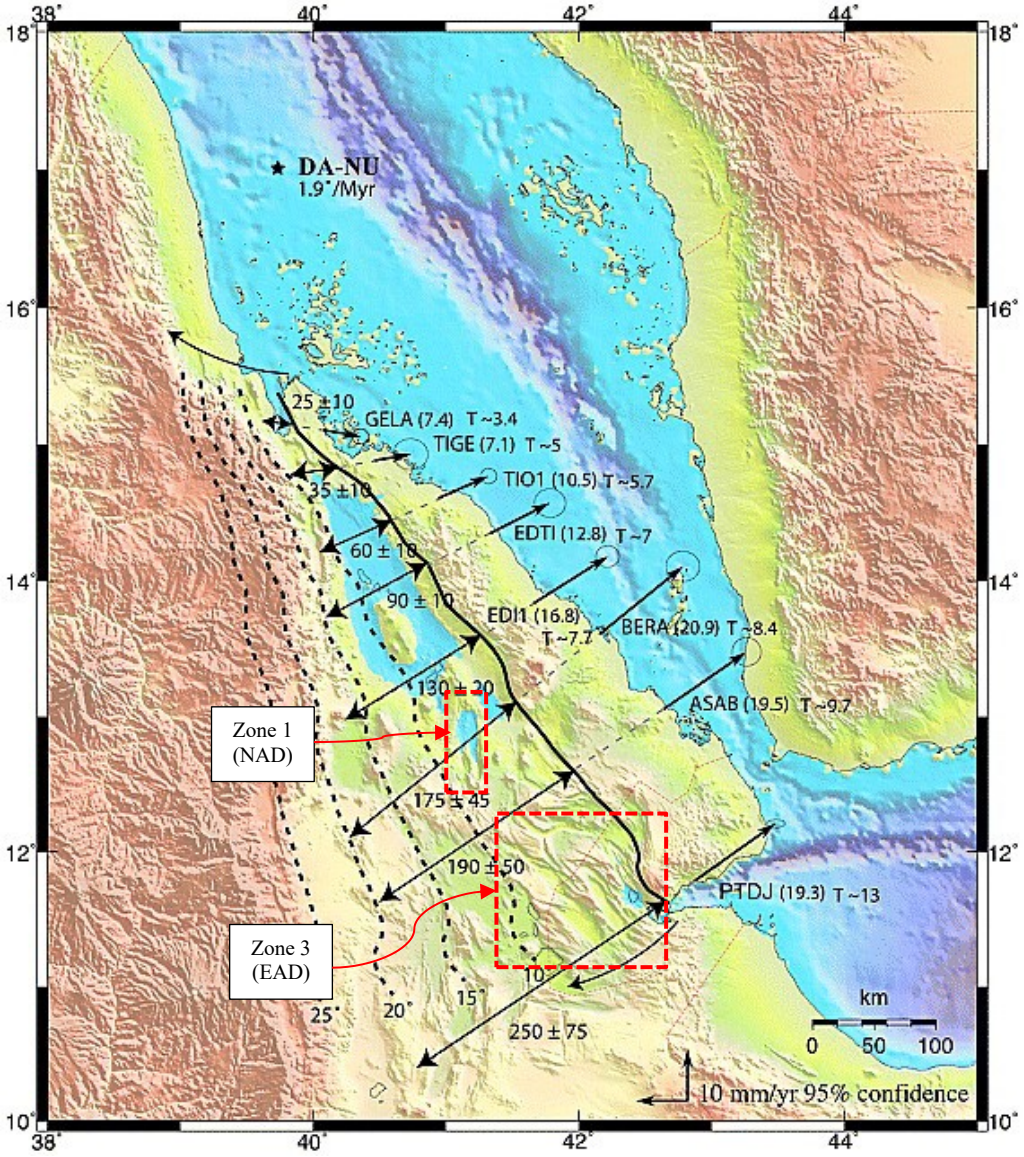


Figure 7.5: GPS-constrained back-rotation model of the Danakil Block relative to Nubia, showing the progressive closure of the Danakil Depression and the relationship between its width, present-day GPS-derived velocities and inferred age. Back-rotation of 10° closes the northern part of the depression, whereas a total rotation of approximately 25° is required to close the southern part. Assuming a constant GPS-derived Danakil–Nubia rotation rate of 1.9 ± 0.1° Myr^{-1}, the inferred age of Danakil Block rotation is approximately 9.3 ± 4 Ma. Red dashed boxes indicate the approximate locations of Zone 1 (NAD) and Zone 3 (EAD) investigated in this study. Modified from McClusky et al. (2010).

In Zone 2 (NMER), the north-eastward increase in minimum apparent elongation is consistent with the established interpretation that Quaternary deformation became increasingly focused towards the rift axis as the northern Main Ethiopian Rift reorganised (Ebinger and Casey, 2001; Wolfenden et al., 2004; Corti, 2009). Independent geodetic and seismic observations support this interpretation. GPS measurements across the Main Ethiopian Rift recorded rift-normal extension of approximately 4.0 ± 0.9 mm yr^{-1} during 1992–2003 and showed maximum strain

centred within the rift valley close to an active magmatic segment rather than on the major rift-bounding faults (Bendick et al., 2006). The regional tectonic setting and location of the geodetic array are shown in Figure 7.6. ADD1 and BOLO are GPS stations located on opposite sides of the Main Ethiopian Rift and form part of the cross-rift geodetic network used by Bendick et al. (2006) to constrain present-day rift opening. Seismicity is similarly concentrated within approximately 20-km-wide Quaternary magmatic segments, where magma intrusion and faulting jointly accommodate extension (Keir et al., 2006). These independent observations therefore support the interpretation of axial strain localisation inferred from the DEM-derived transects.

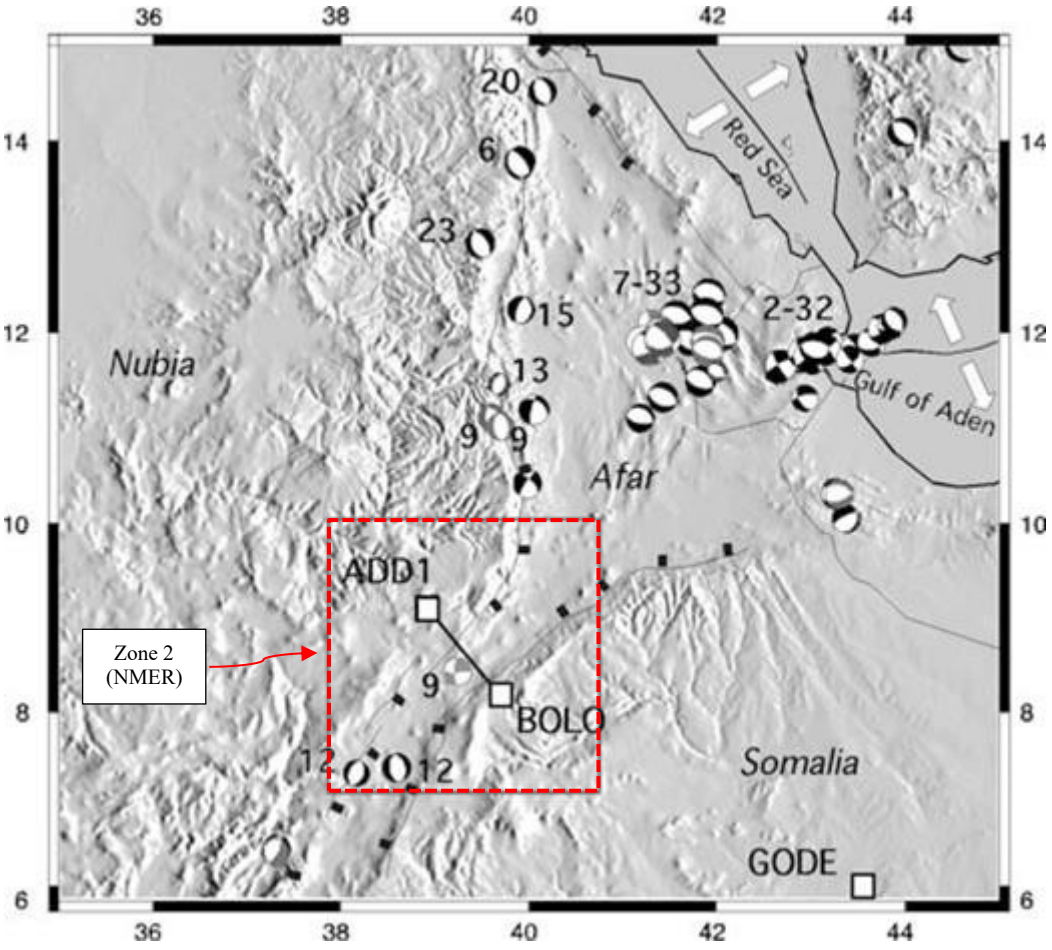


Figure 7.6: Regional tectonic and topographic setting of the Ethiopian Rift, showing earthquake focal mechanisms, relocated earthquake depths and the location of the geodetic array used to constrain present-day deformation across the Main Ethiopian Rift. The solid line marks the position of the geodetic array. The red dashed box and arrow indicate the approximate location of Zone 2 (NMER) investigated in this study. Modified from Bendick et al. (2006).

Importantly, dyke intrusion is not directly represented by the DEM-based line-length balancing used here. The calculated elongation values quantify the component of extension expressed by mapped surface fault scarps, whereas opening accommodated directly by dyke intrusion may contribute to extension without producing an equivalent

cumulative surface-fault displacement. Bendick et al. (2006) showed that a dyke-injection event contributed directly to MER opening during the GPS observation period, while Keir et al. (2006) concluded that upper-crustal strain in the northern MER is accommodated by a combination of magma intrusion and faulting. The minimum apparent elongation values may therefore underestimate total extension, particularly within magma-rich sectors such as the NMER.

In Zone 3 (EAD), Figure 6.20 shows that mapped faults occur across a range of volcanic surfaces, including older volcanic units of approximately 7 Ma age as well as younger volcanic units. The north-westward decrease in minimum apparent elongation therefore cannot be attributed solely to the age of a single surface unit. Instead, it is interpreted as spatial variation in the amount of fault-related extension preserved across the mapped transects, superimposed on differences in surface age, resurfacing and preservation. The geological history of the EAD includes widespread Stratoid-related volcanism of approximately 7.1–4 Ma as well as younger volcanic episodes, providing a long and spatially variable surface record on which faulting has accumulated.

Regional GPS and InSAR observations provide an independent constraint on present-day strain accommodation across Afar. Pagli et al. (2014) combined GPS and InSAR to produce a high-resolution three-dimensional velocity field and showed that strain accommodation varies markedly across the Afar rift. In central Afar, extension is distributed across several overlapping rift segments, including the Manda–Gargori, Dobi and Immino systems, whereas southern Afar shows more strongly focused deformation at the Asal–Ghoubbet segment. The same study also identifies pronounced post-dyking deformation around Dabbahu, demonstrating the importance of magmatic processes in controlling the magnitude and localisation of present-day strain. These observations provide independent support for spatially heterogeneous strain localisation across Afar, although they represent present-day deformation rather than the longer-term cumulative deformation recorded by the DEM-derived fault scarps.

Taken together, the DEM-derived minimum apparent elongation values and independent geodetic observations support spatial variations in strain localisation across the NAD–NMER–EAD system. However, the absolute elongation values remain minimum estimates of the surface fault-related component of extension. The

principal sources of uncertainty and potential bias include the 30 m DEM resolution, unresolved small fault scarps, scarp degradation and erosion, sedimentary burial, volcanic resurfacing, differences in the exposure age of geological surfaces, and the omission of extension accommodated directly by dyke intrusion. The elongation patterns are therefore interpreted together with surface geology, fault-system organisation, magmatic processes and independent geodetic observations rather than as complete measurements of total tectonic extension.

7.4 Tectonic evolution across the continental–oceanic rifting transition

The three study zones lie within the northern part of the East African Rift System and the Afar Depression, where the Red Sea, Gulf of Aden and Main Ethiopian Rift meet in a ridge–ridge–ridge triple junction between the Nubian, Somali and Arabian plates (Ebinger et al., 1993; Wolfenden et al., 2004; Corti, 2009). The regional kinematic framework adopted in this chapter follows the model of Rime et al. (2023), in which the Afar Rift is treated as an independent rift system rather than a simple onshore continuation of the Red Sea Rift. In this model, the Afar and Red Sea rift systems are separated by the Arrata Microplate, while the Danakil Block forms part of the broader rotational kinematic system. Figure 7.7 summarises this regional framework and shows the positions of the North Afar Depression (NAD), North Main Ethiopian Rift (NMER) and East Afar Depression (EAD) relative to the main rift segments and the Arrata Microplate.

Geological reconstructions and geodetic observations provide independent constraints on this regional kinematic framework. GPS observations show anticlockwise rotation of the Danakil Block relative to Nubia and progressive southward transfer of Arabia–Nubia extension from the southern Red Sea into the Danakil Depression (McClusky et al., 2010; Viltres et al., 2020). McClusky et al. (2010) estimated a present-day Danakil–Nubia rotation rate of approximately $1.9 \pm 0.1°\ Myr^{-1}$, whereas Viltres et al. (2020), using a revised block geometry and a longer observation period, estimated approximately $2.83°\ Myr^{-1}$ and identified a broad deformation zone across northern Danakil–Afar. Rime et al. (2023) interpreted the regional configuration as a large-scale relay between the southward-propagating Red Sea Rift system and the northward-propagating Afar Rift, separated by the Arrata Microplate. These observations indicate that deformation is distributed between interacting rift systems and rotating crustal blocks rather than being confined to a single continuous rift axis. This kinematic

framework provides the regional context for interpreting the contrasting fault architectures and strain distributions identified in Zones 1–3.

The three study zones do not, however, represent identical stages or styles of rift development. Differences in fault scaling, linkage, strain localisation and geological context identified in Chapters 4–6 provide a basis for comparing their tectonic evolution. Zone 1 represents an advanced continental rift sector affected by transfer and partitioning of extension within the Danakil–Afar system. Zone 2 represents a mature continental magmatic rift in which deformation has become strongly focused into axial magmatic segments. Zone 3 lies within the Afar–Gulf of Aden transition, where faulting, magmatism and interactions between overlapping rift segments are consistent with an advanced stage of plate-boundary localisation. Importantly, Zone 3 should not be interpreted as a region of simple orthogonal extension; its en-échelon fault and graben geometry indicates oblique and partitioned deformation associated with interaction between the Afar and Gulf of Aden rift systems and local block rotation.

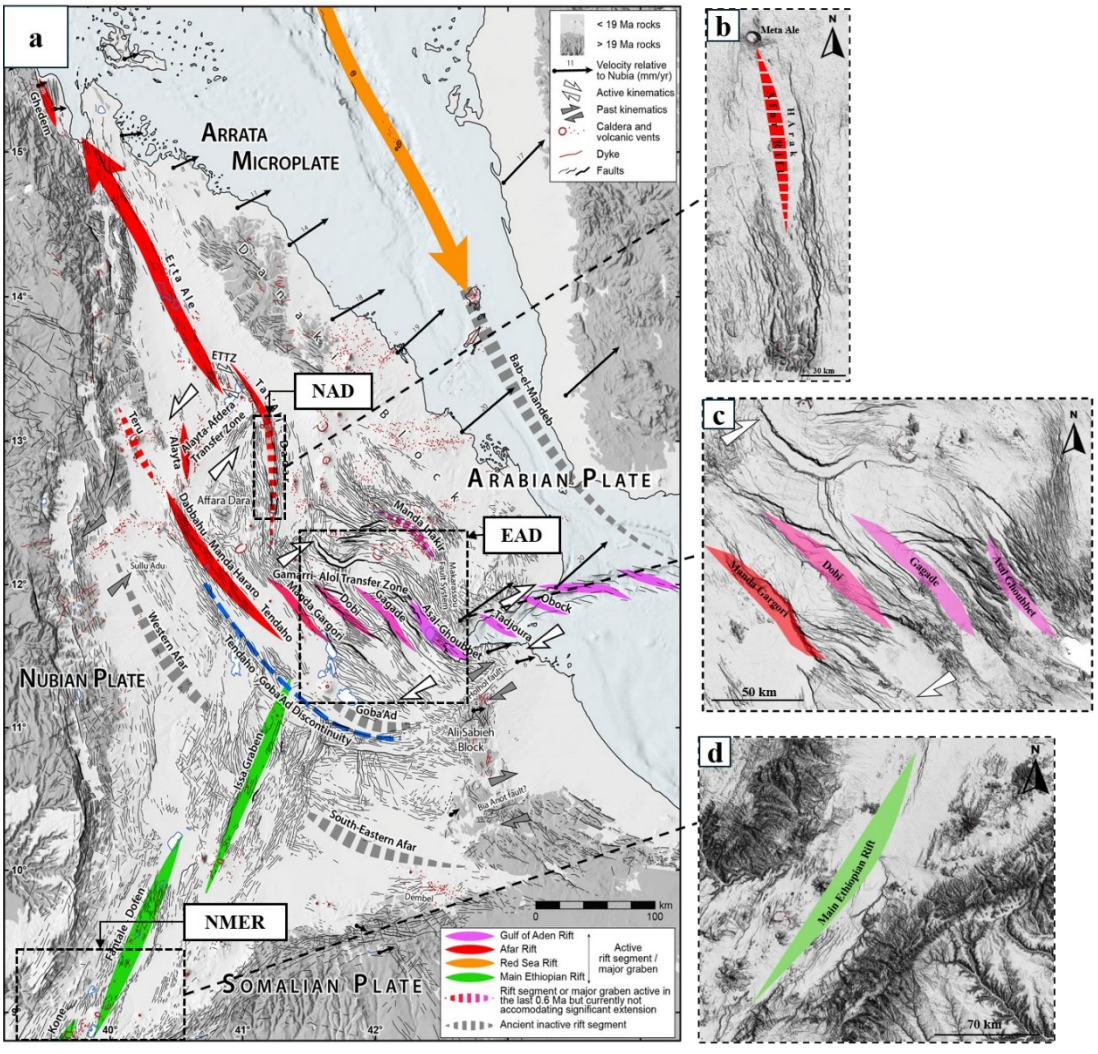


Figure 7.7: Tectonic settings of the three study zones along the northern East African Rift and Afar Depression. (a) Rift dynamics map of the Afar Depression and surrounding rift systems, showing the locations of the three study zones (NAD, NMER and EAD). Modified from Rime et al. (2023), based on Corti (2009), Doubre et al. (2017), Moore et al. (2021), Pagli et al. (2014), Ruch et al. (2021), Sangha et al. (2022) and Viltres et al. (2020). ETTZ = Erta Ale–Tat'Ali Transfer Zone. (b–d) DEM-derived hillshade maps: (b) Zone 1, highlighting the main Afar rift-bounding faults; (c) Zone 3, showing en-échelon grabens linked to the Afar and Gulf of Aden rifts; and (d) Zone 2, illustrating the narrow axial belt of the Main Ethiopian Rift.

Zone 1, the North Afar Depression, lies in northern Afar at the transition between central Afar and the Danakil Depression. The stratigraphy is dominated by Pliocene–Early Pleistocene basalts and syn-rift sediments resting on Oligocene flood basalts, with late Quaternary volcanic and sedimentary deposits filling basins such as the Harak Graben in the southern Danakil Depression (Rime et al., 2023; Hurman et al., 2023).

Within Zone 1, the mapped fault system shows a pronounced along-strike south–north variation, rather than an across-rift asymmetry. In the south, narrow and relatively deep grabens around the Harak area are bounded by long, high-displacement faults, many of which display multi-peak or irregular displacement profiles and evidence of soft and hard linkage. This southern part of the zone also contains the highest minimum apparent strain values. Farther north, the basins become wider and less sharply defined, faults are generally shorter and less strongly segmented, and minimum apparent strain decreases to very low values. Because broadly similar Pliocene–Quaternary rocks occur across much of the zone, this south–north contrast is interpreted primarily as a long-strike variation in the localisation of fault-related extension, rather than as an across-rift asymmetry or a simple lithological effect.

A tectono-magmatic explanation for this variation is provided by regional studies of the Danakil Rift. Hurman et al. (2023) showed that fault density, fault length and connectivity generally increase away from magmatic segment centres, where a greater proportion of extension may instead be accommodated by magmatic intrusion. They also identified oblique opening in the southern Danakil Rift associated with the along-axis step between the Erta Ale and Harak sub-regions. The stronger surface-fault expression in the southern part of Zone 1 is therefore consistent with spatial partitioning of extension between brittle faulting and magmatic intrusion, together with interaction between adjacent rift segments, rather than with a spatially uniform extension field.

The temporal development of central Afar and the Danakil Depression also differs

substantially. Central Afar has experienced long-lived tectono-magmatic activity and large cumulative stretching since approximately 30 Ma, whereas the Danakil Depression developed considerably later and has experienced less cumulative magmatic modification. GPS-constrained reconstruction by McClusky et al. (2010) places the development of Danakil Block rotation and opening of the Danakil Depression at approximately 9.3 ± 4 Ma. Thus, the principal development of the Danakil Depression occurred on the order of ~20 Myr later than the earliest major Oligocene tectono-magmatic activity in central Afar. Rime et al. (2023) further suggested that the Danakil Depression experienced less cumulative magmatic activity than central Afar until relatively recent stages of rifting.

The high minimum apparent strain and mature, segmented faults observed in southern Zone 1 are therefore consistent with substantial Quaternary fault-related extension along this part of the Danakil margin. At the same time, geodetic and seismic observations indicate that present-day plate separation is increasingly concentrated within narrower axial magmatic segments, including Dabbahu–Manda Hararo and Asal–Ghoubbet, where magmatic intrusion and fault slip accommodate active extension (Wright et al., 2006; Pagli et al., 2014; Doubre et al., 2017; Rime et al., 2023).

Importantly, the south–north decrease in minimum apparent strain observed in Zone 1 demonstrates spatial variation in surface fault-related extension but does not by itself demonstrate temporal strain migration. Evidence for temporal reorganisation instead comes from the independent regional geological and geodetic framework, including propagation of the Afar Rift, rotation of the Danakil Block and progressive localisation of active deformation into younger axial magmatic segments (McClusky et al., 2010; Rime et al., 2023). The DEM-derived strain pattern is therefore interpreted as being consistent with regional tectono-magmatic reorganisation, rather than as independent evidence for temporal migration of strain.

Zone 2, the North Main Ethiopian Rift, forms the continental arm of the triple junction. It links southwards to the Main Ethiopian Rift and northwards to Afar. The NMER stratigraphy includes pre-rift plateau flood basalts of the Alaji Group (~24–22 Ma), followed by mid–Late Miocene volcanic rocks and lacustrine sediments (~14–9 Ma), and Mio–Pliocene rift-floor volcanics and sediments overlain by Early Pleistocene lavas (~3.6–2.5 Ma) (Chernet et al., 1998; Wolfenden et al., 2004). Structural and

geochronological evidence indicates that major rifting in the NMER began after approximately 11 Ma, substantially later than the earliest tectono-magmatic activity in central Afar, and that deformation subsequently evolved from broad border-fault-bounded basins towards a narrow belt of Wonji axial magmatic segments active since approximately 2 Ma (Wolfenden et al., 2004; Corti, 2009).

Present-day seismicity provides independent evidence that this localisation remains active. Keir et al. (2006) showed that earthquakes in the northern MER are concentrated within narrow, en-échelon Quaternary magmatic segments rather than predominantly along the older rift-border faults. This indicates that present-day upper-crustal extension is accommodated by a combination of brittle faulting and magmatic intrusion.

The Zone 2 fault population is characterised by large numbers of relatively short faults developed on Pleistocene lavas within the Wonji Fault Belt. These faults are organised into narrow, segmented swarms that follow the axial magmatic segments, whereas the older, longer border faults are less common within the mapped population. Minimum apparent extensional strain is strongly focused within a narrow NNE-trending axial corridor and decreases markedly away from this belt. This distribution indicates that extension in the NMER is presently strongly localised within a narrow magmatic rift, consistent with models in which brittle faulting and magmatism share the extensional budget in the northern MER (Ebinger, 2005; Corti, 2009; Keir et al., 2006).

At the same time, many of the axial faults are relatively short and have small displacements. Their limited geometric development indicates that, despite the long overall history of rifting, much of the present axial fault population remains mechanically young. Zone 2 can therefore be interpreted as a mature continental magmatic rift in which deformation has become strongly localised, while individual faults within the present-day axial system continue to grow, interact and link.

Zone 3, the East Afar Depression, covers central–eastern Afar and the Ethiopia–Djibouti transition, where the Afar Rift interacts with the westward-propagating Gulf of Aden Rift. The surface geology is dominated by Quaternary rocks, including Upper Stratoid basalts of approximately 2.3 Ma and younger and thick Pleistocene–Recent lacustrine and fluvial sediments within the Tendaho, Goba'Ad and Dadar grabens. Very young volcanic rocks of <0.6 Ma also occur around Tendaho–Goba'Ad–Dadar, Manda Hararo–Manda Inakir and Asal–Ghoubbet (Lahitte et al., 2003; Rime et al.,

2023). Stratigraphic and geodetic evidence suggests that Tendaho probably initiated between approximately 1.1 and 0.6 Ma, whereas its activity declined after approximately 0.2 Ma as deformation and magmatism became increasingly focused on younger Afar- and Gulf of Aden-related segments (Stab et al., 2016; Rime et al., 2023).

Fault mapping in Zone 3 revealed a combination of mature Early Pleistocene grabens and very young axial fault systems. Long basin-bounding faults along Tendaho and parts of Goba'Ad cut Upper Stratoid basalts and exhibit large apparent displacements, complex multi-peak displacement profiles and numerous soft and hard linkages, consistent with mechanically mature graben margins. Superimposed on these are shorter faults cutting very young lava flows associated with both Afar Rift segments, such as Dabbahu–Manda Hararo, and Gulf of Aden-related segments, including Dobi–Gaggade–Asal–Ghoubbet.

The en-échelon geometry of faults and grabens in Zone 3 indicates that this sector is not undergoing simple orthogonal extension. Instead, the structural geometry is consistent with oblique and partitioned deformation produced by the interaction and overlap of differently oriented Afar- and Gulf of Aden-related rift segments, together with local block rotation. Independent regional GPS and InSAR observations similarly demonstrate that active extension in central and eastern Afar is distributed between overlapping rift segments rather than accommodated along a single continuous plate boundary (Pagli et al., 2014; Doubre et al., 2017; Rime et al., 2023).

Minimum apparent extensional strain in Zone 3 is generally high but strongly heterogeneous along strike. The highest values occur where Afar- and Gulf of Aden-related segments intersect or overlap older grabens, whereas lower values occur in parts of Goba'Ad that geodetic studies indicate are only weakly active at present. The coexistence of mature grabens, very young magmatic segments and a heterogeneous strain field is therefore consistent with a late localisation phase in which extension is being redistributed from more broadly distributed older grabens towards a smaller number of narrow, actively deforming axial segments closer to the developing oceanic plate boundary (Lahitte et al., 2003; Stab et al., 2016; Rime et al., 2023).

Comparison of the three zones highlights a shared regional tectonic background but distinct structural and magmatic states within the continuum from continental to oceanic rifting. Zone 1 is characterised by pronounced along-strike variation, with

more mature, linked and higher-displacement fault systems in the south and shorter, less strongly segmented structures towards the north. Zone 2 is characterised by strong localisation of strain into the young Wonji axial magmatic belt, although many individual axial faults remain mechanically immature. Zone 3 combines mature Early Pleistocene grabens with very young axial segments associated with both the Afar and Gulf of Aden rifts and exhibits a highly heterogeneous strain field reflecting active redistribution of extension and local block rotation.

The three zones therefore should not be interpreted as a simple chronological sequence from young to old rifting. Instead, each represents a different style and stage of strain localisation across the continent–ocean transition: an advanced Danakil–Afar rift sector characterised by strong along-strike partitioning in Zone 1; a mature but still continental magmatic rift in Zone 2; and an actively evolving transitional sector approaching oceanic-style plate-boundary localisation in Zone 3.

The temporal context for these contrasts is illustrated in Figure 7.5. The reconstruction shows successive stages from the pre-rift configuration through approximately 30, 19, 13, 8, 5, 2.5 and 1 Ma to the present day. These time slices illustrate progressive opening and interaction of the Red Sea, Gulf of Aden and Afar rift systems, development of the Arrata Microplate, anticlockwise rotation of the Danakil Block, and progressive reorganisation and localisation of deformation within central Afar, the Danakil Depression and the Tendaho–Goba'Ad–Asal system (Rime et al., 2023). Figure 7.8 therefore provides the temporal tectono-magmatic framework against which the contrasting fault-system characteristics measured in Zones 1–3 can be compared.

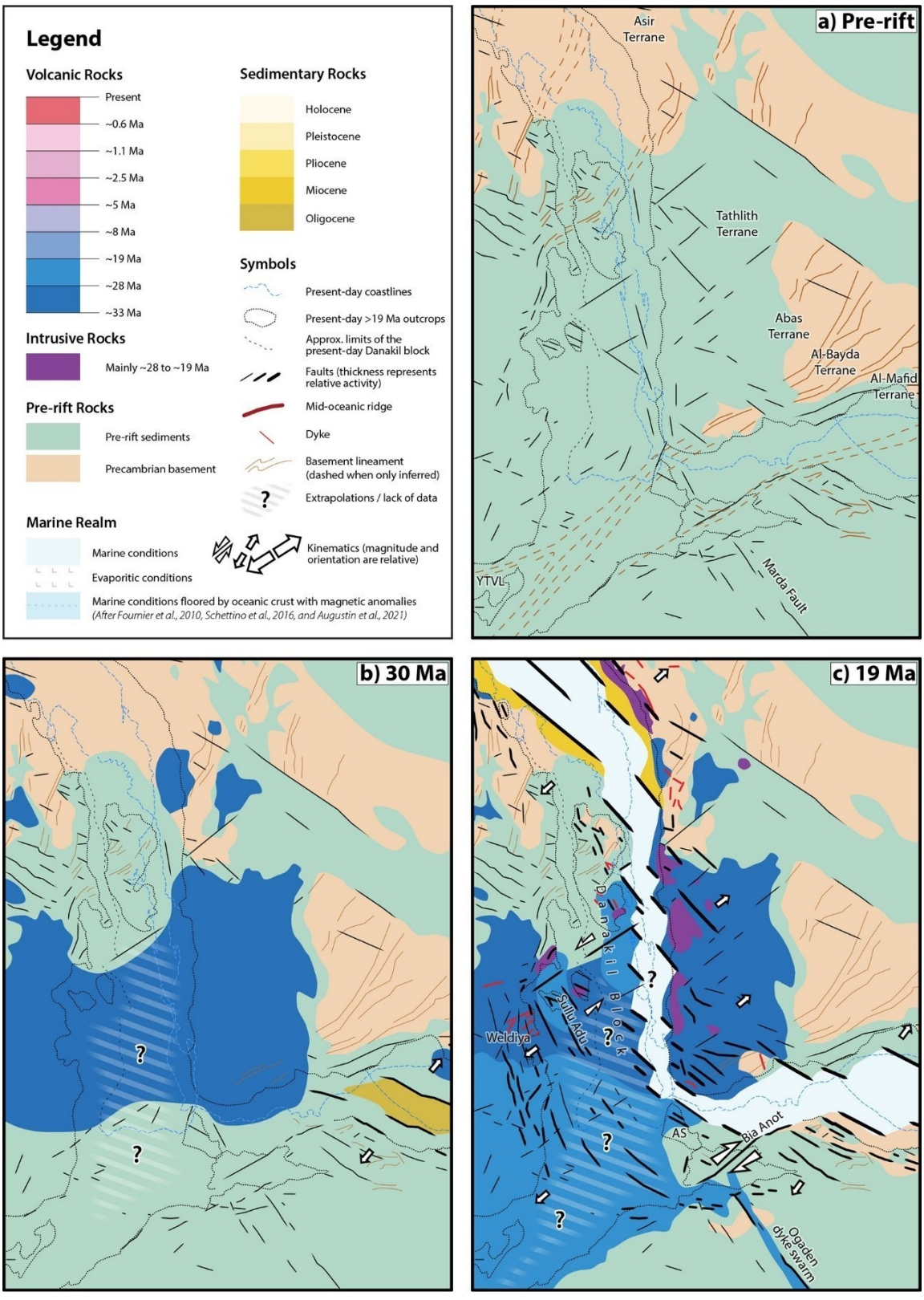


Figure 7.8: Tectonostratigraphic evolution of the Afar Depression and surrounding regions, modified from Rime et al. (2023). Time-slice maps show the pre-rift configuration and subsequent stages at ~30, ~19, ~13, ~8, ~5, ~2.5, and ~1 Ma and at present, illustrating the progressive opening of the Red Sea and Gulf of Aden rifts, anticlockwise rotation of the Arrata (Danakil) Block, and localisation of deformation in Central Afar, the Danakil Depression, and the Tendaho–Goba'Ad–Asal system. The reconstruction is based on a GPlates kinematic model combined with regional geological and stratigraphic constraints and is intended as a conceptual, schematic representation of Afar rift evolution (Rime et al., 2023).

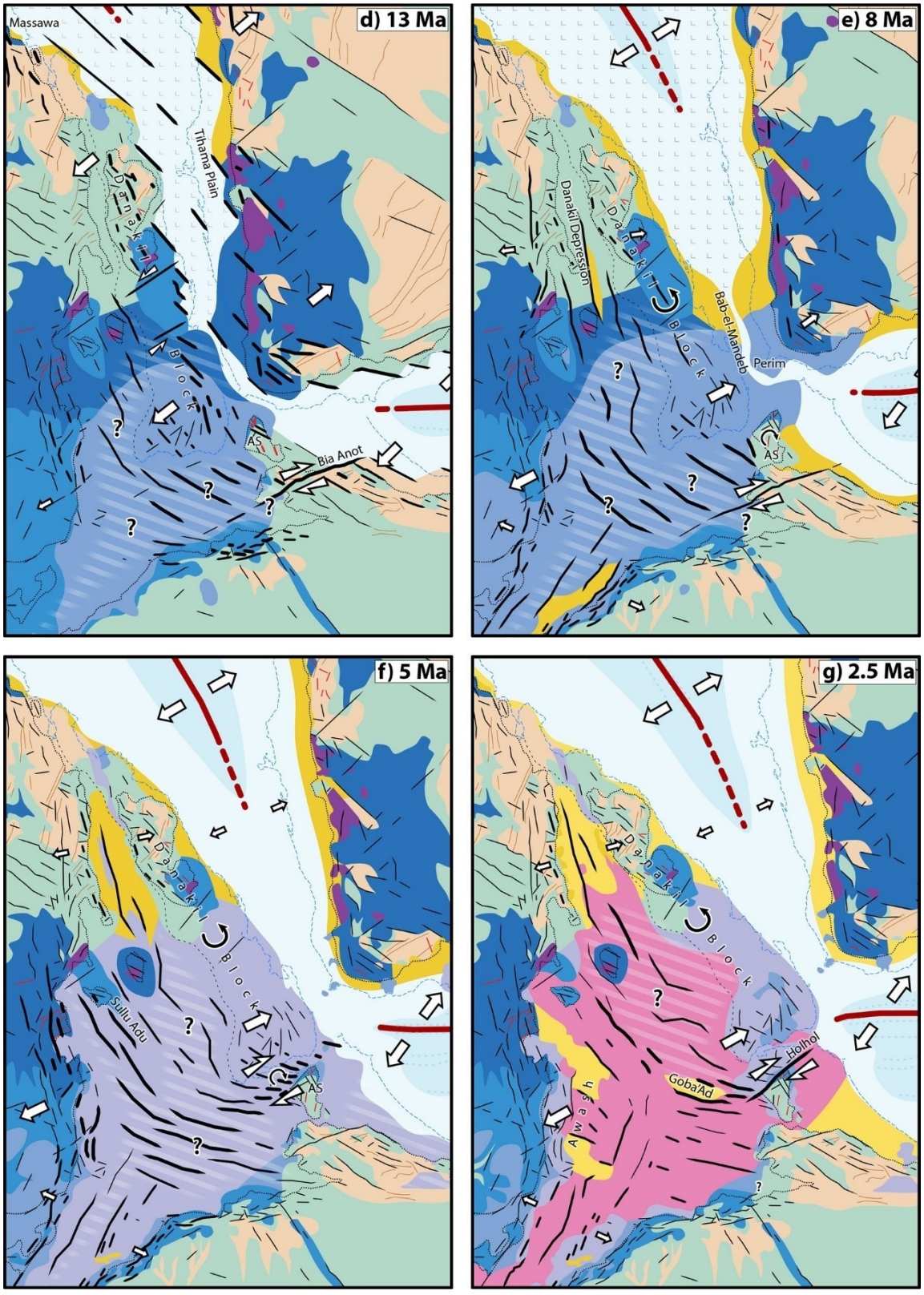


Figure 7.8 (continued)

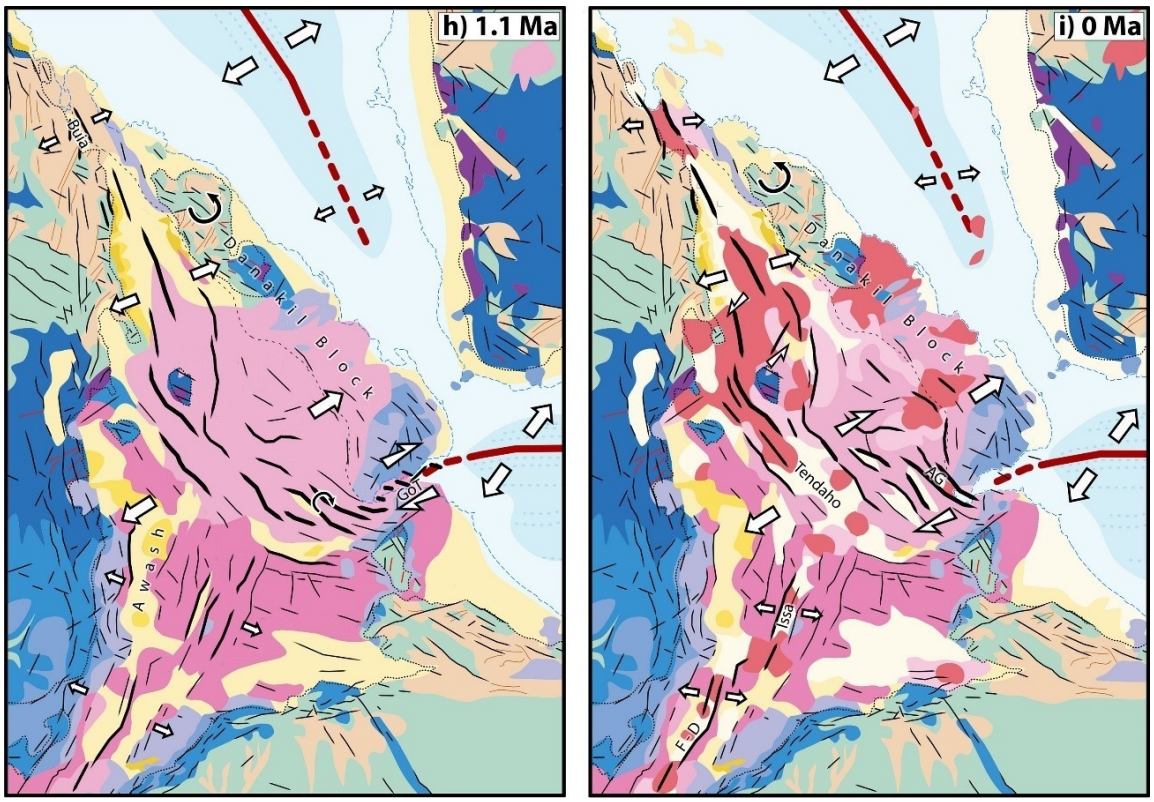


Figure 7.8 (continued)

When the three study zones are considered within the tectono-kinematic evolution illustrated in Figure 7.5, their mapped fault systems provide a partial test of the regional evolutionary model. In Zone 1, pronounced along-strike variations in fault maturity, linkage and minimum apparent strain record spatially variable fault-related extension within the Danakil–Afar system. The DEM-derived strain pattern does not independently demonstrate temporal migration of deformation; rather, its interpretation within an evolving rift system is supported by the independent geological and geodetic evidence for Danakil Block rotation, rift propagation and progressive localisation into younger axial magmatic segments.

Zone 2, where minimum apparent strain is strongly focused into the young Wonji axial belt and many short faults affect young volcanic rocks, is consistent with progressive localisation of continental extension into a narrow axial magmatic system. The coexistence of an evolved rift structure with mechanically young axial faults indicates that localisation of deformation does not require all individual faults within the active rift axis to be mature. Zone 3 combines mature Early Pleistocene grabens with very young Afar- and Gulf of Aden-aligned axial segments, en-échelon fault geometries and a heterogeneous strain field. These observations are consistent with a late-stage transitional configuration in which extension is being redistributed onto overlapping, oceanward-propagating rift segments at the Afar–Gulf of Aden junction.

Together, the structural, stratigraphic, magmatic and geodetic evidence supports the interpretation that the northern East African Rift and Afar Depression have evolved as a diachronous and segmented triple-junction system, rather than through a simple synchronous progression from continental to oceanic rifting. Rift propagation, magmatism and block rotation have progressively reorganised the locations at which fault growth and strain are concentrated through time (Ebinger and Casey, 2001; Wolfenden et al., 2004; Corti, 2009; Rime et al., 2023).

7.5 Implications for the thesis hypotheses

Hypothesis 1: Strain localisation changes systematically between rift domains

This hypothesis is supported by the minimum strain analysis and structural context provided by the surface unit distributions. The NAD shows low elongation values that decrease northwards, reflecting a distributed extension across many immature faults in a wide early-stage rift. In contrast, the NMER displays a marked increase in elongation along the strike, demonstrating strong localisation into the Wonji magmatic belt, where brittle faulting and magmatism now accommodate most of the ongoing extension. The EAD again shows a northward decrease in elongation, indicating that strain is unevenly partitioned within the complex linkage zone between the Afar and Gulf of Aden rifts. Although the absolute values are minimum estimates because DEM-based scarp mapping inherently under-records degraded or buried fault scarps, the relative trends remain robust. Together, these patterns confirm that strain does not evolve uniformly along the rift but instead become more focused within structurally mature sectors and reorganises where rift branches interact. Therefore, the results provide clear support for Hypothesis 1.

Hypothesis 2: Fault growth follows established displacement–length and segmentation/linkage models

The combined D–L relationships, displacement-profile types and linkage patterns provide broad support for this hypothesis. All three fault populations fall within the established global displacement–length envelope and show the expected positive relationship between fault length and displacement. The displacement profiles and mapped linkage relationships are also consistent with progressive interaction and coalescence of initially separate fault segments. Relatively simple single-peak displacement profiles are more commonly associated with less complex fault geometries, whereas multi-peak and irregular profiles occur more frequently where

neighbouring segments interact and become soft- or hard-linked. This behaviour is broadly consistent with established models of normal-fault growth in which isolated segments propagate, interact through relay structures and progressively link to form larger composite faults (Peacock and Sanderson, 1991; Kim and Sanderson, 2005). Peacock and Sanderson (1991), for example, showed that linkage between normal-fault segments produces characteristic displacement minima and more complex displacement–distance profiles at relay structures.

However, the differences between the NAD, NMER and EAD should not be interpreted as a simple temporal progression along a single fault-growth pathway. In magma-rich rifts, fault growth and displacement accumulation occur together with magmatic processes that can accommodate a significant proportion of crustal extension. In the NMER, seismicity is concentrated within narrow Quaternary magmatic segments, and geophysical observations indicate that extension within these segments is accommodated by both dyke intrusion and brittle faulting. Dyke emplacement can therefore accommodate horizontal opening without producing an equivalent amount of long-term displacement on surface faults, while stresses associated with dyke intrusion may also trigger faulting in the upper crust (Keir et al., 2006).

Volcanic resurfacing provides an additional control on the apparent maturity of the mapped fault populations. Repeated lava flows can bury or partly obscure older fault scarps and generate young volcanic surfaces on which subsequent faults develop. Faults mapped on these younger surfaces may therefore be relatively short and have small displacements even where the underlying rift system has experienced a much longer history of extension. Conversely, faults preserved on older surfaces have had more time to accumulate displacement, propagate and interact with neighbouring structures. Consequently, differences in fault length, displacement and profile geometry between the three study zones may reflect not only mechanical fault growth and linkage, but also variations in magmatic intrusion, volcanic resurfacing, surface age and preservation.

The observed fault populations are therefore interpreted as recording the combined effects of fault propagation, displacement accumulation, segment interaction and linkage, superimposed on spatially variable magmatic accommodation of extension. This interpretation is particularly important in the NMER and EAD, where active magmatic segments can localise deformation and redistribute strain between dyke

intrusion and brittle faulting. The agreement between the D–L scaling behaviour, displacement-profile geometry and mapped linkage relationships therefore supports Hypothesis 2, but with the qualification that fault-growth behaviour in Afar is modified by the interaction between tectonic extension and magmatism rather than being controlled by fault mechanics alone.

Hypothesis 3: Fault orientation and cross-cutting relationships record the kinematic evolution of the Danakil Block and Afar triple junction

The broader tectonic evolution synthesised from structural patterns, strain distribution, and surface geology provides a partial test of this hypothesis. In the NAD, the high minimum strain along the southern Danakil margin and the presence of long-lived margin-bounding structures inferred from previous studies are accompanied, in the DEM-mapped population, by predominantly short, low-displacement faults with mainly single-peak profiles and abundant soft linkages, indicating that surface extension is still shared between many mechanically immature structures during the anticlockwise rotation of the Danakil Block. The NMER exhibits strong localisation into the Wonji Belt, with many short, mechanically young axial faults cutting Pleistocene lavas, reflecting a mature but still continental magmatic rift feeding into the triple junction. The EAD combines long Early Pleistocene graben-bounding faults with very young Afar- and Gulf of Aden–aligned axial segments and a heterogeneous strain field, matching the predicted late-stage configuration in which extension is redistributed onto overlapping oceanward-propagating segments. Together, these observations indicate that the present fault orientations, strain patterns, and maturity contrasts are consistent with the diachronous, segmented evolution of the Afar triple junction driven by block rotation and migrating rift activity. Although orientation clustering and cross-cutting relationships provide the most direct evidence elsewhere in the chapter, the tectonic synthesis shows that the three zones occupy the positions expected in the rotational and propagational framework of Rime et al. (2023), thereby supporting Hypothesis 3.

7.6 Implications of the research

The combined D–L results indicate that faults from all three zones occupy the established global displacement–length space for normal faults, despite being derived from DEM-based surface measurements. This supports the inference that the datasets capture first-order fault-growth behaviour and can be used to compare along-system differences in fault maturity and strain partitioning. At the same time, the systematic shift from shorter, lower-displacement populations (dominant in NMER) to longer,

higher-displacement populations (most developed in EAD), with NAD intermediate, implies that the three zones sample different positions within a shared growth framework rather than requiring fundamentally different scaling laws in each sector (Walsh and Watterson, 1988; Cowie and Scholz, 1992; Lathrop et al., 2022).

The results also suggest that fault-system evolution is strongly influenced by the interaction and progressive linkage of segments. Classical end-member growth models (e.g. near-constant length after early establishment versus continuous propagation) provide useful reference trajectories, but the observed overlap of the three fault populations is more consistent with hybrid growth, in which faults experience an early phase of lengthening, followed by a longer phase dominated by displacement accumulation. Within this interpretation, the relative abundance of multi-peak and irregularly-peaked displacement profiles, together with increasing map-scale evidence for breached relays and through-going scarps, is expected to shift populations upwards within the D–L envelope as fault zones integrate and become more displacement-efficient (Peacock and Sanderson, 1991; Rotevatn et al., 2019).

The minimum strain results imply that extension is not organised as a single monotonic along-axis gradient across the wider system. Instead, the opposing northward elongation trends between the NAD, NMER, and EAD suggest sector-dependent localisation that is consistent with rift segmentation, domain-scale reorganisation, and changing rift architecture over time. In this context, the surface unit framework is important because it provides a geological basis for spatial variations in fault populations and scarp preservation. Volcanic resurfacing and sedimentary burial can both reduce the visibility of small scarps, and different surface ages imply different durations for the modification and masking of the fault morphology. Therefore, the combined results support an interpretation in which minimum elongation is best treated as a relative indicator of where fault-related extension is most clearly expressed at the surface, while recognising that the absolute values are underestimates and may vary with lithology, exposure time, and geomorphic overprinting (Walsh and Watterson, 1988; Wolfenden et al., 2004; Corti, 2009; Rime et al., 2023).

More broadly, these results demonstrate that the surface expression of fault-related extension cannot necessarily be treated as a direct measure of total crustal extension within a rift system. Variations in mapped strain may reflect differences in fault maturity and linkage, but may also be modified by magmatic accommodation, lithology, surface age and geomorphic preservation. This has wider implications for

comparisons between continental rifts, because apparent differences in fault density, displacement and strain may partly reflect how deformation is partitioned and preserved at the surface rather than tectonic extension alone. The Afar datasets therefore provide a useful framework for interpreting DEM-derived fault and strain measurements in other magma-rich continental rifts.

7.7 Limitations and uncertainties

A principal limitation is that all measurements are derived from topographic expression at a 30 m resolution; therefore, both displacement and strain are minimum estimates. Small scarps may be missed where slopes are degraded, lava flows resurface the terrain, or sedimentation buries scarp breaks; this under-sampling tends to reduce cumulative heave and lower the calculated elongations, especially in areas dominated by young volcanic flows or active sedimentary infill. In addition, Dmax measured from surface offsets cannot be assumed to represent total slip without independent constraints on the fault dip, subsurface geometry, and stratigraphic separation, which are not available here (Walsh and Watterson, 1988; Lathrop et al., 2022).

A second limitation concerns segmentation and linkage interpretation. Displacement–distance profile types and map-scale linkage classes are reproducible descriptors of DEM observations, but they do not provide a unique solution for subsurface connectivity. Some structures that appear soft-linked at the surface may be connected at shallow depths, and some apparently continuous scarps may remain segmented below the surface; therefore, maturity terms based on surface linkage should be treated as interpretive and scale-dependent (Peacock and Sanderson, 1991; Cartwright et al., 1995).

Finally, this study did not directly measure the deformation rates. Because surface-unit ages are compiled from published frameworks and DEM scarps provide no direct slip timing, the results mainly constrain spatial patterns and relative maturity rather than the absolute timing of fault growth. Comparisons with geodetic syntheses are therefore indicative rather than definitive, as present-day strain localisation can differ from long-term cumulative patterns, particularly in segmented rifts, where strain migrates between adjacent segments over time (Doubre et al., 2017; Rime et al., 2023).

7.8 Conclusion

In each of the three zones, the faults follow the standard displacement–length relationship seen globally in extensional faults; therefore, the DEM-derived values for Dmax and L are consistent with the general behaviour of faults during rifting.

Although the faults in all three zones have the same overall scaling characteristics, there are systematic differences in the frequency of smaller faults, the extent of larger faults, and the proportion of structures that show evidence of advanced fault-segment linkage at the surface (Walsh and Watterson, 1988; Cowie and Scholz, 1992; Lathrop et al., 2022).

The differences in fault-segment linkage among the three zones suggest that interactions among fault segments play a significant role in determining the position of faults within the displacement–length space. The increase in the complexity of thefault-zone architecture, particularly the presence of multiple irregular peaks in the fault-zone profiles and the occurrence of through-going scarps, supports the idea of progressive development from isolated or weakly interacting fault segments to composite fault zones formed through linkage and relay breaching. This provides a mechanical explanation for the scatter in the D–L plots and the differences in apparent fault maturity among the three zones (Peacock and Sanderson, 1991; Cartwright et al., 1995; Rotevatn et al., 2019).

The results also indicate that the strain localisation varies among the three rift sectors rather than following a single along-strike trend throughout the entire rift system. The differing northward elongation gradients observed among the three rift sectors (NAD, NMER, and EAD) suggest that the distribution of extension is reorganised among the neighbouring rift domains. This observation is consistent with previously published models of rift evolution, in which deformation has focused on different structural corridors over time (Ebinger and Casey, 2001; Wolfenden et al., 2004; Corti, 2009; Rime et al., 2023). Overall, the results of this study support a model of segmented and interacting rift domains in the northern East African Rift System and Afar Depression across the continental–oceanic rifting transition zone. In addition to fault scaling, the degree of fault network linkage and the sector-specific localisation of strain, the results also indicate that the maturity of faults and the location of surface-expressed extension are influenced by the evolving organisation of fault networks and by the geological setting (e.g. volcanic resurfacing, sedimentary burial), rather than by a single linear progression along the strike (Corti, 2009; Rime et al., 2023).

7.9 Future work

The following are knowledge gaps or opportunities for future research that, if addressed, would upgrade and reduce uncertainties in some of the analyses presented in this body of work, or are examples of how the techniques used here could be applied or developed further in a range of other geographic and geologic settings, including in studies of planetary geology.

Higher-resolution fault mapping:

Future studies could apply the same analytical workflow to higher-resolution topographic datasets (e.g. LiDAR, drone photogrammetry, or next-generation global DEMs) to refine the identification of low-offset scarps, relay structures, and the small-scale segmentation of these features. This would improve the displacement–length relationships and provide more accurate minimum strain estimates in resurfaced or sediment-covered terrains. One aspect of this might be to develop coding that would allow automated extraction of fault topographic data from DEM datasets.

Integration with subsurface geophysical datasets:

Combining the mapped fault populations with seismic reflection data, seismicity, gravity, magnetotelluric, and InSAR data would allow mapping of buried fault structures and hence analysis of their contribution to accumulated strain, but would also help constrain how deeper crustal structures, intrusion pathways, and magma reservoirs influence fault geometry, linkage, and the redistribution of strain within the Afar triple-junction system.

Testing block-kinematic models:

Incorporating contemporary geodetic data (GPS and InSAR), together with structural orientation trends, would allow for quantitative testing of the inferred anticlockwise rotation of the Danakil Block and the clockwise rotation of the internal Afar crustal blocks. Such work would help reconcile surface-based interpretations of strain migration with present-day regional kinematics.

Geographic extension of the workflow:

Applying the same fault population analysis to the southern Afar Depression or the southern Main Ethiopian Rift would enable a systematic comparison of fault

maturity, segmentation, and strain localisation along the rift system, helping to define whether the patterns observed in this thesis are local or regionally consistent. Extending the study to the less mature southern end of the East African Rift would allow the characterization of the scaling properties and growth behaviour of early continental rift margin faults, which could then be compared with the properties of the faults in the three zones within the continental-oceanic rifting transition which are the focus of this study.

Coupling fault growth with magmatic processes:

The volcanic units mapped across the three study zones span a range of ages and provide an opportunity to evaluate whether fault geometry and maturity vary systematically with the age of the surface on which the faults are preserved. A broad comparison of fault length, maximum displacement, Dmax/L ratio, linkage state and displacement-profile style across volcanic units indicates that surface age may influence the apparent maturity of fault populations, but the relationship is not uniform across the study areas. Older volcanic surfaces have generally had a longer period over which faults could accumulate displacement, propagate and interact, whereas faults cutting younger lava flows may be shorter and less displaced because the exposed surface has been more recently resurfaced. However, this relationship is complicated by spatial variations in magmatic intrusion, burial, erosion and fault reactivation. Consequently, volcanic age should be considered as one control on fault expression rather than as a simple predictor of fault maturity. The volcanic-unit classifications and ages used in the maps, tables and statistical analyses were therefore cross-checked to ensure consistency between Chapters 4–6.

Modelling of fault propagation and linkage:

Numerical or analogue modelling could be useful for simulating the propagation–overlap–linkage patterns observed in Zones 1–3, if the physical properties and mechanics of the faulting process are appropriately parameterised, building on work by, for example, Cowie et al. (2000) and Finch and Gawthorpe (2017). This might be used to provide physical conditions which promote the hybrid fault-growth pathways inferred from displacement-profile analyses.

Application to planetary rifts:

The DEM-based fault-mapping and statistical analysis methodology developed in this thesis is readily transferable to extra-terrestrial surfaces, as previously demonstrated by Orlov et al. (2022) and Shahrzad et al. (2023). Applying the approach to further rifted terrains on Mars or Venus would provide valuable comparative data on fault scaling, segmentation, and strain localisation in tectonic settings with different rheologies, loading conditions, and magmatic influences.

References

Acocella, V. 2006. Regional and local tectonics at Erta Ale caldera, Afar (Ethiopia). Journal of Structural Geology, 28(10), pp.1808–1820.

Acocella, V. 2014. Structural control on magmatism along divergent and convergent plate boundaries: Overview, model, problems. Earth-Science Reviews, 136, pp.226–288.

Acocella, V., Korme, T., Salvini, F. and Funiciello, R. 2003. Elliptic calderas in the Ethiopian Rift: Control of pre-existing structures. Journal of Volcanology and Geothermal Research, 119, pp.189–203.

Agostini, A., Bonini, M., Corti, G., Sani, F. and Mazzarini, F. 2011. Fault architecture in the Main Ethiopian Rift and comparison with experimental models: Implications for rift evolution and Nubia–Somalia kinematics. Earth and Planetary Science Letters, 301(3–4), pp.479–492.

Agostini, A., Corti, G., Zeoli, A. and Mulugeta, G. 2009. Evolution, pattern, and partitioning of deformation during oblique continental rifting: Inferences from lithospheric-scale centrifuge models. Geochemistry, Geophysics, Geosystems. 10, Q11015. doi:10.1029/2009GC002676.

Alghamdi, T. 2025. Python script for fault geometry data analysis [Computer software]. Zenodo. https://doi.org/10.5281/zenodo.17834085

Anders, M.H. and Schlische, R.W. 1994. Overlapping faults, intra-basin highs, and the growth of normal faults. Journal of Geology, 102(2), pp.165–180.

ArRajehi, A., McClusky, S., Reilinger, R. et al. 2010. Geodetic constraints on present-day motion of the Arabian Plate: Implications for Red Sea and Gulf of Aden rifting. Journal of Geophysical Research: Solid Earth, 115(B11), B11421.

Asefa, J. and Ayele, A. 2021. Seismicity of the East African Rift System for the period 2013 to 2016. Journal of African Earth Sciences. 183, 104315. doi:10.1016/j.jafrearsci.2021.104315.

Bailey, W.R., Walsh, J.J. and Manzocchi, T. 2005. Fault populations, strain distribution and basement fault reactivation in the East Pennines Coalfield, UK. Journal of Structural Geology. 27(5), pp.913–928. doi:10.1016/j.jsg.2004.10.014.

Barnett, J.A., Mortimer, J., Rippon, J.H., Walsh, J.J. and Watterson, J. 1987. Displacement geometry in the volume containing a single normal fault. AAPG Bulletin, 71, pp.925–937.

Bastow, I.D. and Keir, D. 2011. The protracted development of the continent–ocean transition in Afar. Nature Geoscience, 4(4), pp.248–250.

Bastow, I.D., Stuart, G.W., Kendall, J.M. and Ebinger, C.J., 2005. Upper-mantle seismic structure in a region of incipient continental breakup: northern Ethiopian rift. Geophysical Journal International, 162(2), pp.479-493.

Begg, J.G. and Mouslopoulou, V. 2010. Analysis of Late Holocene faulting within an active rift using lidar, Taupo Rift, New Zealand. Journal of Volcanology and Geothermal Research, 190, pp.152–167.

Bendick, R., McClusky, S., Bilham, R., Asfaw, L. and Klemperer, S. 2006. Distributed Nubia–Somalia relative motion and dike intrusion in the Main Ethiopian Rift. Geophysical Journal International. 165(1), pp.303–310. doi:10.1111/j.1365-246X.2006.02904.x.

Bonini, M., Corti, G., Innocenti, F. et al. 2005. Evolution of the Main Ethiopian Rift in the frame of Afar and Kenya rifts propagation. Tectonics, 24(1), TC1007.

Buck, W.R. 1991. Modes of continental lithospheric extension. Journal of Geophysical Research, 96(B12), pp.20161–20178.

Burg, J.-P. 2020. Faults. Structural Geology and Tectonics lecture notes. Zürich: ETH Zürich. Available at: https://www.files.ethz.ch/structuralgeology/JPB/files/English/3faults.pdf (Accessed: 29 September 2026).

Burrough, P.A. and McDonnell, R.A. 1998. Principles of Geographical Information Systems. 2nd ed. Oxford: Oxford University Press.

Cartwright, J.A., Mansfield, C. and Trudgill, B.D. 1996. The growth of normal faults by segment linkage. Zeitschrift für Geomorphologie Supplementband, 105, pp.153–168.

Cartwright, J.A., Trudgill, B.D. and Mansfield, C.S. 1995. Fault growth by segment linkage: An explanation for scatter in maximum displacement and trace length data from the Canyonlands Grabens of SE Utah. Journal of Structural Geology, 17(9), pp.1319–1326.

Casey, M., Ebinger, C.J., Keir, D., Gloaguen, R. and Mohamed, F.H. 2006. Strain accommodation in transitional rifts: Extension by dyke intrusion and faulting in the Ethiopian Rift. Geological Society, London, Special Publications, 259(1), pp.143–163.

Chauvet, F., Geoffroy, L., Le Gall, B. and Jaud, M. 2023. Volcanic passive margins and break-up processes in the southern Red Sea. Gondwana Research. 117, pp.169–193. doi:10.1016/j.gr.2023.01.004.

Chernet, T., Hart, W.K., Aronson, J.L. and Walter, R.C. 1998. New age constraints on the timing of volcanism and tectonism in the northern Main Ethiopian Rift–southern Afar transition zone (Ethiopia). Journal of Volcanology and Geothermal Research, 80(3–4), pp.267–280.

Childs, C., Holdsworth, R.E., Jackson, C.A.-L., Manzocchi, T., Walsh, J.J. and Yielding, G. 2017. Introduction to the geometry and growth of normal faults. Geological Society, London, Special Publications. 439(1), pp.1–9. doi:10.1144/SP439.24.

Childs, C., Watterson, J. and Walsh, J.J. 1995. Fault overlap zones within developing normal fault systems. Journal of the Geological Society, 152(3), pp.535–549.

Chorowicz, J. 2005. The East African Rift System. Journal of African Earth Sciences, 43, pp.379–410.

Çiftçi, N.B. and Bozkurt, E. 2007. Anomalous stress field and active breaching at relay ramps: a field example from Gediz Graben, SW Turkey. Geological Magazine. 144(4), pp.687–699. doi:10.1017/S0016756807003500.

Corti, G. 2009. Continental rift evolution: From rift initiation to incipient break-up in the Main Ethiopian Rift, East Africa. Earth-Science Reviews, 96(1–2), pp.1–53.

Corti, G. 2012. Evolution and characteristics of continental rifting: Analog modelling insights. Tectonophysics, 522–523, pp.1–21.

Cowie, P.A. and Scholz, C.H. 1992. Displacement–length scaling relationship for faults: Data synthesis and discussion. Journal of Structural Geology. 14(10), pp.1149–1156. doi:10.1016/0191-8141(92)90066-6.

Cowie, P.A., Gupta, S. and Dawers, N.H. 2000. Implications of fault array evolution for syn-rift depocentre development: Insights from a numerical fault growth model. Basin Research, 12(3–4), pp.241–261.

Cowie, P.A., Underhill, J.R., Behn, M.D., Lin, J. and Gill, C.E. 2005. Spatio-temporal evolution of strain accumulation derived from multi-scale observations of Late Jurassic rifting in the northern North Sea: A critical test of models for lithospheric extension. Earth and Planetary Science Letters. 234(3–4), pp.401–419. doi:10.1016/j.epsl.2005.01.039.

Dawers, N.H. and Underhill, J.R. 2000. The role of fault interaction and linkage in controlling syn-rift stratigraphic sequences: Normal faults in the Upper Jurassic of the Inner Moray Firth Basin, UK. Basin Research, 12(3–4), pp.309–328.

Doubre, C., Déprez, A., Masson, F., Socquet, A., Lewi, E., Grandin, R., Nercessian, A., Ulrich, P., De Chabalier, J.-B., Saad, I., Abayazid, A., Peltzer, G., Delorme, A., Calais, E. and Wright, T. 2017. Current deformation in Central Afar and triple junction kinematics deduced from GPS and InSAR measurements. Geophysical Journal International. 208(2), pp.936–953. doi:10.1093/gji/ggw434.

Ebinger, C.J. 2005. Continental break-up: The East African perspective. Astronomy & Geophysics, 46(2), pp.2.16–2.21.

Ebinger, C.J. and Casey, M. 2001. Continental breakup in magmatic provinces: An Ethiopian example. Geology, 29(6), pp.527–530.

Ebinger, C.J. and Hayward, N.J. 1996. Soft plates and hot spots: Views from Afar. Journal of Geophysical Research: Solid Earth, 101(B10), pp.21859–21876.

Ebinger, C.J., Jackson, J.A., Foster, A.N. and Hayward, N.J. 1999. Extensional basin geometry and the elastic lithosphere. Philosophical Transactions of the Royal Society A. 357(1753), pp.741–765. doi:10.1098/rsta.1999.0351.

Ebinger, C.J., Yemane, T., Woldegabriel, G., Aronson, J.L. and Walter, R.C. 1993. Late Eocene–Recent volcanism and faulting in the southern Main Ethiopian Rift. Journal of the Geological Society, 150(1), pp.99–108.

Finch, E. and Gawthorpe, R.L. 2017. Growth and interaction of normal faults and fault network evolution in rifts: Insights from three-dimensional discrete element modelling. Geological Society, London, Special Publications, 439(1), pp.219–248.

Fossen, H. 2010. Structural Geology. Cambridge: Cambridge University Press.

Fossen, H. and Rotevatn, A. 2016. Fault linkage and relay structures in extensional settings—A review. Earth-Science Reviews, 154, pp.14–28.

Gasse, F. and Street, F.A. 1978. Late Quaternary lake-level fluctuations and environments of the northern Rift Valley and Afar region (Ethiopia and Djibouti). Palaeogeography, Palaeoclimatology, Palaeoecology, 24(4), pp.279–325. doi:10.1016/0031-0182(78)90011-1.

Gawthorpe, R.L. and Leeder, M.R. 2000. Tectono-sedimentary evolution of active extensional basins. Basin Research, 12, pp.195–218.

Gawthorpe, R.L., Fraser, A.J. and Collier, R.E.L. 1994. Sequence stratigraphy in active extensional basins: implications for the interpretation of ancient basin-fills. Marine and Petroleum Geology. 11(6), pp.642–658. doi:10.1016/0264-8172(94)90021-3.

Gesch, D.B., Oimoen, M.J., Danielson, J.J. and Meyer, D. 2016. Validation of the ASTER Global Digital Elevation Model Version 3 over the conterminous United States. ISPRS Archives of the Photogrammetry, Remote Sensing and Spatial Information Sciences. XLI-B4, pp.143–148. doi:10.5194/isprs-archives-XLI-B4-143-2016.

Giba, M., Walsh, J.J. and Nicol, A. 2012. Segmentation and growth of an obliquely reactivated normal fault. Journal of Structural Geology, 39, pp.253–267.

Gillespie, P.A., Walsh, J.J. and Watterson, J. 1992. Limitations of dimension and displacement data from single faults and the consequences for data analysis and interpretation. Journal of Structural Geology. 14(10), pp.1157–1172. doi:10.1016/0191-8141(92)90067-7.

Grandin, R., Socquet, A., Jacques, E., Mazzoni, N., de Chabalier, J.-B. and King, G.C.P. 2009. September 2005 Manda Hararo–Dabbahu rifting event, Afar (Ethiopia): Constraints provided by geodetic data. Journal of Geophysical Research: Solid Earth. 114, B08404. doi:10.1029/2008JB005843.

Gudmundsson, A. 2011. Rock Fractures in Geological Processes. Cambridge: Cambridge University Press.

Gupta, A. and Scholz, C.H. 2000. A model of normal fault interaction based on observations and theory. Journal of Structural Geology, 22(7), pp.865–879.

Hammond, J.O.S., Kendall, J.-M., Stuart, G.W., Keir, D., Ebinger, C., Ayele, A. and Belachew, M. 2011. The nature of the crust beneath the Afar triple junction: Evidence from receiver functions. Geochemistry, Geophysics, Geosystems. 12(12), Q12004. doi:10.1029/2011GC003738.

Hayward, N.J. and Ebinger, C.J. 1996. Variations in the along-axis segmentation of the Afar Rift system. Tectonics, 15(2), pp.244–257.

Hurman, G.L., Keir, D., Bull, J.M., McNeill, L.C., Booth, A.D. and Bastow, I.D. 2023. Quantitative analysis of faulting in the Danakil Depression Rift of Afar: The importance of faulting in the final stages of magma-rich rifting. Tectonics. 42(6), e2022TC007607. doi:10.1029/2022TC007607.

Hutchison, W., Pyle, D.M., Mather, T.A. et al. 2016. Causes of unrest at silicic calderas in the East African Rift: New constraints from Aluto volcano, Ethiopia. Geochemistry, Geophysics, Geosystems, 17, pp.3008–3030.

Jackson, C.A.-L., Bell, R.E., Rotevatn, A. and Tvedt, A.B.M. 2017. Techniques to determine the kinematics of synsedimentary normal faults and implications for fault growth models. Geological Society, London, Special Publications. 439, pp.187–217. doi:10.1144/SP439.22.

Keir, D., Bastow, I.D., Corti, G., Mazzarini, F. and Rooney, T.O. 2015. The origin of along-rift variations in faulting and magmatism in the Ethiopian Rift. Tectonics, 34(3), pp.464–477.

Keir, D., Ebinger, C.J., Stuart, G.W., Daly, E. and Ayele, A. 2006. Strain accommodation by magmatism and faulting as rifting proceeds to breakup: Seismicity of the northern Ethiopian Rift. Journal of Geophysical Research: Solid Earth, 111, B05314.

Kendall, J.-M., Stuart, G.W., Ebinger, C.J. et al. 2005. Magma-assisted rifting in Ethiopia. Nature, 433(7022), pp.146–148.

Keranen, K.M. and Klemperer, S.L. 2008. Discontinuous and diachronous evolution of the Main Ethiopian Rift: Implications for development of continental rifts. Earth and Planetary Science Letters, 265, pp.96–111.

Kim, Y.-S. and Sanderson, D.J. 2005. The relationship between displacement and

length of faults: A review. Earth-Science Reviews, 68(3–4), pp.317–334.

Kim, Y.-S., Andrews, J.R. and Sanderson, D.J. 2000. Damage zones around strike-slip fault systems and strike-slip fault evolution, Crackington Haven, southwest England. Geosciences Journal, 4(2), pp.53–72. doi:10.1007/BF02910127.

Lahitte, P., Gillot, P.-Y. and Courtillot, V. 2003. Silicic central volcanoes as precursors to rifting: The Afar case. Earth and Planetary Science Letters, 207(1–4), pp.103–116.

Lahitte, P., Gillot, P.-Y., Kidane, T., Courtillot, V. and Bekele, A. 2003. New age constraints on the timing of volcanism in central Afar, in the presence of propagating rifts. Journal of Geophysical Research: Solid Earth. 108(B2), 2123. doi:10.1029/2001JB001689.

Lathrop, B.A., Jackson, C.A.-L., Bell, R.E. and Rotevatn, A. 2022. Displacement/length scaling relationships for normal faults: A review, critique, and revised compilation. Frontiers in Earth Science, 10, 907543.

Mackenzie, G.D., Thybo, H. and Maguire, P.K.H. 2005. Crustal velocity structure across the Main Ethiopian Rift: Results from two-dimensional wide-angle seismic modelling. Geophysical Journal International, 162(3), pp.994–1006.

Maguire, P.K.H., Keller, G.R., Klemperer, S.L., Mackenzie, G.D., Keranen, K., Harder, S., O'Reilly, B., Thybo, H., Asfaw, L., Khan, M.A. and Amha, M. 2006. Crustal structure of the northern Main Ethiopian Rift from the EAGLE controlled-source survey; a snapshot of incipient lithospheric break-up. Geological Society, London, Special Publications. 259, pp.269–292. doi:10.1144/GSL.SP.2006.259.01.21.

Makris, J. and Ginzburg, A. 1987. The Afar Depression: Transition between continental rifting and sea floor spreading. Tectonophysics, 141(1–3), pp.199–214.

Manighetti, I., King, G.C.P., Gaudemer, Y., Scholz, C.H. and Doubre, C. 2001. Slip accumulation and lateral propagation of active normal faults in Afar. Journal of Geophysical Research: Solid Earth. 106(B7), pp.13667–13696. doi:10.1029/2000JB900471.

Manighetti, I., Tapponnier, P., Gillot, P.-Y., Jacques, E., Courtillot, V., Armijo, R., Ruegg, J.-C. and King, G. 1998. Propagation of rifting along the Arabia–Somalia Plate Boundary: Into Afar. Journal of Geophysical Research: Solid Earth. 103(B3), pp.4947–4974. doi:10.1029/97JB02758.

Mansfield, C. and Cartwright, J. 2001. Fault growth by linkage: Observations and implications from analogue models. Journal of Structural Geology, 23, pp.745–763.

McClusky, S., Reilinger, R., Ogubazghi, G., Amleson, A., Healeb, B., Vernant, P.,

Sholan, J., Fisseha, S., Asfaw, L., Bendick, R. and Kogan, L. 2010. Kinematics of the southern Red Sea–Afar Triple Junction and implications for plate dynamics. Geophysical Research Letters. 37(5), L05301. doi:10.1029/2009GL041127.

McConnell, R.B. 1972. Geological development of the rift system of eastern Africa. Geological Society of America Bulletin, 83(9), pp.2549–2572. doi:10.1130/0016-7606(1972)83[2549:GDOTRS]2.0.CO;2.

McKenzie, D. 1978. Some remarks on the development of sedimentary basins. Earth and Planetary Science Letters, 40, pp.25–32.

McKenzie, D. and Morgan, W.J. 1969. The evolution of triple junctions. Nature, 224, pp.125–133.

McPhillips, D. and Scharer, K.M. 2018. Quantifying uncertainty in cumulative surface slip along the Cucamonga Fault, a crustal thrust fault in southern California. Journal of Geophysical Research: Solid Earth. 123(10), pp.9063–9083. doi:10.1029/2018JB016301.

Meyer, V., Nicol, A., Childs, C. and Walsh, J.J. 2002. Progressive localisation of strain during the evolution of a normal fault population. Journal of Structural Geology, 24, pp.1215–1231.

Mohr, P.A. and Zanettin, B. 1988. The Ethiopian flood basalt province. In: The Continental Flood Basalts. Dordrecht: Kluwer, pp.63–110.

Moore, C., Wright, T.J. and Hooper, A. 2021. Rift focusing and magmatism during late-stage rifting in Afar. Journal of Geophysical Research: Solid Earth. 126(10), e2020JB021542. doi:10.1029/2020JB021542.

Morewood, N.C. and Roberts, G.P. 2002. Surface observations of active normal fault propagation: Implications for growth. Journal of Structural Geology, 24, pp.193–206.

Morley, C.K. 1999. Patterns of displacement along large normal faults: Implications for basin evolution and fault propagation, based on examples from East Africa. AAPG Bulletin, 83(4), pp.613–634.

Morley, C.K. and Ngenoh, D.K. 1999. Introduction to the East African Rift System. Journal of African Earth Sciences, 29, pp.1–9.

Muirhead, J.D., Kattenhorn, S.A., Lee, H. et al. 2016. Evolution of upper crustal faulting assisted by magmatic diking in the Kenya Rift, East Africa. Geosphere, 12(6), pp.1670–1700.

NASA/METI/AIST/Japan Spacesystems and U.S./Japan ASTER Science Team 2019. ASTER Global Digital Elevation Model V003 [Data set]. NASA Land Processes Distributed Active Archive Center. Available at: https://doi.org/10.5067/ASTER/ASTGTM.003 (Accessed: 10 December

2025).

Nicol, A., Childs, C., Walsh, J.J., Manzocchi, T. and Schöpfer, M.P.J. 2017. Interactions and growth of faults in an outcrop-scale system. Geological Society, London, Special Publications. 439, pp.23–39. doi:10.1144/SP439.9.

Nicol, A., Walsh, J.J., Watterson, J. and Bretan, P. 1996. Three-dimensional geometry and growth of normal faults. Journal of Structural Geology, 18, pp.173–187.

Nicol, A., Walsh, J.J., Berryman, K. and Nodder, S. 2005. Growth of a normal fault by the accumulation of slip over millions of years. Journal of Structural Geology, 27(2), pp.327–342. doi:10.1016/j.jsg.2004.09.002.

Nixon, C.W., Bull, J.M. and Sanderson, D.J. 2014. Localized versus distributed deformation associated with the linkage history of an active normal fault, Whakatane Graben, New Zealand. Journal of Structural Geology. 69(A), pp.266–280. doi:10.1016/j.jsg.2014.06.005.

Orlov, C.J., Bramham, E.K., Thomas, M., Byrne, P.K., Piazolo, S. and Mortimer, E. 2022. Structural architecture and deformation history of Tempe Terra, Mars. Journal of Geophysical Research: Planets, 127(11), e2022JE007407.

Pagli, C., Wang, H., Wright, T.J., Calais, E. and Lewi, E. 2014. Current plate boundary deformation of the Afar rift from a 3-D velocity field inversion of InSAR and GPS. Journal of Geophysical Research: Solid Earth. 119(11), pp.8562–8575. doi:10.1002/2014JB011391.

Pan, S., Bell, R.E., Jackson, C.A.-L. and Naliboff, J. 2022. Evolution of normal fault displacement and length as continental lithosphere stretches. Basin Research. 34(1), pp.121–140. doi:10.1111/bre.12613.

Peacock, D.C.P. 2002. Propagation, interaction and linkage in normal fault systems. Earth-Science Reviews, 58(1–2), pp.121–142.

Peacock, D.C.P. and Sanderson, D.J. 1991. Displacements, segment linkage and relay ramps in normal fault zones. Journal of Structural Geology, 13(6), pp.721–733.

Peacock, D.C.P. and Sanderson, D.J. 1994. Geometry and development of relay ramps in normal fault systems. AAPG Bulletin, 78, pp.147–165.

Persits, F.M., Ahlbrandt, T.S., Tuttle, M.L. et al. 1997. Maps Showing Geology, Oil and Gas Fields, and Geological Provinces of Africa. USGS Open-File Report 97–470A.

Pollard, D.D. and Fletcher, R.C. 2005. Fundamentals of Structural Geology. Cambridge: Cambridge University Press.

Prosser, S. 1993. Rift-related linked depositional systems and their seismic expression. In: G.D. Williams and A. Dobb (eds) Tectonics and Seismic Sequence Stratigraphy. Geological Society, London, Special Publications, 71, pp.35–66.

QGIS Development Team. 2023. QGIS Geographic Information System, version 3.32.0. QGIS Association.

Reilinger, R. and McClusky, S. 2011. Nubia–Arabia–Eurasia plate motions and the dynamics of Mediterranean and Middle East tectonics. Geophysical Journal International. 186(3), pp.971–979. doi:10.1111/j.1365-246X.2011.05133.x.

Rime, V., Foubert, A., Atnafu, B. and Kidane, T. 2022. Geological map of the Afar Depression. Zenodo. Available at: https://doi.org/10.5281/zenodo.7351643

Rime, V., Foubert, A., Ruch, J. and Kidane, T. 2023. Tectonostratigraphic evolution and significance of the Afar Depression. Earth-Science Reviews, 244, 104519.

Roche, V., Camanni, G., Childs, C., Manzocchi, T., Walsh, J., Conneally, J., Saqab, M.M. and Delogkos, E. 2021. Variability in the three-dimensional geometry of segmented normal fault surfaces. Earth-Science Reviews. 216, 103523. doi:10.1016/j.earscirev.2021.103523.

Rooney, T.O. 2020. The Cenozoic magmatism of East Africa: Part II – Rifting of the mobile belt. Lithos, 360–361, 105291.

Rotevatn, A., Jackson, C.A.-L., Tvedt, A.B.M., Bell, R.E. and Blækkan, I. 2019. How do normal faults grow? Journal of Structural Geology. 125, pp.174–184. doi:10.1016/j.jsg.2018.08.005.

Ruch, J., Keir, D., Passarelli, L., Di Giacomo, D., Ogubazghi, G. and Jónsson, S. 2021. Revealing 60 years of earthquake swarms in the Southern Red Sea, Afar and the Gulf of Aden. Frontiers in Earth Science, 9, 664673. doi:10.3389/feart.2021.664673. 5.

Sangha, S.S., Peltzer, G. and Doubre, C. 2022. The evolving deformation field in Central Afar from two decades of InSAR observations: Implications for the decoupling between the upper and lower crusts. ESSOAr Preprint, pp.1–32. doi:10.1002/essoar.10508772.1.

Scholz, C.H. 2002. The Mechanics of Earthquakes and Faulting. 2nd ed. Cambridge: Cambridge University Press.

Shahrzad, S., Bramham, E.K., Thomas, M., Piazolo, S., Byrne, P.K. and Mortimer, E. 2023. Deciphering the structural history of Ulysses Fossae, Mars, using fault pattern analysis. Journal of Geophysical Research: Planets, 128(5), e2022JE007633.

Shmela, A.K., Paton, D.A., Collier, R.E.L. and Bell, R.E. 2021. Normal fault growth in continental rifting: Insights from changes in displacement and length fault populations due to increasing extension in the Central Kenya Rift. Tectonophysics. 814, 228964. doi:10.1016/j.tecto.2021.228964.

Shmela, A.K.M. 2018. Structural evolution of continental rifting, quantitative analysis of fault populations: insights from the central Kenya rift, central and north main

Ethiopian rift. PhD thesis, University of Leeds.

Stab, M., Bellahsen, N., Pik, R., Quidelleur, X., Ayalew, D. and Leroy, S. 2016. Modes of rifting in magma-rich settings: Tectono-magmatic evolution of Central Afar. Tectonics. 35(1), pp.2–38. doi:10.1002/2015TC003893.

Trudgill, B.D. and Cartwright, J.A. 1994. Relay-ramp forms and normal-fault linkages, Canyonlands National Park, Utah. Geological Society of America Bulletin. 106(9), pp.1143–1157. doi:10.1130/0016-7606(1994)106<1143:RRFANF>2.3.CO;2.

USGS EROS Center 2024. Global Imagery and Geospatial Data Products. U.S. Geological Survey. Available at: https://earthexplorer.usgs.gov/ (Accessed: 10 December 2025).

Varet, J. 2018. Geology of Afar (East Africa). Cham: Springer. doi:10.1007/978-3-319-60865-5.

Varet, J. and Gardo, I.A. 2020. Another geothermal site in North-Eastern Afar: Harak (Bidu woreda, Afar Regional State, Ethiopia), that marks the southernmost extension of the Danakil Sea 110 m bsl. Proceedings of the 8th African Rift Geothermal Conference (ARGeo-C8), Nairobi, Kenya, 2–8 November 2020, pp.1–13.

Viltres, R., Jónsson, S., Ruch, J., Doubre, C., Reilinger, R., Floyd, M. and Ogubazghi, G. 2020. Kinematics and deformation of the southern Red Sea region from GPS observations. Geophysical Journal International. 221(3), pp.2143–2154. doi:10.1093/gji/ggaa109.

Walsh, J.J. and Watterson, J. 1988. Analysis of the relationship between displacements and dimensions of faults. Journal of Structural Geology, 10(3), pp.239–247.

Walsh, J.J., Bailey, W.R., Childs, C., Nicol, A. and Bonson, C.G. 2003. Formation of segmented normal faults: A 3-D perspective. Journal of Structural Geology, 25, pp.1251–1262.

Walsh, J.J., Nicol, A. and Childs, C. 2002. An alternative model for the growth of faults. Journal of Structural Geology. 24(11), pp.1669–1675. doi:10.1016/S0191-8141(01)00165-1.

Watterson, J. 1986. Fault dimensions, displacements and growth. Pure and Applied Geophysics, 124, pp.365–373.

Wolfenden, E., Ebinger, C.J., Yirgu, G., Deino, A. and Ayalew, D. 2004. Evolution of the northern Main Ethiopian Rift: Birth of a triple junction. Earth and Planetary Science Letters. 224(1–2), pp.213–228. doi:10.1016/j.epsl.2004.04.022.

Wright, T.J., Ebinger, C., Biggs, J. et al. 2006. Magma-maintained rift segmentation at continental rupture in the 2005 Afar dyking episode. Nature, 442(7100), pp.291–294.

Wright, T.J., Pagli, C., Sigmundsson, F. and Belachew, M. 2012. Geophysical constraints on the dynamics of spreading centres from rifting episodes in Iceland and Afar. Geophysical Journal International, 189(1), pp.389–402

Appendix A

Appendix A provides the fault-level geometric measurements used in the Dmax–L analyses presented in Chapters 4 and 7. Table A.1 lists the individual fault length and maximum displacement measurements for Zone 1.

Table A.1: Fault length (*L*) and maximum displacement (D*max*) measurements for individual faults in the North Afar Depression (Zone 1).

NAD (Zone 1)		
Fault No.	**Fault Length (m)**	**Dmax (m)**
F001	2881	88
F002	9533	185
F003	6557	104
F004	6931	150
F005	2351	200
F006	6297	272
F007	2443	99
F008	3499	215
F009	3096	202
F010	2408	170
F011	2287	47
F012	1261	56
F013	8225	222
F014	2133	130
F015	4070	80
F016	2527	66
F017	2063	45
F018	3844	60
F019	1389	32
F020	3221	40
F021	1347	18
F022	5756	121

F023	3117	102
F024	5065	130
F025	8172	103

F026	13148	170
F027	6969	133
F028	3306	96
F029	12657	210
F030	3907	116
F031	748	45
F032	5388	107
F033	4988	86
F034	5012	60
F035	4202	29
F036	2823	98
F037	1275	69
F038	2526	61
F039	2139	94
F040	901	34
F041	2714	57
F042	2066	33
F043	1894	46
F044	7572	231
F045	2830	174
F046	1019	20

F047	2050	55
F048	7964	288
F049	1174	60
F050	659	59
F051	2880	203
F052	2175	96

F053	1426	118
F054	1557	39
F055	1732	63

F056	10937	379
F057	6732	245
F058	8074	343
F059	8328	593
F060	3926	115
F061	6974	233
F062	2176	134
F063	3807	145
F064	2921	66
F065	2529	87
F066	4339	80
F067	1510	65
F068	2828	55
F069	2216	51
F070	1535	63
F071	2407	104
F072	3397	210
F073	8010	212
F074	4781	222
F075	6150	59
F076	7900	47
F077	7513	191
F078	6185	306
F079	3750	112
F080	4565	185
F081	4135	94
F082	3686	128

F083	1950	67
F084	2413	46
F085	4374	102
F086	2114	37

F087	1511	86
F088	1200	66
F089	1412	55
F090	3245	196
F091	2075	227
F092	3371	205
F093	1948	96
F094	3190	84

F095	1829	87
F096	1661	46
F097	1264	46
F098	5423	53
F099	12400	281
F100	2798	205
F101	3257	111
F102	5688	151
F103	4174	91
F104	5645	127
F105	3657	42
F106	1917	50
F107	2952	135
F108	5999	85
F109	6691	271
F110	3649	120
F111	2716	56

F112	2575	27
F113	1889	291
F114	2851	61
F115	4898	21
F116	8235	38

F117	3073	27
F118	4143	23
F119	1494	37
F120	5696	74
F121	2767	21
F122	1954	34
F123	1553	25
F124	5055	98
F125	4764	104
F126	845	56
F127	2948	106
F128	1438	51
F129	3162	280
F130	3829	288
F131	3380	224
F132	3212	210
F133	1568	184
F134	2794	185
F135	1339	145
F136	1282	36
F137	1540	58
F138	3110	245
F139	2176	133
F140	4522	117
F141	2744	301

F142	3390	139

F143	7662	158
F144	2102	121
F145	2600	37
F146	5674	247

F147	1085	40
F148	3013	149
F149	3013	63
F150	4640	129
F151	2696	128
F152	7771	363
F153	1721	35
F154	1601	110
F155	1844	106
F156	2177	135
F157	1698	167
F158	2823	67
F159	5250	176
F160	6337	218
F161	10825	199
F162	1355	44
F163	4255	68
F164	2579	92
F165	8367	210
F166	3328	109
F167	1147	43
F168	2873	57
F169	2898	47
F170	2128	110

F171	2768	178
F172	1635	50
F173	2074	94
F174	2546	75
F175	8654	235
F176	4172	183
F177	1503	106

F178	2064	95
F179	5938	99
F180	5431	239
F181	621	30
F182	622	22
F183	2114	131
F184	2292	46
F185	2149	73
F186	1366	36
F187	3140	69
F188	4552	171
F189	1990	118
F190	3681	141

F191	5998	175
F192	2565	53
F193	1092	29
F194	3316	89
F195	2071	43
F196	487	28
F197	2325	64
F198	692	27
F199	1650	47

F200	2282	68
F201	2430	79
F202	2447	53
F203	3885	99
F204	7662	227
F205	7789	223
F206	4901	113
F207	3174	49

F208	6048	55
F209	3402	41
F210	2846	45
F211	5367	42
F212	2728	65
F213	903	73
F214	2220	46
F215	9903	337
F216	9313	275
F217	6478	244
F218	16859	307
F219	1218	50
F220	2831	128
F221	6512	191
F222	4277	72
F223	8807	66
F224	2288	38
F225	6035	68
F226	11471	119
F227	9953	45
F228	4008	57
F229	1880	111

F230	1733	29
F231	2636	35
F232	3961	38
F233	1048	32
F234	4725	79
F235	5392	99
F236	9163	90
F237	7922	173
F238	3658	27

F239	5779	63
F240	10139	235
F241	4152	42
F242	4908	127
F243	4422	153
F244	4244	177
F245	5511	184
F246	4925	95
F247	2987	143
F248	2172	153
F249	2493	116
F250	3689	213
F251	2192	36
F252	5739	83
F253	1946	216
F254	1242	35
F255	2246	65
F256	2594	28
F257	938	26
F258	7306	137
F259	3926	83

F260	2200	48
F261	6014	168
F262	4135	114
F263	2174	64
F264	3490	103
F265	6542	68
F266	3612	113
F267	5422	132
F268	3208	56
F269	5688	167
F270	2733	94
F271	2087	50
F272	1268	50
F273	3504	133
F274	3187	43
F275	4511	97
F276	2132	42
F277	1579	32
F278	1646	38
F279	1787	188
F280	5888	312
F281	3194	66
F282	2946	66
F283	2193	57
F284	5435	111
F285	3188	82
F286	4164	198
F287	3023	125

F288	3468	68
F289	1536	26
F290	6091	111
F291	3056	41
F292	4435	165
F293	1081	44
F294	3125	189
F295	3657	56
F296	2410	47
F297	3693	39
F298	2461	106

F299	4019	182
F300	7102	169
F301	7459	44
F302	2060	22
F303	1771	40
F304	4243	36
F305	7276	115
F306	2212	14
F307	2081	87
F308	5682	111
F309	2851	73
F310	1512	23
F311	1623	77
F312	3281	20
F313	3668	63
F314	1132	48
F315	3892	74
F316	5434	46
F317	3284	50

F318	1709	34
F319	1645	36
F320	3996	160
F321	2454	78
F322	5360	82
F323	2077	30
F324	2794	59
F325	5390	102
F326	1280	29
F327	2867	93
F328	2531	70
F329	2048	48

F330	4888	285
F331	2882	176
F332	1739	35
F333	1542	28
F334	4501	187

F335	3062	137
F336	5172	82
F337	4728	98
F338	3168	18
F339	3525	30
F340	5120	46
F341	1709	25
F342	1190	18
F343	1247	63
F344	2998	86
F345	3975	137
F346	2377	54

F347	3074	116
F348	2317	32
F349	1466	84
F350	2615	99

Table A.2: Summary statistics of fault length (L) and D_{max} in the North Main Ethiopian Rift (Zone 2).

NMER (Zone 2)		
Fault No.	**Fault Length (m)**	**Dmax (m)**
F001	1767	39
F002	11732	187
F003	4162	100
F004	7620	96
F005	4690	65
F006	3887	93
F007	1250	43
F008	6149	59
F009	5079	127
F010	8966	116
F011	8900	85
F012	3694	26
F013	4264	58
F014	4530	31
F015	4606	42
F016	917	15
F017	1524	35
F018	1853	49
F019	1770	30
F020	2867	39
F021	3592	25
F022	6024	47
F023	1549	21
F024	4677	39
F025	3533	32
F026	1214	92

F027	1838	24
F028	8225	40
F029	3364	31
F030	3773	32
F031	1640	19
F032	817	31
F033	2336	28
F034	1996	27
F035	5222	55
F036	2520	61
F037	1981	20
F038	2425	127
F039	7482	113
F040	4312	72
F041	2323	339
F042	4079	330
F043	2332	113
F044	1914	201
F045	3560	219
F046	1785	31

F047	1664	37
F048	2421	42
F049	775	55
F050	1232	105
F051	4023	70
F052	5834	78
F053	1620	48
F054	1553	88
F055	2401	53
F056	1528	131

F057	2034	65
F058	1349	73
F059	2111	25
F060	808	13
F061	1028	32
F062	935	51
F063	1602	60
F064	3879	102
F065	1717	114
F066	1835	73
F067	2756	164
F068	2458	140
F069	2807	144
F070	3837	117
F071	2401	111
F072	3012	155
F073	1697	36
F074	1691	34
F075	3420	95
F076	2243	181
F077	1433	103
F078	1684	79
F079	1705	72
F080	1602	45
F081	2157	66
F082	2518	80
F083	723	55
F084	2657	72
F085	1448	62
F086	1030	45
F087	1713	66

F088	1514	60
F089	977	48
F090	678	54
F091	648	72
F092	685	59
F093	391	23
F094	2779	119

F095	855	27
F096	1729	102
F097	1351	51
F098	758	26
F099	1104	46
F100	6891	185
F101	1023	19
F102	1242	22
F103	5235	148
F104	3206	89
F105	6056	77
F106	4042	118
F107	2368	85
F108	2397	67
F109	921	15
F110	1708	68
F111	1072	48
F112	979	43
F113	897	47
F114	608	31
F115	1892	61
F116	4477	186
F117	2278	129

F118	2019	160
F119	2755	184
F120	993	59
F121	628	46
F122	1328	37
F123	2497	119
F124	1156	66
F125	776	44
F126	1800	77
F127	5428	44
F128	2739	104
F129	2127	96
F130	3262	133
F131	2829	76
F132	633	40
F133	441	35
F134	744	70
F135	1113	58
F136	1145	24
F137	1011	26
F138	5237	96
F139	724	25
F140	958	15
F141	568	28
F142	303	15

F143	957	17
F144	529	21
F145	455	35
F146	3006	67
F147	552	18

F148	1997	69
F149	828	32
F150	916	19
F151	1284	92
F152	1165	44
F153	4786	119
F154	4271	120
F155	928	89
F156	880	50
F157	983	72
F158	768	34
F159	1142	52
F160	4964	48
F161	3313	23
F162	7163	41
F163	1004	22
F164	696	13
F165	1103	30
F166	936	60
F167	1571	61
F168	1867	145
F169	868	62
F170	591	48
F171	1212	105
F172	912	29
F173	882	50
F174	621	22
F175	1015	63
F176	513	55
F177	433	48
F178	773	44

F179	667	43
F180	934	79
F181	444	47
F182	650	65
F183	1826	316
F184	1284	58
F185	1132	39
F186	497	29
F187	399	31
F188	797	37
F189	754	92
F190	1839	245

F191	660	197
F192	354	28
F193	613	11
F194	457	48
F195	2008	34
F196	888	51
F197	1174	52
F198	826	41
F199	992	38
F200	493	39
F201	853	33
F202	343	27
F203	709	40
F204	699	35
F205	733	27
F206	538	21
F207	2129	112
F208	4457	270

F209	3373	120
F210	1090	50
F211	1031	53
F212	641	90
F213	2250	250
F214	529	63
F215	671	43
F216	1470	30
F217	858	38
F218	1593	155
F219	698	28
F220	860	113
F221	617	38
F222	523	26
F223	592	103
F224	1047	99
F225	967	31
F226	382	32
F227	927	135
F228	849	106
F229	967	85
F230	570	79
F231	1319	41
F232	1221	30
F233	913	26
F234	697	22
F235	1162	54
F236	3512	147
F237	1164	32
F238	772	52

F239	775	51
F240	2250	40
F241	1809	23
F242	1299	15
F243	1271	22
F244	2477	61
F245	878	26
F246	808	59
F247	2480	25
F248	1386	55
F249	3053	39
F250	1999	47
F251	3319	131
F252	1066	71
F253	1399	41
F254	3076	98
F255	1049	67
F256	999	63
F257	2305	83
F258	1660	30
F259	2027	82
F260	798	35
F261	917	52
F262	1361	38
F263	914	35
F264	1812	48
F265	2215	65
F266	865	40
F267	1609	91
F268	2016	84
F269	923	51

F270	1633	63
F271	1181	85
F272	789	32
F273	1335	30
F274	1932	102
F275	1001	78
F276	1038	51
F277	1031	70
F278	850	38
F279	1360	36
F280	1175	105
F281	3079	34
F282	2149	22
F283	1547	13
F284	831	14
F285	876	15
F286	1012	24

F287	4255	30
F288	2052	29
F289	2039	43
F290	1989	29
F291	2249	125
F292	726	62
F293	1654	23
F294	1545	94
F295	635	35
F296	841	77
F297	539	21
F298	992	13
F299	2239	157

F300	1869	119
F301	1297	26
F302	1007	40
F303	1052	75
F304	1781	48
F305	1833	50
F306	2943	156
F307	1152	39
F308	1455	17
F309	1781	69
F310	1546	85
F311	1730	45
F312	1673	24
F313	611	14
F314	5443	45
F315	642	51
F316	858	34
F317	1287	52
F318	1099	30
F319	653	53
F320	1410	66
F321	896	67
F322	1341	60
F323	1694	98
F324	2140	72
F325	1581	47
F326	682	32
F327	365	10
F328	2927	56
F329	788	18
F330	751	17

F331	1838	33
F332	1300	23
F333	912	26
F334	1394	23

F335	1172	33
F336	1028	60
F337	433	43
F338	1589	78
F339	1688	59
F340	3260	140
F341	2386	49
F342	3350	168
F343	7313	380
F344	1258	60
F345	1728	58
F346	891	114
F347	4223	181
F348	735	109
F349	1255	123
F350	514	47
F351	1892	203
F352	2397	103
F353	3004	62
F354	3360	70
F355	1741	18
F356	3283	99
F357	3188	96
F358	1978	42
F359	10524	476
F360	3476	203

F361	2291	39
F362	1098	34
F363	3384	24
F364	5264	92
F365	1806	27
F366	2848	92
F367	2346	102
F368	733	62
F369	802	45
F370	1751	21
F371	1154	63
F372	750	86
F373	5391	286
F374	3676	48
F375	4842	113
F376	3800	117
F377	1067	54
F378	675	47
F379	1395	98
F380	1301	58
F381	1207	56
F382	1021	193

F383	1451	37
F384	2407	138
F385	1002	124
F386	1339	110
F387	1904	151
F388	1619	24
F389	2828	46
F390	576	17

F391	806	27
F392	2243	164
F393	2264	52
F394	1265	27
F395	1213	45
F396	1955	20
F397	1074	55
F398	9372	172
F399	1421	37
F400	1311	25
F401	5403	159
F402	3593	34
F403	686	47
F404	2176	41
F405	4830	126
F406	2465	187
F407	2023	97
F408	1734	74
F409	1250	44
F410	5483	80
F411	682	26
F412	666	41
F413	4022	117
F414	4287	127
F415	1043	189
F416	3282	82
F417	1590	38
F418	3203	162
F419	1395	97
F420	1537	166
F421	927	31

F422	4044	65
F423	697	50
F424	4457	130
F425	1320	24
F426	1822	77
F427	1142	57
F428	1196	106
F429	7564	225
F430	2573	163

F431	5446	48
F432	2155	154
F433	6469	332
F434	1000	49
F435	4733	225
F436	4090	360
F437	5302	168
F438	1216	36
F439	4199	223
F440	1314	165
F441	1690	211
F442	2295	67
F443	1189	33
F444	2331	126
F445	851	140
F446	2451	86
F447	1494	70
F448	456	69
F449	1334	46
F450	2942	40
F451	3604	25

F452	3775	151
F453	1958	48
F454	592	70
F455	1973	79
F456	2804	202
F457	3007	111
F458	3739	165
F459	2446	64
F460	2664	175
F461	1075	43
F462	1843	150
F463	3717	93
F464	5559	54
F465	4428	52
F466	1968	73
F467	3876	82
F468	3205	30
F469	1694	21
F470	1208	54
F471	1327	101
F472	1469	55
F473	1929	86
F474	3378	53
F475	735	60
F476	5924	147
F477	3792	140
F478	4309	110
F479	2509	60
F480	645	32
F481	3229	86

F482	930	38
F483	3091	55
F484	1176	19
F485	1713	25
F486	2253	117
F487	2588	127
F488	1548	62
F489	1389	80
F490	4969	265
F491	2339	75
F492	4974	109
F493	5614	131
F494	16286	254
F495	2488	139
F496	1647	122
F497	3381	156
F498	4442	85
F499	3429	41
F500	2266	72
F501	5547	73
F502	7061	153
F503	10882	150
F504	5042	33
F505	4950	36
F506	2378	84
F507	1433	82
F508	2384	63
F509	2123	43
F510	1686	89
F511	1369	61
F512	6049	127

F513	7420	168
F514	2490	62
F515	5996	175
F516	2880	43
F517	2800	35
F518	3274	275
F519	3295	231
F520	2295	210
F521	2282	69
F522	4405	104
F523	1738	59
F524	3434	122
F525	11375	241
F526	2633	32

F527	1955	39
F528	11834	74
F529	7408	137
F530	5504	65
F531	5497	44
F532	16153	159
F533	3167	108
F534	3085	44
F535	2621	69
F536	20381	290
F537	6483	86
F538	858	41
F539	2143	27
F540	2404	31
F541	870	98
F542	3506	110

F543	1008	35
F544	998	20
F545	2755	45
F546	2440	149
F547	2173	152
F548	1366	178
F549	13099	299
F550	18091	691
F551	3790	170
F552	8565	74
F553	6563	176
F554	2719	78
F555	10515	192
F556	3123	42
F557	2365	154
F558	2906	133
F559	3406	309
F560	3058	330
F561	3564	204
F562	1194	81
F563	6066	128
F564	2036	66
F565	811	33
F566	1768	57
F567	3601	122
F568	727	42
F569	825	30
F570	523	25
F571	1247	77
F572	3359	48
F573	4469	128

F574	2069	113

F575	1015	42
F576	1030	77
F577	1831	70
F578	1674	89
F579	752	76
F580	1130	68
F581	1709	58
F582	601	67
F583	2138	71
F584	1831	40
F585	657	30
F586	1399	38
F587	817	43
F588	2136	70
F589	680	53
F590	656	19
F591	1299	59
F592	1711	97
F593	1466	35
F594	970	30
F595	1159	60
F596	796	64
F597	1924	78
F598	2760	96
F599	2363	125
F600	1120	68
F601	2162	144
F602	1551	75
F603	1595	121

F604	1411	113
F605	981	37
F606	902	27
F607	1608	100
F608	685	57
F609	1304	85
F610	5407	84
F611	2583	37
F612	2958	51
F613	3484	101
F614	3435	170
F615	747	36
F616	1310	116
F617	1959	130
F618	1079	117
F619	1905	44
F620	1124	108
F621	4691	498
F622	3649	1011

F623	1980	356
F624	2809	854
F625	3090	324
F626	3181	731
F627	3636	431
F628	1980	255
F629	3287	442
F630	1621	204
F631	935	144
F632	2295	75
F633	773	54

F634	938	69
F635	856	99
F636	3257	252
F637	1125	167
F638	1175	185
F639	2490	142
F640	1681	50
F641	1202	64
F642	771	34
F643	2005	161
F644	2564	138
F645	1869	94
F646	1534	67
F647	1676	173
F648	5260	95
F649	1547	72
F650	1437	53
F651	4470	43
F652	4501	57
F653	6775	109
F654	1362	72
F655	1478	221
F656	1600	183
F657	2893	54
F658	3145	77
F659	2909	48
F660	11470	229
F661	7334	179
F662	2860	134
F663	9329	569
F664	7835	102

F665	5159	134
F666	4465	86
F667	5066	80
F668	5337	88
F669	4362	251
F670	3257	70

F671	10841	85
F672	3876	205
F673	3939	133
F674	7655	143
F675	4619	221
F676	2726	147
F677	1825	130
F678	2703	62
F679	997	88
F680	1224	191
F681	4155	234
F682	5384	127
F683	20851	807
F684	3935	698
F685	14852	326
F686	10166	156
F687	2460	159
F688	2680	41
F689	4066	99
F690	6910	248
F691	11309	251
F692	4073	64
F693	2732	181
F694	16877	1045

F695	5976	765
F696	3163	229
F697	17387	432
F698	5549	125
F699	1904	58
F700	1921	150
F701	4290	225
F702	2287	612
F703	11021	157
F704	14450	899
F705	6232	58
F706	4894	61
F707	6642	195
F708	3494	37
F709	4655	222
F710	8530	116
F711	11212	123
F712	13200	176
F713	5132	77
F714	6619	1017
F715	6433	49
F716	4240	99
F717	3874	809
F718	3415	62

F719	2594	145
F720	2724	238
F721	1556	255
F722	1735	109
F723	1666	62
F724	5388	129

F725	3760	115
F726	3926	51
F727	4411	53
F728	1693	61
F729	7230	50
F730	2991	114
F731	4795	26
F732	3590	81
F733	3402	54
F734	11508	281
F735	6179	193
F736	3828	121
F737	7723	250
F738	8393	312
F739	3224	293
F740	2300	321
F741	692	35
F742	1981	126
F743	977	80
F744	2167	59
F745	1448	98
F746	2928	312
F747	4150	94
F748	1853	62
F749	4210	89
F750	3339	104
F751	1895	117
F752	1489	176
F753	2250	154
F754	2419	421
F755	2993	184

F756	3226	109
F757	2598	165
F758	6186	1017
F759	1518	121
F760	2269	131
F761	3241	487
F762	2377	65
F763	2179	45
F764	2670	41
F765	4312	124
F766	2850	221

F767	2416	177
F768	1842	104
F769	1185	243
F770	3015	527
F771	1156	53
F772	2115	140
F773	1272	131
F774	1137	42
F775	2189	53
F776	1248	54
F777	3014	12
F778	2232	11
F779	4148	47
F780	4943	27
F781	2633	44
F782	2440	50
F783	8771	186
F784	3304	54
F785	1408	58

F786	1365	65
F787	3569	54
F788	947	38
F789	774	22
F790	1492	56
F791	810	25
F792	2442	32
F793	2820	49
F794	10479	785
F795	2993	102
F796	3103	109
F797	17288	339
F798	6203	551
F799	2897	154
F800	7186	100
F801	6917	193
F802	3550	103
F803	7823	116
F804	4362	152
F805	2458	158
F806	3036	115
F807	1817	34
F808	1416	46
F809	2689	169
F810	1261	64
F811	1118	81
F812	1314	140
F813	1193	97
F814	9092	172

F815	1579	20

F816	2811	145
F817	3973	376
F818	3634	260
F819	3427	117
F820	2691	86
F821	5446	104
F822	3613	86
F823	13338	258
F824	6792	142
F825	9593	245
F826	4851	36
F827	2777	65
F828	7619	381
F829	4285	193
F830	3147	85
F831	2674	55
F832	1606	57
F833	1540	67
F834	4644	65
F835	1059	20
F836	2834	105
F837	3478	133
F838	12268	570
F839	3974	68
F840	1989	91
F841	5496	93
F842	2556	76
F843	1280	43
F844	2765	86
F845	2193	123
F846	3181	202

F847	5667	245
F848	2907	70
F849	2205	85
F850	2111	75
F851	6806	100
F852	3204	190
F853	2476	55
F854	2710	39
F855	4252	68
F856	1282	18
F857	2677	128
F858	2875	52
F859	1360	219
F860	928	67
F861	2073	36
F862	4503	109

F863	2796	75
F864	1783	144
F865	2008	131
F866	4931	266
F867	1649	60
F868	1870	28
F869	2441	50
F870	3957	80
F871	2519	37
F872	3550	130
F873	4061	82
F874	2457	46
F875	2204	42
F876	715	76

F877	8782	275
F878	3065	232
F879	3576	149
F880	9932	627
F881	3447	156
F882	12442	687
F883	3529	437
F884	2609	86
F885	9344	977
F886	6241	773
F887	3007	236
F888	3268	382
F889	5510	704
F890	5614	202
F891	1637	71
F892	1788	23
F893	3150	48
F894	2204	31
F895	2828	99
F896	1304	37
F897	1882	30
F898	4058	108
F899	5166	101
F900	1975	55

Table A.3: Summary statistics of fault length (L) and D_{max} in the East Afar Depression (Zone 3).

EAD (Zone 2)		
Fault No.	Fault Length (m)	Dmax (m)
F001	6090	120
F002	5394	56
F003	4093	232
F004	5231	195
F005	4464	150
F006	3456	346
F007	1825	133
F008	2227	205
F009	5480	252
F010	5342	351
F011	6083	215
F012	10953	307
F013	4609	96
F014	4360	121
F015	4716	179
F016	4725	182
F017	2999	101
F018	5124	205
F019	8101	359
F020	2156	49
F021	4750	61
F022	26443	481
F023	3139	141
F024	10412	382
F025	4467	196
F026	3175	72
F027	2531	39

F028	4738	255
F029	6813	242
F030	3579	128
F031	9319	434
F032	6318	254
F033	7901	328
F034	7542	336
F035	4122	189
F036	4673	102
F037	3161	104
F038	4838	207
F039	4529	132
F040	8753	892
F041	10162	474
F042	12421	477
F043	28739	548
F044	9672	276
F045	14068	485
F046	9212	371

F047	33588	826
F048	6675	128
F049	9130	228
F050	4410	355
F051	8668	254
F052	9959	199
F053	36037	953
F054	14987	542
F055	2011	121
F056	5753	425
F057	10608	235
F058	19748	431

F059	10130	323
F060	7753	210
F061	20498	514
F062	17292	380
F063	14291	563
F064	4361	276
F065	6550	68
F066	7046	181
F067	20716	664
F068	7404	268
F069	765	16
F070	4679	73
F071	2476	71
F072	3362	78
F073	1217	53
F074	2968	40
F075	3736	99
F076	5176	163
F077	19635	381
F078	2126	157
F079	2922	217
F080	2091	90
F081	3587	206
F082	4355	131
F083	1077	75
F084	3749	113
F085	3786	142
F086	30844	690
F087	24146	687
F088	11651	326
F089	1592	50

F090	2626	52
F091	3911	64
F092	15289	388
F093	11539	316
F094	4808	245

F095	11174	187
F096	7739	267
F097	1635	44
F098	11287	429
F099	7852	279
F100	1402	45
F101	8530	371
F102	4372	112
F103	4081	265
F104	3729	128
F105	2022	71
F106	3608	60
F107	6619	88
F108	5196	94
F109	13761	583
F110	1803	88
F111	9925	291
F112	2303	145
F113	3957	165
F114	7835	227
F115	6982	274
F116	6918	296
F117	5112	266
F118	5591	233
F119	3244	93

F120	4312	163
F121	1637	97
F122	1539	55
F123	1043	39
F124	16789	678
F125	5246	172
F126	12262	277
F127	17553	165
F128	8424	276
F129	17299	348
F130	3692	108
F131	10560	284
F132	5981	201
F133	5405	119
F134	4341	107
F135	3273	84
F136	5823	105
F137	5388	65
F138	6751	149
F139	1418	66
F140	2102	57
F141	17305	351
F142	5585	124

F143	3054	97
F144	2652	53
F145	5633	275
F146	9183	368
F147	6066	160
F148	4950	177
F149	5393	235

F150	1818	52
F151	16399	1215
F152	5061	493
F153	2659	398
F154	12934	590
F155	9977	1068
F156	4490	220
F157	3695	402
F158	6514	271
F159	5737	556
F160	2139	184
F161	2181	101
F162	14723	172
F163	16765	250
F164	5237	290
F165	10869	400
F166	4801	159
F167	7792	106
F168	16445	336
F169	2797	111
F170	2262	91
F171	964	77
F172	2261	77
F173	6802	136
F174	3299	117
F175	8450	535
F176	5658	237
F177	24208	855
F178	11550	357
F179	1629	51
F180	7494	366

F181	9655	417
F182	6931	456
F183	8674	252
F184	7611	392
F185	4134	439
F186	9812	123
F187	5466	117
F188	9685	219
F189	4259	117
F190	6562	184

F191	8765	156
F192	6166	79
F193	6270	92
F194	2977	80
F195	4423	127
F196	6380	79
F197	3177	60
F198	2922	122
F199	3253	92
F200	1354	60
F201	7975	182
F202	8296	123
F203	11424	918
F204	7939	114
F205	8538	187
F206	8576	246
F207	15748	131
F208	13264	288
F209	4408	138
F210	5142	135

F211	4682	37
F212	8660	82
F213	7365	109
F214	5279	51
F215	7281	182
F216	17416	271
F217	12713	208
F218	9001	278
F219	11392	547
F220	33146	621
F221	41556	688
F222	7808	141
F223	4054	89
F224	16688	292
F225	11960	399
F226	12039	166
F227	2044	86
F228	9985	302
F229	12727	238
F230	24522	287
F231	15213	638
F232	5117	374
F233	2525	123
F234	2290	204
F235	3536	136
F236	4331	326
F237	19094	677
F238	8407	124
F239	4564	220
F240	1637	102

F241	6941	400
F242	10032	205
F243	12246	195
F244	7658	132
F245	9102	175
F246	22234	445
F247	39401	634
F248	13929	375
F249	7526	414
F250	7131	354
F251	5454	87
F252	3764	60
F253	7634	262
F254	11102	233
F255	12222	254
F256	4325	183
F257	2006	236
F258	4463	134
F259	2590	157
F260	4678	320
F261	7335	232
F262	5894	69
F263	6588	305
F264	20354	502
F265	4537	171
F266	3721	265
F267	6998	339
F268	5828	93
F269	1575	25
F270	28559	377
F271	18693	677

F272	3081	54
F273	9759	335
F274	5897	207
F275	6113	155
F276	1805	44
F277	7401	71
F278	3052	87
F279	2379	87
F280	4649	147
F281	2067	199
F282	4488	109
F283	2028	198
F284	4188	302
F285	4393	189
F286	4344	52

F287	9144	526
F288	1277	89
F289	2594	232
F290	1947	156
F291	2446	40
F292	7159	501
F293	1424	61
F294	2386	273
F295	6826	290
F296	9248	506
F297	6534	119
F298	2472	106
F299	1835	72
F300	1545	45
F301	3243	367

F302	2266	210
F303	1512	147
F304	2070	54
F305	5903	320
F306	5394	144
F307	5986	432
F308	1462	34
F309	11907	459
F310	3359	172
F311	2887	53
F312	1447	58
F313	13741	540
F314	5038	174
F315	4351	74
F316	4443	108
F317	3522	151
F318	3987	31
F319	3069	40
F320	4932	62
F321	2156	40
F322	1669	58
F323	3167	179
F324	1085	50
F325	4234	107
F326	12975	412
F327	8253	498
F328	3944	360
F329	3318	169
F330	11244	598
F331	4700	275
F332	13666	299

F333	8426	160
F334	9381	123

F335	14035	497
F336	10007	475
F337	1661	129
F338	4469	254
F339	3017	121
F340	2925	97
F341	1926	104
F342	1617	59
F343	5231	294
F344	6476	203
F345	3441	174
F346	20750	639
F347	25082	953
F348	27928	533
F349	7931	331
F350	8219	317
F351	6654	95
F352	4385	164
F353	8343	335
F354	19202	632
F355	3240	43
F356	4015	44
F357	7429	170
F358	5088	179
F359	4264	211
F360	5522	67
F361	5732	216
F362	5553	55

F363	7124	391
F364	7326	404
F365	2938	86
F366	3894	125
F367	1262	72
F368	16603	414
F369	13615	487
F370	39336	710
F371	5438	296
F372	11719	345
F373	5717	213
F374	7745	132
F375	10795	66
F376	5438	124
F377	5359	339
F378	3747	268
F379	4383	107
F380	23019	643
F381	7111	189
F382	2399	90

F383	9999	49
F384	6048	153
F385	11777	290
F386	7269	192
F387	5434	246
F388	5356	182
F389	3545	220
F390	2657	76
F391	1578	26
F392	6085	275

F393	23809	844
F394	8940	346
F395	5490	329
F396	4205	326
F397	10299	192
F398	7320	352
F399	4849	146
F400	24084	353
F401	7834	268
F402	4524	170
F403	12637	287
F404	4210	285
F405	2218	187
F406	1103	69
F407	2425	155
F408	2991	49
F409	17558	355
F410	14039	464
F411	3816	86
F412	8398	300
F413	8190	128
F414	10546	109
F415	2143	135
F416	6377	73
F417	10170	172
F418	6240	201
F419	13803	280
F420	6378	247
F421	6802	147
F422	3928	80
F423	2192	93

F424	13110	259
F425	13987	220
F426	7205	68
F427	12488	80
F428	5404	73
F429	6177	119
F430	6657	249

F431	15281	260
F432	4235	109
F433	3210	130
F434	1257	25
F435	8312	74
F436	6473	80
F437	3183	78
F438	7490	105
F439	5008	68
F440	4524	82
F441	1251	24
F442	3219	26
F443	8799	300
F444	7380	143
F445	4881	191
F446	6128	224
F447	7640	42
F448	12040	207
F449	4122	44
F450	6257	235
F451	2787	74
F452	2042	68
F453	16750	293

F454	8962	119
F455	10744	202
F456	2814	87
F457	10460	211
F458	6403	86
F459	5299	66
F460	3055	113
F461	7384	136
F462	3361	80
F463	6244	105
F464	2548	43
F465	4172	94
F466	4616	142
F467	3382	71
F468	10189	135
F469	3874	99
F470	2762	76
F471	1311	33
F472	2525	78
F473	2476	87
F474	4387	138
F475	15986	781
F476	6698	625
F477	3882	123
F478	2119	52

F479	9932	238
F480	4733	94
F481	5797	97
F482	2700	43
F483	3248	79

F484	3129	40
F485	6125	389
F486	3877	144
F487	7960	129
F488	4847	242
F489	2477	81
F490	5486	332
F491	4234	221
F492	2957	242
F493	5064	220
F494	9973	284
F495	5049	165
F496	2209	19
F497	1383	78
F498	1832	76
F499	2470	96
F500	1816	30
F501	3209	103
F502	9049	129
F503	4858	125
F504	6166	158
F505	2720	81
F506	3339	79
F507	7474	83
F508	2594	41
F509	6436	61
F510	5432	72
F511	844	24
F512	4409	73
F513	830	21
F514	1319	24

F515	2219	61
F516	7628	132
F517	1834	69
F518	3748	404
F519	5191	402
F520	1620	67
F521	12335	136
F522	14996	524
F523	3906	192
F524	3733	406
F525	5218	142
F526	6802	103

F527	4330	235
F528	4280	102
F529	2421	55
F530	2550	181
F531	2006	27
F532	3745	26
F533	2962	31
F534	2989	59
F535	2663	74
F536	1374	25
F537	6959	28
F538	4465	24
F539	1563	91
F540	3698	187
F541	1342	120
F542	2302	68
F543	4385	84
F544	5615	335

F545	3806	220
F546	859	85
F547	2157	183
F548	1567	54
F549	1412	78
F550	6317	143
F551	2707	98
F552	5262	193
F553	5161	46
F554	4074	114
F555	4028	51
F556	1660	31
F557	2003	106
F558	2893	40
F559	5514	97
F560	7434	175
F561	10128	61
F562	4030	83
F563	4743	259
F564	6571	192
F565	3337	54
F566	4817	94
F567	3791	80
F568	2360	98
F569	11371	317
F570	8484	183
F571	1865	70
F572	4158	101
F573	5090	157
F574	6078	97

F575	2902	92
F576	14676	236
F577	4918	98
F578	5997	151
F579	6583	71
F580	2645	93
F581	3387	40
F582	6357	75
F583	7020	127
F584	6037	90
F585	10161	195
F586	5172	102
F587	4054	64
F588	3873	108
F589	1961	45
F590	2137	37
F591	3155	82
F592	3960	616
F593	5306	701
F594	8014	276
F595	4444	213
F596	2597	41
F597	2373	54
F598	5592	238
F599	2597	165
F600	11551	151
F601	3191	177
F602	1949	158
F603	1941	206
F604	3323	134
F605	6045	140

F606	5098	104
F607	7082	293
F608	2467	272
F609	1904	217
F610	1559	87
F611	2629	78
F612	1416	37
F613	5167	109
F614	10731	411
F615	1658	46
F616	1319	21
F617	4042	450
F618	3871	330
F619	4300	171
F620	2471	252
F621	1645	68
F622	20761	613

F623	2901	84
F624	1778	88
F625	2758	72
F626	1471	40
F627	3957	70
F628	6124	91
F629	760	28
F630	4790	215
F631	766	94
F632	1035	52
F633	2027	93
F634	1658	103
F635	1021	95

F636	7794	279
F637	3454	135
F638	2114	104
F639	2473	199
F640	1437	73
F641	2837	191
F642	1472	97
F643	2248	113
F644	8637	186
F645	2503	203
F646	2683	223
F647	5495	452
F648	9336	416
F649	5996	315
F650	5219	359
F651	3191	171
F652	981	91
F653	5679	201
F654	6408	225
F655	3117	226
F656	7208	165
F657	7636	373
F658	1632	95
F659	939	58
F660	1011	133
F661	2077	108
F662	2601	119
F663	1149	97
F664	2344	84
F665	1742	106
F666	729	130

F667	2686	217
F668	2616	175
F669	5482	333
F670	2607	427

F671	994	64
F672	861	67
F673	1850	219
F674	1887	268
F675	5762	187
F676	1652	307
F677	1646	220
F678	3572	225
F679	2235	143
F680	1963	211
F681	1898	142
F682	2756	208
F683	1033	168
F684	2163	162
F685	1442	145
F686	4308	131
F687	1468	134
F688	819	106
F689	2834	88
F690	2055	138
F691	6811	333
F692	1570	77
F693	4021	99
F694	11360	476
F695	1628	50
F696	2526	92

F697	1009	45
F698	1581	43
F699	2104	108
F700	937	91
F701	1705	73
F702	3167	189
F703	4161	237
F704	1783	205
F705	1737	77
F706	1281	112
F707	2810	84
F708	1989	180
F709	1418	44
F710	4088	173
F711	2277	146
F712	1196	38
F713	3836	173
F714	2328	47
F715	2957	53
F716	10061	231
F717	4246	333
F718	2037	117

F719	4372	357
F720	9890	908
F721	3701	144
F722	4129	198
F723	9246	87
F724	5999	61
F725	13466	189
F726	5710	142

F727	3294	55
F728	5372	86
F729	15577	55
F730	7061	50
F731	1206	30
F732	799	43
F733	5170	125
F734	4129	84
F735	3935	123
F736	1256	31
F737	4794	159
F738	777	40
F739	1381	107
F740	3410	131
F741	1469	85
F742	1036	28
F743	2606	115
F744	2694	127
F745	7524	178
F746	3570	98
F747	3337	143
F748	2153	67
F749	1405	39
F750	6185	123
F751	2700	40
F752	2948	87
F753	11723	131
F754	5511	142
F755	2226	66
F756	2868	65
F757	2880	72

F758	4742	60
F759	3559	88
F760	9787	74
F761	6254	146
F762	2368	53
F763	2785	107
F764	824	66
F765	2634	36
F766	3479	82

F767	2482	104
F768	1108	94
F769	1194	29
F770	1674	105
F771	463	40
F772	3139	36
F773	2741	65
F774	2007	81
F775	2260	72
F776	1386	60
F777	5929	125
F778	3701	72
F779	1052	42
F780	2445	39
F781	3763	88
F782	2393	85
F783	2692	128
F784	1399	28
F785	722	38
F786	399	24
F787	911	55

F788	1594	38
F789	938	48
F790	2107	37
F791	4957	315
F792	12058	110
F793	6593	80
F794	4616	94
F795	2096	65
F796	4904	226
F797	1084	107
F798	2218	221
F799	4659	76
F800	7027	189
F801	12940	193
F802	7115	151
F803	22281	516
F804	8911	253
F805	7825	223
F806	22434	484
F807	6460	198
F808	7191	255
F809	4421	80
F810	10293	473
F811	10940	164
F812	2891	164
F813	18724	316
F814	8310	275
F815	6928	150
F816	5274	103
F817	2726	39

F818	7583	139
F819	2758	51
F820	3449	34
F821	3667	163
F822	11859	207
F823	7001	79
F824	10827	116
F825	3357	50
F826	4704	163
F827	8023	359
F828	4113	62
F829	2912	144
F830	8407	237
F831	4587	87
F832	7394	418
F833	4717	340
F834	4048	98
F835	3622	111
F836	3333	215
F837	3067	32
F838	3309	176
F839	11157	226
F840	8952	445
F841	5172	324
F842	4190	299
F843	2649	183
F844	2275	147
F845	2867	26
F846	2888	105
F847	2362	96
F848	4712	57

F849	3704	84
F850	1557	41
F851	2389	47
F852	7779	105
F853	3035	39
F854	2308	32
F855	5586	96
F856	4424	58
F857	4955	145
F858	2047	128
F859	3259	104
F860	8553	76
F861	4375	86
F862	2581	52

F863	8736	176
F864	3239	116
F865	3320	138
F866	7380	122
F867	7172	173
F868	7272	62
F869	7881	88
F870	4587	136
F871	8668	107
F872	5685	156
F873	8905	99
F874	6021	167
F875	3140	139
F876	3462	154
F877	6521	193
F878	1932	74

F879	3532	203
F880	3108	160
F881	1528	94
F882	2181	85
F883	4809	187
F884	2655	181
F885	7602	188
F886	21337	779
F887	4988	283
F888	3851	52
F889	8754	87
F890	4638	218
F891	2416	41
F892	2014	86
F893	2147	57
F894	3412	187
F895	4579	293
F896	5892	227
F897	2446	107
F898	2302	129
F899	1294	80
F900	2760	47
F901	4892	77
F902	1647	104
F903	2185	122
F904	4586	430
F905	6820	429
F906	6304	405
F907	6484	51
F908	5642	276
F909	7411	405

F910	7403	405

F911	14855	260
F912	10392	165
F913	2316	244
F914	5419	62
F915	4561	49
F916	3606	132
F917	1268	159
F918	2231	274
F919	999	56
F920	3735	121
F921	2562	38
F922	5799	194
F923	6177	184
F924	4580	145
F925	4967	134
F926	12591	437
F927	18572	805
F928	7044	122
F929	13856	230
F930	7407	481
F931	1385	94
F932	871	57
F933	1359	66
F934	1271	75
F935	4230	302
F936	7081	344
F937	4657	208
F938	4807	78
F939	1920	32

F940	4372	260
F941	2254	124
F942	2643	107
F943	3013	98
F944	2441	39
F945	4609	135
F946	6520	98
F947	2895	55
F948	4362	131
F949	2942	309
F950	8037	126
F951	1653	48
F952	3410	100
F953	2529	34
F954	2804	334
F955	1757	256
F956	2594	42
F957	2706	73
F958	1961	33

F959	2912	79
F960	4846	241
F961	6354	291
F962	1652	83
F963	3094	257
F964	2122	76
F965	2250	221
F966	1564	87
F967	4323	327
F968	2423	79
F969	1003	179

F970	1553	103
F971	881	45
F972	2268	112
F973	1629	59
F974	1689	75
F975	2512	156
F976	3159	71
F977	4241	118
F978	1619	78
F979	3830	131
F980	6983	176
F981	3656	32
F982	1803	37
F983	1550	40
F984	9785	150
F985	3889	90
F986	5512	172
F987	4810	247
F988	1848	123
F989	5281	233
F990	5289	79
F991	6809	96
F992	3832	112
F993	1849	67
F994	1173	28
F995	1750	91
F996	1486	52
F997	3926	84
F998	2313	72
F999	4553	74
F1000	13629	357

F1001	3278	180
F1002	5675	162
F1003	3544	39
F1004	14931	225
F1005	4954	131
F1006	1488	126

F1007	3476	171
F1008	4268	165
F1009	1224	72
F1010	1462	88
F1011	1744	57
F1012	8513	288
F1013	2362	179
F1014	1626	239
F1015	1504	324
F1016	1486	112
F1017	778	31
F1018	967	47
F1019	1228	277
F1020	635	48
F1021	1552	190
F1022	1593	44
F1023	6970	532
F1024	1927	202
F1025	1794	42
F1026	744	23
F1027	1271	75
F1028	5913	564
F1029	1156	228
F1030	1583	65

F1031	910	45
F1032	10824	267
F1033	2926	42
F1034	1807	97
F1035	2291	158
F1036	1964	94
F1037	3058	304
F1038	3707	303
F1039	4381	116
F1040	2209	67
F1041	1507	99
F1042	2059	94
F1043	2068	181
F1044	3827	544
F1045	2003	315
F1046	1664	133
F1047	3152	393
F1048	1726	168
F1049	4628	227
F1050	3583	148
F1051	3482	206
F1052	1566	187
F1053	3704	337
F1054	2597	270

F1055	9629	440
F1056	666	59
F1057	1078	46
F1058	1299	98
F1059	2508	236
F1060	3404	435

F1061	6743	405
F1062	1489	108
F1063	3181	175
F1064	1167	25
F1065	1653	55
F1066	1448	46
F1067	2229	60
F1068	1136	27
F1069	3250	275
F1070	4273	41
F1071	2612	52
F1072	3641	36
F1073	2433	36
F1074	1268	46
F1075	2432	41
F1076	624	31
F1077	776	29
F1078	1645	38
F1079	4277	114
F1080	1369	173
F1081	1660	44
F1082	1364	24
F1083	2265	22
F1084	4454	339
F1085	3476	110
F1086	3543	58
F1087	4158	25
F1088	1917	141
F1089	2617	176
F1090	20133	176
F1091	8242	72

F1092	1114	41
F1093	1189	13
F1094	6212	62
F1095	4920	84
F1096	2253	221
F1097	4237	508
F1098	1738	179
F1099	3014	122
F1100	3347	155
F1101	3078	381
F1102	1783	144

F1103	2877	262
F1104	1375	204
F1105	2947	279
F1106	1278	217
F1107	5436	249
F1108	4814	208
F1109	1545	76
F1110	1619	89
F1111	1855	124
F1112	3011	157
F1113	3098	106
F1114	2859	127
F1115	5140	323
F1116	988	140
F1117	1641	104
F1118	5291	237
F1119	2892	103
F1120	3283	217
F1121	3920	69

F1122	862	55
F1123	6524	247
F1124	1452	314
F1125	964	206
F1126	1878	331
F1127	1255	123
F1128	2644	77
F1129	4383	200
F1130	1803	69
F1131	1680	247
F1132	1861	98
F1133	802	54
F1134	4488	491
F1135	1451	94
F1136	2481	325
F1137	1945	103
F1138	1405	168
F1139	2241	136
F1140	5564	806
F1141	2645	414
F1142	3190	445
F1143	1665	229
F1144	3071	551
F1145	3840	513
F1146	960	110
F1147	3866	243
F1148	880	108
F1149	2556	65
F1150	5880	75

F1151	1007	79

F1152	7524	426
F1153	10212	307
F1154	1486	20
F1155	3140	24
F1156	2381	199
F1157	2432	168
F1158	1901	261
F1159	2756	219
F1160	1429	55
F1161	2283	49
F1162	5441	84
F1163	4324	107
F1164	8995	251
F1165	4957	467
F1166	8648	96
F1167	3744	267
F1168	3553	129
F1169	2948	87
F1170	2114	306
F1171	965	89
F1172	2326	105
F1173	3637	126
F1174	3538	53
F1175	2220	60
F1176	860	44
F1177	3046	44
F1178	1572	54
F1179	1507	43
F1180	11474	176
F1181	5779	122
F1182	11941	482

F1183	11941	462
F1184	1521	58
F1185	2899	75
F1186	5810	357
F1187	2746	110
F1188	2635	187
F1189	4178	199
F1190	7350	222
F1191	16297	145
F1192	3794	226
F1193	1355	101
F1194	3132	152
F1195	1380	223
F1196	5532	263
F1197	3016	57
F1198	1767	106

F1199	7600	64
F1200	3627	43
F1201	4737	65
F1202	5139	31
F1203	2322	76
F1204	1546	26
F1205	4850	49
F1206	7826	141
F1207	2081	34
F1208	2232	47
F1209	3037	109
F1210	4838	116
F1211	2650	71
F1212	4958	156

F1213	1638	80
F1214	1733	46
F1215	1533	57
F1216	4190	210
F1217	1112	47
F1218	738	18
F1219	1806	77
F1220	3644	87
F1221	3537	178
F1222	7856	494
F1223	2971	186
F1224	935	57
F1225	2759	46
F1226	18066	284
F1227	3787	247
F1228	7765	203
F1229	7005	177
F1230	1998	99
F1231	2317	106
F1232	3245	130
F1233	1663	184
F1234	1141	117
F1235	1571	43
F1236	1241	65
F1237	1767	91
F1238	1052	40
F1239	986	84
F1240	3768	155
F1241	6565	389
F1242	1531	138
F1243	2049	48

F1244	4844	80
F1245	2307	33
F1246	4351	136

F1247	5616	256
F1248	4487	239
F1249	803	49
F1250	2273	94

Appendix B

- Python script for fault-geometry calculations used in this thesis.

The full Python script used to calculate fault length, displacement, and displacement profiles is archived at Zenodo (Alghamdi, 2025).

Python script for fault-geometry data analysis

```
import numpy as np
import pandas as pd
from math import atan2, degrees
import matplotlib.pyplot as plt
from scipy.interpolate import make_interp_spline


# Function to calculate cumulative fault length along the top cut-off trace
def calculate_cumulative_fault_length(x_top, y_top):
    fault_length = np.zeros(len(x_top))
    for i in range(1, len(x_top)):
        fault_length[i] = (
            fault_length[i - 1]
            + np.sqrt((x_top[i] - x_top[i - 1]) ** 2
                      + (y_top[i] - y_top[i - 1]) ** 2)
        )
    return fault_length

# Function to calculate displacement between top and bottom cut-off points
def calculate_displacement(x_top, y_top, x_bot, y_bot):
    return [
        np.sqrt((x_top[i] - x_bot[i]) ** 2 + (y_top[i] - y_bot[i]) ** 2)
        for i in range(len(x_top))
    ]

# Function to calculate overall fault orientation from first to last top cut-off
def calculate_fault_orientation(x_top, y_top):
    orientation_rad = atan2(y_top[-1] - y_top[0], x_top[-1] - x_top[0])
    orientation_deg = degrees(orientation_rad)
    return orientation_deg if orientation_deg >= 0 else orientation_deg + 360


# Function to classify fault direction based on orientation
def determine_fault_direction(orientation):
    # Example: faults with strikes in the 0–90° and 270–360° quadrants
    # are assigned to 'N', and those in 90–270° to 'S'
    return "N" if orientation < 90 or orientation >= 270 else "S"

# Read data from Excel file (update the filename/path as required)
data = pd.read_excel("QC_EAD_Z2_Final_analysis.xlsx")

# Initialise lists to store results
fault_data_list = []
displacement_data_list = []
cumulative_length_displacement_data = []

# Loop through each unique Fault ID
for fault_id in data["FaultID"].unique():
```

```
fault_data = data[data["FaultID"] == fault_id]

if fault_data.empty:
    continue

# Extract coordinates of top and bottom cut-offs
x_top = fault_data["x_top"].values
y_top = fault_data["y_top"].values
x_bot = fault_data["x_bot"].values
y_bot = fault_data["y_bot"].values

# Calculate fault properties
cumulative_length = calculate_cumulative_fault_length(x_top, y_top)
displacements = calculate_displacement(x_top, y_top, x_bot, y_bot)
orientation = calculate_fault_orientation(x_top, y_top)
direction = determine_fault_direction(orientation)
location = fault_data["Loc."].values[0]
Dmax = max(displacements)

# Perform power-law regression (excluding the first point to avoid zero length)
a, b = power_law_regression(cumulative_length[1:], displacements[1:])

# Store general fault data
fault_data_list.append({
    "Fault ID": fault_id,
    "Fault Length (m)": cumulative_length[-1],
    "Dmax (m)": Dmax,
    "Fault Orientation (Direction)": direction,
    "Fault Location (Loc.)": location,
    # "Scaling a": a,
    # "Scaling b": b,
})

# Store pointwise displacement data
for length, disp in zip(cumulative_length, displacements):
    entry = {
        "Fault ID": fault_id,
        "Cumulative Length (m)": length,
        "Displacement (m)": disp,
    }
    displacement_data_list.append(entry)
    cumulative_length_displacement_data.append(entry)

# Plot displacement along fault (example D-L profile)
xnew = np.linspace(min(cumulative_length), max(cumulative_length), 500)
spline = make_interp_spline(cumulative_length, displacements, k=3)
ynew = spline(xnew)

plt.figure()
plt.plot(xnew, ynew, label=f"Fault {fault_id}")
plt.title(f"Cumulative Fault Length vs Displacement for Fault {fault_id}")
plt.xlabel("Cumulative Fault Length (m)")
plt.ylabel("Displacement (m)")
plt.legend()
plt.show()
```